

**Structure, Phase Behavior, Molecular Dynamics and Conductivity  
of Columnar Liquid Crystals in the Bulk State and Under  
Confinement**

Vorgelegt von  
M.Sc.  
**Arda Yildirim**

von der Fakultät II - Institut für Chemie  
der Technischen Universität Berlin  
zur Erlangung des akademischen Grades  
Doktor der Ingenieurwissenschaften  
(Dr. -Ing.)

genehmigte Dissertation

Promotionsausschuss:

Vorsitzender: Prof. Dr. Matthias Bickermann

Gutachter: Prof. Dr. Michael Gradzielski

Gutachter: Prof. Dr. Regine von Klitzing (TU Darmstadt)

Gutachter: Prof. Dr. Andreas Schönhals (BAM)

Tag der wissenschaftlichen Aussprache: 20.12.2019

Berlin 2020

*“For everything in the world – for civilization, for life, for success – the truest guide is knowledge and science. To seek a guide other than knowledge and science is unawareness, ignorance and misguidedness.”*

Mustafa Kemal Atatürk, 1924

## ABSTRACT

Molecules of columnar liquid crystals (CLCs) typically consisting of a rigid aromatic core and flexible alkyl chains, can form a columnar mesophase by self-assembly. This self-assembly of the molecules in the columns are driven by  $\pi$ - $\pi$  interactions among the aromatic cores, while the alkyl chains fill the intercolumnar space. Among other promising features of CLCs for applications, the characteristic one-dimensional (1D) charge transport feature, due to  $\pi$ -orbitals with delocalized electrons, qualifies CLCs for variety of electronic application.

In this work, selected different columnar liquid crystals (CLCs) were systematically studied in order to elucidate their structure, phase behavior, molecular dynamics and conductivity. It is aimed to gain an understanding of the structure-dynamics-property relationships of the CLCs. The systems chosen in this study corresponds to hexakis(n-alkyloxy)triphenylene-based discotic liquid crystals (DLCs), which are extensively studied model systems and considered as “working horse” of the CLC research. In addition to the selected triphenylene-based CLCs, dipole-functionalized CLCs related to these selected CLCs and columnar ionic liquid crystals (ILCs) were chosen due to the interest of both scientific and application points of view.

The research work is focused on two different states of columnar liquid crystalline systems, which are “CLCs in the bulk state” and “a CLC under nanoconfinement”. On the one hand, for the investigations of CLCs in the bulk state, unfunctionalized as well as mono-dipole-functionalized triphenylene-based DLCs, triphenylene crown ether-based DLCs and columnar ILCs were studied. On the other hand, for the investigations of a CLC under nanoconfinement, an unfunctionalized triphenylene-based DLC confined into cylindrical nanopores was investigated. All CLCs studied in this work form a hexagonal columnar ( $\text{Col}_h$ ) mesophase. The main experimental techniques

applied for this study are differential scanning calorimetry (DSC), broadband dielectric spectroscopy (BDS), specific heat spectroscopy (SHS) employing differential AC-chip calorimetry and temperature modulated DSC (TMDSC), as well as fast scanning calorimetry (FSC). In addition, different complementary techniques were also used, including thermogravimetric analysis (TGA), Fourier transform infrared spectroscopy (FTIR), polarizing optical microscopy (POM), and X-ray diffraction (XRD).

In the first part of the thesis regarding the investigations on the different CLCs in the bulk state, the mesomorphic properties of the CLCs were explored using POM and XRD. The POM and XRD investigations evidenced the characteristic mesomorphic properties of the  $Col_h$  mesophases formed. Moreover, an amorphous halo in the XRD pattern was observed for all systems studied, which indicates nanophase separation between the substituents filling the intercolumnar area and the columns formed by the cores. The phase behavior of the CLCs was explored conducting conventional DSC measurements. The phase transition temperatures and enthalpies were determined. The DSC investigations showed that all CLCs studied, except one of the materials, have a plastic crystalline (Cry) phase, a  $Col_h$  mesophase and an isotropic (Iso) phase upon heating from 173 K. Furthermore, at least one thermal glass transition was detected by DSC for all CLCs. For the triphenylene-based DLCs, two different thermal glass transitions were found.

The molecular dynamics taking place in these systems as well as the conductivity were probed using BDS in a broad frequency and temperature range. Additionally, the glassy dynamics were studied using advanced calorimetric techniques; SHS and FSC. Hence, an understanding of the molecular dynamics was obtained from different perspectives. The investigations revealed a  $\gamma$ -process and  $\alpha$ -processes (multiple glassy dynamics) for all CLCs studied in this work. The  $\gamma$ -processes probed by BDS are assigned to the **PE**-like localized fluctuations of the methyl groups

of the alkyl chains filling the intercolumnar area. Among the multiple glassy dynamics detected ( $\alpha_1$ -,  $\alpha_2$ -,  $\alpha_3$ - and  $\alpha_4$ -processes), the  $\alpha_1$ -processes observed for all CLCs are attributed to the **PE**-like cooperative fluctuations taking place in the alkyl chains. Moreover, other glass dynamics ( $\alpha_2$ -,  $\alpha_3$ - and  $\alpha_4$ -processes) detected by BDS are ambiguously attributed to the cooperative fluctuations of the cores. Different possibilities of the molecular assignment of these glassy dynamics are proposed and further discussed in the thesis. In addition to the relaxation processes, a conductivity contribution was observed by BDS for all CLCs. In order to quantify the conductivity contribution as well as to reveal the conductivity mechanism, the conductivity contribution was analyzed in detail and discussed.

In the second part of the thesis regarding the investigations on a CLC under nanoconfinement, a triphenylene-based DLC confined into cylindrical nanopores of anodic aluminum oxide and silica membranes, having pore sizes from 161 nm down to 12 nm, was studied. n-Octylphosphonic acid (OPA) and n-octadecylphosphonic acid (ODPA) modifications were used to graft the hydrophilic inner walls of the pores with alkyl chains, consequently, the hydrophobic pore walls were obtained. The study considers both unmodified and modified pore walls. The phase behavior under the nanoconfinement was explored using DSC. The DSC investigations elucidated the pore size dependencies of the phase transition temperatures and enthalpies. The collective orientational order (dominating molecular ordering) under the confinement was probed using BDS. The molecular ordering under the nanoconfinement was deduced to be pore size and surface chemistry dependent. The results evidenced that the dominating planar axial configuration, only configuration suitable for electronic applications, was successfully achieved by both OPA- and ODPA-modifications for most of the pore sizes probed.

## ZUSAMMENFASSUNG

Moleküle von kolumnaren Flüssigkristallen (CLCs), die typischerweise aus einem starren aromatischen Kern und flexiblen Alkylketten bestehen, können durch Selbstorganisation eine kolumnare Mesophase bilden. Die Selbstorganisation der Moleküle in den Säulen wird durch  $\pi$ - $\pi$ -Interaktionen zwischen den aromatischen Kernen bewirkt, während die Alkylketten, die den zwischenkolumnaren Raum füllen. Neben anderen vielversprechenden Anwendungsmöglichkeit von CLCs qualifiziert die charakteristische eindimensionale (1D) Ladungstransportfunktion aufgrund von  $\pi$ -Orbitalen mit delokalisierten Elektronen die CLCs für eine Vielzahl von elektronischen Anwendungen.

In dieser Arbeit wurden ausgewählte verschiedene kolumnare Flüssigkristalle (CLCs) systematisch untersucht, um ihre Struktur, ihr Phasenverhalten, ihre Molekulardynamik und ihre Leitfähigkeit zu verstehen. Ziel ist es, ein Verständnis der strukturdynamischen Eigenschaftsbeziehungen der CLCs zu gewinnen. Die in dieser Studie ausgewählten Systeme entsprechen hexakis(n-alkyloxy)triphenylenbasierten diskotischen Flüssigkristallen (DLCs), die umfassend untersuchte Modellsysteme sind und als "Arbeitspferd" der CLC-Forschung gelten. Zusätzlich zu den ausgewählten triphenylenbasierten CLCs wurden aufgrund des wissenschaftlichen und anwendungsbezogenen Interesses dipolfunktionalisierte CLCs in Bezug auf diese ausgewählten CLCs und kolumnare ionische Flüssigkristalle (ILCs) ausgewählt.

Die Forschungsarbeiten konzentrieren sich auf zwei verschiedene Zustände kolumnarer flüssigkristalliner Systeme, den "CLCs im Volumentzustand" und "ein CLC unter Nanoconfinement". Zum einen wurden für die Untersuchung von CLCs im Volumentzustand sowohl unfunktionalisierte als auch mono Dipol funktionalisierte triphenylenbasierte DLCs,

triphenylenkronenetherbasierte DLCs und kolumnare ILCs ausgewertet. Andererseits wurde für die Untersuchungen eines CLC unter Nanoconfinement ein unfunctionalisiertes DLC auf Triphenylenbasis untersucht, das in zylindrischen Nanoporen eingeschlossen wurde. Alle CLCs, die in dieser Arbeit untersucht wurden, bilden eine hexagonal geordnete flüssigkristalline Mesophase. Die wichtigsten experimentellen Techniken, die für diese Studie verwendet werden, sind die Differential-Scanning-Kalorimetrie (DSC), die dielektrische Breitbandspektroskopie (BDS), die spezifische Wärmespektroskopie (SHS) mit differentieller AC-Chip-Kalorimetrie und die temperaturmodulierte DSC (TMDSC) sowie die Fastscan-Kalorimetrie (FSC). Darüber hinaus wurden auch unterschiedliche komplementäre Techniken eingesetzt, darunter die thermogravimetrische Analyse (TGA), die Fourier-Transformations-Infrarotspektroskopie (FTIR), die optische Polarisationsmikroskopie (POM) und die Röntgendiffraktion (XRD).

Im ersten Teil der Arbeit der Untersuchungen an den verschiedenen CLCs im Massenzustand wurden die mesomorphen Eigenschaften der CLCs mit POM und XRD studiert. Die POM- und XRD-Untersuchungen zeigten die charakteristischen mesomorphen Eigenschaften der gebildeten hexagonal geordnete flüssigkristalline Mesophase. Darüber hinaus wurde ein amorpher Halogen im XRD-Spektrum für alle untersuchten Systeme beobachtet, was auf eine Nanophasentrennung zwischen den Substituenten, die den interkolumnaren Bereich ausfüllen, und den von den Kernen gebildeten Säulen hinweist. Das Phasenverhalten der CLCs wurde weiter durch konventionelle DSC-Messungen untersucht. Die Phasenübergangstemperaturen und Enthalpien wurden bestimmt. Die DSC-Untersuchungen zeigten, dass alle untersuchten CLCs, mit Ausnahme eines der Materialien, eine plastisch kristalline (Cry)-Phase, eine hexagonal geordnete flüssigkristalline Mesophase und eine isotrope (Iso)-Phase beim Erwärmen von 173 K zu hohen Temperaturen aufweisen. Außerdem wurde mindestens ein thermischer Glasübergang mittels DSC für alle CLCs

nachgewiesen. Für die triphenylenbasierten DLCs wurden zwei unterschiedliche thermische Glasübergänge gefunden.

Die in diesen Systemen stattfindende Molekulardynamik sowie die Leitfähigkeit wurden mit BDS in einem breiten Frequenz- und Temperaturbereich untersucht. Zusätzlich wurde die glasartige Dynamik mit modernen kalorimetrischen Techniken wie SHS und FSC untersucht. Daher wurde ein Verständnis der molekularen Dynamik aus verschiedenen Perspektiven gewonnen. Die Untersuchungen zeigten einen  $\gamma$ -Prozess und  $\alpha$ -Prozesse (multiple glasartige Dynamik) für alle in dieser Arbeit untersuchten CLCs. Die von BDS untersuchten  $\gamma$ -Prozesse sind den PE-ähnlichen lokalisierten Fluktuationen der interkolumnaren Bereich füllenden Alkylketten zugeordnet. Die multiple glasartige Dynamik ( $\alpha_1$ -,  $\alpha_2$ -,  $\alpha_3$ - und  $\alpha_4$ -Prozesse) werden für alle CLCs beobachteten  $\alpha_1$ -Prozesse dem PE zugeschrieben, wie kooperative Schwankungen in den Alkylketten. Darüber hinaus werden andere durch BDS nachgewiesene Glasdynamiken ( $\alpha_2$ -,  $\alpha_3$ - und  $\alpha_4$ -Prozesse) mehrdeutig auf die kooperativen Fluktuationen der Kerne zugeordnet. Verschiedene Möglichkeiten der molekularen Zuordnung dieser glasartigen Dynamik werden vorgeschlagen und in der Arbeit weiter diskutiert. Zusätzlich zu den Relaxationsprozessen wurde durch die BDS ein Leitfähigkeitsbeitrag für alle CLCs beobachtet. Um den Leitfähigkeitsbeitrag zu quantifizieren und den Leitfähigkeitsmechanismus aufzuzeigen, wurde der Leitfähigkeitsbeitrag detailliert analysiert und diskutiert.

Im zweiten Teil der Arbeit wurde ein DLC auf Triphenylenbasis untersucht, das in zylindrischen Nanoporen von anodischen Aluminiumoxid- und Silica-Membranen mit Porengrößen von 161 nm bis 12 nm eingeschlossen wurde. n-Octylphosphonsäure- (OPA) und n-Octadecylphosphonsäure (ODPA)-Modifikationen wurden verwendet, um die hydrophilen Innenwände der Poren mit Alkylketten zu hydrophobieren. Die Studie betrachtet sowohl

unveränderte als auch modifizierte Porenwände. Das Phasenverhalten unter der Nanoconfinement wurde mit Hilfe von DSC untersucht. Die DSC-Untersuchungen erhellten die Porengrößenabhängigkeiten der Phasenübergangstemperaturen und Enthalpien. Die kollektive Orientierungsordnung (dominierende molekulare Ordnung) unter Confinement wurde mit Hilfe von BDS untersucht. Die molekulare Ordnung unter dem Nanoconfinement ist abhängig von der Porengröße und der Oberflächenchemie. Die Ergebnisse zeigten, dass die dominierende planare axiale Konfiguration, die nur für elektronische Anwendungen geeignet ist, erfolgreich durch OPA- und ODPA-Modifikationen für die meisten der untersuchten Porengrößen erreicht wurde.

## ACKNOWLEDGMENTS

First and foremost, I would like to express my deep gratitude to Prof. Dr. Andreas Schönhals for providing me the opportunity to carry out my Ph.D. work on this fascinating topic and to be a part of his research group in Bundesanstalt für Materialforschung und -prüfung (BAM). In addition to his precious guidance and support, he has always been an exemplary scientist and person to me in these four years with both his academic and personal attitude and values. Throughout this demanding journey, it has always been a comfort to feel his guidance, support, encouragement and patience, thanks so which today I became not only a more equipped scientist but also a better person. I would also like to acknowledge the financial support from the German Science Foundation DFG for SCHO-470/20-1.

Moreover, I would like to present my sincere appreciation to Prof. Patrick Huber and Kathrin Sentker from Hamburg University of Technology as well as to Prof. Dr. Sabine Laschat and Andrea Bühlmeier from the University of Stuttgart for their valuable contributions in this collaborative research work with them as well as their continuous support, understanding and valuable suggestions. Thanks to their contributions, this project was broadened the research possibilities including new liquid crystalline systems and different experimental techniques, and therefore this project has flourished. I also announce the German Science Foundation DFG for financial support for HU 850/5-1 and LA 907/17-1. Furthermore, I want to thank Dr. Michael Gradzielski (TU Berlin) and Prof. Dr. Regine von Klitzing (TU Darmstadt) for taking over the duty to review my thesis. In addition, I also would like to thank Dr. Jürgen E. K. Schawe for the experimental help and fruitful discussions about FSC.

I would like to thank all colleagues in BAM who kindly contributed to this work. First, I thank Prof. Dr. Heinz Sturm (BAM) for the guidance, help and support. Dr. Glen Jacob Smales and Dr.

Brian Richard Pauw are thanked for enabling SAXS experiments, Dietmar Neubert for his help in the DSC measurements, Sigrid Benemann for the SEM images, Dr. Jana Falkenhagen for the MALDI-TOF measurements and Christiane Weimann for her assistance in POM measurements. I also want to thank Sergej Petrov and Frank Milczewski for their help with the daily problems faced in the lab. Mohamed Aejaz Kolmangadi as a M.Sc. student working in this presented work, is sincerely thanked due to his considerable contributions for the studies on columnar ionic liquid crystals and triphenylene crown ether-based discotic liquid crystals.

I also would like to express my thankfulness to all my colleagues in my group in BAM, Dr. Sherif Madkour, M.Sc. Paulina Szymoniak, M.Sc. Marcel Gawek, Dr. Shereen Omara, Dr. Huajie Yin, Dr. Anna Maria Elert, Dr. Ievgeniia Topolniak, Maximilian Ebisch, Korinna Altmann, Caroline Goedecke, and Dr. Nora Konnertz not only for all scientific support but also for the countless memories and joy. Especially thanks to Dr. Sherif Madkour and M.Sc. Paulina Szymoniak, this almost four years of my research work at BAM was great pleasure and joy with them despite the challenges, struggles and frustrations I had during my Ph.D. work.

At the end, I would like to thank my friends around the world for their love and support throughout my years of studying. Among them, I need to add specials thanks to Dr. Özgün Attila, Görkem Özmen, M.Sc. Onur Doğu and Özkan Öznar for their countless support and encouragement to move forward as well as their priceless friendship. Also, I want to thank my Berlin Family – Neşe Çakmak Görür, Can Görür, Elif Eryilmaz Sigwarth and Vincent Sigwarth – for providing me the warmth of a family in Berlin and their incorporeal support. Most importantly, I would like to thank my lovely girlfriend, Meriç Benderlioğlu, so much for her endless patience, being there in the good time and (especially) in the bad times, the countless sacrifices she has made and her endless perseverance. She has not only patiently supported me to achieve my goals but

also brought me so much happiness and love. She has been the source of my motivation and strength. Finally, I would like to express my sincere thankfulness and gratitude to my parents, Neşe and Nadir Yıldırım, as well as my brother Tolga Yıldırım for their complete trust and support not only throughout my Ph.D. study but also throughout my whole life. The sentences that I can establish for my family whether written or verbal, are not enough to describe my feelings – full of love and gratitude – towards them. Accomplishment of this work and where I am today, is the result of their constant love, patience, trust, and encouragement throughout my entire life.

To My Parents and Meriç Benderliođlu

# TABLE OF CONTENTS

CHAPTER 1 – INTRODUCTION.....	1
CHAPTER 2 – BACKGROUND.....	6
2.1. Columnar Liquid Crystals.....	6
2.1.1. Discotic Liquid Crystals.....	9
2.1.2. Discotic Liquid Crystals Under Nanoscale Confinement.....	13
2.1.2. Ionic Liquid Crystals.....	15
2.2. Glass Transition and Glassy Dynamics.....	16
2.2.1. Glass Transition.....	16
2.2.2. Glassy Dynamics.....	19
CHAPTER 3 – EXPERIMENTAL TECHNIQUES.....	23
3.1. Principles of Main Experimental Techniques.....	24
3.1.1. Broadband Dielectric Spectroscopy.....	25
3.1.2. Specific Heat Spectroscopy.....	33
3.2 Experimental Section.....	35
3.2.1. Thermogravimetric Analysis.....	35
3.2.2. Fourier Transform Infrared Spectroscopy.....	36
3.2.3. Differential Scanning Calorimetry.....	36
3.3.4. Polarizing Optical Microscopy.....	36
3.3.5. X-ray Scattering.....	37
3.3.6. Broadband Dielectric Spectroscopy.....	39
3.3.7. Specific Heat Spectroscopy.....	41
3.3.8. Fast Scanning Calorimetry.....	44
3.3. Materials.....	45
3.3.1. Triphenylene-Based Discotic Liquid Crystals.....	45
3.3.2. Triphenylene Crown Ether-Based Discotic Liquid Crystals.....	47
3.3.1. Columnar Ionic Liquid Crystals.....	48
3.4. Preparation of the Samples for the Investigation of a CLC under Confinement.....	49
3.4.1 Confining Hosts.....	49
3.4.2. Surface Modification of the Confining Hosts.....	51
3.4.3. Pore Filling Procedure.....	53
CHAPTER 4 – COLUMNAR LIQUID CRYSTALS IN THE BULK STATE.....	54

4.1. Triphenylene-Based Discotic Liquid Crystals .....	54
4.1.1. Mesomorphic Properties .....	55
4.1.2. Phase Behavior .....	58
4.1.3. Molecular Mobility .....	61
4.1.4. Conclusions .....	72
4.2. Triphenylene Crown Ether-Based Discotic Liquid Crystals .....	74
4.2.1. Phase Behavior .....	75
4.2.2. Molecular Mobility .....	77
4.2.3. Conductivity .....	83
4.2.4. Conclusion .....	85
4.3. Ionic Liquid Crystals .....	87
4.3.1. Phase Behavior .....	88
4.3.2. Molecular Mobility .....	90
4.3.3. Conductivity .....	98
4.3.4. Conclusion .....	100
CHAPTER 5 – A COLUMNAR DISCOTIC LIQUID CRYSTAL UNDER NANOSCALE CONFINEMENT .....	102
5.1. Mesomorphic Properties of Bulk .....	103
5.2. Phase Behavior Under Nanoscale Confinement .....	105
5.3. Orientational Order under Nanoscale Confinement .....	112
5.4. Conclusion .....	116
CHAPTER 6 – CONCLUSION & OUTLOOK .....	119
APPENDIX I .....	128
APPENDIX II – Supporting Information for Section 4.1 .....	134
APPENDIX III – Supporting Information for Section 4.2 .....	146
APPENDIX IV – Supporting Information for Section 4.3 .....	148
APPENDIX V – Supporting Information for Chapter 5 .....	151
APPENDIX VI .....	156
References .....	162

## CHAPTER 1 – INTRODUCTION

Plastics have been used as insulators since they were considered as materials do not conduct electricity until the 1970s. In 1977, conductive polymers were discovered and developed by Alan Heeger, Alan MacDiarmid, and Hideki Shirakawa, who were awarded by Nobel Prize in Chemistry in 2000 for their “*discovery and development of conductive polymers*”.<sup>1</sup> Their discovery has revealed the possibility of using conjugated organic materials as alternative of silicon for electronic applications. The presence of a conjugated bond system (double bonds), consisting of  $\pi$ -orbitals with delocalized electrons, is a prerequisite for conductive polymers. As an alternative to conductive (conjugated) polymers, columnar liquid crystals (CLCs), liquid crystals forming a columnar mesophase, are promising conjugated materials for electronic applications.<sup>2,3</sup> CLCs features advantageous properties for electronic applications such as long-range self-assembling ability (order), one-dimensional (1D) charge transport and light-harvesting ability due to the  $\pi$ - $\pi$  stacked columnar structure.<sup>4</sup> Thus, CLCs are considered as a new generation of organic semiconductors.<sup>5</sup>

The charge carrier mobility and the stability of the columnar mesophase are the most important properties of CLCs for their applications in electronics. Their conductivity is related to the charge carrier mobility, and their phase behavior is associated with the stability of the columnar structure, therefore, that of the mesophase. Furthermore, it is more than likely that the molecular mobility (molecular dynamics) on different timescales and the columnar structure of CLCs play an important role for the conductivity.<sup>6,7</sup> Therefore, the structure, the phase behavior and the molecular dynamics of CLCs must be revealed. An understanding of the structure-property

relationships, the molecular mobility as well as the electrical conductivity is crucial to tailor and to optimize the properties of CLCs for electronic applications.

From the basic research point of view, CLCs are perfect candidates to study the molecular mobility in systems where order and mobility competes. This is because the columnar mesophase has a morphology in between a three-dimensional ordered crystal and amorphous systems which can be tuned by the chemistry of the molecules. This concerns especially the glassy dynamics related to the glass transition which has been one of the intensely and controversially debated topics in condensed matter science. The detailed investigation of such materials might shine some light to understand the glass transition not only for CLCs but also for polymers, silicate or metallic glasses, for novel types of electrolytes like ionic liquids, and even for biological systems such as proteins or DNA. Because of the fact the structure of the CLCs can be tuned by chemistry, special problems can be addressed like self-confinement effects or a glass transition in lower spatial dimensions because a since the columns can be considered as a one-dimensional (1D) fluid.<sup>8</sup>

For the applications, CLCs must be confined into a certain geometry; thin films (1D confinement) or the confinement into nanochannels (2D confinement). The phase behavior under confinement must be explored since the confinement influences the phase behavior. Moreover, from the application point of view, controlling the alignment of columnar direction (molecular ordering) is a prerequisite. To do so, many strategies have been developed to control the alignment of CLCs such as alignment by surface modifications of the pore walls of confining hosts, application of magnetic and electric fields, zone casting, etc..<sup>9</sup>

The aim of this work is to understand molecular dynamics, phase behavior and conductivity of different columnar liquid crystalline systems and to reveal their structure-property relationships

by employing a combination of different investigation techniques. The CLCs selected and investigated in the research work presented in this dissertation are symmetrical unfunctionalized as well as asymmetrical mono-dipole-functionalized triphenylene-based discotic liquid crystals (DLCs), triphenylene crown ether-based unsymmetrical DLCs and columnar ionic liquid crystals. For this purpose, the molecular dynamics and conductivity were investigated by broadband dielectric spectroscopy (BDS). In addition to the molecular dynamics probed from the dipole fluctuations perspective using BDS, advanced calorimetric techniques such as specific heat spectroscopy (SHS) and fast scanning calorimetry (FSC) were applied to probe glassy dynamics from entropy fluctuations perspective. Conventional differential scanning calorimetry (DSC) measurements were conducted to study the phase behavior including the thermal glass transitions at temperatures down to 173 K and to 103 K using nitrogen and helium as purge gases respectively. In addition, it is aimed to explore the phase behavior and the molecular ordering (alignment) of a symmetrical triphenylene-based DLC confined into nanopores. It is also intended to control the molecular ordering under the confinement by surface modification of the nanopores to achieve the type of molecular ordering required for the applications. The molecular ordering inside the nanopores was determined by BDS and the phase behavior under confinement was explored by DSC.

This thesis is organized as follows. *Chapter 1*, introducing to the CLCs and the motivation behind the research, is followed in *Chapter 2* by an overview of CLCs in the bulk and confined states as well as glass transition and glassy dynamics. *Chapter 3* provides the fundamental information about the main experimental techniques. It starts with giving the idea behind the investigation strategy using different techniques. Then, it continues with the principles of main

characterization techniques. Afterwards, all the experimental procedures and the materials used in this work are introduced in detail.

*Chapter 4* addresses the main results and discussions of different CLCs in the bulk state. *Section 4.1* presents the investigation of the molecular dynamics of a selected series of dipole functionalized triphenylene-based DLCs, which was investigated in a systematic way to reveal the phase behavior and the molecular dynamics. The investigated DLCs are pentapentyloxytriphenylenes carrying ethyl glycolate (**SHU09**), hexanoyl (**SHU10**), trifluoromethyl (**SHU11**), and diethyleneglycol (**SHU12**) units. The mesomorphic properties and the phase behavior of the DLCs **SHU09-SHU12** were studied by polarizing optical microscopy (POM), X-ray diffraction (XRD), and DSC. The molecular dynamics of all compounds were investigated by a combination of state-of-the-art BDS and advanced calorimetric techniques such as FSC and SHS. Glassy dynamics were proven for the detected processes unambiguously due to the extraordinary broad frequency range covered. The results were compared to the corresponding unfunctionalized symmetrical DLC (**HAT5**), which was also studied in this work.

A study on the phase behavior and the molecular dynamics of triphenylene crown ether-based DLCs having different lengths of alkyl chains, is given in *Section 4.2*. The phase behavior and the molecular dynamics were explored by DSC and BDS respectively. *Section 4.3* presents the results of the investigation of the molecular mobility of two linear-shaped tetramethylated guanidinium triflate ionic liquid crystals (ILCs) having different lengths of alkyl chains using BDS and SHS. The results are discussed in detail, and different molecular assignments of the processes are suggested. Furthermore, at higher temperatures electrical conductivity is detected, and was analyzed in detail. This result is discussed by a change in the charge transport mechanism upon phase transition from the plastic crystalline phase to the columnar mesophase.

*Chapter 5* provides a study on the effect of cylindrical confinement on the phase behavior and the molecular ordering of hexakis(hexyloxy)triphenylene (**HAT6**), a triphenylene-based DLC, confined within nanochannels. Anodic aluminum oxide (AAO) and silica membranes with varying pore diameters, from 161 nm down to 12 nm, were used as confining hosts. Furthermore, it is aimed to obtain an axial ordering or to increase the degree of axial ordering by chemical modification of the pore walls. Therefore, both unmodified and modified pore walls were considered. In the latter case, the pore walls of AAO membranes were chemically treated with n-octylphosphonic acid (OPA) and n-octadecylphosphonic acid (ODPA). The study covers a broad pore size range, and therefore a more detailed understanding of the confinement effect on the phase behavior is obtained. The phase behavior was explored by differential scanning calorimetry (DSC) allowing the detection of changes in the phase behavior. The pore size dependencies of the phase transition temperatures were approximated using the Gibbs-Thomson-equation, where the estimated surface tension is dependent on the molecular ordering of **HAT6** molecules within the pores. BDS was used to investigate the collective orientational order of the molecules of **HAT6** confined into cylindrical nanopores.

The last but not the least, *Chapter 6* summarizes the research work presented, drawing a general conclusion for all the above-mentioned studies, followed by a short outlook on the next interesting research work in the field.

## CHAPTER 2 – BACKGROUND

### 2.1. Columnar Liquid Crystals

Liquid crystals (LCs) are unique materials, possessing the properties of both the crystalline and the liquid states where they have liquid crystalline mesophases in the temperature range between these two states.<sup>10</sup> Molecules which form liquid crystalline mesophases have high orientational and positional order in their crystalline phases (order) and low positional order in their liquid state (mobility).<sup>11,12</sup> Due to the properties of LCs combining that of liquids and solid crystals, they are sometimes described as ordered fluids.<sup>13</sup> The features of LCs such as their fluidic and elastic properties allow them to respond to different types of external stimuli (e.g. heat, light, mechanical force, electric and magnetic fields) and interact with surfaces.<sup>13</sup> These features bring advantageous properties for their application such as ease of processability, ability of the alignment of the molecules between electrodes and self-healing of structural defects, where charge carriers are stuck at grain boundaries.<sup>14</sup> They also feature properties such as dynamic molecular order and self-assembling as well as anisotropic optical, electrical, and magnetic properties.<sup>10,12</sup> Due to these properties, LCs are qualified for a wide variety of electronic applications. Today, flat-panel display application of LCs is still the most significant application of LCs since LCs are optically functional molecules possessing both optical anisotropy leading to parallel and perpendicular refraction effects and fluidity bringing controlled switching of molecular alignment under electric fields.<sup>13</sup> They are also used in optical connectors, switches, molecular sensors and detectors, etc.<sup>15-18</sup> It is important to note that LCs in general are classified either as thermotropic or as lyotropic and, in the scope of the research work presented here, only thermotropic LCs are considered.

LCs form a rich variety of mesophase; smectic, nematic, cholesteric, columnar phases. The mesophases are characterized according to their symmetry in terms of the orientational and translational degrees of freedom.<sup>10</sup> Among these mesophases formed by LCs, columnar mesophase, exhibiting long-range positional/translational order in at least one direction and orientational order, is quite interesting regarding their applications. This is due to the fact that columnar nanostructures, formed by the self-assembly in a columnar mesophase, feature 1D high charge mobility along the column axis owing to the delocalization of  $\pi$ -electrons of the LC molecules. This makes LCs forming a columnar (columnar liquid crystals (CLCs)) mesophase promising candidates for electronic applications. Thus, CLCs have gained a growing interest<sup>19</sup> since the first clear-cut report of a columnar mesophase formed by a hexasubstituted benzene-based LC in 1977.<sup>20</sup> Since then, a large number of CLCs has been synthesized. The molecules of most of the CLCs typically consist of a rigid aromatic core and several flexible groups (alkyl chains) substituted the core by different linkers such as ether, ester, benzoate, alkyne, etc. The aromatic core of CLCs is usually benzene or polyaromatics such as triphenylenes, perylenes, hexa-peri-hexabenzocoronenes, triphenylene crown ethers, etc.<sup>4,8</sup> The chemical structure of molecules of CLCs and the mesophase morphologies of CLCs are illustrated in Figure 1. Discotic liquid crystals (DLCs) are typical examples of CLCs besides others. Furthermore, ionic liquid crystals (ILCs) forming a columnar mesophase is also classified as CLCs.

The self-assembly of molecules of CLCs into the columns is driven by the unfavorable interactions between the aromatic core and the flexible substituents (leading to nanophase separation) and the favorable core-core interactions ( $\pi$ - $\pi$  interaction among the aromatic cores).<sup>3</sup> On the one hand, the  $\pi$ - $\pi$  interactions of the aromatic cores stacked in the columns also result in 1D high charge carrier mobility along the column axis. On the other hand, the flexible alkyl chains

fill the intercolumnar space and act as an insulator. The flexible alkyl chains are disordered among ordered columns of the core in the intercolumnar area. This disorder prevents a 3D crystal formation while a mesophase is formed upon cooling from the isotropic phase. This is essential for the formation of a columnar mesophase, where the nanophase separation between the ordered columns and the disordered intercolumnar area is present.<sup>8</sup> Nanophase separation has been evidenced by an amorphous halo observed in the X-ray pattern of CLCs.<sup>8,21</sup> Such a nanophase separation was reported also for different systems such as a series of poly(*n*-alkyl acrylates),<sup>22</sup> poly(*n*-alkyl methacrylates)<sup>22</sup>, poly(3-alkyl thiophenes)<sup>23</sup> and poly(1,4-phenylene-2,5-*n*-dialkyloxy terephthalates)<sup>24</sup> having longer *n*-alkyl side chains.

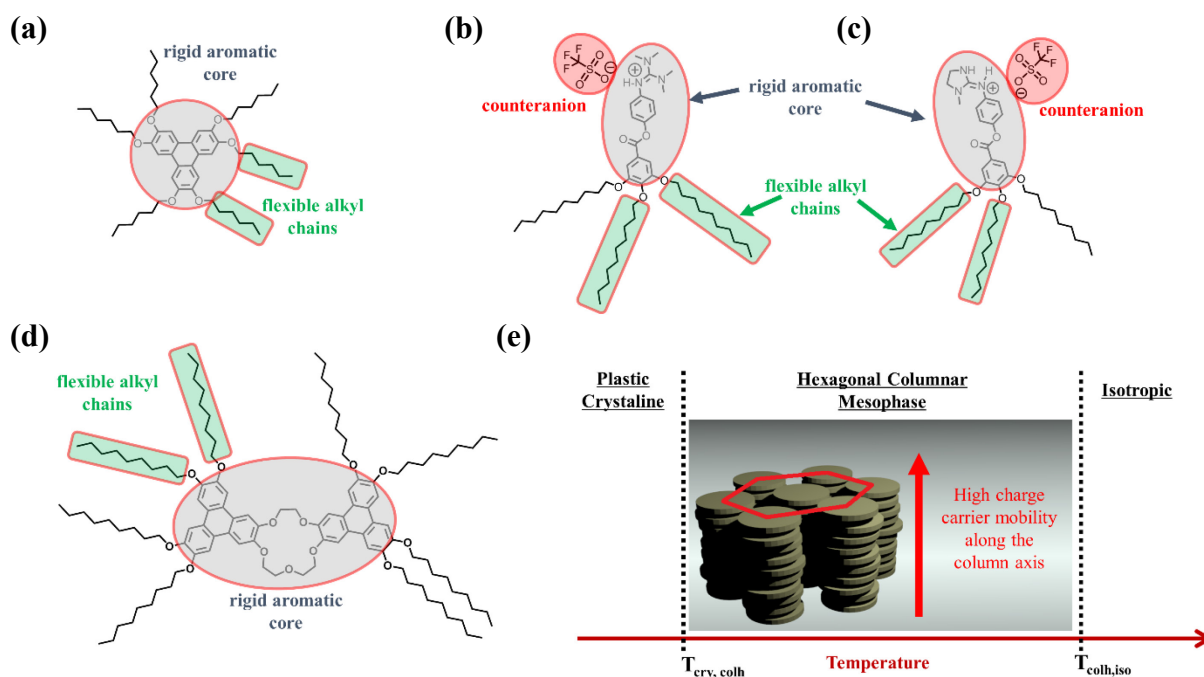


**Figure 1.** Chemical structure of molecules of CLCs; (a) a triphenylene-based DLC, (b) a guanidinium phenylalkoxybenzoates-based columnar ILCs with acyclic guanidinium head group and triflate counteranion, (c) a guanidinium phenylalkoxybenzoates-based columnar ILCs with cyclic guanidinium head group and triflate counteranion, and (d) a triphenylene crown ether-based DLC. (e) Illustration of phase behavior of CLCs and structure formed in a hexagonal columnar mesophase by CLCs (adapted from ref. 25). For the sake of simplicity, drawing does not show alkyl chains and shows only aromatic cores for the columnar structure.

An understanding of the structure-property relationships, the molecular mobility and the electrical conductivity is crucial to tailor and to optimize their properties for electronic

applications. Therefore, CLCs have been studied by differential scanning calorimetry (DSC), X-ray diffraction (XRD), neutron scattering, Raman and UV-Vis spectroscopy, nuclear magnetic resonance (NMR), optical birefringence, broadband dielectric spectroscopy (BDS), specific heat spectroscopy (SHS), etc.<sup>8,21,26-40</sup>

### 2.1.1. Discotic Liquid Crystals

Discotic liquid crystals (DLCs) consist of molecules that have a disk-like (also bowl-like, cone-like, or pyramidal<sup>12</sup>) rigid aromatic cores connected *via* flexible alkyl chains. DLCs form variety of columnar mesophases such as square, oblique, rectangular and hexagonal columnar phases; therefore, they are classified as CLCs. The hexagonal columnar ( $Col_h$ ) mesophase is commonly formed by DLCs, between plastic crystalline (Cry) and isotropic (Iso) phases as the molecules can self-organize and stack into hexagonal ordered columns in a 2D-lattice where column axes are parallel to each other. According to the classification of columnar phases pioneered by Tschierske<sup>10</sup>,  $Col_h$  phase is described by the plane group  $p6mm$ .<sup>8</sup> This classification is not only valid for DLCs but also more generally for CLCs. An example for the chemical structure of the molecule of a DLC and the phase morphologies of DLCs is given in Figure 2 for a thermotropic triphenylene-based DLC. The red rhombuses shown in Figure 2b represent  $p6mm$  plane groups. In the scope of the work presented here, only CLCs forming  $Col_h$  mesophases are considered.

It is important to note that the plastic crystalline phase usually formed by DLCs at low temperatures phase should be called discotic plastic crystalline phase to distinguish it from the plastic crystalline that of small molecules.<sup>41,42</sup> However, this is not generally done in the literature. Therefore, in this presented thesis also the term plastic crystalline (Cry) phase is used.

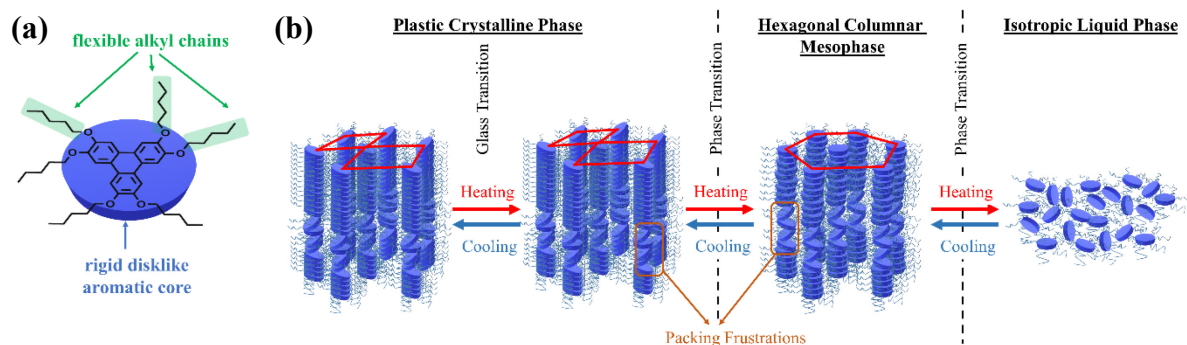


**Figure 2.** (a) Chemical structure of molecule of a triphenylene-based DLC hexakis(pentyloxy)triphenylene **HAT5**. (b) Structures formed by **HAT5** in different phases. Figure was taken from ref. 43 with permission (see Section 4.1 for the permission).

Application of DLCs, e.g. as optical compensation films for LC displays<sup>44,45</sup> and gas sensors<sup>46,47</sup>, are still in the proof-of-concept state. However, research on DLCs over the last decades has shown that they can be considered promising materials for use in electronic applications such as organic field-effect transistors (OFETs), organic light emitting diodes (OLEDs) and organic photovoltaics (OPVs) because they exhibit 1D high charge mobility along the axis of the column in Col<sub>h</sub> mesophase and light-harvesting ability due to the  $\pi$ - $\pi$  stacked columnar structure.<sup>5,13,48,49</sup> Although a number of studies has been done and efforts have been made to get an understanding of their intrinsic properties,<sup>13,31,50-52</sup> they are not completely understood. Therefore, they should be further investigated in a systematic way and understood to uncover their fundamental properties and potential for applications.

One of the first DLCs reported in the literature is triphenylenes (triphenylene-based DLCs). Therefore, most of the studies were carried out on triphenylene-based DLCs, especially on symmetric triphenylenes, in the bulk and under spatial confinement.<sup>8,10,21,25,53,54</sup> Beside the symmetric triphenylenes, since the early work of Rego<sup>55</sup>, Kilburn<sup>56</sup>, Cooke<sup>57</sup>, Kumar<sup>58</sup>, and Kelly<sup>59</sup> there is also a considerable interest in dipole functionalized low symmetry triphenylenes,<sup>60,61</sup> because they can be used as building blocks in liquid crystalline dimers and hybrid materials.<sup>8</sup> Recent studies on such triphenylene derivatives revealed promising

self-assembly and photophysical properties, e.g. blue-light emitters<sup>62</sup> and high birefringence, which are useful for terahertz communication optical elements, optical attenuators and holographic devices.<sup>63</sup> As mentioned in *Introduction* in general for CLCs, also low symmetry triphenylene-based DLCs are unique materials, which can provide knowledge to uncover the glass transition phenomena, a longstanding topical problem of condensed matter science. Investigating the molecular mobility in such a system where order and mobility competes, helps to gain an insight into the glass transition phenomena. Moreover, the structure of these DLCs can be tuned by chemistry. This ability to tailor their structure can provide opportunity to address a glass transition in intercolumnar area and/or in intracolumnar area. For example, a dipole functionalization of the core of molecules of a DLC allows to probe the glassy dynamics (molecular mobility related to a glass transition) in the intracolumnar area using BDS (see ref.s 39 and 64). Since the columns can be considered as one-dimensional fluid<sup>8</sup>, a glass transition taking place in the intracolumnar area can be considered as a glass transition of one-dimensional fluid.

The competition in DLCs takes place between the ordered columns formed by the aromatic cores and the disordered substituents filling the intercolumnar space. Moreover, such a competition in the intracolumnar area might presumably occur between the ordered part of the columns and the disordered portion of the columns, where packing frustrations are present (Figure 2b). From the basic research point of view, it is interesting to study these complex liquid crystalline systems where order and mobility compete. As it is also mentioned in *Introduction*, this is because different physical phenomena, for instance self-confinement effects and/or a glass transition in lower spatial dimensions (one-dimensional fluid), can be addressed by investigating the molecular dynamics of these systems. There are only a few number of studies reporting a glass transition observed in the Cry phase for columnar DLCs.<sup>21,25,35-38,49,64</sup> For plastic crystals, a glass transition was reported by

Suga and Seki for the first time.<sup>65</sup> Further examples for glassy dynamics in plastic and also condis (conformationally disordered) crystals are discussed in literature (see ref.s 66-69).

It is more than likely that the molecular mobility in both the Cry and the Col<sub>h</sub> phases of DLCs plays an important role for the conductivity.<sup>6,7</sup> A change in the conductivity at the phase transition from the Cry phase to the Col<sub>h</sub> phase can be used as a switch in the application where for field-effect transistors conductivity in the liquid crystalline phase has to be considered. Therefore, investigations on the molecular mobility and understanding of it are highly demanded from both fundamental research and application point of views.

Werth et al.<sup>70</sup> reported different monofunctionalization of the symmetrical triphenylene hexakis(pentyloxy)triphenylene **HAT5** with an ester group, which prevents crystallization. Consequently, a glassy columnar phase is formed. Their study illustrates further that small molecular structural changes, such as dipole functionalization, may considerably affect the phase behavior due to the specific conformation of the functional group including dipole interactions. Such a dipole functionalization gives not only the possibility to study its effect on the phase behavior but also enables to investigate the molecular dynamics including possible glassy dynamics using BDS. In the literature, dipole functionalized low symmetry hexabenzocoronene-based DLCs were studied to investigate the molecular dynamics including glass dynamics using BDS.<sup>37,39,64</sup> In general, BDS is a powerful tool to explore the molecular dynamics with a high sensitivity over a broad frequency and temperature range. The investigation of the molecular dynamics of symmetrical DLCs using BDS is challenging and limited to a certain extent due to their weak dipole movement.

### 2.1.2. Discotic Liquid Crystals Under Nanoscale Confinement

DLCs can also be nanoconfined into a specific geometry, e.g. as thin films or in cylindrical nanochannels, in order to optimize their use in electronic applications. Metal oxide membranes that have a parallel alignment of cylindrical nanopores and narrow pore size distribution, can be produced by electrochemical etching. Confining DLCs into the cylindrical nanopores of metal oxide membranes has gained much interest. This is due to the fact that investigations on such confined systems can address fundamental questions such as phase behavior and glass transition dynamics, whilst also helping to shed light upon the structure-property relationship of soft matter systems under confinement.<sup>50,52</sup> Moreover, from the application point of view, it opens up the possibility to prepare nanowires through the dissolution of the host membrane since the columns formed by DLCs can be considered as isolated, one-dimensional, conducting nanowires.<sup>71</sup>

Nanoconfinement influences the properties of DLCs like for other soft mater systems<sup>72</sup> which have to be revealed for the applications at the nanoscale. The phase behavior under confinement and the molecular ordering of DLCs within pore structures are two of the main properties defining their applications in nanotechnology.<sup>5</sup> Hence, several investigations have been carried out to elucidate the phase behavior and molecular ordering of DLCs confined within the nanopores of metal oxide membranes.<sup>31,51,52,73-75</sup> Compared to bulk DLCs, a decrease in phase transition temperatures is observed along with the formation of additional structures under confinement that has been reported for pyrene- and triphenylene-based DLCs.<sup>50,52,74</sup> On the other hand, controlling the molecular ordering within the pore structures is highly desirable for improving application relevant properties such as conductivity and light-harvesting abilities. Hence, aligning the columns of DLCs parallel to the axis of the pores is therefore crucial for their success in specific applications.

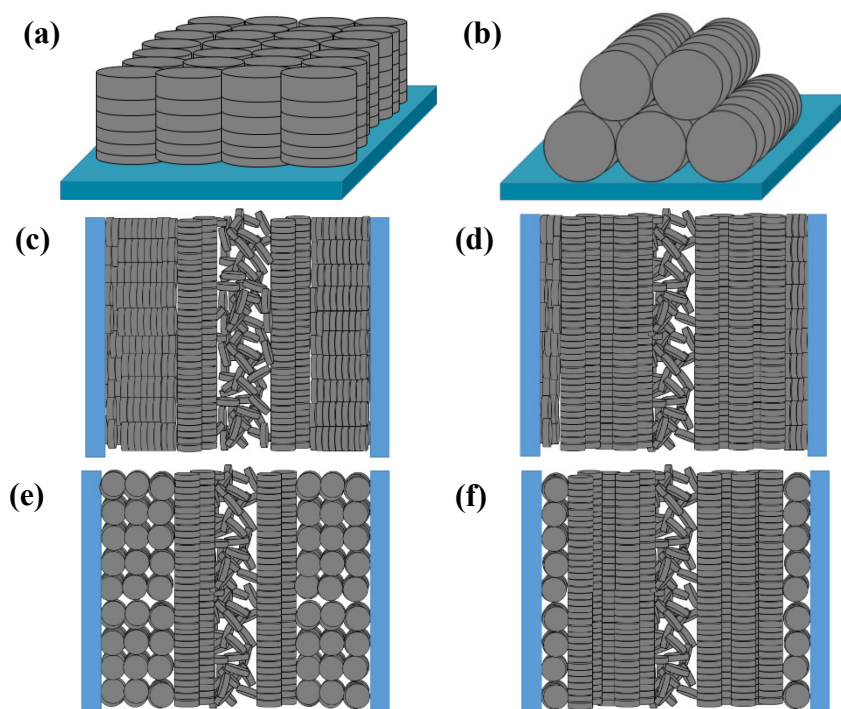


**Figure 3.** Types of molecular ordering of DLCs under confinement (a) Homeotropic (face-on) alignment and (b) planar (edge-on) alignment on a free surface. (c) Homeotropic radial configuration, (d) planar axial configuration, (e) planar radial configuration, and (f) another planar axial configuration dominating configuration type inside a cylindrical channel with a disordered isotropic core. For the sake of simplicity, drawings do not show alkyl chains and show only aromatic cores for the molecular ordering. Figure was taken from ref. 25 with permission (see *Chapter 5* for the permission).

Planar (edge-on anchoring) and homeotropic (face-on anchoring) alignments are the two possible types of molecular ordering of DLC molecules with respect to a flat surface (Figure 3a and Figure 3b). These two alignments describe the ordering in thin films of DLCs and DLCs confined between two parallel solid substrates.<sup>26</sup> However, by confining DLCs within cylindrical pores, describing the molecular ordering becomes more complicated. The molecules of the confined DLCs possess multiple types of ordering, and thus, describing this ordering within cylindrical pores solely as planar or homeotropic is insufficient. Hence, additional directional characterization terms such as ‘axial’ and ‘radial’ should be used together with the anchoring type for clarity. It has been shown that planar axial, planar radial (circular concentric)<sup>54,76</sup> and homeotropic radial (logpile)<sup>77</sup> configurations are the predominant forms of ordering within cylindrical pore structures (Figure 3c-f). There is a competition between these configurations,

caused by different interfacial tensions observed between air/liquid crystal, liquid crystal/pore walls and liquid crystal/liquid crystal. The dominating type defines the configuration for the overall system.

Among the above-mentioned types of configurations found within the pores, only the axial configuration is suitable for electronic applications. Studies have shown that axial configurations are scarcely achieved, whereas homeotropic radial and planar radial configurations are more commonly observed for DLCs confined within the nanopores of metal oxide membranes.<sup>31,54,73-77</sup> However, a dominating axial configuration might be obtained through chemical modification of the pore surface.<sup>31</sup> Beside the surface modifications changing the host-guest interactions, a proper choice of the host pore size with respect to that of the guest DLC can lead to better configurational control. Recently, Zhang *et al.*<sup>76</sup> reported that the dominating ordering type changes with pore size.<sup>76,77</sup> Furthermore, they observed a transition from a planar radial configuration to an axial configuration with increasing columnar rigidity of the DLC.<sup>76</sup> The column rigidity increases with aromatic core size, hence, it can be tuned to obtain the desired configuration through proper choice of the DLC.

### **2.1.2. Ionic Liquid Crystals**

Ionic liquid crystals (ILCs) are classified as liquid crystalline compounds containing anions and cations. They combine the properties of LCs and ionic liquids such as dynamic molecular order, self-assembly, anisotropic physical properties with ionic conductivity. Ionic conductivity in that case is the characteristic property of ILCs that differentiate them from conventional LCs.<sup>78</sup> Similar to DLCs, ILCs can also form columnar mesophases.<sup>78,79</sup> Columnar ILCs possess both ion conductivity and high charge carrier mobility along the column axis.

Recently, Axenov and Laschat<sup>79</sup> as well as Binnemans<sup>78</sup> have published reviews on ILCs including also a discussion of the columnar case. As it is reported in these reviews, ILCs are currently receiving a great interest as highly conductive solid-state electrolytes, nonvolatile phase-change (energy storage) materials, catalysts, nanocomposites, separation membranes, proton-conducting membranes for applications in molecular electronics, batteries, fuel cells, membrane and capacitors. Columnar ILCs are more promising candidates for the most these applications, especially for applications in molecular electronics, due to their anisotropic 1D ionic conductivity feature in a Col<sub>h</sub> mesophase. Furthermore, most literature works about columnar ILCs cited in these reviews focused on the synthesis and the characterization of the mesomorphic properties by DSC, XRD as well as polarized optical microscopy (POM).<sup>80-85</sup> Only a few studies investigating the ionic conductivity of the columnar ILCs have been reported.<sup>86-89</sup> Therefore, a molecular level understanding of the dynamics and of the conductivity of ILCs is required to design and tune their properties for the electronic applications as generally discussed for CLCs above.

## **2.2. Glass Transition and Glassy Dynamics**

Here in this section, both the thermodynamic and kinetic aspects of the glass transition are discussed. Furthermore, an understanding of the underlying physics of glass-forming materials is introduced.

### **2.2.1. Glass Transition**

The glass transition is a thermo-kinetic phenomenon.<sup>90</sup> It determines the use temperature for practical applications and processing temperature for glass-forming materials.<sup>91</sup> Glass-forming materials, including a wide variety of materials ranging from metals and liquids to polymers,

solidifies as glasses rather than crystals. Glass-forming materials experience a drastic kinetic slowdown of the molecular dynamics when they are cooled toward their glass transition temperature without any obvious structural change.<sup>92</sup> Understanding the origin of this behavior as well as the underlying physics of glass-formers is a major scientific challenge. Although glass transition has been extensively studied, it has been on a debate in condensed matter science for a long time and is still not fully understood.

The temperature dependence of the characteristic thermodynamic quantities such as specific volume and enthalpy changes but continuously upon the glass transition, where the mid-point of this region is often defined as thermal glass transition temperature ( $T_g^{\text{thermal}}$ ). Due to the continuity of the change in the characteristic thermodynamic quantities upon a glass transition, glass transition is not a phase transition. Indeed, it is a thermo-kinetic phenomenon (see Figure 4a).

At high temperatures, a glass-former flows more or less like an ordinary fluid, which has a shear modulus value of approximately zero. Cooling a glass-former material or system from its liquid state without crystallizing, increases its density and viscosity. As a result, the molecular motions slow down. The supercooled melt behaves like a viscoelastic material. In a certain temperature range, the characteristic time of the molecular motions responsible for the structural rearmament of the molecules into a thermodynamics equilibrium state becomes longer than the timescale of the experiment. Consequently, the system falls out of equilibrium and freezes into a non-equilibrium disordered glassy state without having long-range order, where the system can be considered as glass due its exceedingly high viscosity. At this transition, the shear modulus increases, consequently, the shear modulus of the glass is in order of magnitude of approximately  $10^9$  Pa –  $10^{10}$  Pa. This reversible transition process from the equilibrium state to the solid-like glassy state takes place over a certain temperature range, called the glass transition region, which

is characterized by the  $T_g^{\text{thermal}}$ . Above  $T_g^{\text{thermal}}$ , the state of the glass-formers is called supercooled melt, and below  $T_g^{\text{thermal}}$  the state is referred as glassy state (Figure 4b). The short-range order of the glassy state is similar to that of the supercooled melt.

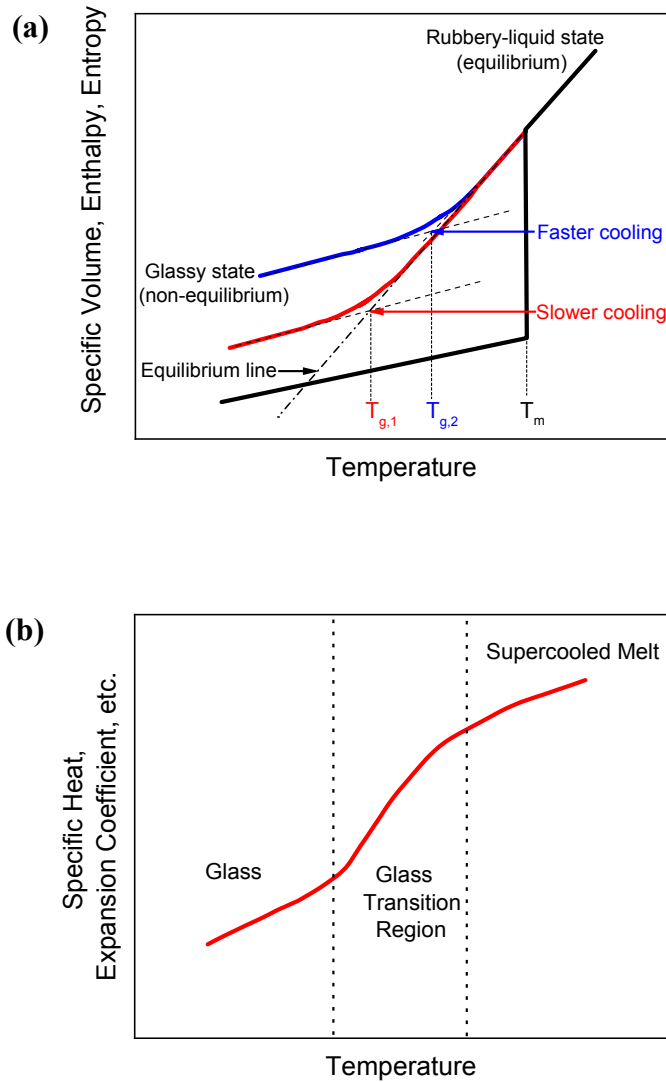


**Figure 4.** A schematic of the thermal glass transition (a) The temperature dependence of specific volume or enthalpy for a glass-former, exposed to different cooling rates.  $T_m$  stands for a (hypothetical) melting temperature and solid black line represents the case of a melting process. (b) Temperature dependence of the material properties of the glass-formers at the glass transition. Figure was adapted from ref. .93.

$T_g^{\text{thermal}}$  depends on the cooling rate. Upon faster cooling, a glass-forming material falls out of the equilibrium state at a higher temperature than that observed in the case of slower cooling as shown in Figure 4a. Thus, a higher cooling rate resulting in a higher  $T_g^{\text{thermal}}$ .

### 2.2.2. Glassy Dynamics

Molecular dynamics related to glassy dynamics occur at timescales covering more than 12 orders of magnitude from picoseconds to seconds and even longer. Therefore, glassy dynamics have been studied in a wide range of frequency windows by various methods like dynamic mechanical analysis (DMA),<sup>94</sup> neutron scattering,<sup>95</sup> light scattering,<sup>96</sup> nuclear magnetic resonance (NMR),<sup>97</sup> SHS,<sup>98</sup> and especially BDS.<sup>99, 100</sup>

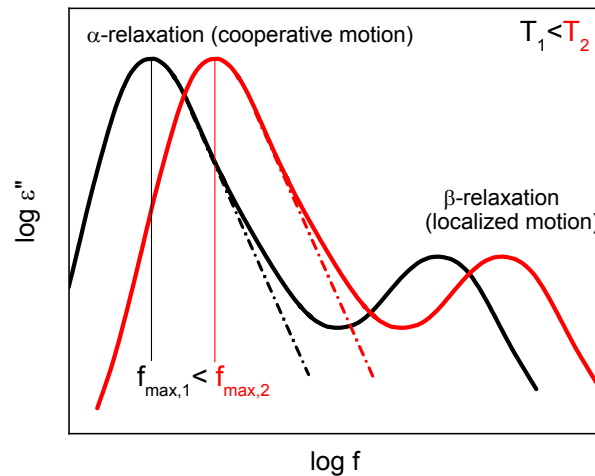


**Figure 5.** Schematic representation of a typical dielectric loss spectra in a broad frequency range for two temperatures  $T_1$  – black solid line - and  $T_2$  –red solid line. Two relaxation processes, the  $\alpha$ -relaxation (dynamic glass transition) and the  $\beta$ -relaxation, are indicated. Figure was adapted from ref. 101.

Figure 5 gives a schematic overview about the different dynamical processes taking place in glass-forming materials given in dielectric loss spectra obtained from BDS as an example. The dielectric spectra show two dielectric relaxation processes, indicated as peaks,  $\alpha$ - and  $\beta$ -relaxations. The asymmetric peak at low frequencies (high temperatures) is the  $\alpha$ -process which

is also called as glassy dynamics. For a glass-former,  $\beta$ -process appears at higher frequencies (low temperatures) which is related to localized motions having a relatively shorter length scale compared to the typical 1-3 nm length scale of  $\alpha$ -process at glass transition temperature<sup>106</sup>. Above  $T_g^{\text{thermal}}$ , cooperative molecular motions responsible for the glassy dynamics are active. For the temperatures below  $T_g^{\text{thermal}}$ , the cooperative molecular motions corresponding to the  $\alpha$ -process is frozen, however, localized fluctuations ( $\beta$ -process) might still be active.

The relaxation rates  $f_{max}$  of a process are determined from the relaxation peaks in dielectric spectra. For a dielectric relaxation process,  $f_{max}$  is defined as the frequency at which the dielectric loss is maximum (see  $f_{max,1}$  and  $f_{max,2}$  in Figure 5). For the quantitative analysis, the temperature dependencies of relaxation rates are commonly presented in a relaxation map, which is also called activation plot or Arrhenius plot. In relaxation map, the relaxation rates are plotted as a function of reciprocal temperature, given in Figure 6a as an example.

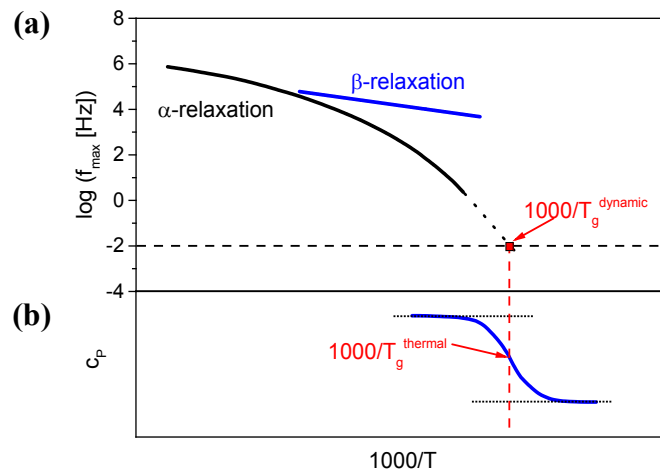


**Figure 6.** Schematic illustrations of the dynamics taking place at a glass transition for a glass-former. (a) Relaxation map for the  $\alpha$ - and the  $\beta$ -relaxation processes. The former can be described by a VFT-equation (eqn. (2)) and the latter follows an Arrhenius-dependency (eqn. (1)) (b) Specific heat capacity,  $c_p$ , as function of inverse temperature.  $T_g^{\text{thermal}}$  is determined as the middle point temperature of the step-like change in the specific heat capacity. Figure was adapted from ref. [101].

On the one hand, the temperature dependence of the relaxation rates of a  $\beta$ -relaxation is a straight line as expected when plotted versus inverse temperature in a relaxation map, which indicates localized molecular fluctuations ( $\beta$ -process in Figure 6a). The temperature dependence of the relaxation rates of the  $\beta$ -relaxation follows generally the Arrhenius-equation

$$\log f_{max} = \log f_{\infty} - \frac{E_A}{\ln(10) RT} \quad (1)$$

Here  $f_{\infty}$  is the relaxation rate at infinite temperature,  $E_A$  symbolizes the activation energy and R is the gas constant. On the other hand, the temperature dependence of the relaxation rates of an  $\alpha$ -relaxation is curved when plotted in a relaxation map ( $\alpha$ -process in Figure 6a). Such a temperature dependence of the relaxation rates can be considered as an indication of glassy dynamics ( $\alpha$ -relaxation) and can be well-approximated by the empirical Vogel/Fulcher/Tammann (VFT-) equation.<sup>102</sup>

$$\log f_{max} = \log f_{\infty} - \frac{1}{\ln(10)} \frac{D T_0}{T - T_0} \quad (2)$$

where  $T_0$  is the so-called Vogel or ideal glass transition temperature which is often found for conventional glass-forming systems to be 30–70 K below the thermal glass transition temperature.  $D$  is the so-called fragility parameter or fragility strength and provides a parameter to classify glass-forming systems into fragile and strong glasses. Glass-forming systems are called “fragile” when the temperature dependence of the relaxation rates of an  $\alpha$ -relaxation deviates strongly from Arrhenius-behavior, and “strong” when that of an  $\alpha$ -relaxation is close to Arrhenius-behavior. It is worth to note that also conventional glass-forming materials shows a crossover behavior of the  $\alpha$ -relaxation, where the temperature dependence of the relaxation rates of an  $\alpha$ -relaxation has a transition from the VFT-behavior to the Arrhenius-behavior.<sup>103, 104</sup> The crossover behavior might

be explained by the cooperativity approach to the glass transition pioneered by Adam and Gibbs.<sup>105</sup>

As already mentioned above and can be seen from Figure 6b, the relaxation shows up as a step-like change in the specific heat capacity ( $c_p$ ), indicating a thermal glass transition. At  $T_g^{\text{thermal}}$ , the relaxation rate of glass dynamics has reached a typical value of  $\sim 10^{-2}$  Hz (Figure 6). This value of the relaxation rate is a good approximation for a  $T_g^{\text{thermal}}$  obtained from DSC experiments run at a standard heating/cooling rate of  $10 \text{ K min}^{-1}$ . However, the relaxation rate corresponding to a  $T_g^{\text{thermal}}$  can be accurately estimated rather than using the typical value of  $\sim 10^{-2}$  Hz in order to compare it with the relaxation rates estimated from BDS measurements as well as from the other methods probing glass dynamics. Donth derived a relationship between the heating/cooling rate and the relaxation rate in the frame of the fluctuation approach to the glass transition<sup>93,106</sup>, which is

$$f_{max} = \frac{\dot{T}}{2 \pi a \Delta T_g} \quad (3)$$

Here  $\dot{T}$  is the heating/cooling rate and  $\Delta T_g$  is the width of the glass transition.  $a$  is a constant with a value of approximately one.  $\Delta T_g$  was estimated as the difference between the endset and the onset temperatures of the step of the glass transition.

## CHAPTER 3 – EXPERIMENTAL TECHNIQUES

Different experimental techniques were used in a complementary way in this work. The main techniques used in this work are broadband dielectric spectroscopy (BDS), specific heat spectroscopy (SHS), differential scanning calorimetry (DSC) and fast scanning calorimetry (FSC). In addition, thermogravimetric analysis (TGA), Fourier transform infrared spectroscopy (FTIR), polarizing optical microscopy (POM), small-angle and wide-angle X-ray scattering (SAXS and WAXS) are also used as complementary techniques. The main idea behind using these different techniques is given as follows. Investigation of all CLC in this work starts with the determination of its thermal decomposition temperatures using TGA. The determined thermal decomposition temperature is the upper temperature limit for the sample preparations (including both the sample preparation for the investigation of a CLC under confinement and the preparation of the samples for the measurements) and measurements. After that conventional DSC experiments are conducted to determine phase transition temperatures and enthalpies as well as thermal glass transition temperature. Determining the clearing temperatures (the phase transition temperature of the transition from  $Col_h$  phase to Iso phase) by the DSC experiments is required for the sample preparation. It is needed, since the sample preparations take place in the isotropic liquid (Iso) phase of the CLCs, at temperatures above their clearing temperature and below their decomposition temperature. After this step, the investigations of the CLCs in bulk state and under confinement proceeds differently. In the bulk investigations, the molecular dynamics is investigated first using BDS. If glassy dynamics are detected using BDS and a thermal glass transition by DSC, the glass dynamics are further investigated by SHS and/or FSC. POM and XRD are used to characterize the liquid crystalline texture and structure.

For the samples for the investigation of a CLC under confinement, BDS is used to determine the collective orientational order. In the investigation of a CLC under confinement, FTIR is used to confirm the surface modification and XRD to estimate the thickness of the surface coatings.

In this chapter, the principles of the main characterization techniques used in this work are briefly introduced. After that, the experimental procedures of the main characterization techniques and all other complementary techniques used in this work are described in detail. Lastly, the sample preparation for the investigation of a CLC embedded into unmodified and modified nanopores of membranes, including the detailed description of the surface modification process as well as the characterization of unmodified and modified membranes are elucidated.

### **3.1. Principles of Main Experimental Techniques**

The main characterization techniques used in this work are broadband dielectric spectroscopy (BDS) and specific heat spectroscopy (SHS). Both BDS and SHS are based on the linear response theory (LRT).<sup>107, 108</sup> LRT describes the relation between an input (disturbance) and an output (response) for a system and provides a framework in order to describe dynamic properties of a soft matter system. In LRT, an outer disturbance  $x(t)$  (external perturbation) applied on a system may cause a response  $y(t)$ , which is linear to the applied perturbation.<sup>99</sup> In other words, the time-dependent response of the system, caused by the time-dependent processes taking place in the system, to the disturbance can be described by a linear equation. The time-dependent processes in the system can be probed by applying a small outer disturbance to the system. Outer disturbance  $x(t)$  can be temperature, electric field, shear force or magnetic field. Different outer disturbances yield different responses. However, different outer disturbances applied to a system allow to probe different aspect of the same process in the system. Thus, combination of different techniques based

on linear response theory is advantageous in order to understand and reveal a process in a system from different perspectives in a complementary manner. For example, BDS probes molecular dynamics from the dipole fluctuations perspective, on the other hand, SHS probes the same molecular dynamics from the enthalpy fluctuations perspective.

### 3.1.1. Broadband Dielectric Spectroscopy

Broadband dielectric spectroscopy (BDS) is a powerful and versatile technique to study the molecular dynamics of polar liquids, biological systems, polymers, LCs and so on. BDS can be defined as the measurement of the dielectric properties of a material under investigation through the interaction of electromagnetic waves with matter in the frequency range from  $10^{-4}$  Hz to  $10^{12}$  Hz. The dielectric properties of a material are defined by the processes taking place in the material such as the molecular dipole fluctuations, collective dipole fluctuations, charge transport and polarization effects at inner and outer boundaries. Thus, BDS is used to investigate the molecular dynamics including glassy dynamics, charge transport (electric conductivity) and the collective orientational order of CLCs in the bulk and the confined state. This section is based on ref.s 99, 100 and 109.

The relation between small electric field strength  $E$  ( $\leq 10^6$  V m<sup>-1</sup>) and the dielectric displacement  $D$  can be expressed as

$$D(\omega) = \varepsilon^*(\omega) \varepsilon_0 E(\omega) \quad (4)$$

where  $\varepsilon_0$  is the dielectric permittivity of vacuum ( $\varepsilon_0 = 8.854 \cdot 10^{-12}$  AsV<sup>-1</sup>m<sup>-1</sup>) and  $\omega$  is the angular frequency ( $\omega = 2\pi f$ ).  $\varepsilon^*$  is the complex dielectric permittivity.

When an external electric field applied to a material, the response of the material causes the dielectric displacement which is described by the polarization  $P$  (Figure 7)

$$P(\omega) = D(\omega) - D_0 = (\varepsilon^*(\omega) - 1) \varepsilon_0 E(\omega) = \chi^*(\omega) \varepsilon_0 E(\omega) \quad (5)$$

with  $\chi^*(\omega) = (\varepsilon^*(\omega) - 1)$

where  $\chi^*$  is the dielectric susceptibility.

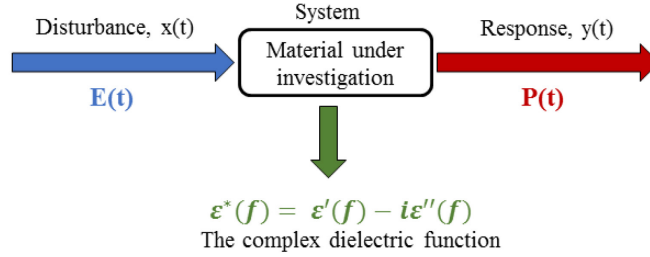


**Figure 7.** Schematic representation of LRT for the case of BDS.

In macroscopic scale,  $P$  is the sum of microscopic dipole moments, can have either a permanent or an induced character, in a volume. Disturbing the natural charge distribution by a local electric field results in an induced polarization. Electronic polarization (the shift of the electron cloud of an atom with respect to the nucleus) and atomic polarization are the typical types of induced polarization. Additionally, many molecules carry permanent dipole moment due to their chemical structure. Applying an external electric field causes an orientational polarization of the permanent dipoles in a molecule. Under the assumption of non-interacting dipoles, the contribution of the orientational polarizations corresponds to dielectric strength ( $\Delta\varepsilon$ ) for a given dipole density and temperature.

When the applied electric field is periodic in a stationary state,  $E(t)(\omega) = E_0 e^{-i\omega t}$ ; where  $i = \sqrt{-1}$ , the phase-shifted polarization is the response (Figure 8), and eqn. (5) is Fourier transformed, consequently, becomes

$$P(t) = (\varepsilon^*(\omega) - 1) \varepsilon_0 E(t) \quad (6)$$

where  $\varepsilon^*(\omega) = \varepsilon'(\omega) - i\varepsilon''(\omega)$  is the complex dielectric permittivity (or the complex dielectric function) and  $\delta$  is the phase shift, where  $\tan \delta = \frac{\varepsilon''}{\varepsilon'}$ . On the one hand,  $\varepsilon'(\omega)$  is the real part of the complex dielectric function, and related to the energy stored reversibly during one cycle.  $\varepsilon'(\omega)$  is in-phase with  $E(t)$ . On the other hand,  $\varepsilon''(\omega)$  is the imaginary part (or the loss part) of the complex dielectric function and related to the energy dissipated during one cycle.  $\varepsilon''(\omega)$  is often called as dielectric loss and is 90°-phase-shifted to  $E(t)$ .

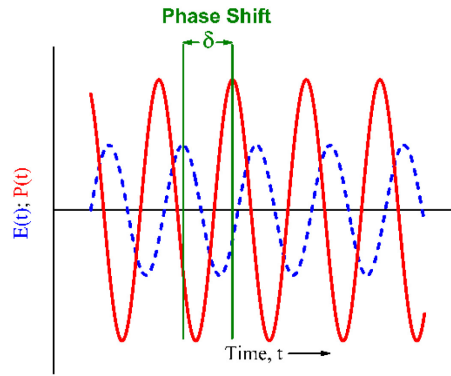


**Figure 8.** Schematic relationships between the time dependence of the periodic electric field  $E(t)$  and that of the periodic phase-shifted polarization  $P(t)$  in the framework of LRT for the case of BDS.

One-sided Fourier or full imaginary Laplace transformation is applied to obtain the relationship of  $\varepsilon^*(\omega)$  to the time-dependent dielectric function  $\varepsilon(t)$

$$\varepsilon^*(\omega) = \varepsilon'(\omega) - i\varepsilon''(\omega) = \varepsilon_\infty - \int_0^\infty \frac{d\varepsilon(t)}{dt} e^{-i\omega t} dt \quad (7)$$

where  $\varepsilon_\infty$  represents the real part  $\varepsilon'$  in the limit of  $\varepsilon_\infty = \lim_{\omega \rightarrow \infty} \varepsilon'(\omega)$ .

The Kramers/Kronig relations describe the relation between the real and the imaginary part of a complex compliance obtained from one-sided Fourier transformation. The relation between  $\varepsilon'(\omega)$  and  $\varepsilon''(\omega)$  is described the Kramers/Kronig relations is

$$\varepsilon'(\omega) - \varepsilon_\infty = \frac{1}{\pi} \oint \frac{\varepsilon''(\xi)}{\xi - \omega} d\xi \quad \text{and} \quad \varepsilon''(\omega) = \frac{1}{\pi} \oint \frac{\varepsilon'(\xi)}{\xi - \omega} d\xi \quad (8)$$

**Analysis of Dielectric Spectra:** Dielectric relaxation processes, due to the fluctuations of molecular dipoles, are characterized as a step-like decrease of the real part  $\varepsilon'$  with increasing frequency and a peak in imaginary part  $\varepsilon''$ . An illustration of a dielectric relaxation process is given for frequency dependence of  $\varepsilon'$  and  $\varepsilon''$  in Figure 9. Quantitative analysis of the dielectric relaxation processes is usually done using model functions in order to obtain information about the molecular dynamics; particularly to estimate the relaxation rate ( $f_{max}$ ).

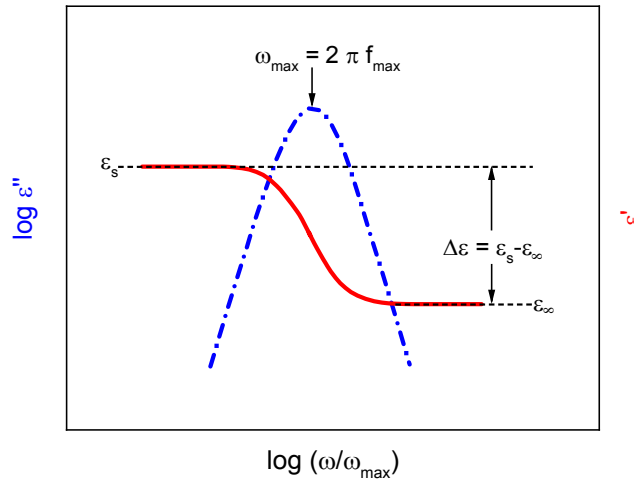


**Figure 9.** Frequency dependence of the real part,  $\varepsilon'$ , and the imaginary part,  $\varepsilon''$ , of the complex dielectric function given for dielectric relaxation process.

**Debye-Behavior:** Debye developed the first theory for dielectric relaxation.<sup>110</sup> This theory assumes that the change in polarization is proportional to its actual value,<sup>111</sup> and time dependence of a dielectric process is given as

$$\frac{dP(t)}{dt} = -\frac{1}{\tau_D} P(t) \quad (9)$$

where  $\tau_D = \frac{1}{2\pi f_{max}} = \frac{1}{\omega_{max}}$  is the relaxation time of a dielectric process. From eqn. (9), a dielectric function in the frequency domain is derived. The function is called the Debye function, which is given for  $\varepsilon^*(\omega)$

$$\varepsilon^*(\omega) = \varepsilon'(\omega) - i\varepsilon''(\omega) = \varepsilon_\infty + \frac{\Delta\varepsilon}{1 + i\omega\tau_D} \quad (10)$$

where  $\Delta\varepsilon$  is the dielectric strength, which is equal to the step height of the real part of a relaxation process or the area under the dielectric loss peak.

**Non-Debye-Behavior:** In practice, the relaxation processes of the systems having amorphous regions in their structures, e.g. amorphous polymers and LCs, are broader than what it is predicted by Debye function given in eqn. (10). Therefore, the Debye function is insufficient to describe these processes having a so-called non-Debye-behavior.

The broadening of a symmetric relaxation peak, with respect to the Debye one, is described by Cole/Cole function (CC-function)<sup>112</sup>

$$\varepsilon^*(\omega) = \varepsilon'(\omega) - i\varepsilon''(\omega) = \varepsilon_\infty + \frac{\Delta\varepsilon}{(1 + i\omega\tau_{CC})^\beta} \quad (11)$$

where  $\beta$  describe the symmetric broadening of the relaxation peak with respect to the Debye one.  $\beta$  has its value within the boundary condition of  $0 < \beta \leq 1$ .  $\tau_{CC}$  is the relaxation time.

In addition to the symmetric broadening, the broadening of a relaxation peak can also be asymmetric, which can be defined by the Cole/Davidson function (CD-function)<sup>113, 114</sup>

$$\varepsilon^*(\omega) = \varepsilon'(\omega) - i\varepsilon''(\omega) = \varepsilon_\infty + \frac{\Delta\varepsilon}{(1 + i\omega\tau_{CD})^\gamma} \quad (12)$$

where  $\gamma$  describe the asymmetric broadening of the relaxation peak with respect to the Debye one.  $\gamma$  has its value within the boundary condition of  $0 < \gamma \leq 1$ .  $\tau_{CD}$  is the relaxation time.

In most of the cases, non-Debye relaxation processes can be well-described by Havrilian/Negami function (HN-function). HN-function considers both symmetric and asymmetric broadening of a relaxation peak, therefore, it is the most generalized form of the Debye function among the model functions. HN-function reads

$$\varepsilon^*(\omega) = \varepsilon'(\omega) - i\varepsilon''(\omega) = \varepsilon_\infty + \frac{\Delta\varepsilon}{(1 + (i\omega\tau_{HN})^\beta)^\gamma} \quad (13)$$

where the fractional parameters  $\beta$  and  $\gamma$  ( $0 < \beta; \beta\gamma \leq 1$ ) describe the symmetric and asymmetric broadening of the relaxation spectrum with respect to the Debye one.  $\tau_{HN}$  denotes the relaxation time corresponding to the frequency of maximal dielectric loss  $f_{max}$ .

The real and the imaginary parts of the HN-function are given in eqn. (14) and (15).

$$\varepsilon'_{HN} = \varepsilon_\infty + \Delta\varepsilon \left[ 1 + 2(\omega\tau_{HN})^\beta \cos\left(\frac{\beta\pi}{2}\right) + (\omega\tau_{HN})^{2\beta} \right]^{-\gamma/2} \cos[\gamma\Psi(\omega)] \quad (14)$$

$$\varepsilon''_{HN} = \Delta\varepsilon \left[ 1 + 2(\omega\tau_{HN})^\beta \cos\left(\frac{\beta\pi}{2}\right) + (\omega\tau_{HN})^{2\beta} \right]^{-\gamma/2} \sin[\gamma\Psi(\omega)] \quad (15)$$

where  $\Psi(\omega)$  is defined as

$$\Psi(\omega) = \arctan \left[ \frac{\sin\left(\frac{\beta\pi}{2}\right)}{(\omega\tau_{HN})^{-\beta} + \cos\left(\frac{\beta\pi}{2}\right)} \right] \quad (16)$$

The HN function can be considered as a combination of the Debye function, the CC- and the CD-function. In case of  $\beta=1$  and  $\gamma=1$ , HN-function is reduced to Debye function (eqn. (10)); in case of  $\beta \neq 1$  and  $\gamma=1$ , comes to be CC-function (eqn. (11)); and in case of  $\beta=1$  and  $\gamma \neq 1$ , gives

CD-function (eqn. (12)). Therefore, the HN-function is mostly used to describe the dielectric relaxation peaks having both Debye-behavior and non-Debye-behavior. Thus, in the course of this study, all relaxation processes have been analyzed by fitting HN-function to the dielectric loss spectra given in eqn. (17). Eqn. (17) takes into account the conductivity contribution, which is often observed in the dielectric loss spectra of materials having high-charge carrier mobility such as CLCs, during the data analysis using HN-function.  $\varepsilon'' = \frac{\sigma}{\omega^s \varepsilon_0}$  describes the conductivity contribution to the dielectric loss, where  $\sigma$  is connected to the DC conductivity,  $s$  is a parameter to model non-Ohmic effects. For Ohmic-behavior,  $s$  is equal to 1, and  $s < 1$  holds for a non-Ohmic-behavior.

$$\varepsilon''_{Fit\_Func} = \varepsilon''_{HN}(\omega) + \frac{\sigma}{\omega^s \varepsilon_0} \quad (17)$$

Furthermore, Wübbenhorst and van Turnhout developed the derivative-based analysis technique called “conduction-free” dielectric loss ( $\varepsilon''_{deriv}$ ) spectra analysis in order to eliminate Ohmic conductivity contribution to dielectric spectra.<sup>115</sup> It is based on the idea of  $\varepsilon'$  and  $\varepsilon''$  carry the same information due to the Kramers/Kronig relations. This is a powerful way of analyzing the data for relatively strong conducting dielectric materials, which eliminates the conduction contribution.  $\varepsilon''_{deriv}$  is obtained by taking the first derivative of the real part ( $\varepsilon'$ ) with respect to the logarithm of the frequency. For a Debye function it holds

$$\varepsilon''_{deriv} = -\frac{\pi}{2} \frac{\partial \varepsilon'}{\partial \ln \omega} \approx \varepsilon'' \quad (18)$$

From eqn. (18) it is concluded that  $\varepsilon''_{deriv}$  displays a peak like the dielectric loss. Because of the square in eqn. (18) the peak in  $\varepsilon''_{deriv}$  is much narrower than that in the dielectric loss. Moreover,

Ohmic-conduction is removed, because in that case  $\varepsilon'$  is independent of frequency. For the HN-function, one obtains

$$-\frac{\partial \varepsilon'_{HN}}{\partial \ln \omega} = \frac{\beta \gamma \Delta \varepsilon_{HN} (\omega \tau_{HN})^\beta \cos\left(\frac{\beta \pi}{2} - (1 + \gamma) \Psi(\omega)\right)}{\left[1 + 2(\omega \tau_{HN})^\beta \cos\left(\frac{\beta \pi}{2}\right) + (\omega \tau_{HN})^{2\beta}\right]^{\frac{1+\gamma}{2}}} \quad (19)$$

where  $\Psi(\omega)$  is given in eqn. (16).

**Conductivity Contribution:** The relationship between the complex dielectric function  $\varepsilon^*$  and the complex conductivity  $\sigma^*$  is given by

$$\sigma^*(\omega) = \sigma'(\omega) + i\sigma''(\omega) = i\omega \varepsilon_0 \varepsilon^*(\omega) \quad (20)$$

where  $\sigma'$  and  $\sigma''$  are the real and imaginary part of the complex conductivity  $\sigma^*$ .  $\sigma'$  and  $\sigma''$  are defined as

$$\sigma'(\omega) = \omega \varepsilon_0 \varepsilon''(\omega) \quad (21)$$

and

$$\sigma''(\omega) = \omega \varepsilon_0 \varepsilon'(\omega) \quad (22)$$

The frequency dependence of the real part of the complex conductivity  $\sigma'$ , given in Figure 10, shows the typical behavior of semiconducting disordered materials such as ionic glasses, ion conducting polymers, and electron-conducting conjugated polymers.<sup>99</sup> At high frequencies (dispersive region),  $\sigma'$  decreases with decreasing frequency with a power law down to a characteristic frequency  $f_c$  characterizing the onset of dispersion. A plateau value corresponds to the DC conductivity ( $\sigma_{DC}$ ) is observed for frequencies at  $f < f_c$ . For higher temperatures, electrode polarization shows up at lower frequencies by a further decrease of  $\sigma'$  with decreasing frequency. Electrode polarization is an unwanted effect due to a partial blocking of charge carriers at the external electrodes.<sup>99</sup>

The frequency dependence of  $\sigma'(f)$  can be approximated by the well-known power law introduced by Jonscher

$$\sigma'(f) = \sigma_{DC} \left( 1 + \left( \frac{f}{f_c} \right)^n \right) \quad (23)$$

besides other models.<sup>99</sup> The exponent  $n$  is found to be between 0.5 and 1.  $f_c$  is related to  $\sigma_{DC}$  by the empirical Barton-Nakajima-Namikawa relation (BNN)  $\sigma_{DC} \sim f_c^{-116, 117, 118}$ . By fitting the Jonscher-equation (eqn. (23)), the  $\sigma_{DC}$  is estimated and its temperature dependence is obtained.

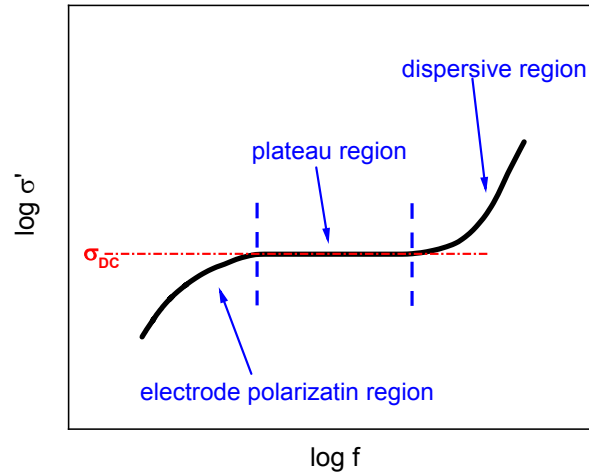


**Figure 10.** Typical frequency dependence of the real part of the complex conductivity  $\sigma'$  for semiconducting disordered materials. Dashed-dotted lines indicate the plateau corresponding to the DC conductivity.

### 3.1.2. Specific Heat Spectroscopy

Specific heat spectroscopy (SHS) is used to investigate glass dynamics in the frequency range from  $10^{-6}$  Hz to  $10^5$  Hz by employing different techniques for the different frequency ranges. SHS is carried out by differential AC-chip calorimetry in the frequency range from  $10^{-2}$  Hz to  $10^5$  kHz, temperature modulated DSC (TMDSC) in the frequency range from  $10^{-6}$  Hz to  $10^2$  Hz, and fast

scanning calorimetry employing StepScan approach (see *Section 3.2.3* for the StepScan approach) in the frequency range from  $10^{-1}$  Hz to  $10^4$  Hz.<sup>119</sup>

SHS is a powerful technique to study the glassy dynamics from the perspective of enthalpy fluctuations. In SHS, when heat is not simultaneously distributed in a material under investigation, time dependency occurs.<sup>120</sup> This results in time and frequency dependence of the change of temperature or heat in the material. In consequence, heat capacity of the material under investigation becomes frequency-dependent. Therefore, the frequency-dependent heat capacity obtained from SHS measurements can be compared to the complex dielectric permittivity obtained from BDS measurement.<sup>119</sup>

Similar to BDS, SHS can be also described in the framework of LRT.<sup>107,108</sup> To understand principles of SHS, thermodynamic relation between specific heat and enthalpy should be considered. Thermodynamic relaxation between constant pressure specific heat,  $c_P$ , and the change in specific enthalpy of a system,  $\partial H$ , is given in eqn. (24).<sup>121</sup>

$$c_P = \left( \frac{\partial H}{\partial T} \right)_P \quad (24)$$

In this case of SHS in the framework of LRT, a periodic temperature having a small amplitude,  $T(t) = T_0 + A_T \sin(\omega t)$  (where  $A_T$  is amplitude of the applied temperature perturbation), is externally applied as disturbance to a system under investigation. Consequently, the response of the system to this disturbance is the phase-shifted enthalpy (see Figure 11),<sup>122</sup> where eqn. (24) becomes

$$\partial H(t) = \int_{-\infty}^t \frac{dc_P(t-t')}{dt} \partial T(t') dt' \quad (25)$$

When this equation is Fourier transformed, it would yield

$$H(\omega) = c_p^*(\omega)T(\omega) \quad (26)$$

where  $c_p^*(\omega) = c_p'(\omega) - ic_p''(\omega)$  is the complex specific heat and  $\delta$  is the phase shift, where  $\tan \delta = \frac{c_p''}{c_p'}$ .  $c_p'(\omega)$  is the real part of the complex specific heat, whereas  $c_p''(\omega)$  is the imaginary part of the complex specific heat.

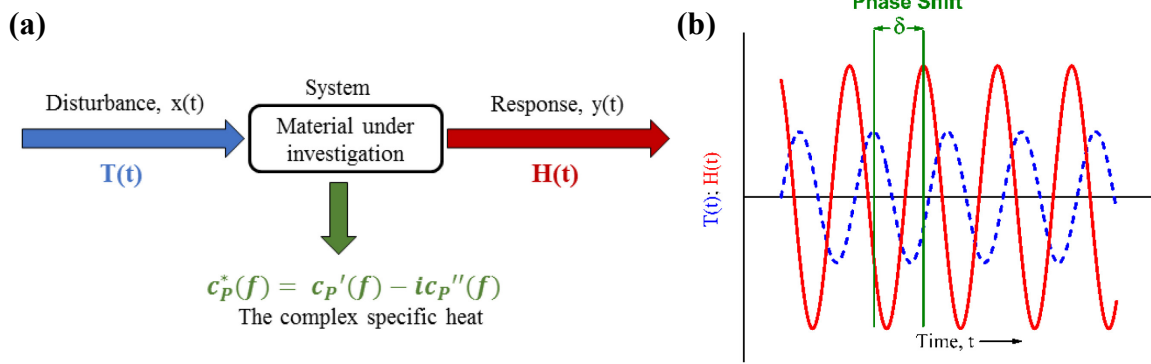


**Figure 11.** (a) Schematic representation of LRT for the case of SHS. (b) Schematic relationships between the time dependence of the periodic electric field  $E(t)$  and that of the periodic phase-shifted polarization  $P(t)$  in the framework of LRT for the case of SHS.

Fourier transformation can be applied to obtain the relationship of  $c_p^*(\omega)$  to the time-dependent dielectric function  $c_p(t)$ <sup>123</sup>

$$c_p^*(\omega) = c_p'(\omega) - ic_p''(\omega) = c_{P\infty} - i\omega \int_0^{\infty} \frac{dc_p(t)}{dt} e^{-i\omega t} dt \quad (27)$$

where  $c_{P\infty}$  represents the real part  $c_p'$  in the limit of  $c_{P\infty} = \lim_{\omega \rightarrow \infty} c_p'(\omega)$ .

## 3.2 Experimental Section

### 3.2.1. Thermogravimetric Analysis

TGA measurements were carried out by a Seiko TG/DTA 220. A heating rate of 10 K min<sup>-1</sup> was applied from 303 K to 1073 K, under synthetic air having a flow rate of 200 ml min<sup>-1</sup>.

### **3.2.2. Fourier Transform Infrared Spectroscopy**

The attenuated total reflection Fourier transform infrared spectroscopy (ATR-FTIR) measurements were performed for the empty unmodified and the modified membranes. The measurements were carried out at room temperature using a Thermo Scientific Nicolet 6700 FTIR with a Smart Orbit diamond ATR accessory. The number of accumulated scans was 32 with a resolution of  $4\text{ cm}^{-1}$  in the wavenumber range from  $4000\text{ cm}^{-1}$  to  $400\text{ cm}^{-1}$ .

### **3.2.3. Differential Scanning Calorimetry**

Conventional differential scanning calorimetry (DSC) measurement was carried out by a Perkin Elmer DSC 8500. The sample (ca. 6 mg) was encapsulated in a standard 50  $\mu\text{l}$  aluminum pan. The sample was measured with a heating/cooling rate of  $10\text{ K min}^{-1}$ . A cryofill LN2 system from Perkin Elmer was used to control the temperature. Nitrogen was used as a purge gas at a flow rate of  $20\text{ ml min}^{-1}$  for the measurements down to 173 K. In addition to nitrogen, helium was also used as a purge gas at a flow rate of  $20\text{ ml min}^{-1}$  for the measurements down to 103 K. One heating/cooling cycle followed by a second heating run was employed. The second heating and the cooling runs were used to determine the phase transitions temperatures. A baseline measurement was conducted by measuring an empty 50  $\mu\text{l}$  aluminum pan under the same conditions. The obtained baseline was subtracted from the data measured for the sample. Moreover, the calibration of the DSC was checked before the measurement by measuring an indium standard.

### **3.3.4. Polarizing Optical Microscopy**

The polarizing optical microscopy (POM) measurements were carried out by a Zeiss Axioskop Scope A1 optical microscope, with crossed polarizers, connected to a Linkam THMS600 heating

stage. The stage was equipped with a liquid nitrogen dewar allowing precise control of heating and cooling rates.

A commercially available ITO-coated liquid crystalline cell was used for the POM investigations. The liquid crystalline cells, having square (10 mm x 10 mm) patterned ITO-coated electrodes and an average cell gap of 4 $\mu$ m, were purchased from Instec, Inc. (Colorado, USA). It was capillary filled with **HAT6** in the Iso phase at 383 K by placing a small amount of sample to the front gate of the cell. Three heating/cooling cycles in the temperature range from 350 K to 383 K, with a heating and cooling rate of 1 K min<sup>-1</sup>, were applied during the POM measurements for **HAT6** in the liquid crystalline cell.

For the POM investigations on the dipole functionalized triphenylene-based DLCs, the samples were prepared on glass slides and studied using an Olympus BX50 polarizing microscope which is combined with a Linkam LTS350 heating stage. Pictures of the textures were taken with a SC35 Type 12 camera from Olympus. These measurements regarding the POM investigation of the dipole functionalized triphenylenes were performed by Prof. Sabine Laschat's group in the University of Stuttgart.

### **3.3.5. X-ray Scattering**

Long-range ordering of unmodified and modified AAO membranes as well as that of **HAT6** confined AAO membranes with 38 nm diameter pores was studied by small angle X-ray scattering (SAXS) in the "MAUS": a heavily customized Xeuss 2.0 (Xenocs, France). Here, MAUS stands for the so-called abbreviation of the XRD setup used: multi-scale analyzer for ultrafine structures. X-rays are generated from a microfocus X-ray tube with a copper target, followed by a multilayer optic to parallelize and monochromatize the X-ray beam to a wavelength of 0.154 nm. The detector

consists of an in-vacuum motorized Eiger 1M, for this investigation placed at distances of 208, 558, and 1258 mm from the sample. After correction, the data from the different distances are combined into a single curve. The space between the start of the collimation until the detector is a continuous, uninterrupted vacuum to reduce background. The membranes (discs) were mounted with their surface perpendicular to the beam in the evacuated sample chamber. The resulting data has been processed using the DAWN software package<sup>124, 125</sup> with the following processing steps in order: masking, correction for counting time, dark-current, transmission, primary beam flux, background (no sample in the beam), flat-field, polarization and solid angle, followed by azimuthal averaging. The data has not been scaled to absolute units. Photon counting uncertainties were estimated from the raw image, and propagated through the correction steps. For the alignment experiment, the membrane was held upright between two LEGO bricks, on top of a PhysikInstrumente H811.12V hexapod. 200 second exposures were taken at various tilt angles, to seek the tilt angle that would produce a radially isotropic pattern. The measurements and the simulations were performed by Dr. Brian Richard Pauw and Dr. Glen Jacob Smales from Bundesanstalt für Materialforschung und -prüfung (BAM).

The dipole functionalized triphenylenes were also studied using SAXS and WAXS. The samples were placed in mark tubes from Hilgenberg (diameter of 0.7 mm) and sealed by melting. X-ray powder experiments were performed by a Bruker AXS Nanostar C diffractometer employing monochromatic Ni-filtered  $\text{Cu}_{K\alpha}$  radiation ( $\lambda = 1.5418 \text{ \AA}$ ). A HI-STAR-detector from Bruker was used for recording and calibrated by silver behenate at 298 K. The diffraction images were processed by SAXS-software from Bruker, and the diffraction patterns were analyzed by Datasqueeze Software and Origin. The measurements were performed by Prof. Sabine Laschat's group in the University of Stuttgart.

### 3.3.6. Broadband Dielectric Spectroscopy

The dielectric properties of samples were measured in the frequency range from  $10^{-1}$  Hz to  $10^9$  Hz using broadband dielectric spectroscopy (BDS). In BDS measurements, the complex dielectric function of a capacitor filled with a material under investigation is expressed as<sup>100</sup>

$$\varepsilon^*(\omega) = \varepsilon'(\omega) - i\varepsilon''(\omega) = \frac{C^*(\omega)}{C_0} \quad (28)$$

where  $C^*(\omega)$  represents the complex capacitance of the capacitor filled with the material and  $C_0$  is the vacuum capacitance of the arrangement of the empty capacitor.  $\varepsilon^*(\omega)$  can be derived by measuring the complex impedance,  $Z^*(\omega)$ , of the sample

$$\varepsilon^*(\omega) = \frac{J^*(\omega)}{i\omega\varepsilon_0 E^*(\omega)} = \frac{1}{i\omega Z^*(\omega)C_0} \quad (29)$$

where  $J^*(\omega)$  is the complex current density.

**Measurement of Bulk Samples:** For bulk samples, in the frequency range from  $10^{-1}$  Hz to  $10^6$  Hz, a high-resolution ALPHA analyzer (Novocontrol, Montabaur, Germany) including a sample holder with an active sample head was used. Isothermal frequency scans were carried out temperatures down to 133 K. Samples were first heated to a temperature higher than their clearing temperatures ( $T > T_{\text{Colh-Iso}}$ ), and then cooled to 133 K with a cooling rate of  $5 \text{ K min}^{-1}$  to define a specific thermal history. One heating/cooling cycle followed by a second heating run was employed in the temperature range from 133 K to  $T \approx T_{\text{Colh-Iso}} - 10 \text{ K}$ . In this temperature range, the sample temperature was increased (heating run) and decreased (cooling run) with an increment of 2 K upon heating/cooling. When the sample temperature is stabilized at the set temperature, isothermal frequency scans were applied in this temperature range.

From  $10^6$  Hz to  $10^9$  Hz, the bulk measurements were performed using a coaxial reflectometer based on an Agilent E4991A RF impedance analyzer. The sample was modeled as integral part of the inner conductor. For details see ref. 100. The measurements were also carried out isothermally.

For both measurements performed at different frequency windows, the samples were prepared between two disk-shaped gold-plated brass electrodes with a diameter of 10 mm (parallel plate geometry). A spacing of 50  $\mu\text{m}$  was maintained by fused silica spacers. For both measurement setup, the temperature of the sample was controlled by a Quatro Novocontrol temperature controller with nitrogen as a heating agent providing a temperature stability better than 0.1 K. For details see ref.s 99 and 100.

***Measurement of the Samples for the Investigation of a CLC Under Confinement:*** The measurements of **HAT6** confined into nanochannels of the membranes were carried out using a high-resolution ALPHA analyzer (Novocontrol, Montabaur, Germany) including a sample holder with an active sample head. The temperature of the sample was also controlled by the Quatro Novocontrol temperature controller with nitrogen as a heating agent. The measurements were also performed in parallel plate geometry. This means that the disk-shaped samples were placed between two gold-plated brass electrodes with a diameter of 10 mm or 15 mm depending on the outer diameter of the membranes. Spacing between electrodes was defined by the thickness of the membranes. Bulk **HAT6** measurements were conducted using the liquid crystalline cell purchased from Instec, Inc.. The cell was capillary filled with **HAT6** in the Iso phase at 383 K by placing a small amount of sample to the front gate of the cell.

For confined **HAT6**, the complex dielectric permittivity,  $\epsilon^*$ , was measured by temperature scans with a heating and cooling rate of  $1 \text{ K min}^{-1}$  at a constant frequency of 35 kHz. The reason

of running measurement at 35 kHz is explained in detail in *Section 5.3*. Three heating/cooling cycles, in the temperature range from 340 K to 383 K for smaller pore sizes ( $d < 34$  nm) and that from 350 K to 383 K for the larger pore sizes ( $d > 34$  nm), were employed to probe all samples. Similarly, three heating/cooling cycles were applied for **HAT6** in the liquid crystalline cell in the temperature range from 350 K to 383 K.

### 3.3.7. Specific Heat Spectroscopy

Specific heat spectroscopy (SHS) was carried out by differential AC-chip calorimetry<sup>126</sup> and temperature modulated DSC (TMDSC).

***Differential AC-Chip Calorimetry:*** Differential AC-chip calorimetry is based on an approach that is obtained by measuring a chip with a sample against an empty chip in a differential set-up. Most of the other calorimetric techniques is also based on the differential approach. This approach minimizes the heat capacity contribution originating from the empty chip itself. The differential approach brings two orders of magnitude increase in the sensitivity ( $\approx$  pJ K<sup>-1</sup>) for this technique compared to an AC-chip calorimetry (non-differential approach). In this technique, an alternating current (AC) is applied to the material under study, and periodic heat flow is measured as the respond of the material.

The nanocalorimeter chips XEN 39390, purchased from Xensor Integration and shown in Figure 12, were employed to carry out the AC-chip calorimetry measurements. The chip has two four-wire heaters located in the middle of a free-standing 1  $\mu$ m thick silicon nitride (SiN) membrane. The heated area of about 30  $\mu$ m x 30  $\mu$ m is in the center of thin SiN membrane. Six-couple thermopile, integrated in the heated area, senses the temperature..<sup>127</sup>

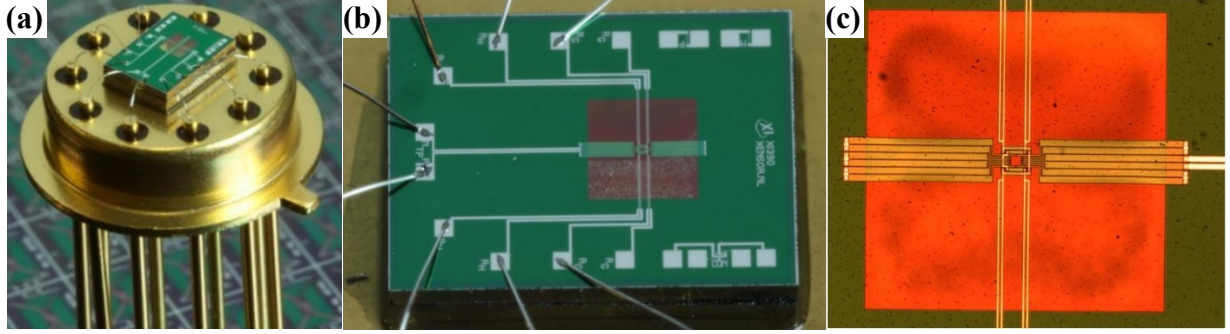


**Figure 12.** Pictures of (a) XEN 39390AC-chip sensor, (b) SiN membrane fixed on a rectangular silicon nitride substrate, and (c) The heated area of about 30  $\mu\text{m}$  x 30  $\mu\text{m}$  in the center of the rectangular silicon substrate. The pictures were adapted from ref. 127.

In the differential approach, two identical chips are assumed.<sup>126</sup> In this approximation, the heat capacity of the sample  $C_s$  is given by

$$C_s = \frac{i\omega C_{eff}(\Delta U - \Delta U_0)}{P_0 S} \quad (30)$$

where  $S$  is the sensitivity of the thermopile, and  $P_0$  is the applied heating power.  $C_{eff} = C_0 + \frac{G}{i\omega}$  denotes the effective heat capacity of the empty sensor where  $\frac{G}{i\omega}$  is the heat loss to the surrounding atmosphere.  $\Delta U$  is the complex differential thermopile signal for an empty and a sensor with a sample, and  $\Delta U_0$  is the complex differential voltage measured for two empty sensors. The measured complex differential voltage can be considered as measure for the complex heat capacity.

The AC-chip calorimetry measurements were carried out in the temperature scan mode. Temperature was ramped at a fixed modulation frequency by applying a heating and cooling rate in the range between 1.0 and 2.0  $\text{K min}^{-1}$  depending on the programmed frequency to ensure a stationary state. After each heating and cooling runs the frequency was changed stepwise in the range of 1 Hz - 10 kHz. To ensure a linear regime, the amplitude of the temperature modulation was set to be less than 0.25 K.<sup>126</sup> Further details can be found in ref. 126. The AC-chip sensors for

the measurement were prepared by placing a small amount of a sample onto the SiN membrane under an optical microscope. After that, the sample was melted on the heated area.

***Temperature Modulated DSC:*** Temperature modulated DSC (TMDSC) measurements are applied to measure the complex heat capacity besides the total heat capacity.<sup>128</sup> TMDSC measurements were conducted by a Perkin Elmer DSC 8500 using the StepScan approach (StepScan DSC – SSDSC). SSDSC is a special variant of TMDSC, which combines alternating short heating and isothermal steps. Here, the height and time of the isothermal step and the heating rate between the steps are predefined and the heat-flow rate response is measured (see Figure 13). The modulation frequency corresponds to the time of the isothermal step. Due to the periodic perturbation, the real part of the complex heat capacity of a system (related to the reversing heat capacity<sup>128</sup>) can be extracted from the ratio of the area under the heat-flow peak and height of the temperature step. Fourier analysis of the raw data is not absolutely required.<sup>128</sup> Calibration of the heat flow was performed with synthetic sapphire ( $\alpha\text{-Al}_2\text{O}_3$ ) as a reference material. SSDSC was carried out in the frequency range from  $3.2 \times 10^{-3}$  Hz to  $5.6 \times 10^{-2}$  Hz with a constant step height of 1 K and the heating rates in the range from  $40 \text{ K min}^{-1}$  to  $120 \text{ K min}^{-1}$ .

For the temperature control, a cryofill LN2 system from Perkin Elmer was used. Nitrogen was used as a purge gas at a flow rate of  $20 \text{ ml min}^{-1}$  for the measurements down to 173 K, and helium to reach the lower temperatures down to 103 K.

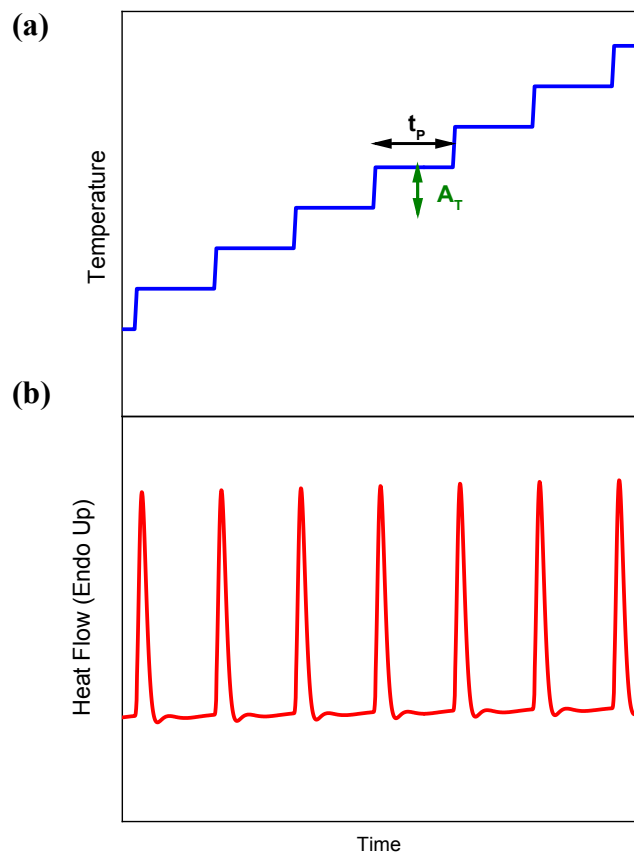


**Figure 13.** (a) Temperature program applied for a SSDSC measurement. It illustrates the predefined height and time of the isothermal step ( $A_T$  and  $t_p$ ) and the heating rate between the steps are used in the temperature program. (b) Measured heat-flow rate response of the material to the applied temperature program given in Figure 13a.

### 3.3.8. Fast Scanning Calorimetry

The glass transitions detected using conventional DSC were further investigated through fast scanning calorimetry (FSC) experiments allowing heating rates from  $10 \text{ K s}^{-1}$  to  $10000 \text{ K s}^{-1}$ . FSC measurements were performed using a Mettler Toledo Flash DSC 1, which is a chip-based power compensated differential calorimetry.<sup>119, 129</sup> MultiSTAR UFS 1 twin chip sensors, shown in Figure 14, were used for the measurements (for details see ref. 130). Nitrogen was used as a purge gas at a flow rate of  $40 \text{ ml min}^{-1}$ . A Huber TC100 intercooler was used to control the temperature.

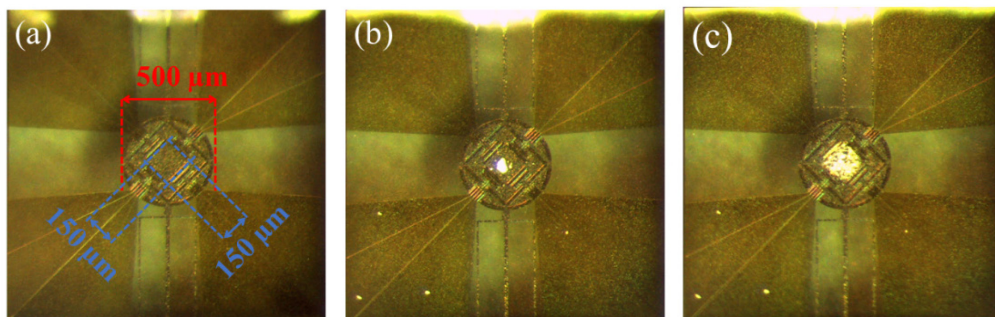


**Figure 14.** Sample area of the MultiSTAR UFS 1 twin chip sensor (a) before placing a sample at the heated area, (b) after a sample was placed at the heated area, and (c) after the placed sample was melted on the heated area. Figure was taken from ref. 43 with permission (see *Section 4.1* for the permission).

“Conditioning” and “correction” procedures given by the manufacturer were applied before the measurements. The samples were placed at heated area (Figure 14b), and then melted at temperatures above their clearing temperatures by heating from room temperature with a heating rate of  $500 \text{ K s}^{-1}$  (Figure 14c). The measurements were carried out by heating the samples from  $178 \text{ K}$  to  $T \approx T_{\text{Coll-Iso}} - 10 \text{ K}$  with heating rates from  $10 \text{ K s}^{-1}$  to  $10000 \text{ K s}^{-1}$ . A cooling run with a rate of  $1000 \text{ K s}^{-1}$  was applied prior to every heating measurement to ensure that the samples have the same thermal history before a heating run.

### 3.3. Materials

#### 3.3.1. Triphenylene-Based Discotic Liquid Crystals

Triphenylene-based DLCs 2,3,6,7,10,11-hexakis[hexyloxy] triphenylene (**HAT6**) and 2,3,6,7,10,11-hexakis[pentyloxy] triphenylene (**HAT5**) were purchased from Synthron Chemicals (Bitterfeld, Germany, CAS-no.: 70351-86-9 for **HAT6**, CAS-no.: 69079-52-3 for **HAT5**) and used as received. The molecular weight of **HAT6** was confirmed by matrix-assisted laser desorption/ionization-time of flight (MALDI-TOF) measurement. The molecular weight of **HAT6** was found to be  $828.63 \text{ g mol}^{-1}$  by MALDI-TOF MS (see *Appendix I*, Figure S1), and it is in

agreement with its reported value<sup>21</sup>. According to the producer, their purities are at least 98 %. At room temperature, the appearances of **HAT5** and **HAT6** are that of white crystals.

The chemical structures of **HAT6** (sum formula  $C_{54}H_{84}O_6$ ) and **HAT5** (sum formula  $C_{48}H_{72}O_6$ ) are shown in Figure 15. Moreover, a schematic illustration of their molecular organization and the thermotropic phases is shown in Figure 2 for DLCs including **HAT6** and **HAT5**. At low temperatures, both **HAT6** and **HAT5** form a Cry phase. Upon further heating from the Cry phase, they have a  $Col_h$  mesophase. With further heating from the  $Col_h$  phase, they undergo a clearing transition to a more or less Iso liquid state.

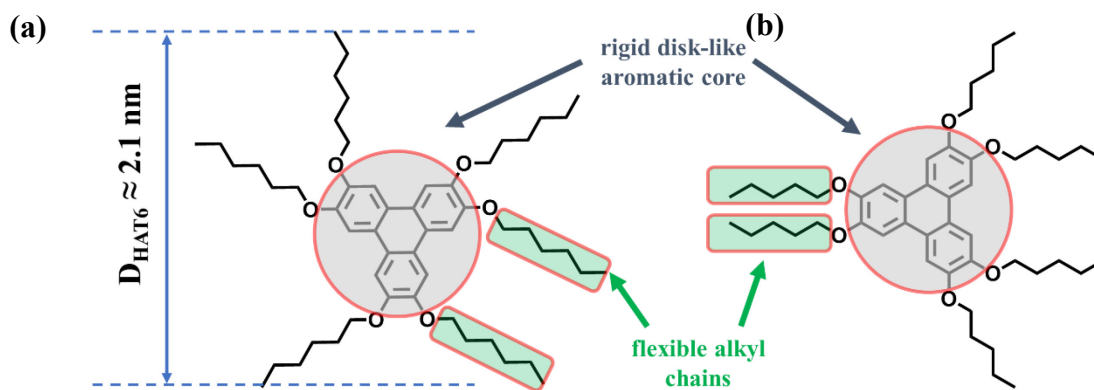


**Figure 15.** (a) Chemical structure of 2,3,6,7,10,11-hexakis[hexyloxy] triphenylene (**HAT6**).  $D_{HAT6}$  is diameter of **HAT6** molecules, reported to be ca. 2.1 nm.<sup>131</sup> Figure was taken/adapted from ref. 25 with permission (see *Chapter 5* for the permission). (b) Chemical structure of 2,3,6,7,10,11 hexakis[pentyloxy] triphenylene (**HAT5**).

In addition to the above-mentioned symmetrical triphenylene-based DLCs, a selected series of dipole functionalized triphenylene-based DLCs were also studied in this work, which are pentapentyloxytriphenylenes carrying ethyl glycolate (**SHU09**), hexanoyl (**SHU10**), trifluoromethyl (**SHU11**), and diethyleneglycol (**SHU12**) units. The triphenylene derivatives, **SHU09**-**SHU12**, can be regarded as monofunctionalized derivatives of **HAT5**. The chemical structures of the triphenylene derivatives are given in Figure 16. The monofunctionalized

triphenylene derivatives **SHU09-SHU12** were synthesized by Prof. Sabine Laschat's group in the University of Stuttgart. The synthesis of **SHU09-SHU12** is given in ref. 43.

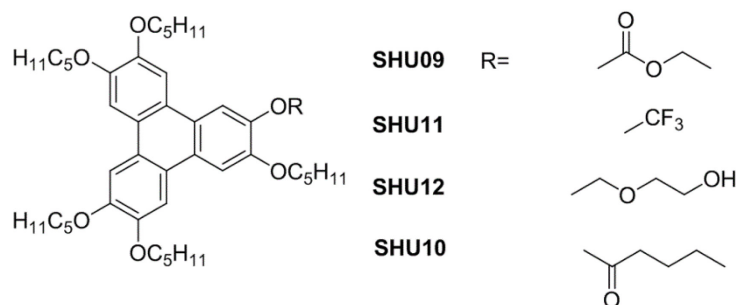


**Figure 16.** Chemical structures of the monofunctionalized triphenylene derivatives **SHU09-SHU12**. Figure was taken from ref. 43 with permission (see *Section 4.1* for the permission).

All monofunctionalized triphenylene derivatives are thermally stable at least up to 533 K, determined using TGA (see *Appendix I*, Figure S2).

### 3.3.2. Triphenylene Crown Ether-Based Discotic Liquid Crystals

Triphenylene crown ether-based unsymmetrical DLCs, termed as **KAL465** and **KAL468**, were studied. The synthesis of **KAL465** and **KAL468** was done by Prof. Sabine Laschat's group in the University of Stuttgart. The synthesis and the mesomorphic properties of these DLCs are given in ref. 132. Figure 17 shows the chemical structures of the DLCs and a schematic illustration of their molecular organization. The molecules of the **KAL** compounds have a central [15]crown-5 with two separate triphenylenes connected to each other through the central crown and alkyl chains attached to the triphenylenes. This is the main difference between the triphenylene crown ether-based DLCs and conventional triphenylene-based DLCs (e.g. above-mentioned **HAT** and **SHU** compounds) having molecules made of a core consisting of only one triphenylene. Having such a core made of two separate triphenylenes, the molecules of the **KAL** compounds might presumably form columns interconnected to the neighboring columns in a way that two triphenylenes of a single molecule are the building blocks of two separate neighboring columns.

They have a Cry phase at low temperatures. With increasing temperature, they first form a Cry phase, and then a Col<sub>h</sub> mesophase, after that an Iso phase at higher temperatures.

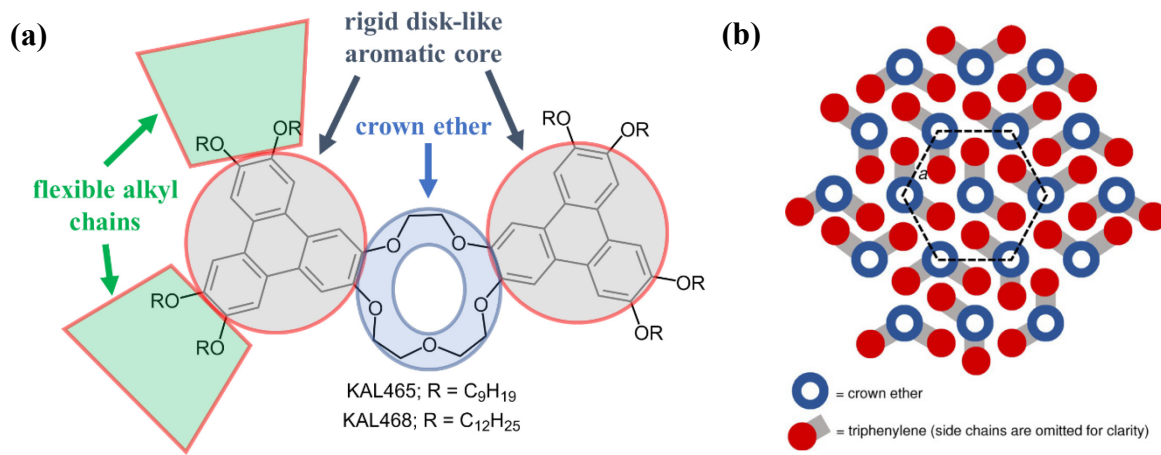


**Figure 17.** (a) Chemical structures of the of the triphenylene crown ether-based DLCs; **KAL465** and **KAL468**. (b) Hexagonal lattice formed in the Col<sub>h</sub> phase. Figure was taken from ref. .133.

### 3.3.1. Columnar Ionic Liquid Crystals

The synthesis and the mesomorphic properties of the investigated linear-shaped tetramethylated guanidinium triflate ILCs, denoted as **LC536** and **LC537**, are given in ref. .134. The ILCs **LC536** and **LC537** were synthesized by Prof. Sabine Laschat's group in the University of Stuttgart. Their chemical structures and a schematic illustration of their molecular organization are shown in Figure 18. They consist of an aromatic guanidinium-based core with a triflate (OTf) counteranion and alkyl chains attached to the core via ether groups. At low temperatures, **LC536** and **LC537** form two different plastic crystalline phases (Cry<sub>1</sub> and Cry<sub>2</sub>). Upon further heating from the Cry<sub>1</sub> and Cry<sub>2</sub> phases, they have a Col<sub>h</sub> mesophase. In the Col<sub>h</sub> phase for both materials, six molecules built a hexagonal lattice in a layer, and the layers stuck on top of each other to form columns. The triflate counteranions are located close to the guanidinium groups in the aromatic core. With further heating from the Col<sub>h</sub> phase, they undergo a clearing transition to the Iso liquid state.<sup>134</sup>

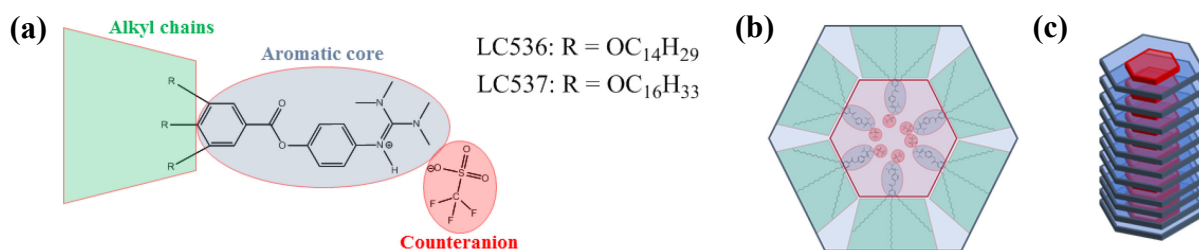


**Figure 18.** (a) Chemical structures of the linear-shaped tetramethylated guanidinium triflates ILCs; LC536 and LC537. (b) Six molecules forming the building blocks of the hexagonal lattice in the hexagonal columnar phase. (c) Hexagonal columnar phase. Figure was taken from ref. 135 with permission (see Section 4.3 for the permission).

### 3.4. Preparation of the Samples for the Investigation of a CLC under Confinement

In this section, the confining host (anodic aluminum oxide and silica membranes), the surface modification of the confining hosts as well as the related characterization of the confining host, and the pore filling procedure used in this work are presented.

#### 3.4.1 Confining Hosts

Disk-shaped anodic aluminum oxide (AAO) membranes with a variety of pore diameters, thicknesses and porosities were purchased from Smart Membranes GmbH (Halle, Germany) and InRedox (Longmont, USA). In addition, silica membranes having a pore diameter of ca. 12 nm were prepared by electrochemical anodic etching. The silica membranes were produced by Prof. Patrick Huber's group in Hamburg University of Technology. The etching procedure used in this work is given in ref. 25.

The porosities and pore diameters of the membranes were characterized by volumetric  $N_2$ -sorption measurements at 77 K. Volumetric  $N_2$ -sorption experiments were carried out by an autosorb iQ Quantachrome Instruments gas sorption system. The determined pore sizes and porosities (number of pores per unit area) are given in Table 1 together with the specifications of

the producers. The volumetric N<sub>2</sub>-sorption experiments were performed by Prof. Patrick Huber's group in Hamburg University of Technology.

**Table 1.** Properties of the nanoporous membranes

<u>Membrane</u>	<u>Producer's values</u>			<u>Determined values</u>		<u>Producer</u>
	Pore depth ( $\mu\text{m}$ )	Pore size, d (nm)	Porosity (%)	Pore size, d (nm)	Porosity (%)	
Silicon	-	-	-	$11.8 \pm 0.2$	$61.2 \pm 0.2$	-
AAO	80	25	10	$16.7 \pm 0.6$	$16.0 \pm 1.0$	Smart Membranes
AAO	100	20	12	$17.8 \pm 1.8$	$19.4 \pm 1.6$	InRedox
AAO	80	30	30	$24.3 \pm 0.2$	$28.7 \pm 1.0$	Smart Membranes
AAO	80	40*	34	$34.2 \pm 0.7$	$44.0 \pm 0.2$	Smart Membranes
AAO	80	40**	10	$37.8 \pm 0.7$	$15.8 \pm 0.9$	Smart Membranes
AAO	80	50	15	$47.3 \pm 0.3$	$21.5 \pm 0.2$	Smart Membranes
AAO	80	80	35	$72.9 \pm 3.1$	$36.4 \pm 1.6$	Smart Membranes
AAO	100	120	12	$95.0 \pm 13.0$	$7.6 \pm 0.6$	InRedox
AAO	80	180	10	$161.1 \pm 9.7$	$13.8 \pm 1.7$	Smart Membranes

\*is etched in oxalate acid. \*\*is etched in sulfuric acid. Table was taken/adapted from ref. 25 with permission.

The membranes have parallel cylindrical hexagonal ordered pores which are open at both sides.

Figure 19 demonstrates that the pore distribution of the membranes is narrow, and the pores have an almost parallel arrangement.

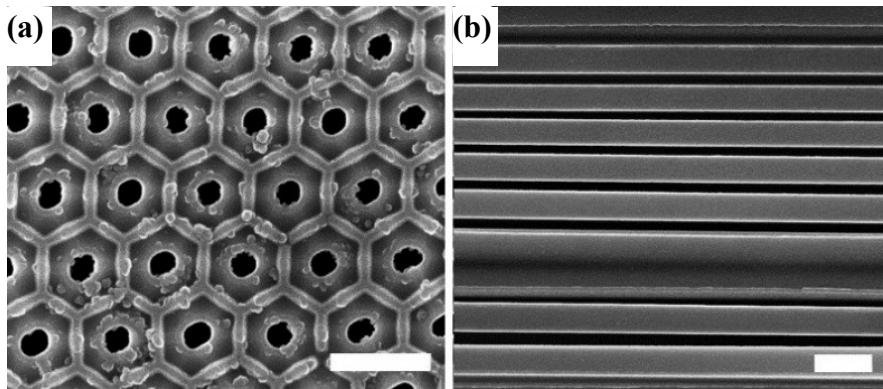


**Figure 19.** Scanning electron microscopy images (Zeiss Gemini Supra 40) of an AAO membrane with a pore size of 161 nm. (a) The top view of the membrane. (b) The side view of the edge broken membrane. The white scale bars represent 600 nm. The measurements were performed by Sigrid Benemann from Bundesanstalt für Materialforschung und -prüfung (BAM). Figure was taken from ref. 25 with permission (see *Chapter 5* for the permission).

### 3.4.2. Surface Modification of the Confining Hosts

The investigations for **HAT6** under confinement were carried out on both modified and unmodified pore walls. In the latter case, the pore walls of the AAO membranes were chemically modified with n-octylphosphonic acid ( $C_8H_{19}O_3P$ ; OPA) and n-octadecylphosphonic acid ( $C_{18}H_{39}O_3P$ ; ODPA) following the procedure reported in the literature.<sup>136, 137</sup> OPA has shorter lengths of the alkyl chains compared to ODPA (see Figure 20.a and b). OPA and ODPA were purchased from Alfa Aesar and used as received.

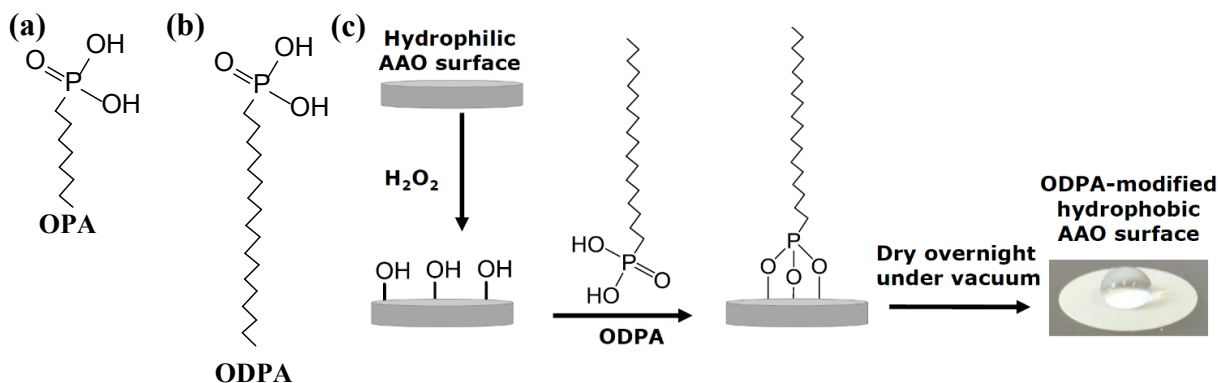


**Figure 20.** Chemical structure of the surface modifiers; (a) n-octylphosphonic acid (OPA) and (b) n-octadecylphosphonic acid (ODPA). (c) Schematic illustration of the surface modification of AAO membranes with ODPA. The photo on the right shows a water droplet on a modified membrane to visualize the hydrophobicity of the modified membrane. Figure was adapted from ref. 25 with permission (see *Chapter 5* for the permission).

A scheme of the surface treatment process is illustrated for ODPA-modification in Figure 20. First, the hydroxide groups on the pore walls of the AAO membranes were activated with 30% aqueous  $H_2O_2$  solution for 2 h at 45 °C, then dried at 120 °C for 15 minutes. The membranes, having the activated hydroxides on the pore walls, were immersed into a 4 mM solution of ODPA (or OPA) in a n-heptane/isopropyl alcohol solution (volume ratio of 5:1) for 48 h at 25 °C. The membranes were then washed several times and sonicated for 15 minutes with the n-heptane/isopropyl alcohol solution to remove any physically absorbed ODPA (or OPA). The sonicated samples were then washed several times with the n-heptane/isopropyl alcohol solution,

and then with acetone before being left to dry overnight under vacuum at room temperature. The modifications of the pore walls were confirmed by FTIR, given in *Appendix I*, in Figure S5.

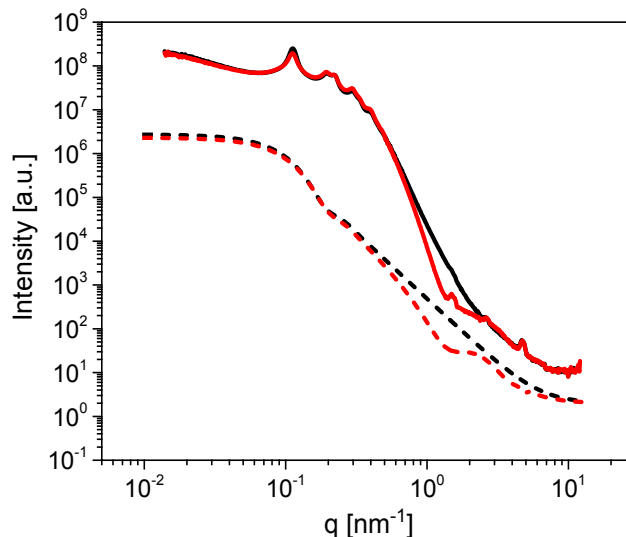


**Figure 21.** SAXS patterns of unmodified (black solid line) and ODPA-modified (red solid line) empty AAO membranes having the pore size of 38 nm. Dashed lines represent simulations based on 2D core-shell cylinder model for unmodified (black dashed line) and modified (red dashed line) membranes. The simulations were performed for a core-shell cylinder, looking on-axis, with the following parameters: core diameter 15 nm, polydispersity 0.3 (in 45 points), shell thickness: 2.2 nm, polydispersity 0.25 (in 45 points), cylinder angle phi: 0 (around-axis rotation), cylinder angle theta: 0 (face-on view), length: 600 nm (only affects the intensity) - background:  $1e^{-1}$  (avoiding deep dips). See also *Appendix I*. Figure was taken from ref. 25 with permission (see *Chapter 5* for the permission).

The long-range ordering of both, the unmodified and modified membranes, was studied by Small Angle X-ray Scattering (SAXS) in order to estimate the thickness of the ODPA-coating. Figure 21 shows the measured SAXS patterns and corresponding simulations. The simulations were carried out by model of 2D core-shell cylinders from the SasModels library.<sup>138</sup> Similar models are applied elsewhere.<sup>139,140</sup> The scattering pattern simulations are done with the cylindrical axis parallel to the beam, and using the scattering length densities estimated for bulk ODPA and alumina phases. Simulations with different shell parameters (cylinder diameter, shell thickness, polydispersity) were carried out. The simulation with a shell thickness parameter of 2.2 nm is the closest approximation to the SAXS pattern of the ODPA modified membranes.<sup>141</sup> Hence,

it is concluded that the ODP A-coating has a thickness of ca.  $2.2 \pm 0.2$  nm. The details of the SAXS measurements and some additional results are given in *Appendix I*, in Figure S6.

### 3.4.3. Pore Filling Procedure

A reproducible pore filling procedure was developed to embed **HAT6** into nanochannels<sup>50</sup>, and this procedure is followed to prepare the samples for the investigation of a CLC under confinement. In short, the membranes were outgassed in vacuum of  $10^{-4}$  mbar at 473 K for 12 hours, to clean the pores and remove adsorbed water. Then the membranes were transferred under vacuum to an argon-filled glovebox. The amount of material required to fill the membranes completely was calculated from the porosity and the volume of the membranes according to

$$m_{\text{HAT6}} = \left[ \Phi_{\text{AAO}} \times \left( \pi \left( \frac{d_{\text{AAO}}}{2} \right)^2 \lambda_{\text{AAO}} \right) \right] \times \rho_{\text{HAT6}} \quad (31)$$

where  $\Phi_{\text{AAO}}$  is the porosity,  $d_{\text{AAO}}$  is the diameter of the membrane,  $\lambda_{\text{AAO}}$  is the thickness of the membrane and  $\rho_{\text{HAT6}}$  is the bulk density of **HAT6** found to be  $0.92 \text{ g cm}^{-3}$ .<sup>142</sup> A bulk-like density was assumed when **HAT6** is confined into nanopores. The calculated amount of the liquid crystal and a small surplus of the calculated amount were placed on the top of the membrane and heated to 418 K in the isotropic state. At this temperature, the pores were filled by melt infiltration under argon atmosphere for 48 h. After filling, the excess of the material on the top and bottom of the membranes was carefully scratched off with a sharp scalpel.

The filling degree of the membranes with **HAT6** was estimated by TGA. A complete pore filling was obtained for all samples investigated in this study (see *Appendix I*, Figure S4).

## CHAPTER 4 – COLUMNAR LIQUID CRYSTALS IN THE BULK STATE

### 4.1. Triphenylene-Based Discotic Liquid Crystals

This section is reproduced/adapted from A. Yildirim, A. Bühlmeier, S. Hayashi, J. C. Haenle, K. Sentker, C. Krause, P. Huber, S. Laschat, A. Schönhal, Multiple glassy dynamics in dipole functionalized triphenylene-based discotic liquid crystals revealed by broadband dielectric spectroscopy and advanced calorimetry – Assessment of the molecular origin, *Phys. Chem. Chem. Phys.* 2019, 21, 18265–18277 with permission from the PCCP Owner Societies (DOI: <https://doi.org/10.1039/C9CP03499D>).

With respect to the understanding of molecular dynamics of triphenylene-derived columnar DLCs, a comparison of symmetrical hexakis(n-alkyloxy)triphenylenes **HATn** with structurally related dipole functionalized low symmetry triphenylenes seems highly recommended. **HATn** are model DLCs and considered as “working horse” of the DLC research, which have been extensively studied.<sup>4</sup> For this purpose, a series of pentapentyloxytriphenylenes carrying different functional units, **SHU09-SHU12** (see Figure 16), was chosen because they provide dipole functionalities and also H-bonding ability for **SHU12**.

The monofunctionalized compounds were investigated in a systematic way to reveal the influence of the dipole functionalization on the mesomorphic properties, the phase behavior and the molecular dynamics. The latter point is of particular importance to understand the charge transport in such systems which is the key property for their applications such as organic field-effect transistors, solar cells or as nanowires in molecular electronics and to tune DLCs for applications. The mesomorphic properties were studied by POM, XRD, and DSC, which were

compared to the unfunctionalized symmetrical triphenylene-based DLC **HAT5** (see Figure 15b). The molecular dynamics of all compounds were investigated by a combination of BDS, FSC and SHS. To best of our knowledge, it is the first study applying FSC to discotic liquid crystals. SHS investigations were conducted at low temperatures using helium as purge gas. This unique combination of methods to investigate the molecular dynamics has never been reported before and enables to address both the intercolumnar space and the columns as well.

Besides localized fluctuations, surprisingly multiple glassy dynamics were detected for all materials for the first time. Glassy dynamics were proven for both processes unambiguously due to the extraordinary broad frequency range covered. The  $\alpha_1$ -process is attributed to the cooperative fluctuations of the alkyl chains in the intercolumnar space because a polyethylene-like glassy dynamics is observed. This corresponds to a glass transition in a confined three-dimensional space. The  $\alpha_2$ -process found at temperatures lower than  $\alpha_1$ -process, is assigned to the cooperative fluctuation of translational in-plane movements and/or small angle rotational fluctuations of the triphenylene core inside the part of distorted columns, where the frustration of the column packing is present. This result can be considered as a glass transition of a 1D fluid. Therefore, obtained results are of general importance to understand the glass transition, which is a topical unsolved problem of condensed matter science.

#### **4.1.1. Mesomorphic Properties**

The liquid crystalline textures of the monofunctionalized triphenylene derivatives **SHU09-SHU12** were investigated by POM. Two textures of **SHU12** are depicted as examples in Figure 22 taken during cooling from the isotropic phase. The POM pictures for the other compounds are shown in *Appendix II*, in Figure S7-S10. The taken pictures showed dendrimeric growth and pseudo focal conic fan-shaped textures, which are typical for  $\text{Col}_h$  mesophases.

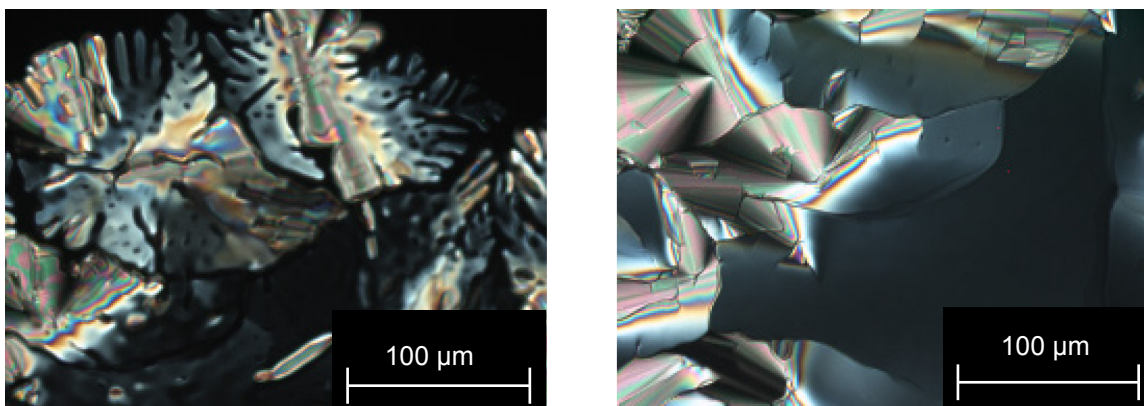


**Figure 22.** POM picture of **SHU12** at 373 K for the Iso phase (left) and at 346 K for the Col<sub>h</sub> mesophase (right) taken during cooling from the isotropic liquid (cooling rate 5 K min<sup>-1</sup>, magnification 200x).

To estimate the lattice parameters of the columnar structure, XRD measurements were performed where the results are summarized in Table 2. The X-ray pattern for all triphenylene derivatives **SHU09-SHU12** display a diffuse halo in the  $q$  vector range around  $1.4 \text{ \AA}^{-1}$  which is due to the flexible alkyl chains. Furthermore, the diffraction pattern of **SHU11** shows four distinct reflections in a ratio of the moduli of  $q$  vectors of  $1 : 1/\sqrt{3} : 1/2 : 1/\sqrt{7}$  which are indexed to (10), (11), (20), and (21). These data are characteristic for a Col<sub>h</sub> mesophase with a  $p6mm$  symmetry (Figure 23).

The diffraction pattern of the compound **SHU10** shows also the (10), (20) and the (21) reflections where that of **SHU09** and **SHU12** have only the peak corresponding to (10) (For details see *Appendix II*, Figure S11-S17). Due to the structural similarity of the molecules, the existence of a Col<sub>h</sub> phase can be assumed for these compounds, despite the absence of higher order reflections. The lattice parameters range from 19.9 Å to 20.4 Å. The lattice parameter of **SHU10** determined here is similar to that found for **SHU10** in the literature ( $a = 20.3 \text{ \AA}$  at  $T = 303 \text{ K}$ ).<sup>70</sup> The further discussion is organized in the following way. The results obtained for **SHU09** (phase behavior) and **SHU10** (molecular mobility) are discussed in detail as showcases followed by an

intense comparison of the behavior of all materials including **HAT5** where the original data are collected in *Appendix II*.

**Table 2.** Results of the XRD experiments for monofunctionalized triphenylene derivatives **SHU09-SHU12**

Compound	Mesophase	Lattice spacing /Å	d-spacing /Å experimental (calculated)	Miller Indices
<b>SHU09</b>	Col <sub>h</sub> at 363 K <i>p6mm</i>	a = 20.20	17.5 4.5	(10) halo
<b>SHU10</b>	Col <sub>h</sub> at 353 K <i>p6mm</i>	a = 20.40	17.7 6.6 (6.7) 4.5	(10) (21) halo
<b>SHU10</b> from ref. 70	Col <sub>h</sub> at 303 K <i>p6mm</i>	a = 20.30	17.6 3.5	(10) $\pi$ - $\pi$
<b>SHU11</b>	Col <sub>h</sub> at 353 K <i>p6mm</i>	a = 20.00	17.4 10.0 (10.0) 8.9 (8.7) 6.5 (6.6) 4.5	(10) (11) (20) (21) halo
<b>SHU12</b>	Col <sub>h</sub> at 353 K <i>p6mm</i>	a = 19.90	17.3 4.4	(10) halo
<b>HAT5</b> from ref. 70	Col <sub>h</sub> at 353 K <i>p6mm</i>	a = 19.86	17.2 3.6	(10) $\pi$ - $\pi$

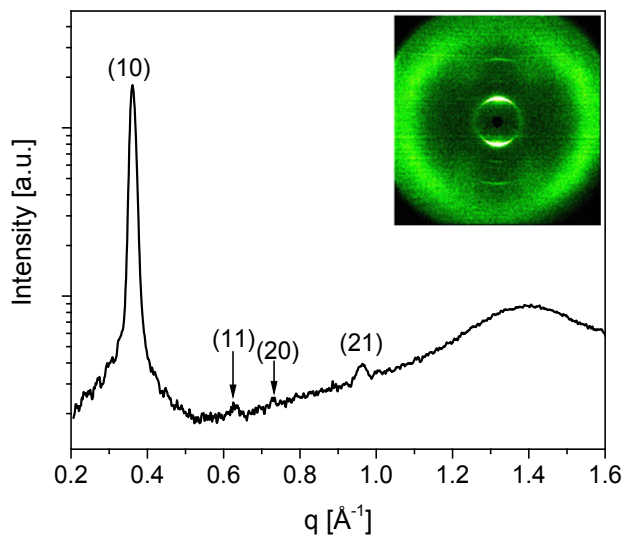


**Figure 23.** WAXS diffractogram of **SHU11** at 353 K for the Col<sub>h</sub> mesophase with the corresponding diffraction pattern (inset).

Figure 24 depicts the X-ray pattern for **HAT5** measured with the setup discussed in ref. 21 at room temperature as reference for a Cr<sub>y</sub> phase. The diffractogram shows numerous reflections

corresponding to the Cry phase. This indicates a more or less crystalline structure. Moreover, in the  $q$  range from ca.  $1 \text{ \AA}^{-1}$  to  $2 \text{ \AA}^{-1}$  an amorphous halo is present which can be taken like for the hexagonal columnar liquid crystalline as an indication for nanophase separated structure containing some disorder. It was discussed in ref. 21 that this part of the X-ray pattern is quite similar to that of semi-crystalline polyethylene. Therefore, it is concluded that also the Cry state consists of columns and disordered alkyl chains in between. For the **SHU** materials (besides **SHU10**) also a Cry phase is assumed at low temperatures which might be less ordered than that of **HAT5** as reference.

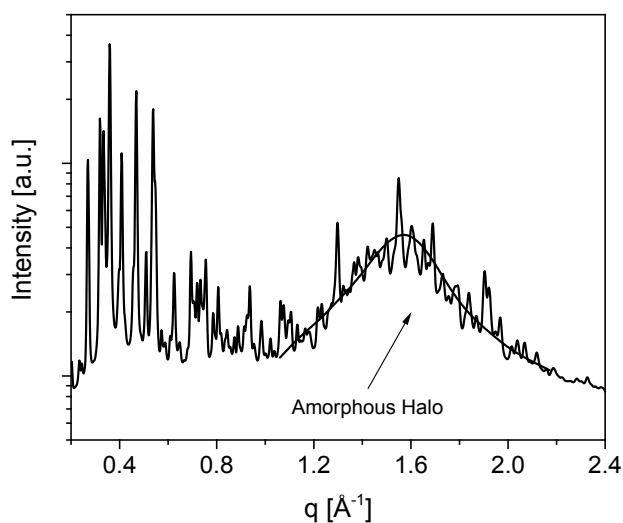
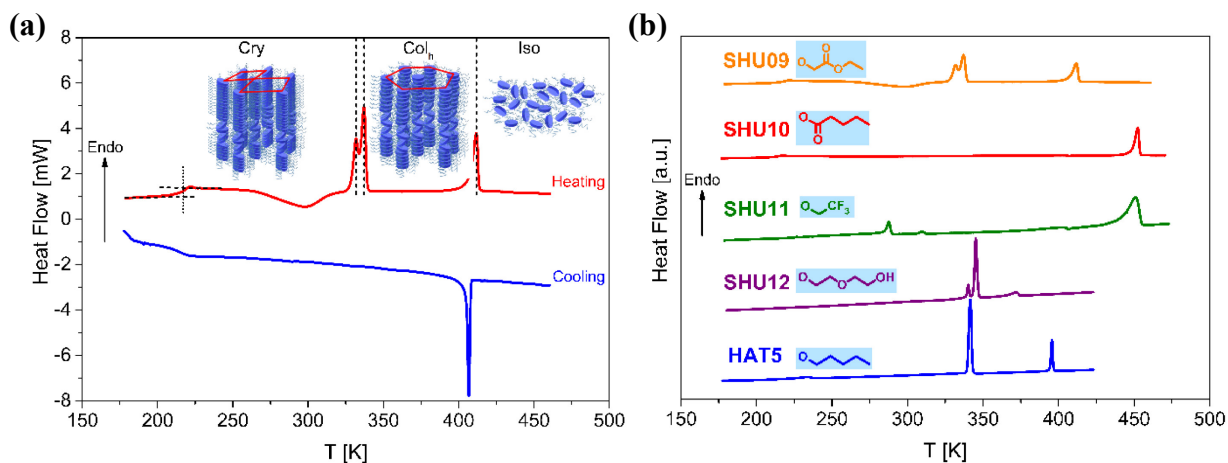


**Figure 24.** XRD diffractogram of **HAT5** at 303 K for the Cry phase.

#### 4.1.2. Phase Behavior

The phase behavior of the **SHU** compounds and **HAT5** was characterized further by conventional DSC experiments. Figure 25a shows DSC thermograms of **SHU09** for the first cooling and the second heating run. A comparison of the DSC thermograms of **SHU09**-**SHU12** and **HAT5** for the second heating runs are given in Figure 25b. The estimated phase transition temperatures and enthalpies of the materials are collected in Table 3. The DSC investigations

revealed that all DLCs, except **SHU10**, form a Cry phase at low temperatures. At higher temperatures, a Col<sub>h</sub> phase is established, where a hexagonal lattice is built by six self-assembled columns. With further increase of temperature from the Col<sub>h</sub> phase, all materials undergo a clearing transition to the Iso phase. Additionally, a crystalline to crystalline transition is detected during the heating run at 333 K, 288 K and 340 K for **SHU09**, **SHU11** and **SHU12**, respectively (see *Appendix II*). From the literature, it is known that **SHU10** crystallizes only from solution.<sup>70</sup> This is also confirmed by X-ray measurements (see Figure S13).



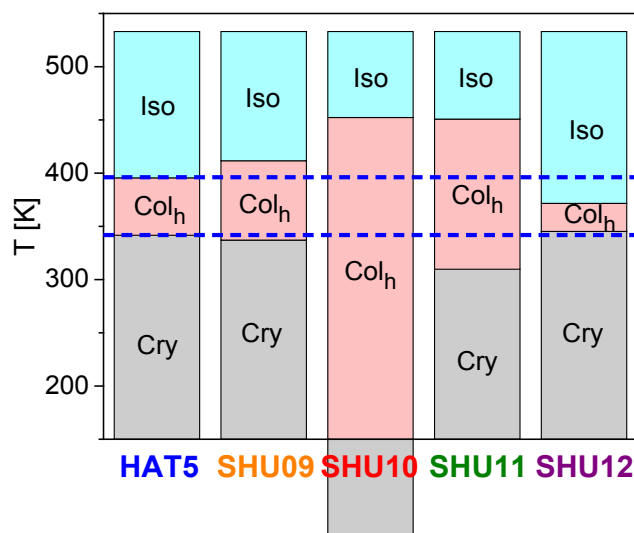
**Figure 25.** (a) DSC thermograms of **SHU09** for the first cooling and the second heating run at a rate of 10 K min<sup>-1</sup>. Dashed lines point out the phase transition temperatures observed during the second heating runs. Dotted line indicates the glass transition temperature observed during the second heating run. (b) DSC thermograms of **SHU09**-**SHU12** and **HAT5** for the second heating run at a heating rate of 10 K min<sup>-1</sup> as indicated.

Table 3 shows that the temperature range of the Col<sub>h</sub> mesophase is considerably broadened for all monofunctionalized triphenylene derivatives, except for **SHU12**, compared to unfunctionalized symmetrical **HAT5**. This result can be better comprehended from the bar chart representation of the mesophase stabilities, which is given in Figure 26. For triphenylenes functionalized with ester groups such as **SHU09** and **SHU10**, a stabilization of the columnar structure and a wider range of 2D lattice correlations with the functionalization were reported.<sup>70, 143</sup>

**Table 3.** Phase transitions temperatures and enthalpies determined by DSC

Compound	$T_{g,2}^{\text{thermal}}$ [K]	$T_{g,1}^{\text{thermal}}$ [K] ( $\Delta c_p$ [ $\text{J K}^{-1} \text{g}^{-1}$ ])	Phase	T [K] ( $\Delta H$ [ $\text{J g}^{-1}$ ])	Phase	T [K] ( $\Delta H$ [ $\text{J g}^{-1}$ ])	Phase
<b>SHU09</b>	142.7	217.1 (0.29)	Cry	337.1 (24.0)	Col <sub>h</sub>	411.7 (13.4)	Iso
<b>SHU10</b>	140.5	213.5 (0.32)	-	-	Col <sub>h</sub>	452.3 (21.9)	Iso
<b>SHU10</b> from ref. 70	-	215 (-)	Cry	317* (-)	Col <sub>h</sub>	450 (16.8)	Iso
<b>SHU11</b>	145.8	231.8 (0.05)	Cry	309.7 (0.3)	Col <sub>h</sub>	450.8 (14.7)	Iso
<b>SHU12</b>	142.9	258.5 (0.15)	Cry	345.2 (36.0)	Col <sub>h</sub>	371.6 (5.9)	Iso
<b>HAT5</b>	162.3	206.6 (0.15)	Cry	341.6 (48.0)	Col <sub>h</sub>	395.6 (13.5)	Iso
<b>HAT5</b> from ref. 21	-	-	Cry	341.7 (42.3)	Col <sub>h</sub>	396.1 (12.1)	Iso

\*The phase transition temperature is taken from ref. 70. As it is reported in ref. 70, **SHU10** crystallizes only from solution.



**Figure 26.** Mesophase stabilities of **SHU09-SHU12** in comparison with that of **HAT5**, constructed from the results given in Table 3.

This is related to the specific conformation of the ester groups including also dipole-dipole interaction. Similarly, the dipole-dipole interactions of trifluoromethyl groups may lead to the broader temperature range of Col<sub>h</sub> mesophase, observed for **SHU11**. In contrast, the temperature range of the Col<sub>h</sub> mesophase of **SHU12** is quite narrow. The reason of the narrow Col<sub>h</sub> phase for

**SHU12** might be the different interactions between the polar groups which might influence the structure and the stability of the columns. In the molecular structure of **SHU12**, there are ether and hydroxyl groups which presumably form hydrogen bonds.

In the Cry phase, a step-like change is observed in the temperature dependence of the heat flow for **SHU09**, which is characteristic for a thermal glass transition. All DLCs discussed here also undergo a thermal glass transition. The thermal glass transition temperatures ( $T_{g,1}^{\text{thermal}}$ ) as well as the corresponding increments in the specific heat capacity ( $\Delta c_p$ ) are summarized in Table 3. In the same temperature range of  $T_{g,1}^{\text{thermal}}$  found for **SHU09-SHU12** here, a glass transition is observed also for several other DLCs.<sup>25,40,70,135,144</sup> As it is reported for those DLCs, a certain disorder caused by nanophase separation of the aromatic cores and the alkyl chains surrounding the aromatic core, is held responsible for the glass transition. The halos observed in the XRD diffractograms of **SHU09-SHU12** further support the nanophase separation.

#### 4.1.3. Molecular Mobility

The molecular dynamics of the dipole functionalized triphenylene derivatives **SHU09-SHU12** and that of **HAT5** were investigated by BDS. An example for the BDS investigations is depicted in Figure 27, in a 3D representation of the dielectric loss spectra as a function of frequency and temperature for **SHU10**. Besides a conductivity contribution at low frequencies and high temperatures, three dielectrically active processes denoted as  $\gamma$ -,  $\alpha_2$ - and  $\alpha_1$ -relaxation are observed as peaks in the dielectric loss for **SHU10**. A similar behavior is observed for the compounds **SHU09**, **SHU11** and **SHU12**. For **HAT5**, two dielectrically active processes, the  $\gamma$ - and the  $\alpha_2$ -relaxation, are observed. For **SHU09** and **SHU12**, all relaxation processes take place in the Cry phase. For **SHU11**, the  $\alpha_1$ -process is also observed partly in the Col<sub>h</sub> phase due to the relatively low value of the phase transition temperature from the Cry to the Col<sub>h</sub> phase. For **SHU10**, the

relaxation processes take place in the Col<sub>h</sub> phase because **SHU10** does not undergo the phase transition from the Col<sub>h</sub> to the Cry phase during cooling.

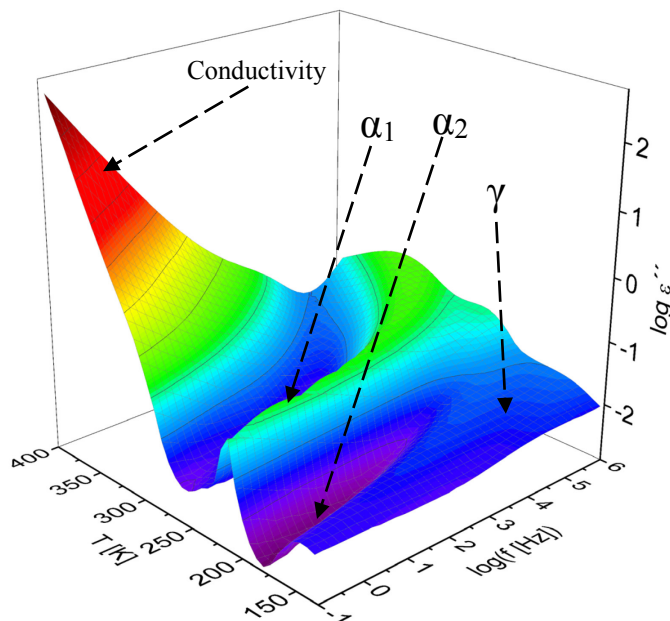


**Figure 27.** 3D representation of the dielectric loss as function of frequency and temperature for **SHU10** for the second heating run. Arrows indicate the dielectric processes. The data is shown for the Col<sub>h</sub> mesophase of **SHU10**.

The relaxation processes were quantitatively analyzed by fitting the model function of HN-function, given in eqn. (13), to the data. Examples of fits of the HN-function to the processes of **SHU10** are given in Figure 28. For each temperature, the relaxation rates  $f_{max}$  are obtained from the fits. The obtained relaxation rates  $f_{max}$  for all detected processes are plotted versus inverse temperature for **SHU10** in the relaxation map (see Figure 29) including the data for **HAT5** for comparison as an example for the temperature dependencies of the relaxation processes of the monofunctionalized triphenylenes. In addition, the relaxation maps for the other **SHU** compounds as well as the data for the related relaxation processes, are shown in *Appendix II* in Figure S23-S24.

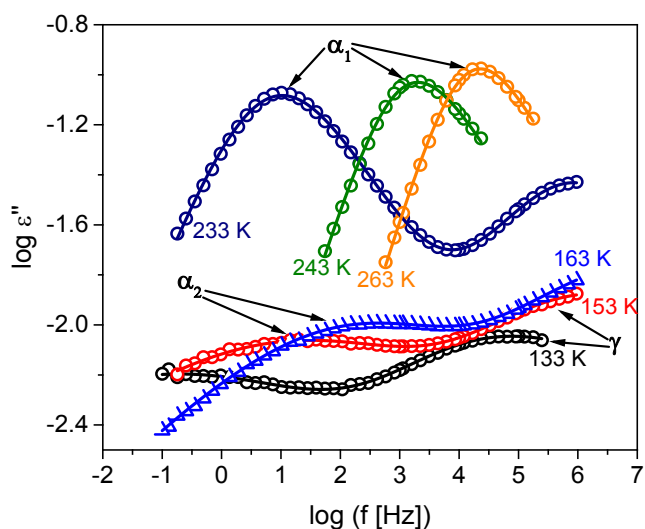


**Figure 28.** Frequency dependency of dielectric loss for **SHU10** for the second heating at the indicated temperatures. Arrows point out the dielectrically active relaxation processes. Solid lines are the fits of the HN-function to the data.

The temperature dependence of the relaxation rates of the  $\gamma$ -relaxation was approximated by the Arrhenius-equation (eqn. (1)). The temperature dependences of the relaxation rates of the  $\gamma$ -processes of **SHU09-SHU12** and **HAT5** are quite similar to that of polyethylene (**PE**) (see Figure 29).<sup>40</sup> Thus,  $\gamma$ -process of these materials is assigned to the localized fluctuations taking place in the alkyl chains probed even further by the polar groups. The activation energies for the  $\gamma$ -relaxations are calculated to be  $19 \text{ kJ mol}^{-1}$  for **SHU09**,  $17 \text{ kJ mol}^{-1}$  for **SHU10**,  $12 \text{ kJ mol}^{-1}$  for **SHU11**, and  $26 \text{ kJ mol}^{-1}$  for **SHU12** and **HAT5** (see *Appendix II*, Table S1). While the activation energies for **SHU09-11** are rather like, that for **SHU12** is essentially higher. To understand this result, one must consider that among the triphenylene derivatives, the substituents of **SHU12** are the only ones which can form hydrogen bonds with each other. The hydrogen bonds will increase the constraints to the localized molecular fluctuations and therefore its activation energy.

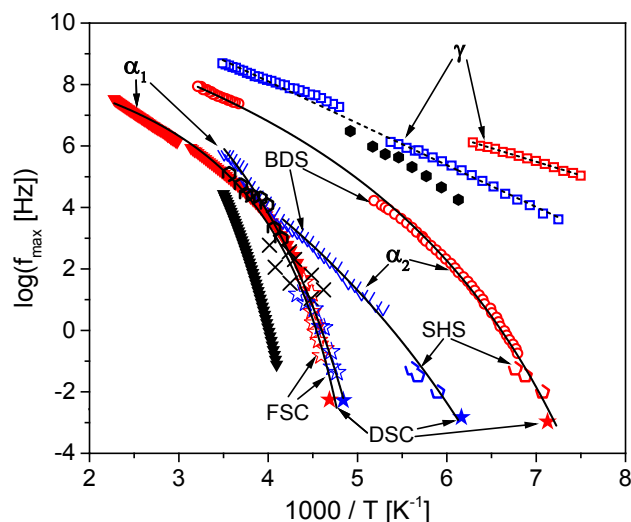


**Figure 29.** Combined relaxation map of **SHU10** constructed from data obtained by BDS, FSC and DSC. Red symbols – data for **SHU10** and blue symbols – data for **HAT5**. Triangles –  $\alpha_1$ -relaxation (BDS); open circles –  $\alpha_2$ -relaxation (BDS); filled squares –  $\gamma$ -relaxation (BDS); open stars –  $\alpha_1$ -relaxation (FSC); open pentagons –  $\alpha_2$ -relaxation (SHS); and filled stars – thermal glass transition temperatures (DSC). The relaxation rates were calculated by eqn. (3) for the given FSC and DSC data. Different symbols are used to differentiate between the different relaxation processes. Solid lines are the fits of VFT-equation (eqn. (2)) to the corresponding data. Dashed lines are fits of the Arrhenius-equation (eqn. (1)) to the data. Black filled triangles denote the dielectric  $\alpha$ -relaxation of **PE** taken from ref. 145. Black hexagons symbolize the dielectric  $\gamma$ -relaxation of **PE** taken from ref. 40. Black crosses represent the calorimetric **PE**-like glassy dynamics of poly(n-decyl methacrylate) from ref. 146. Black open hexagons symbolize the dielectric **PE**-like glassy dynamics of poly(n-decyl methacrylate) taken from ref. 147. The data shown here correspond to the Col<sub>h</sub> mesophase of **SHU10** and for the Cry phase of **HAT5**.

The relaxation rates of the  $\gamma$ -processes vary slightly, which are ranged from fast to slow: **SHU10** > **SHU09** > **SHU11** > **HAT5** > **SHU12**. A similar ordering is found for the ranking of the lattice spacing (or the distances between the columns) in the Col<sub>h</sub> phase, shown in Table 2. The lattice spacings were plotted against the relaxation rates of  $\gamma$ -process at the chosen temperature, shown in *Appendix II* in Figure S25, and the plot shows a linear relation. Since the same ranking of the distance between the columns in the Cry phase is realized,<sup>21</sup> the ranking of the relaxation rates can be explained by a self-confinement effect originating from the confinement of the alkyl chain in between the column. In other words, a shorter the distance between the columns causes higher restrictions on the localized fluctuations in the groups of the alkyl chains.

The temperature dependencies of the relaxation rates of the  $\alpha_1$ - and  $\alpha_2$ -relaxations are curved in the relaxation map, indicating glassy dynamics. Hence, they were approximated by the VFT-equation (eqn. (2)). Furthermore, as a complementary technique to BDS, FSC was performed to further investigate the glassy dynamics detected by BDS. In BDS, molecular dynamics is probed through the dipole fluctuations. Unlike BDS, FSC probes the glassy transition through the entropy fluctuations. FSC thermograms, obtained by performing measurements with heating rates from  $10 \text{ K s}^{-1}$  to  $10000 \text{ K s}^{-1}$ , are shown for **SHU10** in Figure 30 and for **SHU09**, **SHU11**, **SHU12** and **HAT5** in *Appendix II* in Figure S27-S29.

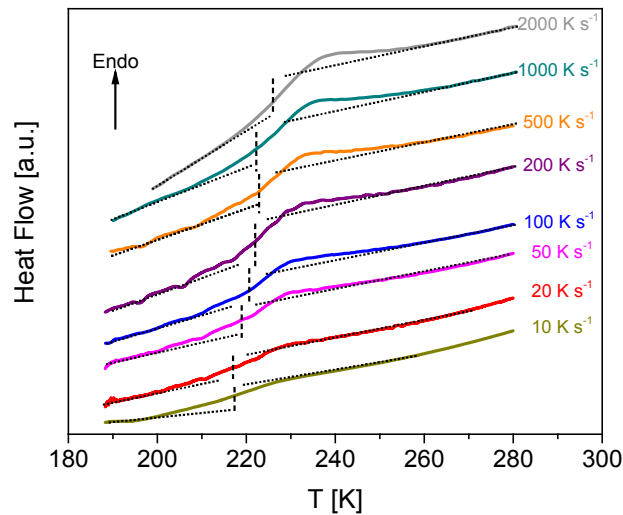


**Figure 30.** FSC thermograms of **SHU10** for heating runs at different heating rates as indicated. Dashed lines indicate the estimated thermal glass transition temperatures. The thermograms are shifted along the y-scale for clarity.

The steps in the heat flows indicate a glass transition, which is shifted to the higher temperature with increasing heating rate as expected. The temperature of the half step-height of the step was taken to determine the glass transition temperature for each heating rate. The heating rates are converted using eqn. (3) into thermal relaxation rates to compare the relaxation rates estimated from BDS measurements with the thermal ones. The estimated relaxation rates together with corresponding glass transition temperatures are included in Figure 29 together with the dielectric

data. Additionally, the data measured by conventional DSC were also converted into a relaxation rate and added to Figure 29.

The relaxation rates estimated by FSC and conventional DSC agree with dielectric  $\alpha_1$ -processes. This agreement was observed for all monofunctionalized triphenylene derivatives. This result proves that both BDS and FSC probe the same molecular process. The both data sets also agree with the relaxation rates estimated from conventional DSC measurements for  $T_{g,1}^{\text{thermal}}$  with a heating rate of  $10 \text{ K min}^{-1}$ . It is further important to note that the FSC data of **HAT5** agree with the calorimetric and dielectric data of **SHU10** but not with the dielectric relaxation rates of **HAT5**.

Haverkate et al.<sup>49</sup> revealed the structure and dynamics of **HAT6** at picosecond timescale by comparing the results of molecular dynamics (MD) simulations by addressing mainly the cores. It should be noted that the model used for simulations consist only of twelve columns having six molecules. It does not consider the full liquid crystalline structure. They found two characteristic modes of molecular motion; fast and slow motions which are separated by two orders of magnitude. The slow process is attributed to rotational movements of the core (tilt and twist), where the fluctuations of the core and alkyl chains are correlated (see Figure 31a). The fast process, which is found approximal two orders of magnitude faster than the slow process, is attributed to the translational movements of the core (parallel and perpendicular to the column axis), where alkyl chains motions only weakly correlate with the parallel motion of the core (see Figure 31b). At least the simulations evidence that the columnar like structure allows for some molecular mobility inside the column which can be also small angle rotational fluctuations. These findings about fast and slow motions of **HAT6** by simulations could shed light on the molecular assignment of the fast ( $\alpha_2$ -processes) and slow ( $\alpha_1$ -processes) glassy dynamics detected for the triphenylene

derivatives. In the following it is firstly concentrated on the  $\alpha_1$ -processes. The temperature dependence of the relaxation rates of the  $\alpha_1$ -processes for **SHU10** have close resemblance with that of dielectric  $\alpha$ -process of **PE**<sup>145</sup> (see Figure 29). A similar behavior is observed for all **SHU** materials (see *Appendix II*, Figure S23). **PE**-like glassy dynamics have been reported for columnar DLCs<sup>33,40</sup>, and columnar ILCs<sup>135</sup>. Moreover, polymers having longer n-alkyl side chains, which form a nanophase separated morphology<sup>22,147</sup>, show a **PE**-like glassy dynamics due to nanophase separated alkyl chains. This means that the observed similarity of the relaxation rates of the  $\alpha_1$ -relaxation is not accidental but is typical for nanophase system having longer alkyl chains. This is demonstrated for poly(n-decyl methacrylate) investigated by BDS. The detected **PE**-like glassy dynamics assigned to **PE**-like cooperative fluctuations of the alkyl side chains, which are connected to the main chain via ester linkage<sup>147</sup>, overlaps with the dielectric data measured for **SHU10**. This result gives further evidence that  $\alpha_1$ -relaxation of the **SHU** materials has to be assigned mainly to the cooperative fluctuations of the alkyl chains in the intercolumnar space. This corresponds to a glass transition in a confined 3D space. A further proof of this assignment comes from the calorimetric relaxation rates of the **PE**-like glassy dynamics measured also for poly(n-decyl methacrylate)<sup>146</sup>. These data are included in Figure 29 and agree with the dielectric and thermal relaxation rate estimated for the  $\alpha_1$ -relaxation of **SHU10** and are also close to those of the other **SHU** materials. This assignment agrees with the observation that the temperature dependence of the relaxation rates of the  $\alpha_1$  is more or less similar for different triphenylenes, as shown in Figure S23. The assignment of the  $\alpha_1$ -relaxation to fluctuations of the alkyl chains in the intercolumnar space does not exclude small angle rotational fluctuations of the cores. As it is evidenced by MD simulations,<sup>49</sup> the rotational fluctuations of the cores are coupled to this process. The assignment of the  $\alpha_1$ -relaxation is illustrated in Figure 31a and c. The alkyl chains are located

in the intercolumnar area between the columns built by the triphenylene unites. This corresponds to a self-assembled or a self-organized spatial confinement as also discussed for the excess low frequency excitation (Boson Peak) in the related materials.<sup>21</sup> Therefore, the  $\alpha_1$ -relaxation is considered as a glass transition in a 3D confinement.

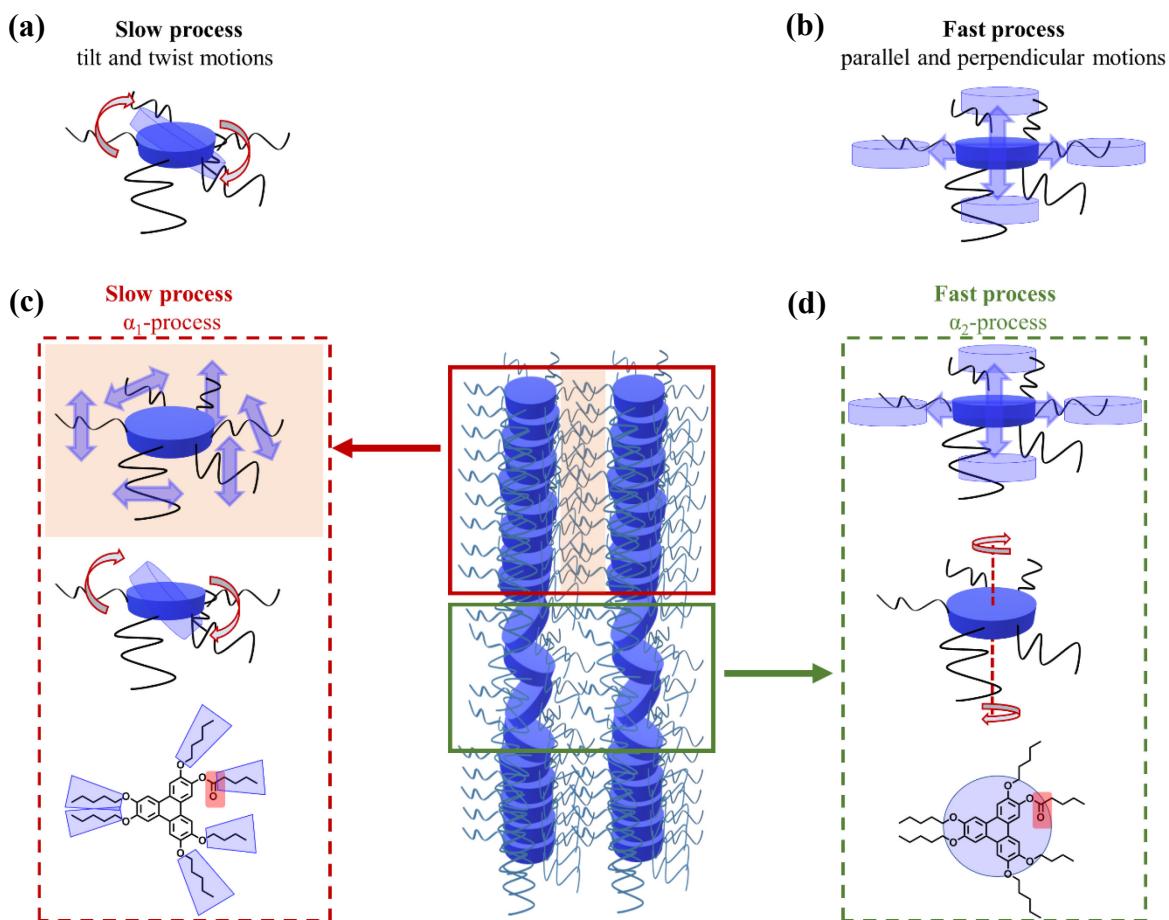


**Figure 31.** Illustrations of the characteristic (a) tilt and twist motions (slow process) and (b) parallel and perpendicular motions (fast process) for a single molecule, adapted from ref. 49. Illustrations of cooperative molecular fluctuations are attributed to (c)  $\alpha_1$ -process and (d)  $\alpha_2$ -processes for **SHU10**. Blue colored parts of **SHU10** molecules indicate the parts are assigned to the glassy dynamics and red colored parts of the molecules are the parts where these glass dynamics are sensed by BDS.

Figure 29 shows that the dielectric and thermal relaxation rates of  $\alpha_1$ -relaxation for **SHU10** are similar to the thermal relaxation rates of  $\alpha_1$ -relaxation for **HAT5**, although the former material is in the hexagonal ordered liquid crystalline state and the latter in the Cry phase. This indicates that

the molecular origin of the  $\alpha_1$ -relaxation is similar as expected because it is assigned to the fluctuation of the nanophase separated alkyl tails. Moreover, it further evidences that the phase structure of the Cry and the Col<sub>h</sub> phase is not that different on a molecular level. Also, the data for **SHU09** agree with the results obtained for **HAT5** and **SUH10**. The data for the  $\alpha_1$ -relaxation of **SHU11** and **SHU12** are slightly shifted to higher temperatures because different interactions like hydrogen bonding take place between the alkyl chains.

As discussed above, the FSC data of **HAT5** agree with calorimetric and dielectric data of **SHU10** but not with the dielectric relaxation rates of **HAT5**. Therefore, the question arises whether the dielectric process measured for **HAT5** corresponds to the  $\alpha_1$ - or may be to the  $\alpha_2$ -process. Similar deviations in the temperature dependencies of the relaxation rates of the dielectric relaxation process have been reported, when the unfunctionalized symmetrical **HAT6** is compared with asymmetrical a monofunctionalized **HAT6** (**HAT6-C<sub>10</sub>Br**).<sup>40</sup> A corresponding behavior is observed for the triphenylene-based symmetrical DLC **THA11** compared with the asymmetrical monofunctionalized DLC **Tri11**<sup>144</sup>. **Tri11** has a quite similar chemical structure to **SHU09** and **SHU10** and can be also considered as monofunctionalized **HAT5**. Therefore, the glassy dynamics of **Tri11** and **THA11** compared with that of **SHU09-SHU12** in a relaxation map given in Figure S24. Figure S24 depicts that the temperature dependence of relaxation rates of **Tri11** overlaps with that of **SHU09-SHU10**, however, that of symmetrical **THA11** deviates like **HAT5** and **HAT6**. This comparison might further evidence that the dielectric process measured for **HAT5** is not  $\alpha_1$ -process observed for the functionalized discotic liquid crystals but might be due to the  $\alpha_2$ -process.

To proof whether the  $\alpha_2$ -process corresponds to a second of glassy dynamics in these systems, calorimetric investigation should be useful. Unfortunately, by conventional DSC experiments

using nitrogen as purge gas cannot be carried out at the required low temperatures below 173 K. Thus, DSC measurements were also conducted at temperatures down to 103 K using helium as purge gas. Selected examples for thermograms for the DLCs for these measurements are given in *Appendix II* in Figure S22. A glass transition at lower temperatures than  $T_{g,1}^{\text{thermal}}$ , which is called  $T_{g,2}^{\text{thermal}}$ , is detected for the all monofunctionalized triphenylene derivatives. To best of our knowledge for the first time, a glass transition for DLCs at such low temperatures is observed besides the one observed commonly at temperatures above 173 K. The estimated values for  $T_{g,2}^{\text{thermal}}$  are given in Table 3.  $\Delta c_p$  at this low temperature glass transition is too small to be quantitatively discussed. Furthermore, the  $\alpha_2$ -processes of **HAT5** and **SHU10** were also investigated by conducting SHS experiments, employing temperature modulated DSC in the step scan approach<sup>128</sup>, at low temperatures using helium as purge gas. Figure 32 gives the temperature dependence of the real part of the complex specific heat capacity,  $c_p'$ , at a frequency of  $3.3 \times 10^{-2}$  Hz for **HAT5** and **SHU10**. The temperature dependency of  $c_p'$  shows a step-like increase with increasing temperature which is characteristic for a glass transition.

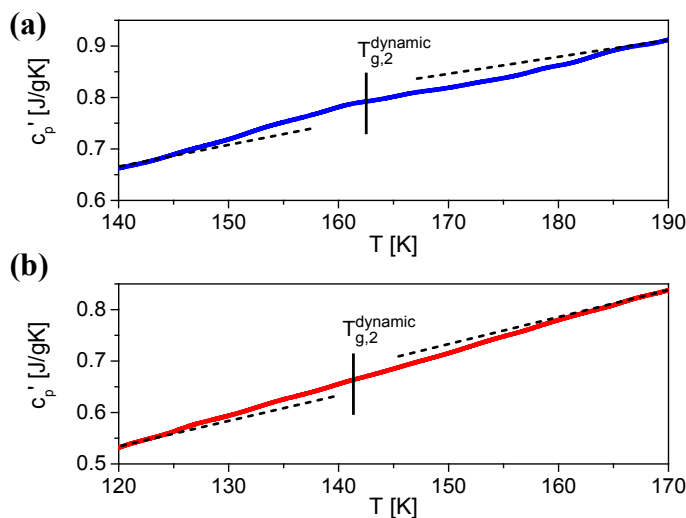


**Figure 32.** Temperature dependence of the real part of the complex specific heat capacity,  $c_p'$ , for (a) **HAT5** and (b) **SHU10** at a modulation frequency of  $3.3 \times 10^{-2}$  Hz. Solid lines indicate the mid-step positions.

SHS data were analyzed by taking the mid-step position of  $c_p'(T)$  to determine a corresponding  $T_g^{\text{dynamic}}$  for the given frequency. A thermal relaxation rate is also estimated for  $T_{g,2}^{\text{thermal}}$  obtained from DSC investigation using eqn. (3). These calorimetric data agree well with the dielectric relaxation rates for the  $\alpha_2$ -relaxation as depicted in Figure 29 and Figure S23-S24. This agreement proves firstly that the dielectric  $\alpha_2$ -relaxation corresponds to a low temperature glass transition for the **SHU** materials. Secondly, also for **HAT5** the dielectric data coincidence with the relaxation rates obtained from calorimetric investigations at low temperatures. This result proves that the dielectric process observed for **HAT5** corresponds to the  $\alpha_2$ -relaxation. A dielectric  $\alpha_2$ -relaxation is not observed for **HAT5** due to the lack of a net dipole moment.

The  $\alpha_1$ -relaxation is assigned to cooperative fluctuations of the alkyl chain in the intercolumnar space correlated to rotational fluctuations of the core (tilt and twist). This molecular process is frozen at temperatures below  $T_{g,1}^{\text{thermal}}$ . Freezing of the disk rotation below  $T_g^{\text{thermal}}$  (here  $T_{g,1}^{\text{thermal}}$ ) has been reported for DLCs.<sup>37,64</sup> According to the picture of molecular dynamics drawn for **HAT6** in ref. 49 discussed above, the only remaining unfrozen type of movement below  $T_{g,1}^{\text{thermal}}$  is translational in-plane movements or small angle rotational fluctuations of the triphenylene core. Thus,  $\alpha_2$ -processes is attributed to the cooperative fluctuations of translational in-plane movements and/or small angle rotational fluctuations of the triphenylene core inside the columns, where relatively distorted packing of the cores leads to a frustration of the column packing. This molecular assignment of  $\alpha_2$ -process is illustrated in Figure 31d and the frustration of the column packing Figure 2b. Translational movements of the core are restricted by the core-core distance; the distance between the adjacent cores in the columns. The relaxation rates of the  $\alpha_2$ -processes seem to be correlated with the core-core distance (see Figure 29 and Table 2). Since the columns

can be considered a one-dimensional liquid, the  $\alpha_2$ -processes can be considered as glassy dynamics in a one-dimensional liquid.

Comparing the temperature dependence of the  $\alpha_2$ -processes for the **SHU** materials with that of **HAT5** (see Figure 29), it reveals that at the same temperature the relaxation rates for the **SHU** systems are higher than that of **HAT5**. The  $\alpha_2$ -processes are related to the disorder in the column, therefore, it might be concluded that the disorder or distortions of the columns are higher for the functionalized DLCs than that of **HAT5**.

#### 4.1.4. Conclusions

Here, the mesomorphic properties, phase behavior and molecular dynamics of a selected series of monofunctionalized triphenylene-based DLCs, **SHU09-SHU12**, were studied. The obtained results were compared with that of the commercially available **HAT5**, which is the corresponding unfunctionalized symmetrical DLC.

The mesomorphic properties were studied using POM as well as employing XRD, and columnar mesophases were revealed. Besides the characteristic Bragg peaks, a diffuse halo is observed in the XRD pattern indicates nanophase separation between intercolumnar area filled with the disordered flexible alkyl chains and columns built of the aromatic cores.

The phase behavior of the **SHU09-SHU12** compounds and **HAT5** was investigated using conventional DSC. Except for **SHU12**, broadened temperature range of the Col<sub>h</sub> mesophase was found for the other **SHU** materials compared to unfunctionalized **HAT5**. Thus, it is concluded that monofunctionalization of one of the six alkyl arms of **HAT5** with ethyl glycolate, hexanoyl, or trifluoromethyl results in better stabilization of the Col<sub>h</sub> mesophase, in contrast to the functionalization with diethyleneglycol. Moreover, two thermal glass transitions,  $T_{g,1}^{\text{thermal}}$  at high

temperatures and  $T_{g,2}^{\text{thermal}}$  at low temperatures, were detected in the Cry phase for **SHU09**, **SHU11**, **SHU12** as well as **HAT5** and in the Col<sub>h</sub> phase for **SHU10**.

The molecular dynamics were explored by BDS. Besides localized fluctuations, two processes are detected ( $\alpha_2$ - and  $\alpha_1$ -relaxation), where the corresponding relaxation rates are both curved when plotted versus inverse temperature indicating glassy dynamics. The temperature dependencies of relaxation rates of  $\alpha_1$ -processes are further investigated using FSC. As a first result, the data obtained from BDS, FSC and conventional DSC corresponding  $T_{g,1}^{\text{thermal}}$  agree with each other, and can be well described by a single VTF dependency. This is found for all materials.

The  $\alpha_1$ -process is attributed to the cooperative fluctuations of the alky chains in the intercolumnar space, partly coupled with small angle rotational fluctuations of the core. This assignment is reasoned by the detected **PE**-like glassy dynamics for **SHU** compounds. Such an assignment of glassy dynamics to **PE**-like glassy dynamics has been reported for columnar DLCs<sup>33,40</sup> and columnar ILCs<sup>135</sup>. The alkyl chains are arranged in the intercolumnar space between the self-assembled columns of the aromatic moieties which induces a spatial confinement to the alkyl chains. Therefore, the  $\alpha_1$ -process must be regarded as a glass transition in a three-dimensional confinement.

At temperatures lower than the characteristic temperatures for the  $\alpha_1$ -process, the dielectric  $\alpha_2$ -process was found. Moreover, SHS was performed as a complementary technique to BDS in order to investigate the glass dynamics related to  $\alpha_2$ -process. Similar to the  $\alpha_1$ -process, it is concluded that the dielectric and calorimetric data are in good agreement for  $\alpha_2$ -processes. This agreement evidences the fact that the  $\alpha_2$ -process corresponds to a glass transition. At these temperatures, the cooperative fluctuations responsible for the  $\alpha_1$ -process are frozen. The only

remaining unfrozen types of fluctuations are parallel and perpendicular movements (translational movements) or small angle rotational fluctuations of the cores. Thus,  $\alpha_2$ -process is assigned to the cooperative fluctuation of translational in-plane movements and/or small angle rotational fluctuations of the triphenylene core inside the part of columns, where a frustration of the column packing is present. Because of the presence of the certain amount of disorder in the column, it can be considered as a one-dimensional liquid. Because the  $\alpha_2$ -process is related only to the columns, it can be considered as a glass transition in a one-dimensional liquid.

In summary, multiple glassy dynamics in triphenylene-based DLCs have been revealed by combining BDS and advanced calorimetry techniques. The dipole functionalization of triphenylene derivatives gave possibility to probe molecular dynamics in detail through dipole fluctuations perspective by BDS. For unfunctionalized triphenylenes, it is difficult to distinguish the different glassy dynamics, as it is in case of **HAT5**, by BDS due to the weak dipole movement. On the other hand, advanced calorimetry techniques, FSC and SHS, probe glassy dynamics through the perspective of entropy fluctuations. Thus, the combination of different techniques is very beneficial in order to understand and reveal a process in a system from different perspectives in a complementary manner.

## 4.2. Triphenylene Crown Ether-Based Discotic Liquid Crystals

The phase behavior of two unsymmetrical triphenylene crown ether-based DLCs having different lengths of alkyl chains, **KAL465** and **KAL468** (see Figure 17a), was investigated using DSC. Two glass transitions were observed in the Cry phase by DSC. The molecular mobility of the **KAL** compounds was studied using BDS. In the BDS investigations, three dielectric active relaxation processes were observed for both samples. At low temperatures, a  $\gamma$ -process in the Cry

state was detected and is assigned to the localized fluctuations taking place in the alkyl chains. The  $\alpha_1$ -process takes place at higher temperatures in the Cry phase. An  $\alpha_3$ -process was found in the Col<sub>h</sub> mesophase. The temperature dependence of the relaxation rates of the  $\alpha_3$ -process is a completely different than that of the  $\alpha_1$ -relaxation. Molecular assignments of these different glassy dynamics are proposed.  $T_g^{\text{thermal}}$  determined by DSC agrees with the dielectric data corresponding to the detected glassy dynamics. In addition, a conductivity contribution was explored by BDS for both **KAL** compounds. The conductivity contribution appears in both Cry and Col<sub>h</sub> phases at temperatures above 300 K.

#### 4.2.1. Phase Behavior

The phase behavior of the **KAL** compounds was explored by DSC experiments. The obtained DSC thermograms for **KAL465** and **KAL468** are given in Figure 33a and b for the first cooling and the second heating run. Table 4 shows the estimated phase transition temperatures and enthalpies determined together with the corresponding literature values.

A hysteresis was observed between the cooling and heating cycles for the phase transition temperatures for both materials. The hysteresis for the Cry-Col<sub>h</sub> transition is more pronounced than that for the Col<sub>h</sub>-Iso transition. On the one hand, the phase transition enthalpies of Cry-Col<sub>h</sub> for **KAL465** is higher than that for **KAL468**. On the other hand, the phase transition enthalpies of Col<sub>h</sub>-Iso are similar for both **KAL465** and **KAL 468**. This might imply that longer alkyl chains result in higher the enthalpies of Cry-Col<sub>h</sub> transition, although, it seems to be the length of alkyl chains has no significant effect on the enthalpies of Col<sub>h</sub>-Iso transition for these two compounds. Moreover, the shorter alkyl chains lead to the broader temperature range of the mesophase (91 K for **KAL465** > 84 K for **KAL468**).

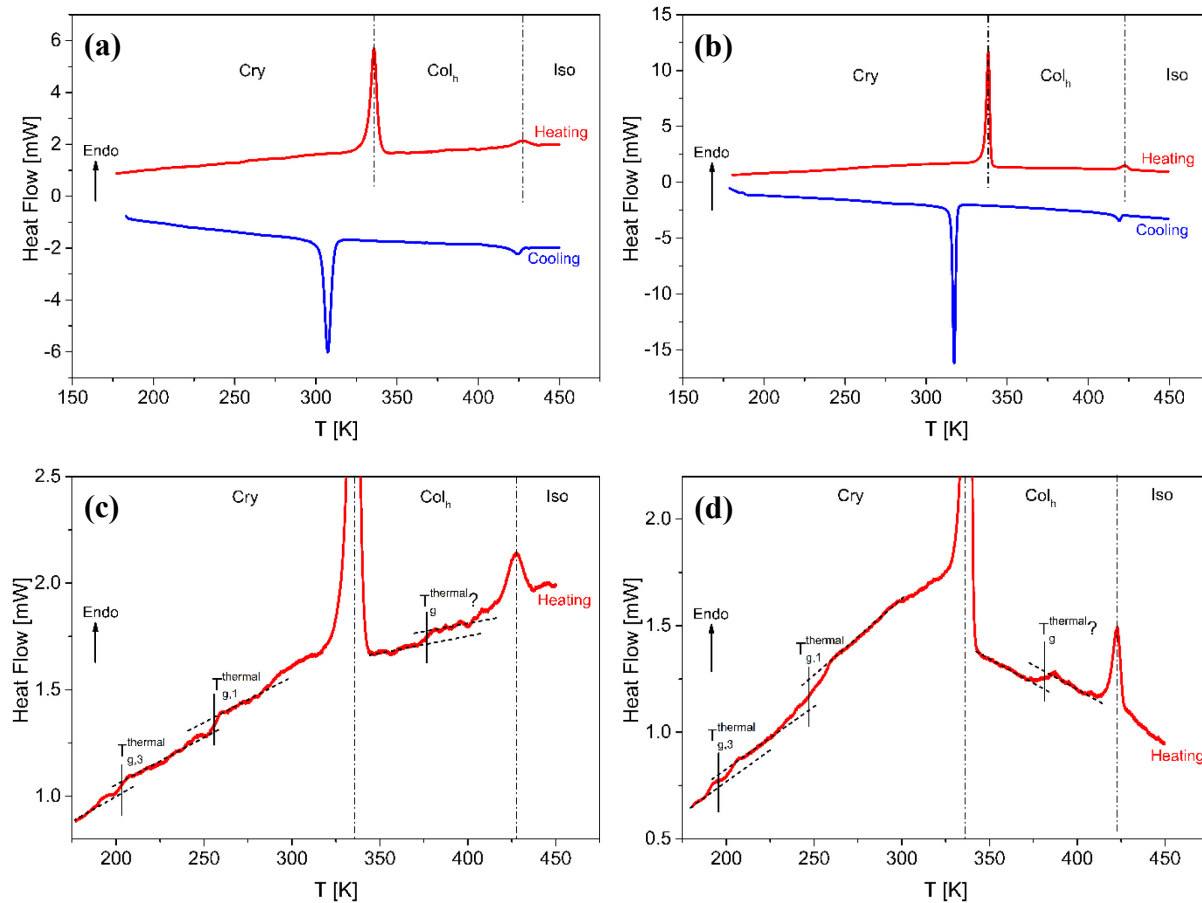


**Figure 33.** DSC thermograms of (a) KAL465 and (b) KAL468 during heating (red line) and cooling (blue line) with a heating/cooling rate of 10 K min<sup>-1</sup>. Dashed-dotted lines point out the phase transition temperatures observed during the heating cycle. DSC thermograms of (c) KAL465 and (d) KAL468 zooming the temperature range between 175 K and 475 K for the heating run. Black solid vertical lines indicate the determined thermal transition temperatures.

**Table 4.** Phase transitions temperatures and enthalpies determined by DSC

Compound	Run	T <sub>g,1</sub> <sup>thermal</sup> [K]		Phase	T [K]		T [K]		Phase
		(Δc <sub>p</sub> [J K <sup>-1</sup> g <sup>-1</sup> ])	(Δc <sub>p</sub> [J K <sup>-1</sup> g <sup>-1</sup> ])		(ΔH [J g <sup>-1</sup> ])	(ΔH [J g <sup>-1</sup> ])			
KAL465	2 <sup>nd</sup> H	202.9 (0.05)	255.5 (0.10)	Cry	335.8 (28.5)	Col <sub>h</sub>	427.3 (2.2)	Iso	
	1 <sup>st</sup> C	-	-	Cry	307.4 (30.1)	Col <sub>h</sub>	424.3 (2.2)	Iso	
KAL468	2 <sup>nd</sup> H	195.4 (0.06)	246.8 (0.08)	Cry	339.2 (33.4)	Col <sub>h</sub>	422.8 (2.4)	Iso	
	1 <sup>st</sup> C	-	-	Cry	317.3 (39.6)	Col <sub>h</sub>	419.1 (2.2)	Iso	
KAL465*	2 <sup>nd</sup> H	-	-	Cry	329.2 (28.3)	Col <sub>h</sub>	426.2 (1.8)	Iso	
	1 <sup>st</sup> C	-	-	Cry	310.2 (33.4)	Col <sub>h</sub>	416.2 (1.4)	Iso	
KAL468*	2 <sup>nd</sup> H	-	-	Cry	338.2 (32.4)	Col <sub>h</sub>	422.2 (2.4)	Iso	
	1 <sup>st</sup> C	-	-	Cry	321.2 (37.1)	Col <sub>h</sub>	421.2 (1.9)	Iso	

H: Heating, C: Cooling. \*The data was taken from ref. 132 for comparison.

Two different steps observed in the temperature dependence of the heat flows shown in Figure 33 in the Cry phase for both compounds indicate two thermal glass transitions. The mid-step positions of the steps were taken as  $T_{g,1}^{\text{thermal}}$  and  $T_{g,3}^{\text{thermal}}$  for the glass transitions at higher and lower temperatures respectively. The determined thermal glass transition temperatures ( $T_{g,1}^{\text{thermal}}$  and  $T_{g,3}^{\text{thermal}}$ ) as well as corresponding  $\Delta c_p$  values are given in Table 4. These glass transition implying some disorder in the material might be caused by a kind of nanophase separation of the alkyl chains and the aromatic cores. Such a nanophase separation was evidenced by an amorphous halo observed in the X-ray patterns of the different CLCs in the Cry phase.<sup>21,25,37,135</sup> Additionally, a step-like change in the temperature dependence of the heat flows, in the temperature range from 365 K to 240 K, is observed in the Col<sub>h</sub> phase for both **KAL465** and **KAL468**. Although, it might imply a columnar thermal glass transition, the reproducibility of the data for this step is questionable. A more detailed investigation by means of SHS and/or FSC is needed to evidence that it is a glass transition; therefore, it is not further discussed here.

#### 4.2.2. Molecular Mobility

The molecular dynamics of the triphenylene crown ether-based unsymmetrical DLCs were investigated using BDS. The BDS investigations are shown in Figure 34 in 3D representations of the dielectric loss spectra as a function of frequency and temperature. three dielectrically active Tprocesses denoted as  $\gamma$ -,  $\alpha_3$ - and  $\alpha_1$ -relaxation are observed. In the Cry phase, the  $\gamma$ -process appears at low temperatures and  $\alpha_1$ -process at higher temperatures.  $\alpha_3$ -process is observed at even higher temperatures in the Col<sub>h</sub> mesophase. In addition, a conductivity contribution is detected at low frequencies and high temperatures in the Cry and Col<sub>h</sub> phases.

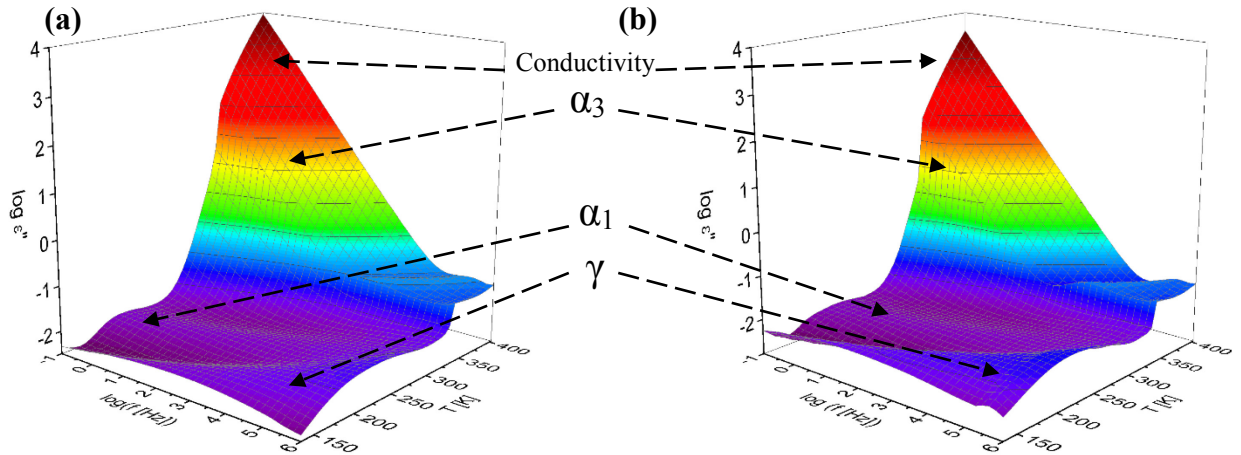


**Figure 34.** 3D representation of the dielectric loss as function of frequency and temperature for (a) **KAL465** and (b) **KAL468** for the second heating run. Arrows indicate the dielectric processes and the conductivity contribution.

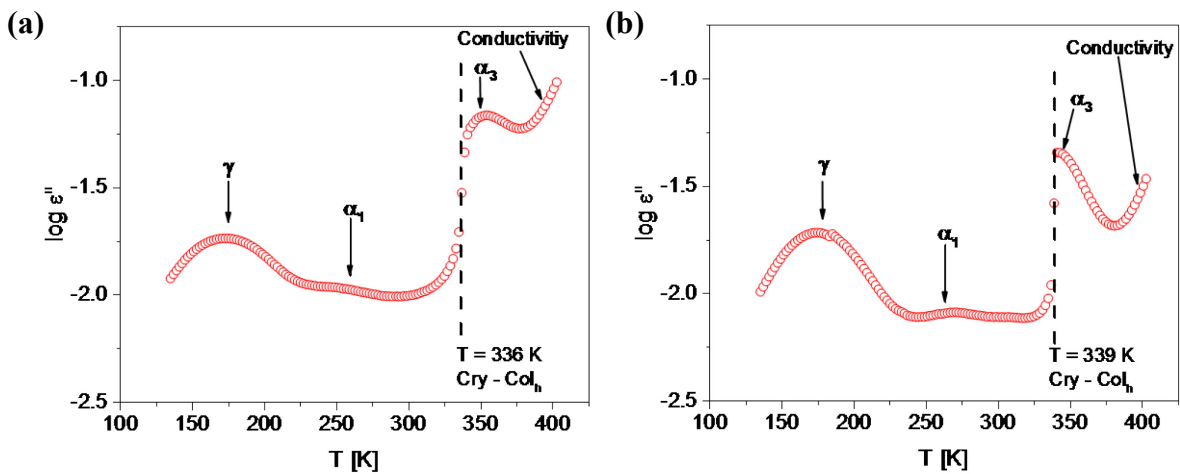


**Figure 35.** Temperature dependence of the dielectric loss ( $\log \epsilon''$ ) at 1000 Hz for (a) **KAL465** and (b) **KAL468** for the second heating run. Dashed lines point out the phase transition temperatures detected during the heating cycle as indicated.

Figure 35 depicts the overview of the BDS measurements for the second heating run, represented as the temperature dependence of the dielectric loss ( $\log \epsilon''$ ) at 1000 Hz, **KAL465** and **KAL468**. The observed sharp changes in the temperature dependence of the  $\epsilon''$  for both samples at temperatures close to the  $\text{Col}_h$ -Iso phase transition temperature ( $T_{\text{Col}_h\text{-Iso}}$ ) could be further taken as a measure for the phase transition temperatures. The  $T_{\text{Col}_h\text{-Iso}}$  determined by DSC is in good

agreement with the  $T_{\text{Colh-Iso}}$  obtained from the dielectric data. As it is revealed by DSC, a pronounced thermal hysteresis was also observed in the dielectric data for the  $\text{Col}_h$ -Iso transition.

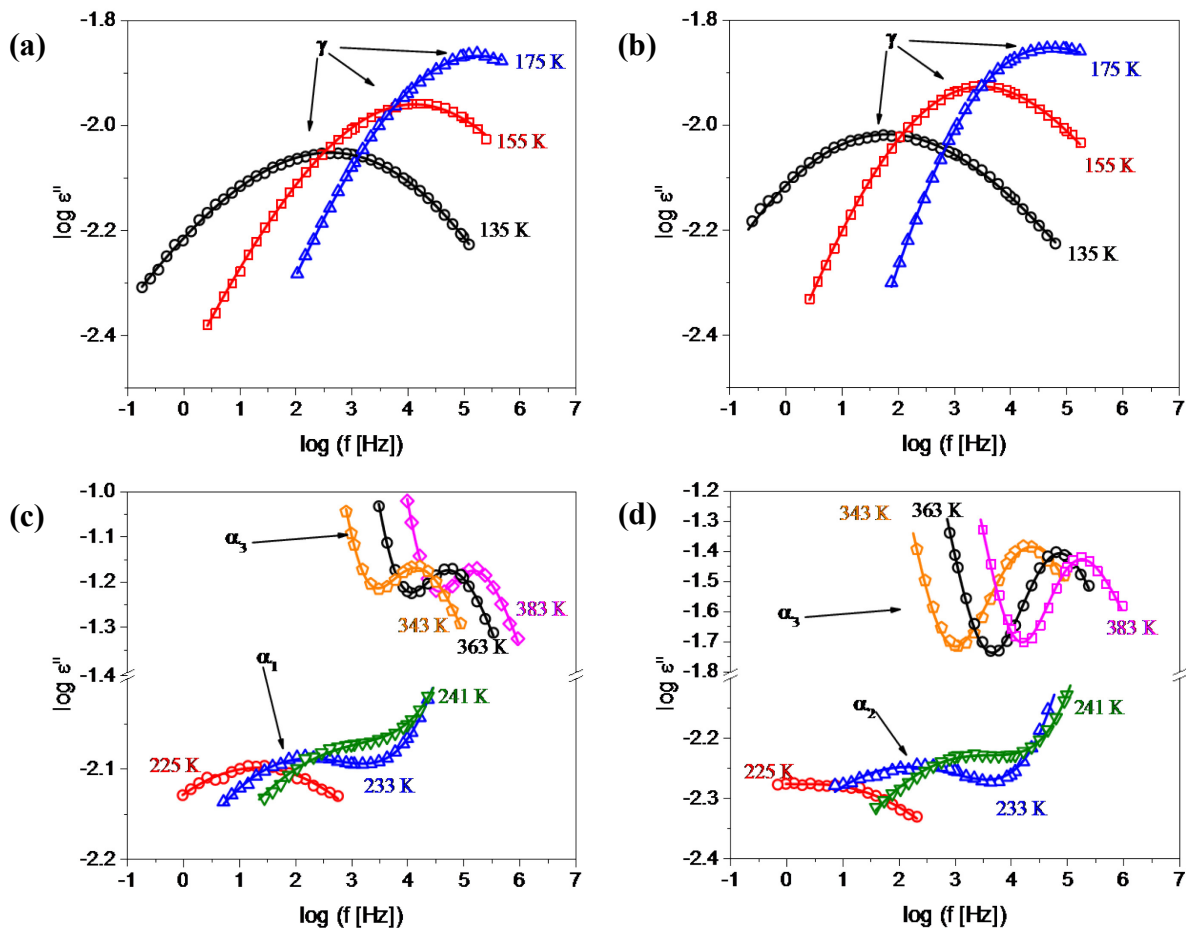


**Figure 36.** Frequency dependency of dielectric loss for the  $\gamma$ -processes of (a) **KAL465** and (b) **KAL468** as well as that for the  $\alpha_1$ - and  $\alpha_3$ -processes of (c) **KAL465** and (d) **KAL468**.

The HN-function (eqn. (13)) was fitted to the data in order to analyze the relaxation processes quantitatively. Examples of the HN-function fittings to the dielectric processes are shown for **KAL465** and **KAL468** in Figure 36. The relaxation rates  $f_{max}$  obtained from the fits for each temperature, are collected in the relaxation map given in Figure 37. Similar to the case of **SHU** compound in the previous section, the dielectric data of **PE** are added to Figure 37 for comparison since the repeating units of **PE** have a comparable structure to the structure of the alkyl substituents of **KAL** compounds. Therefore, such a comparison of the temperature dependencies of the

relaxation rates  $f_{max}$  of the relaxations processes for **PE** and that for CLCs having substituent alkyl chains seems to be useful in order to assign the detected processes to the molecular fluctuations.

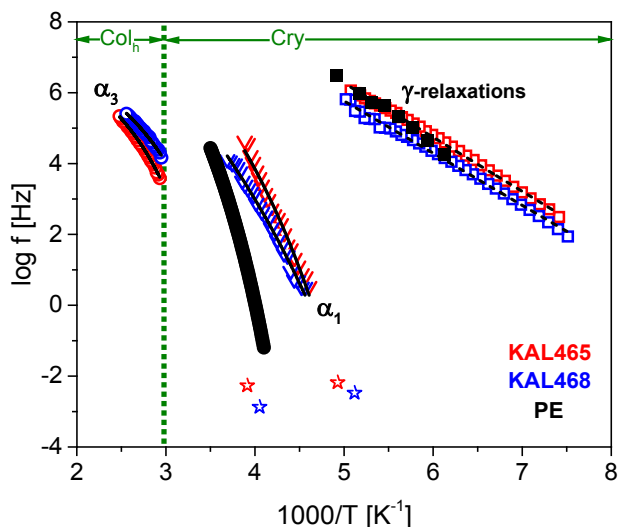


**Figure 37.** Relaxation map of **KAL465** and **KAL468**. Open red symbols – data for **KAL 465**; open blue symbols – data for **KAL468**. Squares –  $\gamma$ -relaxation (BDS); triangles –  $\alpha_1$ -relaxation (BDS); circles –  $\alpha_3$ -relaxation (BDS); filled stars – thermal glass transition temperatures (DSC). The relaxation rates were calculated by eqn. (3) for the given DSC data. Solid lines are the fits of the VFT-equation (eqn. (2)) to the data. Dashed lines are the fits of Arrhenius-equation (eqn. (1)) to the data. Filled black circles and squares indicate the dielectric  $\alpha$ - and  $\gamma$ -relaxations of **PE** taken from the ref.s 145 and 40 respectively.

The temperature dependence of the relaxation rates of the  $\gamma$ -relaxation was approximated by the Arrhenius equation (eqn. (1)). As it has been revealed for **SHU** compounds, similarly the  $\gamma$ -process of **KAL** compounds is assigned to the localized fluctuations taking place in the alkyl chains since the temperature dependences of the relaxation rates of the  $\gamma$ -processes for **KAL465** and **KAL468** are quite similar to that for **PE**.<sup>40</sup> Furthermore, the temperature dependences of the relaxation rates of the  $\gamma$ -processes for **KAL** compounds and that for **HAT5** (as well as that for **SHU09-12**) closely resemble each other (see Figure S30). The activation energies for the  $\gamma$ -relaxations are calculated to be and  $29 \text{ kJ mol}^{-1}$  for **KAL465** and  $28 \text{ kJ mol}^{-1}$  for **KAL468** (see *Appendix III*, Table S2). Moreover, the relaxation rates of the  $\gamma$ -process of **KAL465** are higher

than that of **KAL468**, although as reported in ref. 132 the lattice spacing of the columns in Col<sub>h</sub> phase is smaller for **KAL465** than that for **KAL468**. For **SHU** compounds, a linear relation of the lattice spacings and  $f_{max}$  of  $\gamma$ -processes has been realized and explained by the self-confinement effect. However, such a relation is not recognized for the **KAL** compounds.

The temperature dependencies of the relaxation rates of the  $\alpha_1$ - and  $\alpha_3$ -relaxations are curved when they are plotted in the relaxation map, indicating glassy dynamics. Therefore, they are approximated by the VFT-equation (eqn. (2)). The calculated VFT parameters are summarized in Table S2. The relaxation rates corresponding to the  $T_{g,1}^{thermal}$  and  $T_{g,3}^{thermal}$  obtained by DSC were calculated by eqn. (3), and is added to Figure 37. On the one hand, the relaxation rates related to the  $T_{g,1}^{thermal}$  estimated by DSC is in a good agreement with dielectric  $\alpha_1$ -processes. On the other hand, the relaxation rates of dielectric  $\alpha_3$ -processes detected in the Col<sub>h</sub> mesophase almost comply well with the calorimetric data for  $T_{g,3}^{thermal}$  detected in the Cry phase. However, the comparison of the temperature dependencies of the dielectric and thermal relaxation rates of the  $\alpha_1$ -processes elucidated that  $\alpha_3$ -processes seem to have faster dynamics in Cry phase than that in the Col<sub>h</sub> phase. In order to get more understanding of the reason of this discrepancy, the glass dynamics related to the  $\alpha_3$ -processes should be further studied using the calorimetric techniques like SHS and/or FSC.

The temperature dependencies of the relaxation rate of the  $\alpha_1$ -processes for **KAL** compounds is similar to that for the dielectric  $\alpha$ -process of **PE**. Moreover, the data for the calorimetric  $\alpha$ -process of **PE**<sup>146</sup> and the **PE**-like glassy dynamics detected for poly(*n*-decyl methacrylate)<sup>147</sup> as well as the data for  $\alpha_1$ -process of **HAT5** overlap with the dielectric data measured for  $\alpha_1$ -processes of **KAL** compounds (see Figure S30). For this reason, the  $\alpha_1$ -processes of **KAL465** and **KAL468** are attributed to the **PE**-like cooperative fluctuations of the alkyl chains. Similar **PE**-like glassy

dynamics reported for **SHU** compounds (*Section 4.1.3*)<sup>43</sup>, triphenylene-based<sup>40,144</sup> and pyrene-based DLCs<sup>33</sup> further proof this assignment.

The  $\alpha_3$ -processes of the **KAL** compounds were observed (in the Col<sub>h</sub> phase) at temperatures higher than the temperatures where the  $\alpha_1$ -processes were detected (in the Cry phase). This implies that molecular origins are presumably different for the  $\alpha_1$ - and  $\alpha_3$ -processes. For the molecular assignment of the  $\alpha_3$ -process, the molecular motions of the molecules of the triphenylene-based DLCs discussed in the *Section 4.1.3* should be considered (see Figure 31). This is because the molecular motions of the molecules of the **KAL** compounds are expected to be similar to that of the triphenylene-based DLCs owing to the presence of triphenylene groups also in the core of the molecules of **KAL465** and **KAL468** (see Figure 16 and Figure 17a). After assigning the  $\alpha_1$ -processes to the **PE**-like glassy dynamics of the alkyl chains, according the discussions in the *Section 4.1.3* the remaining interpretation possibility for the molecular assignment is the cooperative fluctuations of the molecules of the core; translational in-plane movements and/or small angle rotational fluctuations. The temperature dependencies of the relaxation rates of the  $\alpha_2$ -processes detected in the Cry phase for **SHU09**, **SHU12** and **HAT5** are similar to that for  $\alpha_3$ -processes of the **KAL465** and **KAL468**. Therefore, the  $\alpha_3$ -processes of **KAL465** and **KAL468** might be assigned to the cooperative fluctuations of the cores made of triphenylenes including the crown ether groups. For this interpretation, it should be considered that interconnected columnar structure formed by the **KAL** compounds might result in higher restrictions on the glass dynamics attributed to the core. This might explain why the  $\alpha_3$ -processes were detected at temperatures approximately 180 K higher than the temperature where  $\alpha_2$ -processes were observed. Although, this interpretation possibility seems to be likely, also different interpretation possibilities might be discussed. Another possibility for the molecular assignment of the  $\alpha_3$ -process might be the

cooperative fluctuations of the crown ether (since the crown ether carries a considerable dipole moment) or rotational fluctuations. The understanding gained here by BDS is insufficient to further discuss the interpretation possibilities for the molecular assignment of the  $\alpha_3$ -process without any further investigations, e.g. SHS and/or FSC investigations.

#### 4.2.3. Conductivity

The dielectric spectra are dominated by conductivity contribution at the temperatures above 300 K for **KAL465** and **KAL468**. The conductivity contributions observed were also analyzed to quantify the conductivity contribution as well as to reveal the conductivity mechanism. The complex conductivity  $\sigma^*$  is related to the complex dielectric function  $\epsilon^*$  through the relationships given in eqn.s (20), (21) and (22). Figure 38 depicts frequency dependencies of the  $\sigma'$  for **KAL465** and **KAL468** at different temperatures in the Cry phase and the Col<sub>h</sub> phase. As it is discussed in the *Section 3.1.1* and also shown in Figure 10, the frequency dependence of the  $\sigma'$  given in Figure 38 shows the typical behavior of semiconducting disordered materials. For such a behavior, the plateau values correspond to the DC conductivity ( $\sigma_{DC}$ ).

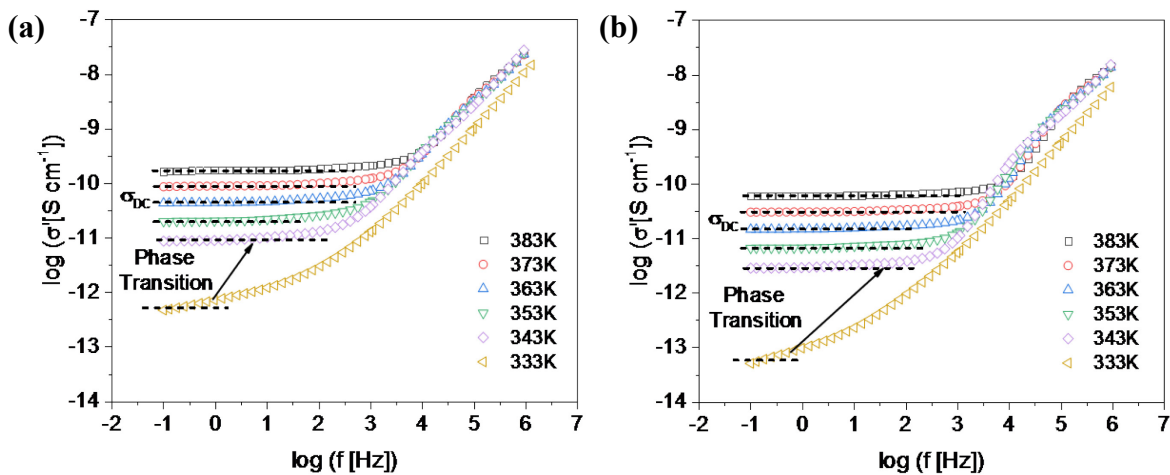


**Figure 38.** Frequency dependence of the  $\sigma'$  at the indicated temperatures for the second heating run; (a) **KAL465** and (b) **KAL468**. Dashed lines indicate the plateau corresponding to the DC conductivity.

Jonscher-equation (eqn. (23)) was used to describe the frequency dependencies of the  $\sigma'$  given in Figure 38. The temperature dependence of the  $\sigma_{DC}$  is shown in Figure 39, which constructed by the  $\sigma_{DC}$  estimated using Jonscher-equation. The phase transition for the Cry-Col<sub>h</sub> transition were recognized as a change in the temperature dependence of the  $\sigma_{DC}$ .

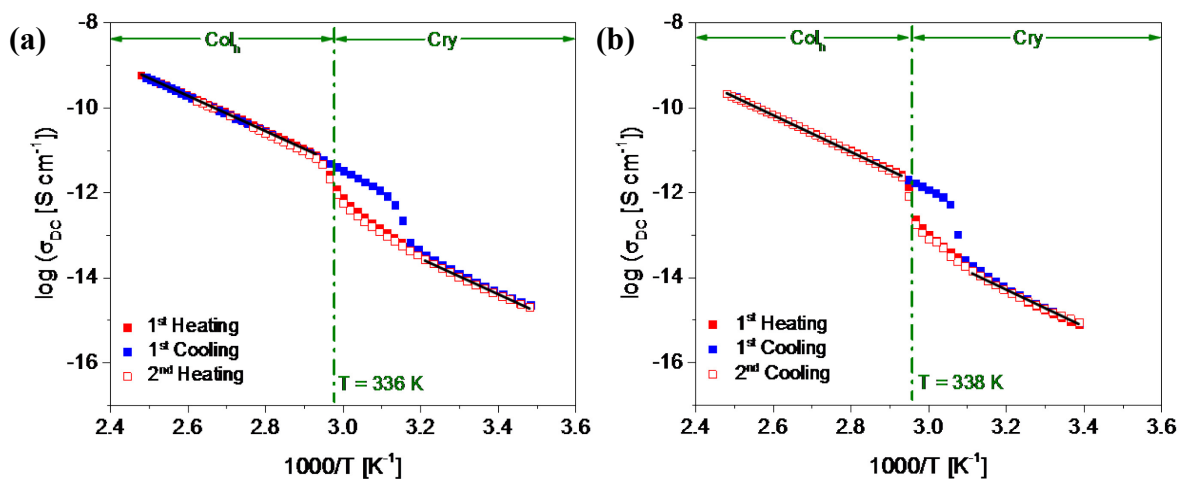


**Figure 39.** DC conductivity  $\sigma_{DC}$  for (a) **KAL465** and (b) **KAL468** versus inverse temperature. The dashed-dotted line indicates the phase transition temperatures for the heating cycle as indicated. Solid black lines are the fits of Arrhenius-equation (eqn. (1)) to the data.

As it has been revealed by DSC, a hysteresis between heating and cooling runs were also recognized from the temperature dependence of the  $\sigma_{DC}$  for both materials. Moreover, the phase transition temperatures for the Cry-Col<sub>h</sub> transition observed in the dependency of  $\sigma_{DC}$  agree with those determined using DSC. In the Cry phase, the values of the  $\sigma_{DC}$  are low compared to the values in the Col<sub>h</sub> mesophase. Upon transition from the Cry phase to the Col<sub>h</sub> mesophase, the values of the  $\sigma_{DC}$  changes by approximately 1 orders of magnitude. The  $\sigma_{DC}$  values determined for **KAL465** and **KAL468** are typical for triphenylene-based DLCs (see Figure S31 for the comparison of the  $\sigma_{DC}$  for **KAL** and **SHU** compounds as well as **HAT6**).<sup>148</sup> Since the similar values of the  $\sigma_{DC}$  found for **KAL** and **SHU** compounds as well as **HAT6** (see Figure S31), it is assumed for **KAL465** and **KAL468** that the main conduction mechanism might be due to the

delocalized electrons of the  $\pi$ - $\pi$  stacked aromatic cores. As it can be better seen in Figure S31, it is realized that the values of the  $\sigma_{DC}$  for **KAL465** is slightly higher than that for **KAL468**. For DLCs, the disc mobility as well as the mobility of the alkyl chains might affect the charge carrier mobility.<sup>33,39</sup> Thus, this might be interpreted as the shorter alkyl chains result in higher  $\sigma_{DC}$  for the **KAL** compounds, since the only difference between **KAL465** and **KAL468** in the chemical structure of their molecules is the length of the alkyl chains.

In both Cry and Col<sub>h</sub> phases, the temperature dependence of the DC conductivity was described by Arrhenius-equation (eqn. (1)) for both materials. In both phases, activation energies of 80 kJ mol<sup>-1</sup> for **KAL465** and 83 kJ mol<sup>-1</sup> for **KAL468** were estimated. This implies for both materials similar restrictions on the charge transport unexpectedly for both phases and/or no change in the conduction mechanism upon Cry-Col<sub>h</sub> phase transition.

#### 4.2.4. Conclusion

Two unsymmetrical triphenylene crown ether-based DLCs having different lengths of the alkyl chains were investigated using DSC and BDS. The phase behavior of **KAL465** and **KAL468** was explored by DSC. Two thermal glass transition ( $T_{g,1}^{\text{thermal}}$  and  $T_{g,3}^{\text{thermal}}$ ) were detected for both materials in the Cry phase. In addition, one thermal glass transition was found for both **KAL** compounds in the Col<sub>h</sub> mesophase.

Besides the conductivity contribution detected, three dielectric active relaxation processes were probed for both samples. At low temperatures in the Cry state, the  $\gamma$ -process was detected, and is assigned to the **PE**-like localized fluctuations taking place in the alkyl chains. On the contrary to the **SHU** compounds, the self-confinement effect is not observed for the **KAL** compounds since the calculated activation energies for the  $\gamma$ -process are similar for both **KAL465**

and **KAL468**. Moreover, a linear relation of the lattice spacings and the  $f_{max}$  of the  $\gamma$ -processes are not recognized, therefore, it is concluded that length of the alkyl chains has no considerable effect on these localized dynamics.

Multiple glassy dynamics were probed for both materials by BDS;  $\alpha_1$ -process in the Cry phase and  $\alpha_3$ -process in the Col<sub>h</sub> mesophase. The probed glassy dynamics have different temperature dependence of the relaxation times, consequently, different molecular assignments of these different glassy dynamics have been proposed. On the one hand, the  $\alpha_1$ -processes of **KAL465** and **KAL468** are assigned to the **PE**-like cooperative fluctuations taking place in the alkyl chains, since the temperature dependence of the relaxation rates of the  $\alpha_1$ -process is quite similar to that of **PE** as well as that of **SHU09**, **SHU10** and **HAT5**. On the other hand, the  $\alpha_3$ -process of the **KAL** compounds might be ambiguously attributed to the cooperative fluctuations of the cores, where each core consists of two triphenylenes connected to each other through the crown ether. For more ambiguous molecular assignment of the  $\alpha_3$ -process, it is concluded that further investigations are required. Furthermore, dielectric data corresponding to the  $\alpha_1$ - and  $\alpha_3$ -processes agrees with the calorimetric data (the  $T_{g,1}^{\text{thermal}}$  and  $T_{g,3}^{\text{thermal}}$  probed by DSC).

Besides the molecular dynamics, a conductivity process was also explored by BDS for both materials. This process appears at even higher temperatures than the probed relaxation processes. The values of the  $\sigma_{DC}$  were estimated using Jonscher-equation from the frequency dependency of the  $\sigma'$ . According to the obtained temperature dependencies of the  $\sigma_{DC}$  for **KAL465** and **KAL468**, it is concluded that the determined  $\sigma_{DC}$  values are typical for triphenylene-based DLCs. Moreover, it is concluded that the delocalized electrons of the  $\pi$ - $\pi$  stacked aromatic cores might be the main conduction mechanism in both Cry and Col<sub>h</sub> phases.

### 4.3. Ionic Liquid Crystals

This section is reproduced/adapted from A. Yildirim, P. Szymoniak, K. Sentker, M. Butschies, A. Bühlmeier, P. Huber, S. Laschat, A. Schönhals, Dynamics and ionic conductivity of ionic liquid crystals forming a hexagonal columnar mesophase, *Phys. Chem. Chem. Phys.* 2018, 20, 5626–5635, with permission from the PCCP Owner Societies (DOI: <https://doi.org/10.1039/C7CP08186C>).

For the first time, the molecular mobility of two linear-shaped tetramethylated guanidinium triflate ILCs having different lengths of alkyl chains, **LC536** and **LC537** (see Figure 18a), was investigated by a combination of BDS and SHS. By self-assembly, these ILCs can form a  $\text{Col}_h$  mesophase besides Cry phases and Iso liquid state. Three dielectric active processes were found by BDS for both samples. At low temperatures, a  $\gamma$ -process in the Cry state is observed which is assigned to localized fluctuations of methyl groups including nitrogen atoms in the guanidinium head. At higher temperatures but still in the Cry state, an  $\alpha_4$ -process takes place. An  $\alpha_1$ -process was detected by SHS but with a completely different temperature dependence of the relaxation times than that of the  $\alpha_4$ -relaxation. This result is discussed in detail, and different molecular assignments of the processes are suggested. At even higher temperatures, electrical conductivity is detected and an increase in the DC conductivity by four orders of magnitude at the phase transition from the Cry to the  $\text{Col}_h$  mesophase is found. This result is traced to a change in the charge transport mechanism from a delocalized electron hopping in the stacked aromatic systems (in the Cry phase) to one dominated by ionic conduction in the quasi-1D ion channels formed along the supramolecular columns in the ILCs'  $\text{Col}_h$  mesophases.

### 4.3.1. Phase Behavior

Figure 40a and b show the DSC thermograms for **LC536** and **LC537** for the second heating and the cooling cycle. The phase transition temperatures were estimated from the maximum positions of the peaks in the heat flow, given in Table 5.

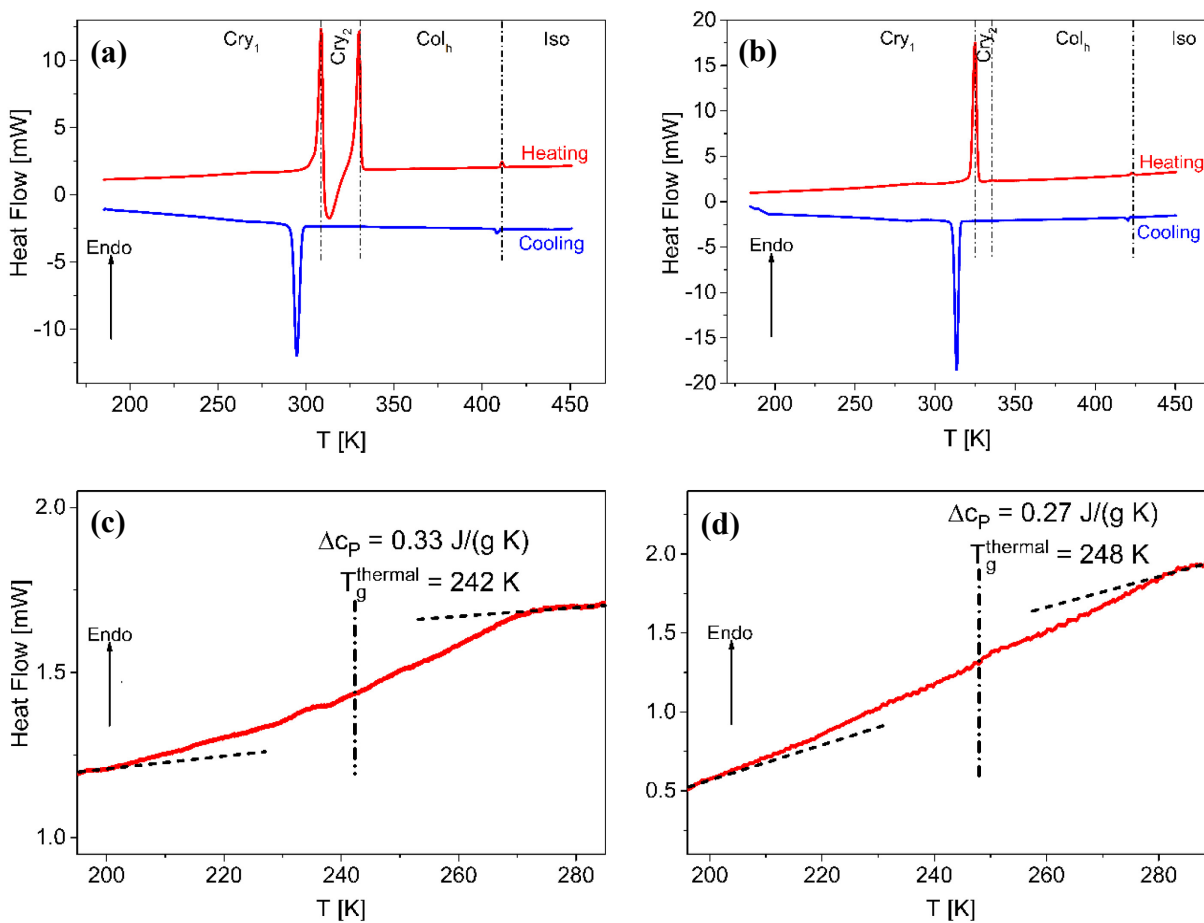


**Figure 40.** DSC thermograms of (a) **LC536** and (b) **LC537** during heating (red line) and cooling (blue line) with a heating/cooling rate of 10 K min<sup>-1</sup>. Dashed-dotted lines point out the phase transition temperatures observed during the heating cycle. DSC thermograms of (c) **LC536** and (d) **LC537** given in the temperature range between 195 K and 285 K for the heating run.

**Table 5.** Phases and phase transitions temperatures determined by DSC and BDS

Compound	Run	Phases and Transitions T [K]											
		DSC			BDS								
LC536	1 <sup>st</sup> Cooling	Cry <sub>1</sub>	295	Col <sub>h</sub>	408	Iso	Cry <sub>1</sub>	301	Col <sub>h</sub>				
	2 <sup>nd</sup> Heating	Cry <sub>1</sub>	309	Cry <sub>2</sub>	330	Col <sub>h</sub>	411	Iso	Cry <sub>1</sub>	309	Cry <sub>2</sub>	327	Col <sub>h</sub>
	2 <sup>nd</sup> Heating*	Cry <sub>1</sub>	310	Cry <sub>2</sub>	324	Col <sub>h</sub>	419	Iso	-				
LC537	1 <sup>st</sup> Cooling	Cry <sub>1</sub>	313	Col <sub>h</sub>	420	Iso	Cry <sub>1</sub>	322	Col <sub>h</sub>				
	2 <sup>nd</sup> Heating	Cry <sub>1</sub>	325	Cry <sub>2</sub>	336	Col <sub>h</sub>	423	Iso	Cry <sub>1</sub>	324	Cry <sub>2</sub>	337	Col <sub>h</sub>
	2 <sup>nd</sup> Heating*	Cry <sub>1</sub>	323	Cry <sub>2</sub>	338	Col <sub>h</sub>	429	Iso	-				

\*DSC results taken from ref. 134.

A hysteresis was observed between the cooling and heating cycles. The hysteresis for the transition from the Cry to the Col<sub>h</sub> phase is more pronounced than that for the transition from the Col<sub>h</sub> mesophase to the Iso phase. The phase transition enthalpies of Cry<sub>1</sub>-Cry<sub>2</sub> (32.6 J g<sup>-1</sup> for **LC536**; 45.8 J g<sup>-1</sup> for **LC537**) and Cry<sub>2</sub>-Col<sub>h</sub> (31.6 J g<sup>-1</sup> for **LC536**; 0.7 J g<sup>-1</sup> for **LC537**) transition are higher than the enthalpy of Col<sub>h</sub>-Iso (0.7 J g<sup>-1</sup> for **LC536**; 0.6 J g<sup>-1</sup> for **LC537**) transition. This is expected due to larger structural changes taking place during the first two transitions. Moreover, the Cry<sub>1</sub>-Cry<sub>2</sub> transition appears only upon heating, and therefore the corresponding phase is thermodynamically metastable.<sup>78</sup>

A step observed in the temperature range between 195 K and 285 K is observed indicating a thermal glass transition (see Figure 40c and d). The T<sub>g</sub><sup>thermal</sup> were determined from the mid-step position and found to be 242 K for **LC536** and 248 K for **LC537**. The Δc<sub>p</sub> for the thermal glass transitions were found to be 0.33 J K<sup>-1</sup> g<sup>-1</sup> for **LC536** and 0.27 J K<sup>-1</sup> g<sup>-1</sup> for **LC537**. For a material, undergoing a glass transition implies some disorder in the material. Disorder in **LC536** and **LC537** leading to the glass transition might be caused by a kind of nanophase separation of the alkyl chain and the aromatic parts of the ILC in the Cry<sub>1</sub> phase. Such a nanophase separation, reported for a

series of triphenylene-based DLCs, was evidenced by an amorphous halo observed in the X-ray patterns of these DLCs.<sup>21</sup>

### 4.3.2. Molecular Mobility

Figure 41 depicts 3D representations of the dielectric loss spectra as a function of frequency and temperature for the second heating run for **LC536** and **LC537**. Two dielectrically active processes can be identified as peaks, labeled;  $\gamma$ - and  $\alpha_4$ -processes. Both relaxation processes take place in the  $Cry_1$  phase. At low temperatures (or high frequencies), the  $\gamma$ -process appears, while the  $\alpha_4$ -process is observed at higher temperatures (or lower frequencies) than that for the  $\gamma$ -process. The conductivity contribution appears at even higher temperatures.

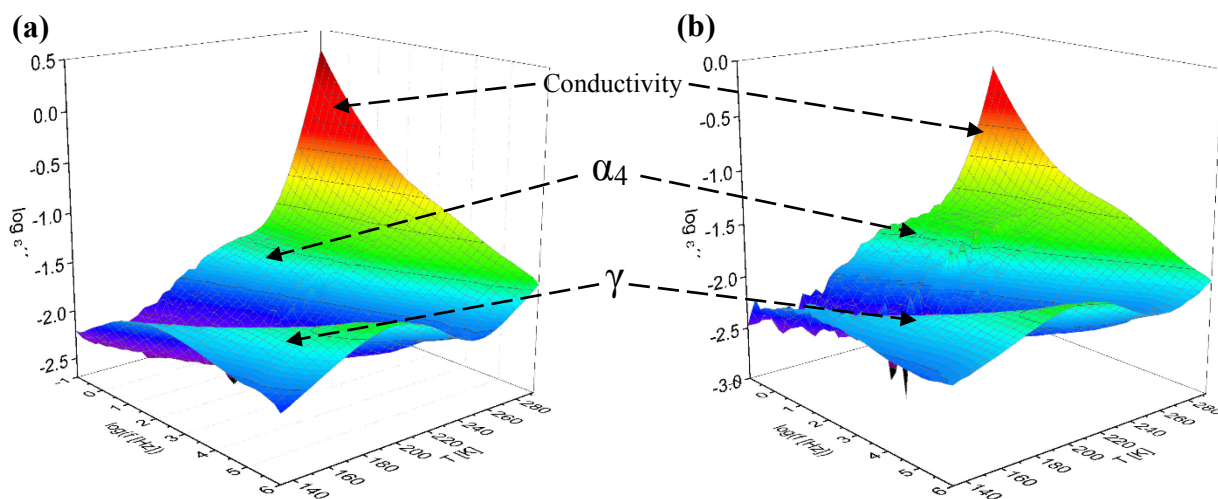


**Figure 41.** 3D representation of the dielectric loss ( $\log \epsilon''$ ) as a function of frequency and temperature for the second heating run; (a) **LC536** and (b) **LC537**.

Figure 42 depicts the temperature dependence of the dielectric ( $\log \epsilon''$ ) at 1000 Hz, for **LC536** and **LC537**. No significant differences between heating and cooling runs were observed in the temperature range of the plastic crystalline phase. However, a sudden change in the temperature dependence of the dielectric loss is observed for both samples at temperatures close to the phase transition temperatures. These changes in the temperature dependence of  $\epsilon''$  could be further used to determine the phase transition temperatures from the dielectric measurements in addition to the

DSC data. The phase transition temperatures found in the dielectric data agree with the transition temperatures determined by DSC. Like for the DSC experiments, a pronounced thermal hysteresis was observed in the dielectric data for the transition from the plastic crystalline phase to the Col<sub>h</sub> phase. Furthermore, the Cry<sub>1</sub>-Cry<sub>2</sub> transition was observed only upon heating like for the DSC investigations.

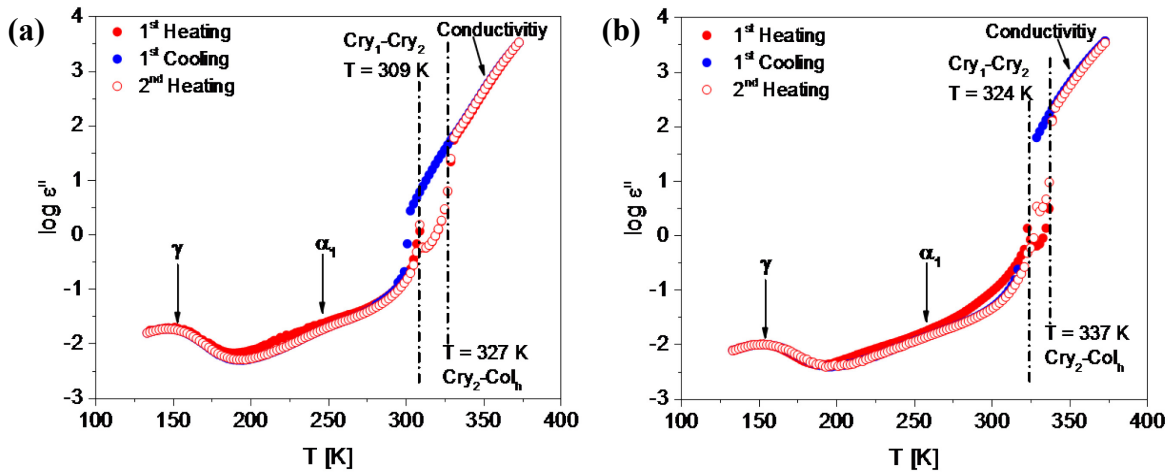


**Figure 42.** Temperature dependence of the dielectric loss ( $\log \epsilon''$ ) at 1000 Hz for (a) LC536 and (b) LC537 for the heating and cooling runs. Dashed-dotted lines point out the phase transition temperatures detected during the heating cycle as indicated.

For the quantitative analysis of the relaxation processes, the model function of HN-function, given in eqn. (13), was fitted to the data. As an example, Figure 43 illustrates the fit of the HN-function to the data of LC536 in the temperature range of the  $\gamma$ -process. An example for the analysis of the data for LC537 is given in *Appendix IV* in Figure S32. From the fits, the relaxation rate  $f_{max}$  is obtained as the maximum position of the dielectric loss. In Figure 44 the relaxation rates  $f_{max}$  are plotted versus inverse temperature in the relaxation map for both LC536 and LC537. The temperature dependence of the relaxation rates of  $\gamma$ -relaxation can be described by Arrhenius-equation (eqn. (1)).

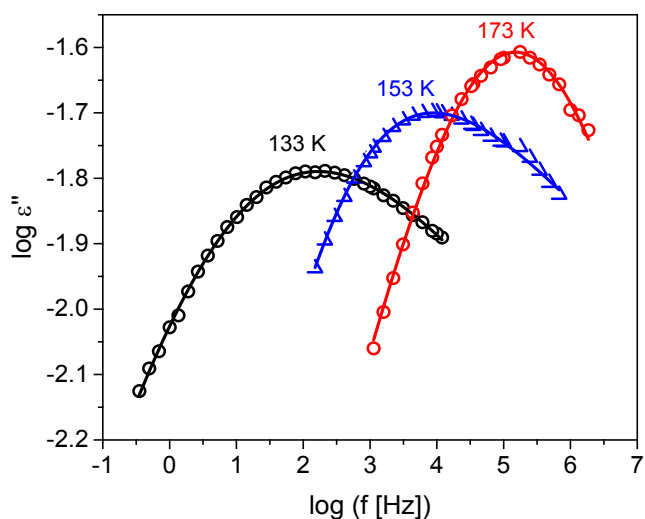


**Figure 43.** Frequency dependency of dielectric loss for **LC536** for the second heating at the indicated temperatures ( $\gamma$ -process). Solid lines are the fits of the HN-function to the data.

The temperature dependence of relaxation rates due to localized molecular fluctuation follows generally the Arrhenius-equation (eqn. (1)). Here for the activation energy of  $\gamma$ -relaxation for both **LC536** and **LC537**, a value of ca.  $33 \text{ kJ mol}^{-1}$  is found. Because no dependence of the activation energy on the number of carbon atoms in the substituent is observed, the  $\gamma$ -relaxation of both **LC536** and **LC537** is assigned to the localized fluctuations of the nitrogen atoms in the guanidinium head including the methyl groups. This is in good agreement with the literature values for activation energies of localized fluctuations of polar groups bonded to methyl groups.<sup>33,40,149,150</sup> Moreover, the temperature dependence of the relaxation rates of the  $\gamma$ -process of our ILCs is quite similar to that of the  $\gamma$ -process of **PE**.<sup>40</sup> The dielectric  $\gamma$ -relaxation of **PE** taken from ref. 40 is included in Figure 44 for comparison.

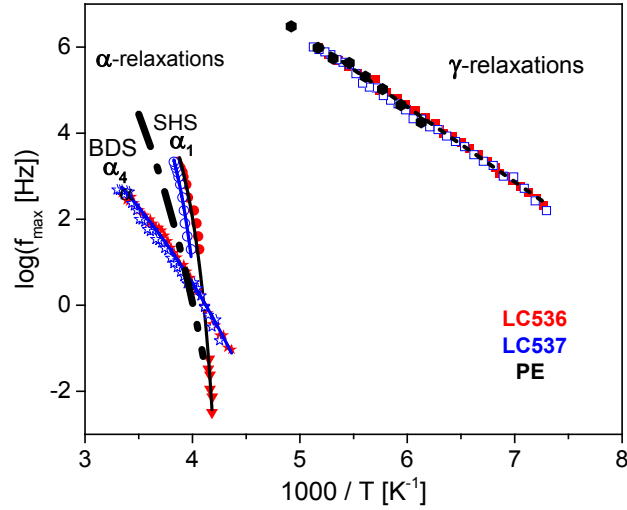


**Figure 44.** Relaxation map of **LC536** and **LC537**. Filled red symbols – data for **LC536**; Open blue symbols – data for **LC537**. Squares –  $\gamma$ -relaxation; stars –  $\alpha_4$ -relaxation; circles (AC-chip calorimetry) and triangles (TMDSC) –  $\alpha_1$ -relaxation. Solid lines are the fits of VFT-equation (eqn. (2)) to the data. Dashed line is the fit of the Arrhenius-equation (eqn. (1)) to the data of the  $\gamma$ -relaxation. Dashed-dotted line denotes the dielectric  $\alpha$ -relaxation of polyethylene taken from ref. 145. Black hexagons symbolize the dielectric  $\gamma$ -relaxation of **PE** taken from ref. 40.

Figure 42 shows that compared to the  $\gamma$ -relaxation the  $\alpha_4$ -process is quite broad. Therefore, in addition to the analysis of the  $\alpha_4$ -process by fitting the HN-function to the data, it was also analyzed by a derivative-based analysis technique given by eqn. (18). For the HN-function, one obtains eqn. (19). Figure 45 demonstrates the fit of the derivative of the HN-function (eqn. (19)) to the  $\epsilon''_{deriv}$  data of **LC536** in the temperature range of the  $\alpha_4$ -process. The temperature dependence of the relaxation rates of the  $\alpha_4$ -relaxations is curved when plotted versus inverse temperature, indicating of glassy dynamics ( $\alpha$ -relaxation). It is described by the VFT-equation (eqn. (2)).

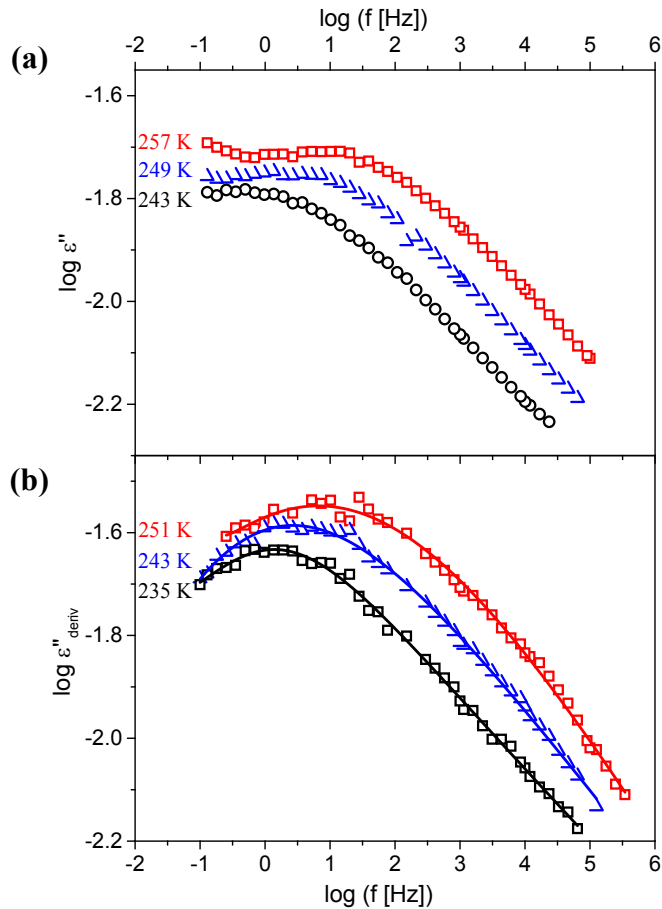


**Figure 45.** Frequency dependency of (a)  $\log \varepsilon''$  and (b)  $\varepsilon''_{deriv}$  of **LC536** for the second heating at the indicated temperatures ( $\alpha_4$ -process). Solid lines are the fits of the eqn. (19) to the data.

The temperature dependence of the relaxation rates of the  $\alpha_4$ -relaxation of **LC536** and **LC537** measured by BDS has to be described by the VFT-equation which might indicate glassy dynamics also for the ILCs. The estimated VFT parameters are summarized in Table 6.

**Table 6.** VFT parameters obtained from the BDS and SHS data. To reduce the number of free fit parameters,  $\log f_\infty$  was fixed to 8.

Compound	Run	BDS			SHS		
		$\log (f_\infty [\text{Hz}])$	D	$T_0 [\text{K}]$	$\log (f_\infty [\text{Hz}])$	D	$T_0 [\text{K}]$
LC536	Cooling	8	2.8	$133 \pm 10$	8	0.3	$224 \pm 5$
	Heating	8	2.9	$130 \pm 10$	8	0.3	$220 \pm 5$
LC536	Cooling	8	3.1	$140 \pm 10$	8	0.3	$229 \pm 5$
	Heating	8	2.6	$130 \pm 10$	8	0.1	$241 \pm 5$

In addition to BDS sensing dipole fluctuations, SHS was carried out to investigate the glassy dynamics from the perspective of entropy fluctuations. A similar combination of methods was applied for low molecular weight liquid crystal systems<sup>33,151</sup> and a polymeric liquid crystalline system.<sup>152</sup> For AC-chip calorimetry, the real part of the complex differential voltage,  $U_R$ , can be taken as a measure of the real part of the complex heat capacity. Temperature dependences of  $U_R$  obtained by SHS carried out by differential AC-chip calorimetry for **LC536** are given in Figure 46a for four measured frequencies. For lower frequencies than covered by AC-chip calorimetry, SHS is carried out by TMDSC. Figure 46b gives the temperature dependence of the  $c_p'$  at a frequency of  $5.6 \times 10^{-2}$  Hz. The temperature dependencies of both  $U_R$  and  $c_p'$  show a step-like increase with increasing temperature which is characteristic for a glass transition. Moreover, the steps shift to higher temperatures with increasing frequency as expected.<sup>33,126</sup>

Both sets of SHS data were analyzed by taking either the mid-step position of  $U_R(T)$  or of  $c_p'(T)$  to determine a corresponding dynamic glass  $T_g^{\text{dynamic}}$  for the given frequency.<sup>33,149</sup> The dynamic glass transition temperatures obtained from this analysis together with the corresponding measured frequencies are included in Figure 44 (relaxation map) combining the results of BDS and SHS for comparison. Like for the  $\alpha_4$ -relaxation, the temperature dependence of the relaxation rates of the  $\alpha_1$ -relaxation is curved when plotted versus  $1/T$  and has to be described by a VFT-equation. The estimated VFT parameters are summarized in Table S3.  $T_g^{\text{thermal}}$  found to be 242 K for **LC536** and 248 K for **LC537** are in good agreement with the temperature where the relaxation time of the  $\alpha_1$ -relaxation is 100 s. The temperature dependence of the relaxation rates of the  $\alpha_1$ -process has a close resemblance with that of **PE** which is included in Figure 44. For that reason, the  $\alpha_1$ -process detected in the  $\text{Cry}_1$  phase is attributed to the cooperative fluctuations of

alkyl chains. A similar **PE**-like glassy dynamics have been found for pyrene-based DLC<sup>33</sup> and polymers having long alkyl groups in the side chain<sup>22</sup>.

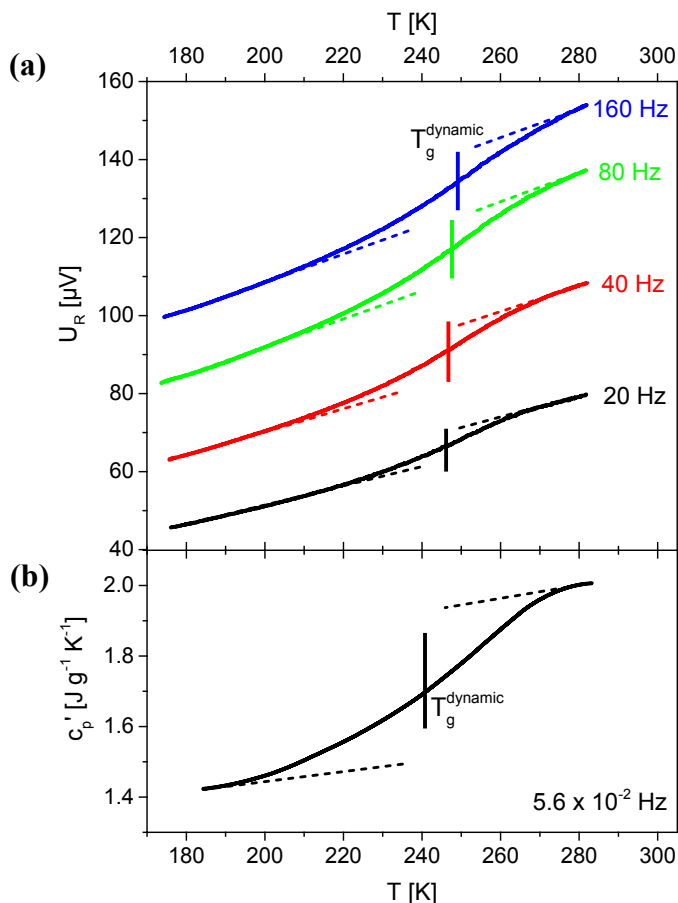


**Figure 46.** (a) Temperature dependence of the real part of the complex differential voltage  $U_R$  for **LC536** for the heating run at different frequencies as indicated. (b) Temperature dependence of the  $c_p'$  for **LC536** at  $5.6 \times 10^{-2}$  Hz. Solid vertical lines indicate the mid-step positions.

However, the temperature dependence of the relaxation rates of the  $\alpha_4$ -processes probed by BDS is completely different from that of the  $\alpha_1$ -processes as well as from that of the  $\alpha$ -process of **PE**. Therefore, the molecular origin of the  $\alpha_4$ -relaxation should be different from that for the  $\alpha_1$ -relaxation. Different possibilities for a molecular assignment of the  $\alpha_4$ -relaxation can be discussed. Firstly, in the chemical structure of **LC536** and **LC537**, the alkyl arms are attached to the phenyl ring which is also linked to an ester group (see Figure 18). The ester groups might be

involved in the fluctuation of the alkyl arms but on a shorter length scale.<sup>33</sup> Therefore, the  $\alpha_4$ -relaxation might be related to cooperative fluctuations of the ester group together with parts of the alkyl groups. It is important to underline again that BDS senses dipole fluctuations and SHS senses entropy fluctuations. The densely packed crystals in the Cry<sub>1</sub> phase exert higher restrictions on the ester groups than the alkyl arms. This would explain why the temperature dependence of the relaxation rates of the  $\alpha_4$ -processes is much stronger in the sense of the fragility concept of glass formation<sup>153</sup> (closer to an Arrhenius-dependence) than that of  $\alpha_1$ -processes.

Secondly, one also has to consider that the triflate counteranions carry also a considerable dipole moment. To ensure electrical neutrality the triflate counteranions must be located close to the guanidinium group also in the plastic crystal phase. In this second approach, the  $\alpha_4$ -processes might be also assigned to cooperative fluctuations of the triflate counteranions together with the guanidinium groups. Due to the plastic crystalline structure, these fluctuations will be highly restricted which will also explain the observed relatively strong behavior of the  $\alpha_4$ -processes. Till now it could be not discriminated between both interpretation possibilities. This would require additional investigations. Nevertheless, in the light of the results presented in ref. 154, the second interpretation seems to be more likely.

Finally, it should be recalled that the  $\alpha_4$ -relaxation is quite broad. The reason for this broad peak might be that there is an underlying second relaxation process corresponding to the  $\alpha_1$ -process. But the intensity of the second process is quite low due to the low dipole moment. Therefore, it could be not analyzed unambiguously.

### 4.3.3. Conductivity

In addition to the relaxation processes, also a conductivity contribution is observed and analyzed for both ionic liquid crystals. Both the aromatic moieties (due to  $\pi$ - $\pi$  stacking) and triflate anions may distinctively contribute to the conductivity. Therefore, the conductivity mechanism should be revealed. The relationship between the complex dielectric function  $\epsilon^*$  and the complex conductivity  $\sigma^*$  is given in eqn.s (20), (21) and (22).

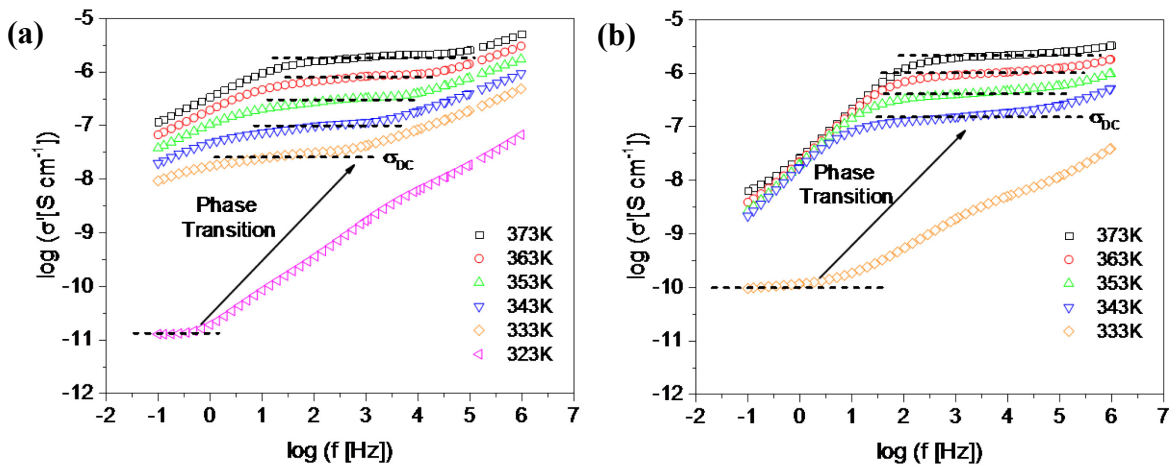


**Figure 47.** Frequency dependence of the real part of the complex conductivity  $\sigma'$  at the indicated temperatures for the second heating run; (a) LC536 and (b) LC537. Dashed lines indicate the plateau corresponding to the DC conductivity.

The frequency dependence of the  $\sigma'$ , given in Figure 47, shows the typical behavior of semiconducting disordered materials such as ionic glasses, ion conducting polymers, and electron-conducting conjugated polymers, which is shown in Figure 10. The frequency dependence of  $\sigma'(f)$  can be approximated by Jonscher-equation given by eqn.(23). By fitting the Jonscher-equation the DC conductivity is estimated, and its temperature dependence is given in Figure 48. Conductivity contributions were observed in the  $\text{Col}_h$  phase as well as in the Cry phase. The phase transitions were also recognized as changes in the temperature dependence of the  $\sigma_{DC}$ .

The thermodynamically metastable Cry<sub>1</sub>-Cry<sub>2</sub> transition appearing only upon heating is also not reflected during cooling in the temperature dependence of the DC conductivity.

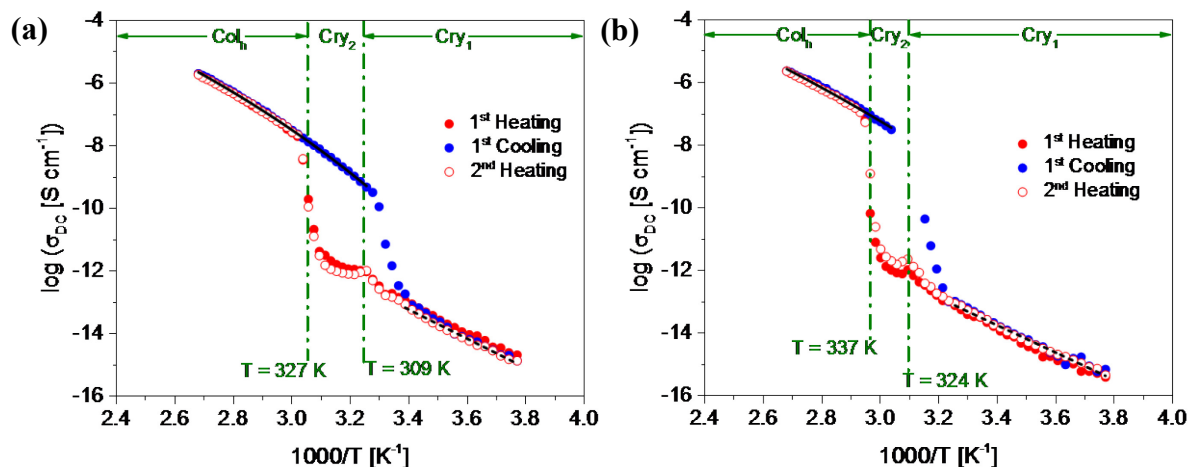


**Figure 48.** DC conductivity  $\sigma_{DC}$  for (a) LC536 and (b) LC537 in dependence of the inverse temperature. The solid and dashed black lines are the fits of VFT-equation (eqn. (2)) and Arrhenius-equation (eqn. (1)) to the data respectively. The dashed-dotted lines point out the phase transition temperatures for the heating cycle as indicated.

In the plastic crystalline phases, the values of the  $\sigma_{DC}$  are quite low. With increasing temperature, at the phase transition from the crystalline Cry<sub>2</sub> phase the  $\sigma_{DC}$  changes by approximately 4 orders of magnitude to values which are typical for semiconductors ( $10^{-8}$  -  $10^{-5}$  S cm<sup>-1</sup>). This indicates a change in the underlying conduction mechanism. Recently, Floudas et al.<sup>154</sup> have investigated the ionic conduction in hexa-peri-hexabenzocoronenes-based liquid crystals doped with LiOTf. This system can be considered as a related system compared to the ILCs considered here because a similar phase behavior is observed. Furthermore, a similar ionic moiety, LiOTf, is used as doping agent, and similar values of the DC conductivity are reported. Therefore, it is concluded that in the Col<sub>h</sub> phase the main conduction mechanism is due to ionic mobility rather than due to the electrons of the  $\pi$ - $\pi$  stacked aromatic cores. In a further study, ionic conductivities of imidazolium-based ILCs having various alkyl chain lengths were investigated.<sup>155</sup> The ionic conductivity values in Col<sub>h</sub> and Iso phases were also reported in the range of  $10^{-2}$  -  $10^{-7}$

S cm<sup>-1</sup> for those ILCs. This further supports the assignment of OTf ions as the main active charge carrier in the Col<sub>h</sub> phase. As illustrated in Figure 18b, the triflate counteranions are located in the center of the columns forming the Col<sub>h</sub> phase. Therefore, it is assumed that the conductivity in the columnar phase is due to a long-range diffusion of the triflate anions inside the columns (ion channels). In the Cry phase, the ion channels do not exist. Furthermore, the ionic mobility is restricted by the close-packed crystals. Therefore, it is concluded that the nature of the conduction process is due to the electrons of the  $\pi$ - $\pi$  stacked aromatic cores. This assumption is further supported by the similar conductivity values found for the Cry phase for a non-ionic triphenylene-based DLC ( $\sim 10^{-13}$  S cm<sup>-1</sup>), in which the conduction is due to electrons of the  $\pi$ - $\pi$  stacked aromatic cores.<sup>148</sup>

On the one hand, in the columnar phase, the temperature dependence of the DC conductivity is curved when plotted versus 1/T and has to be described by the VFT-equation (eqn. (2)). The estimated parameters are given in *Appendix IV* in Table S3. This temperature dependence of the DC conductivity might be related to the glassy dynamics in the plastic crystalline phase observed by dielectric spectroscopy. On the other hand, in the Cry<sub>1</sub> phase, it follows the Arrhenius-equation (eqn. (1)). Activation energies of 89 kJ mol<sup>-1</sup> for **LC536** and 83 kJ mol<sup>-1</sup> for **LC537** were estimated.

#### 4.3.4. Conclusion

The molecular mobility in two linear-shaped tetramethylated guanidinium triflate ILCs having different lengths of alkyl chains was explored by BDS and SHS. Two relaxation processes were detected in the Cry phase by BDS for both ILCs. The  $\gamma$ -processes at lower temperatures are assigned to localized fluctuations of methyl groups including nitrogen atoms in the guanidinium head. The  $\alpha_4$ -processes at the higher temperature having a VFT-like temperature dependence of the relaxation rates are attributed to cooperative fluctuations. In addition to the  $\alpha_4$ -processes

detected by BDS, an  $\alpha_1$ -process is observed by SHS for both ILCs which has also a VFT-like temperature dependence of the relaxation rates. The temperature dependence of the relaxation rates of the  $\alpha_1$ -relaxation is completely different than that of the  $\alpha_4$ -relaxation. Thus, it is concluded that the molecular origins of the glassy dynamics detected by BDS and SHS are different. On the one hand, the dipole fluctuations of  $\alpha_4$ -processes sensed by BDS are either assigned to the cooperative fluctuations taking place in the aromatic core or in the vicinity of the aromatic core of the ILC molecules or to cooperative fluctuations of the triflate counteranions together with the guanidinium groups. On the other hand, the molecular mobility of  $\alpha_1$ -processes sensed by SHS which is sensitive to entropy fluctuations is assigned to the alkyl arms due to their quite similar temperature dependence of the relaxation rates of the  $\alpha_1$ -relaxation to that of dielectric  $\alpha$ -relaxation of **PE**. Moreover, the conductivity of both ILCs was also investigated by BDS. The temperature dependence of the DC conductivity observed in the Col<sub>h</sub> mesophase has to be described by VFT-equation which indicates cooperative processes. However, in the Cry phase, the DC conductivity follows the Arrhenius-equation. These different dependencies of the DC conductivity in the different phases indicates a change in the conductivity mechanism from ionic conduction in the Col<sub>h</sub> mesophase to a mechanism which is due to the delocalized electrons of the stacked aromatic systems.

## CHAPTER 5 – A COLUMNAR DISCOTIC LIQUID CRYSTAL UNDER NANOSCALE CONFINEMENT

This chapter is reproduced/adapted from A. Yildirim, K. Sentker, G. J. Smales, B. R. Pauw, P. Huber, A. Schönhals, Collective orientational order and phase behavior of a discotic liquid crystal under nanoscale confinement, *Nanoscale Adv.* 2019, 1, 1104–1116., with permission from the Royal Society of Chemistry (DOI: <https://doi.org/10.1039/C8NA00308D>).

The phase behavior and molecular ordering of triphenylene-based DLC **HAT6** (see Figure 15a) under cylindrical nanoconfinement are studied utilizing DSC and BDS, where cylindrical nanoconfinement is established through embedding **HAT6** into the nanopores of AAO, and a silica membrane with pore diameters ranging from 161 nm down to 12 nm. Both unmodified and modified pore walls were considered. In the latter case, the pore walls of AAO membranes were chemically treated with the surface modifiers OPA and ODPA. Phase transition enthalpies decrease with decreasing pore size, indicating that a large proportion of the **HAT6** molecules within the pores has a disordered structure, which increases with decreasing pore size for both pore walls. In the cases of the OPA- and ODPA-modifications the amount of ordered **HAT6** is increased compared to the unmodified case. The pore size dependencies of the phase transition temperatures were approximated using the Gibbs-Thomson-equation, where the estimated surface tension is dependent on the molecular ordering of **HAT6** molecules within the pores and upon their surface. BDS was employed to investigate the molecular ordering of **HAT6** within the nanopores. These investigations revealed that with a pore size of around 38 nm, for the samples with the unmodified pore walls, the molecular ordering changes from planar axial to homeotropic radial. However, the planar axial configuration, which is suitable for electronic applications, can be successfully preserved through OPA- and ODPA-modifications for most of the pore sizes.

## 5.1. Mesomorphic Properties of Bulk

The mesomorphic properties of **HAT6** in the bulk state were studied by DSC and POM. DSC thermograms of **HAT6** are given for the second heating and the cooling runs in Figure 49. The phase transition temperatures and enthalpies are estimated from the maximum positions of the peaks and the area under the peaks respectively and given in Table 7. Moreover, the Col<sub>h</sub>-Iso phase transition temperatures were also determined by BDS from the first derivative of  $\epsilon'$  with respect to temperature. A hysteresis between the cooling and heating cycles was observed where the hysteresis is more pronounced for Cry-Col<sub>h</sub> transition ( $\Delta T = 15.9$  K) than Col<sub>h</sub>-Iso transition ( $\Delta T = 2.8$  K).

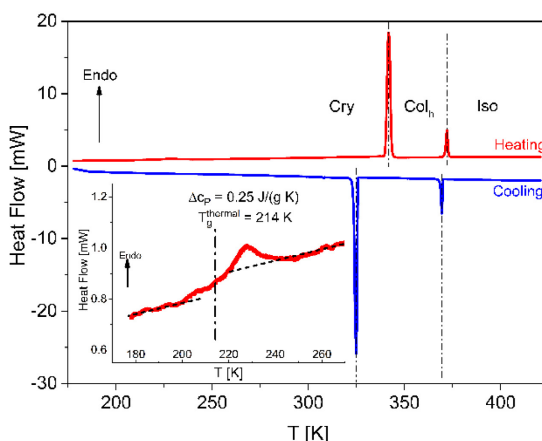
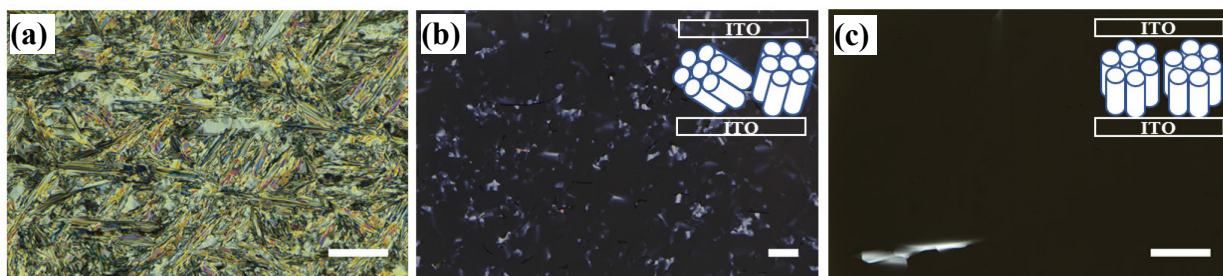


**Figure 49.** DSC thermograms of **HAT6** during heating (red line) and cooling (blue line) with a heating/cooling rate of  $10 \text{ K min}^{-1}$ . Dashed lines point out the phase transition temperatures upon heating and cooling. The inset enlarges the temperature range between 170 K and 270 K for the heating run.

**Table 7.** Phase transition temperatures and enthalpies determined together with the literature values

Source	Run	Transitions Temperatures and Enthalpies			
		DSC		BDS	
In this study	Cooling	Cry 325.9 K (52.5 J g <sup>-1</sup> )	Col <sub>h</sub> 369.3 K (6.8 J g <sup>-1</sup> )	Iso	Col <sub>h</sub> 369.6 K Iso
	Heating	Cry 341.8 K (51.3 J g <sup>-1</sup> )	Col <sub>h</sub> 372.1 K (6.8 J g <sup>-1</sup> )	Iso	Col <sub>h</sub> 370.3 K Iso
Ref. 40	Heating	Cry 340.6 K (50.6 J g <sup>-1</sup> )	Col <sub>h</sub> 371.5 K (5.9 J g <sup>-1</sup> )	Iso	-
Ref. 77	Heating	Cry 342.7 K	Col <sub>h</sub> 372.7 K	Iso	-
Ref. 21	Heating	Cry 342.0 (49.9 J g <sup>-1</sup> ) K	Col <sub>h</sub> 372.3 K (6.8 J g <sup>-1</sup> )	Iso	-
Ref. 51	Heating	Cry 342.0 (49.9 J g <sup>-1</sup> ) K	Col <sub>h</sub> 372.3 K (6.8 J g <sup>-1</sup> )	Iso	-

A step indicating a thermal glass transition was observed in the temperature range between 170 K and 270 K, see inset of Figure 49. The mid-step position of the step was taken to determine the  $T_g^{\text{thermal}}$  of 214 K. The  $\Delta c_p$  was found to be  $0.25 \text{ J K}^{-1} \text{ g}^{-1}$ . Undergoing a glass transition implies that there are some disordered or amorphous structures within the material. Such disorder, which leads to a glass transition may be caused by a nanophase separation of the alkyl chain and the aromatic core of **HAT6**, is evidenced by the amorphous halo observed in the X-ray pattern of **HAT6**.<sup>21</sup> Similarly, Yildirim et al.<sup>40</sup> reported a glass transition for **HAT6** also detected by DSC. In contrary to our findings, they found a  $T_g^{\text{thermal}}$  at 186 K. Furthermore, Krause et al.<sup>21</sup> observed a step, which might indicate a glass transition, in the temperature range of 180 K-220 K upon cooling. They did not observe a glass transition during the heating run. Clarifying these contradicting findings requires further detailed calorimetric investigations, such as conventional DSC investigations covering temperatures lower than 150 K or Hyper / Flash DSC investigations allowing for higher heating rates.



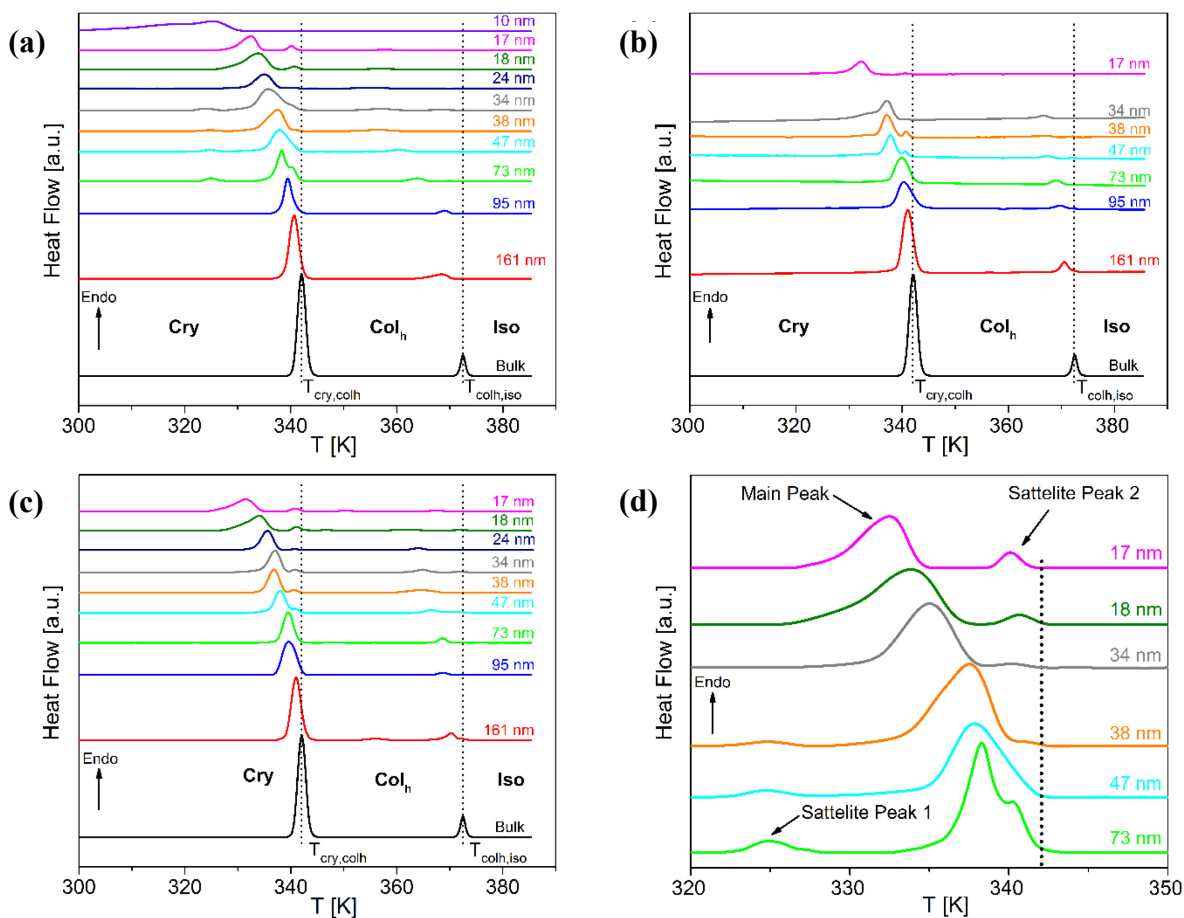
**Figure 50.** POM images of **HAT6**, recorded under crossed polarizers, in the liquid crystalline cell having ITO-coated electrodes (a) at 328 K in the Cry phase during the first heating run from room temperature (b) at 363 K in the Col<sub>h</sub> phase during the first heating run (c) at 363 K in the Col<sub>h</sub> phase during the third heating run. The insets of (b) and (c) are the drawings representing the molecular ordering for a given image. Scale bars represent 200  $\mu\text{m}$ .

Figure 50 illustrates the texture and the column alignment of bulk **HAT6** obtained by POM. Upon first heating from room temperature, in the Cry phase at 328 K the texture is very bright under cross polarizers. This indicates a lack of a homeotropic alignment due to tilted columns in the Cry phase (herringbone-like crystal packing<sup>37,154</sup>) causing a high birefringence. This results in

a bright texture with colored crystal domains.<sup>48</sup> A fan-shaped texture accompanied by dark areas was observed during the first heating ramp in the Col<sub>h</sub> phase at 363 K. The fans-shape texture is typical for a Col<sub>h</sub> phase of DLCs. It indicates that a column alignment in large spatial regions is not present. As it is shown in the inset of Figure 50.b the columns are randomly tilted.<sup>13, 156</sup> In addition to the fans, the small dark areas were also observed, which indicate that the columns are partially aligned homeotropically among the tilted columns causing a minimal birefringence. However, during the third heating run (after applying two heating/cooling cycles in the range from 350 K to 383 K) at 363 K, large dark areas are observed (see Figure 50.c), where the columns are mostly aligned homeotropically. The reason of the homeotropic alignment of the columns in large spatial regions compared to the first heating, probably is the temperature program applied due to the self-healing ability of DLCs for the structural defects with thermal annealing. It could also be reasoned that the heating/cooling rate applied, 1 K min<sup>-1</sup>, is not slow enough to align the columns during the first heating due to what is assumed to be slow orientation kinetics.

## 5.2. Phase Behavior Under Nanoscale Confinement

Figure 51a and b depict the DSC thermograms of bulk **HAT6** as well as **HAT6** confined into the nanopores of unmodified, OPA- and ODPA-modified AAO membranes. It is concluded that the confined **HAT6** undergoes both phase transitions (Cry-Col<sub>h</sub> and Col<sub>h</sub>-Iso) with decreasing pore size for both unmodified and modified pore walls. One exception to this is observed with **HAT6** confined within 12 nm pores in a silicon membrane, where the Col<sub>h</sub>-Iso phase transition is completely suppressed. Such a complete suppression of the phase transition has previously been reported for rod-like LCs.<sup>136</sup>



**Figure 51.** DSC thermograms of bulk **HAT6** and **HAT6** confined into (a) unmodified (b) OPA-modified and (c) ODPA-modified nanopores of the membranes having different pore sizes as indicated (the second heating cycle). The dashed lines indicate the phase transitions temperatures of bulk **HAT6**. (d) DSC thermograms of **HAT6** confined into unmodified nanopores of the membranes having different pore sizes as indicated, enlarging the temperature range from 320 K to 350 K for the heat flows of the samples given in Figure 51a. The dotted line indicates the Cry-Col<sub>h</sub> phase transitions temperature of the bulk.

As previously reported for the phase behavior of **HAT6** under confinement for a limited range of pore sizes,<sup>51</sup> three conclusions can be drawn for both kinds of samples with unmodified and modified pore walls. Firstly, both phase transition temperatures shift to lower temperatures with decreasing pore size. Secondly, both phase transition peaks split into two or three for pore sizes smaller than 95 nm (see Figure 51d). The appearance of so-called satellite peaks in addition to the main transition peak for the smaller pore sizes was reported for nanoconfined pyrene-based DLC and also for **HAT6**.<sup>51,52</sup> In the first interpretation, the satellite peaks can be due to remaining

bulk-like **HAT6** located at the surface of the sample although it was tried to remove it carefully. A similar interpretation is used elsewhere.<sup>157</sup> Secondly, the main and the satellite peaks might be assigned to different configurations of the molecules near the pore walls and the pore center. This conclusion is supported by the observation that the satellite peaks are shifted to lower temperatures with respect to the phase transition of the bulk and depend slightly on pore size. For these reasons the second interpretation is favored. However, such assignments are controversial due to the lack of experimental techniques available to characterize the different structures and their location within the pore space. Thirdly, for both phase transitions, the enthalpies decrease with decreasing pore size. However, this conclusion cannot be drawn directly from Figure 51, as the measured values are normalized to the confined mass of **HAT6**. This third conclusion is discussed in detail below.

The dependence of phase transition enthalpies normalized to sample mass inside the pores and the phase transition temperatures are shown in Figure 52. Moreover, the effect of the different host/guest interactions on the phase behavior under nanoconfinement is revealed by comparing the behavior of **HAT6** confined in both unmodified and modified pores. The OPA and ODPA modifications form a stable grafted alkyl chain monolayer, which results in hydrophobic pore walls with a lower value of the surface energy compared to unmodified pores.<sup>158, 159</sup> The thickness of ODPA-coating was reported to be 1.8-2.4 nm on aluminum oxide surface,<sup>160</sup> which is comparable to the thickness revealed from SAXS investigations. Hence, the modification leads to an observed decrease of the pore diameter of ca. 4.4 nm for the ODPA-modified AAO membranes. The influence of the decreased pore size should be greater for smaller pores than for larger ones considering inverse pore sizes. Figure 52 shows the dependencies for the nominal pore sizes. However, the dependencies given in *Appendix V* in Figure S35 for the sample with the

ODPA-modified pore surfaces were drawn considering a 4.4 nm decreased pore size. It should be noted that the thickness of the ODP A-coating is not known for the pores filled with **HAT6**. When the modified pores are filled with **HAT6**, the thickness of the coating can, in principle, have a value between 0 nm- 4.4 nm, whereas in reality values tend to lie towards the latter end of this scale.

The dependencies of the phase transition enthalpies of the main peak (normalized to the mass of the confined material) on pore size are given in Figure 52a and c for the Cry-Col<sub>h</sub> and the Col<sub>h</sub>-Iso transitions respectively. The normalized phase transition enthalpies decrease with decreasing pore size, which provides evidence that a portion of confined **HAT6** does not undergo the phase transition. This part of the confined **HAT6** should be disordered and may have an amorphous structure. As discussed in ref.s 51 and 52, the observed increase in surface curvature, with decreasing pore size, leads to stronger elastic distortion of the ordered phase, which prevents the molecules from forming an ordered structure and consequently limits the amount of observed ordered phase.

The dependencies of the enthalpies for the Col<sub>h</sub>-Iso transition reveal that more than half of the material confined in the pore (by volume) is disordered for pore sizes smaller than 47 nm. This is an amount that cannot be neglected in the interpretation of the results for nanoconfined **HAT6**. The spatial location of this disordered portion inside the pore cannot be assigned by methods characterizing the structure such as XRD or neutron scattering. As it has been discussed that the disordered portion is likely to be located at the center of the pore due to divergence of the excess energies toward the pore center.<sup>31,72,75</sup> A disordered core at the center of the pore was also visualized by molecular dynamics simulations of confined **HAT6**.<sup>54</sup>

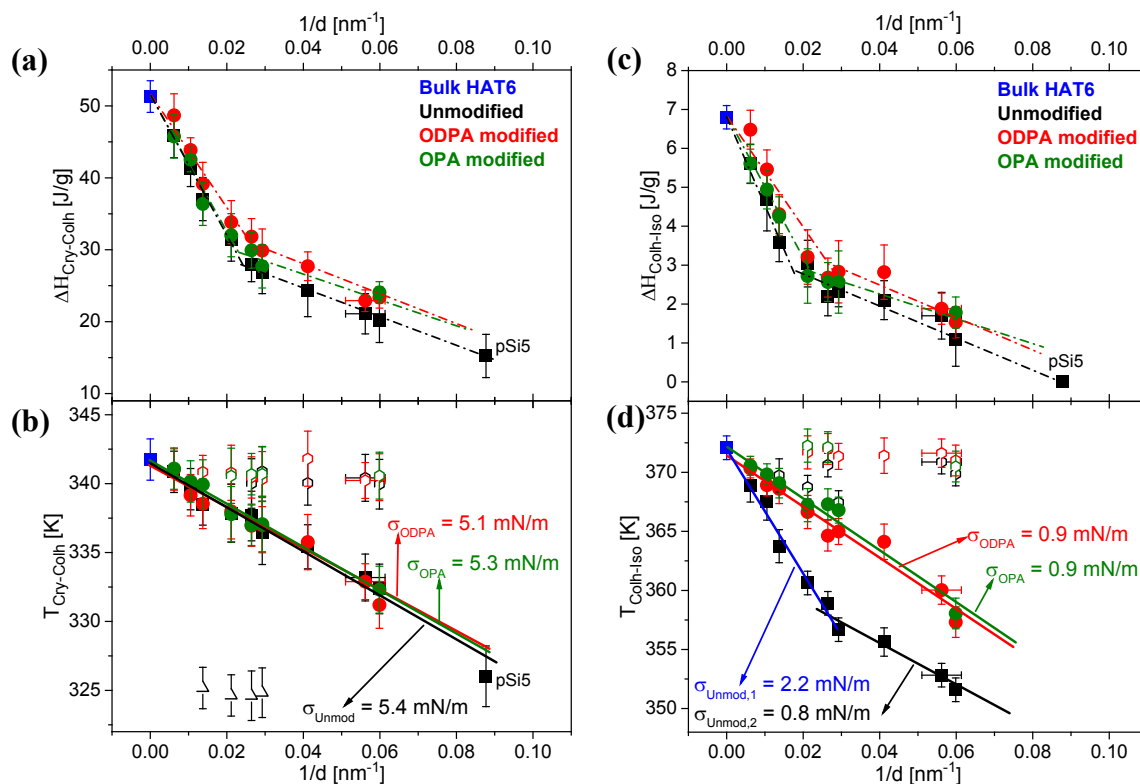


**Figure 52.** Dependencies of the phase transition enthalpies for (a) the Cry-Col<sub>h</sub> transition and (c) the Col<sub>h</sub>-Iso transition, as well as the dependencies of the phase transition temperatures for (b) the Cry-Col<sub>h</sub> transition and (d) the Col<sub>h</sub>-Iso transition versus inverse pore size. Blues squares indicate data for bulk HAT6, black symbols indicate data for HAT6 confined into unmodified membranes, green symbols indicate data for HAT6 confined into OPA-modified membranes, and red symbols indicate data for HAT6 confined into ODPA-modified membranes (filled circles: main peak, open symbols: satellite peak). Dashed-dotted lines are guide for eyes. Solid lines are the fits of eqn. (32) to the dependencies. Note that for the samples with modified pore surfaces, the pore diameter was corrected regarding the estimated thickness of the surface layer.

The pore size dependencies of the phase transition enthalpies show stronger dependence on pore size for larger pores in comparison to smaller ones. Similar findings were reported for a series of organic materials confined within nanopores.<sup>161</sup> The surface area of the pores per unit of mass is significantly higher for smaller pores. This can lead to stronger confinement effects on the enthalpies for smaller pores for nanoconfined materials, which could explain similar trends observed with different nanoconfined materials. In addition, higher values of the transition enthalpies were found for surface modified samples compared to unmodified ones. This means that the amount of ordered HAT6 increases for the samples with the OPA- and ODPA-modified

pore walls even though there is still a considerable amount of disordered material inside the pores, most likely located in the pore center.

Figure 52b and d show the dependencies of the phase transition temperatures on inverse pore size for both phase transitions. It can be seen that the phase transition temperatures decrease with decreasing pore size. In general, the pore size dependence of phase transition temperatures can be well described by the Gibbs-Thomson-equation for a variety of materials including LCs.<sup>51,52,162,163</sup> The Gibbs-Thomson-equation reads

$$\Delta T = T_{m,bulk} - T_m(d) = T_{m,bulk} \frac{4\sigma}{\Delta H_{m,bulk} \rho_{HAT6} d} \quad (32)$$

where  $T_{m,bulk}$  is the phase transition temperature of the bulk material,  $d$  is the pore diameter,  $T_m(d)$  is the phase transition temperature of **HAT6** within the pores of diameter,  $d$ , and  $\sigma$  is the surface tension of the interface.  $\Delta H_{m,bulk}$  is the phase transition enthalpy of the bulk material.

For the phase transition from the Cry to Col<sub>h</sub> phase, the data seems to follow the Gibbs-Thomson-equation for both probed types of samples. The surface tensions were calculated to be 5.4 mN m<sup>-1</sup>, 5.3 mN m<sup>-1</sup> and 5.1 mN m<sup>-1</sup> from the dependencies of Cry-Col<sub>h</sub> phase transition temperatures for the samples with unmodified, OPA- and ODPA-modified pore walls, respectively. The OPA and ODPA modifications make the pore wall more hydrophobic in comparison to the unmodified pore walls. Therefore, the interfacial tension is lower for samples with modified pore walls than for unmodified ones. Figure 52d depicts that the dependence of phase transition temperatures of the Col<sub>h</sub>-Iso phase transition changes at a pore size of ca. 38 nm for the samples with the unmodified pore walls. Assuming that both pore size dependencies can be described by a Gibbs-Thomson-equation for pore sizes larger than 38 nm, the surface tension was calculated as 2.2 mN m<sup>-1</sup>, whilst for pore sizes smaller than 38 nm a value of 0.8 mN m<sup>-1</sup> was

calculated. As it will be discussed below in more detail, this change in the pore size dependence of the phase transition temperature for the Col<sub>h</sub>-Iso phase transition goes along with a change in the dominating order. It is also important to note that the pore size dependence of the Col<sub>h</sub>-Iso phase transition observed here is different from that reported in ref. 73. The reason for this is not quite clear and requires additional experiments.

The pore size dependency of the phase transition temperature of the Col<sub>h</sub>-Iso phase transition for the samples with the OPA and ODPA modified pore walls can be described with a single Gibbs-Thomson-equation where a value of 0.9 mN m<sup>-1</sup> was calculated for the surface tension. This value is quite similar to the one obtained for the unmodified pore walls for smaller pore sizes. It might be concluded that the type of dominating anchoring is the same in both cases. Moreover, a study on the effect of orientation on the reduction of the phase transition temperature revealed by SHS for a confined rod-like liquid crystal.<sup>162</sup> demonstrated the stronger decrease of the transition temperatures for a radial configuration. In addition, the favorable interactions between the aromatic core and the polar surface of the unmodified membranes enforce likely face-on anchoring leading to homeotropic radial configuration (logpile). Hence, it can be concluded that the homeotropic radial configuration is the dominant type of ordering found in larger unmodified pores. Recently, Zhang et al.<sup>77</sup> found also dominant logpile configuration for **HAT6** confined in native nanopores of AAO membranes.

For the smaller unmodified pores and for the modified pores, it was assumed that the dominating type of ordering is a planar axial configuration. The similar values obtained for the surface tensions ( $\sigma_{Unmod,2} \approx \sigma_{ODPA} = \sigma_{OPA}$ , Figure 52d) further support this assumption. The planar configuration is assumed for samples with the modified pore walls due to the similarity between the alkyl chains and the alkyl chains grafted to the surface of the modified membranes.

On the contrary, findings in the literature for confined **HAT6** point out logpile configurations in unmodified small pores<sup>77</sup> and circular concentric (planar radial) configurations in nanopores grafted by alkyl chains.<sup>76</sup> Although the calorimetric investigations give a clear picture of the phase behavior under confinement, they reflect some understanding about the dominating configuration in the nanopores based on the pore size dependencies of the phase transitions temperatures and enthalpies. These predictions will be reevaluated with respect to the orientational order characterized by BDS in the next section.

### **5.3. Orientational Order under Nanoscale Confinement**

The collective orientational order of **HAT6** in the bulk and confined **HAT6** was revealed by BDS. Of course, BDS is not a tool to estimate the structure directly. BDS is sensitive to dipole orientation (dipole vector with respect to the outer electrical field). Therefore, a change in the orientation at the phase transition can be monitored when a change of the orientation of the dipole moment is involved. Together with a reference measurement on the bulk material where the orientation is known conclusion based on facts about the orientation can be drawn. The measurements were-carried out at a frequency of 35 kHz, where results from the third heating run are provided in Figure 53. A frequency of 35 kHz was selected for these investigations as no dielectric active processes due to molecular fluctuations for **HAT6** take place in the temperature range from 350 K to 383 K. In this temperature range, the relaxation processes take place at frequencies between 1.9 MHz to 1.2 GHz (obtained from the extrapolation of the data given in ref. 40). Hence, a measurement frequency of 35 kHz is significantly lower than the frequency window of the dielectric relaxation processes, and the measurements shown in Figure 53 correspond to quasi-static dielectric measurements where only the collective orientation of **HAT6** contributes to  $\epsilon'$ , which can be considered as frequency-independent.

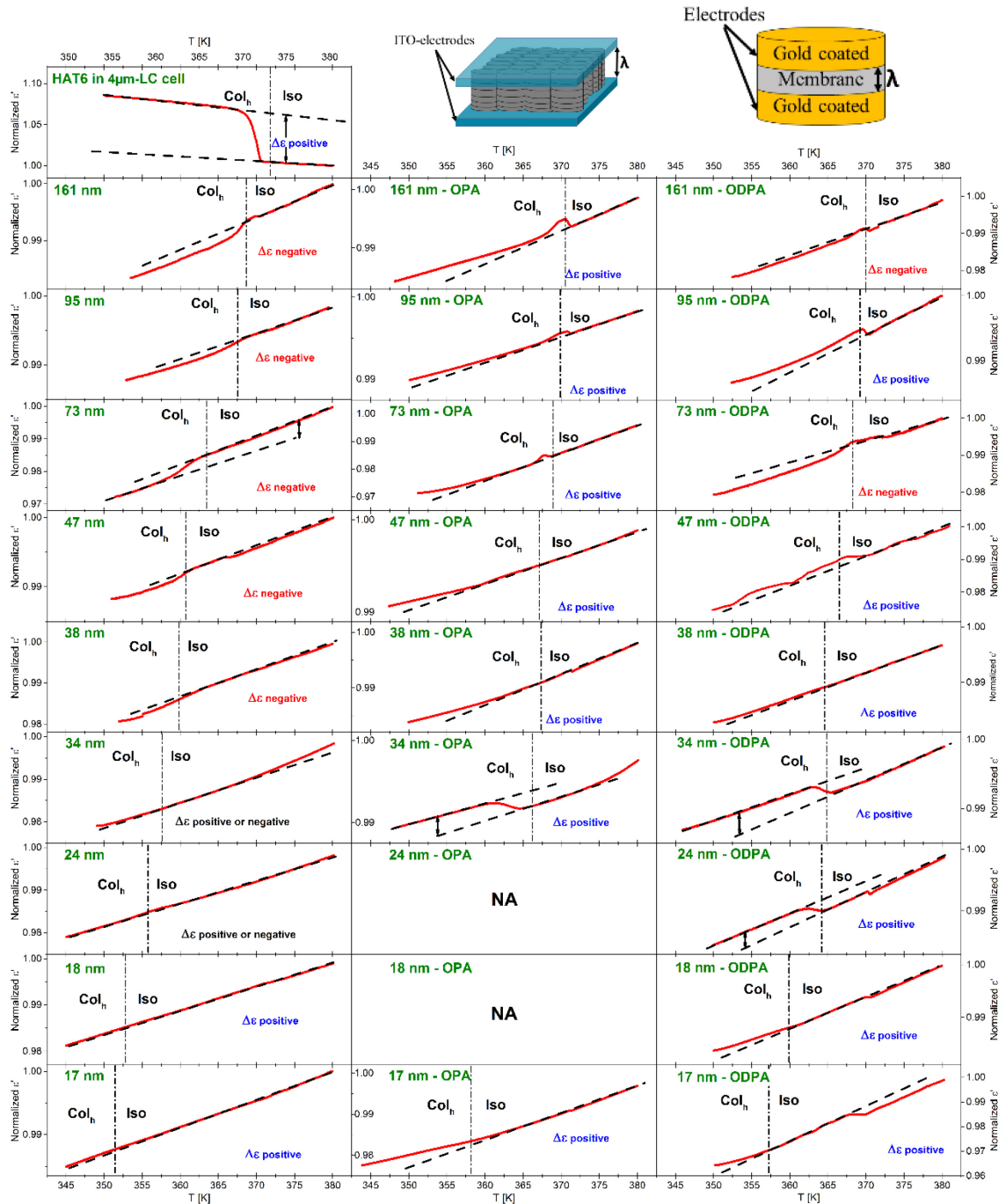


**Figure 53.** Normalized dielectric permittivities as a function of temperature during the third heating run for the bulk, samples with unmodified, OPA- and ODPA-modified pore walls as indicated. All measurements were done with a heating/cooling rate of  $1 \text{ K min}^{-1}$  at a frequency of  $35 \text{ kHz}$ . The dashed-dotted lines indicate the  $\text{Col}_h$ -Iso phase transition temperatures determined by DSC. The dashed lines represent temperature dependencies of  $\epsilon'$  extrapolated from  $\text{Col}_h$  and Iso phases. The insets on the right-top are the drawings illustrating the measurement geometry used for the dielectric measurement for bulk **HAT6** in the cell and the confined **HAT6**.

In the BDS measurements, the cylindrical pores were oriented parallel to the electric field applied due to the parallel plate geometry (see the inset of Figure 53). Therefore, the system can be considered as AAO and **HAT6** capacitors connected in parallel yielding to an additive response.<sup>136</sup> Thus, the absolute value of the permittivity of such a system is related to the porosity of the membrane. For this reason, the measured  $\epsilon'$  values were normalized with respect to the values of  $\epsilon'$  at 383 K for each sample.

The excess permittivity ( $\Delta\epsilon$ ) can be defined as the difference between the temperature dependence of  $\epsilon'$  in the Col<sub>h</sub> phase, and that of  $\epsilon'$  extrapolated to the Col<sub>h</sub> phase from the dependence in the Iso phase. A positive  $\Delta\epsilon$  was determined for bulk **HAT6**, where **HAT6** molecules are homeotropically aligned, which was also confirmed by POM. The positive  $\Delta\epsilon$  indicates that the columns are perpendicularly aligned to the electrodes. Hence, a positive  $\Delta\epsilon$  can be attributed to a dominating axial configuration, whilst a negative  $\Delta\epsilon$  corresponds to a dominating radial configuration. In some cases, from the overview given in Figure 53, it is hard to detect whether  $\Delta\epsilon$  is positive or negative. Therefore, enlarged figures are prepared and added to *Appendix V* (see Figure S36-S41).

For the unmodified pores with diameters smaller than 38 nm, the  $\Delta\epsilon$  was estimated to be positive and assigned to a planar axial configuration. For pore sizes greater than 38 nm, a negative  $\Delta\epsilon$  observed and assigned to the homeotropic radial configuration. This is in good agreement with the discussion given above concerning the pore size dependency of the phase transition temperatures. The DSC investigations indicate that a change in the anchoring type occurs at a pore diameter of ca. 38 nm, which was also observed using BDS. Conversely, a positive value of  $\Delta\epsilon$  was found for samples with ODPA-modified surfaces, except for the pore sizes of 73 nm and 161 nm. This has been attributed to the planar axial configuration, where a planar radial configuration

was assumed for 73 nm and 161 nm due to the negative value of  $\Delta\epsilon$ . Similarly, a positive value of  $\Delta\epsilon$ , attributed to the planar axial configuration, was found for all samples with OPA-modified surfaces. For the sample with a pore size of 47 nm with ODPA-modified pore walls, generally a positive value of  $\Delta\epsilon$  was found, however it was observed that the phase transition occurs in several steps (see also Figure S36). As shown recently with high resolution optical birefringence experiments on **HAT6** confined within porous silica and molecular dynamic simulations,<sup>54</sup> such steps can be attributed to a circular concentric (planar radial) configuration. Therefore, it might be concluded that the orientation of **HAT6** in 47 nm modified AAO pores also possesses a circular concentric (planar radial) configuration.

In addition to the dielectric investigations, the molecular ordering for the samples presented here (except the samples with OPA-modified pore walls) was also characterized by optical birefringence (OB) measurement and temperature-dependent XRD. These measurements will be reported elsewhere.<sup>163</sup> Nevertheless, the results of these measurements are included here in Table 8. Some primarily have been already published discussing also the methodology of the measurements (see supporting information of ref. 54). Combining the results of the interpretations based on the DSC investigation and the ordering characterized by BDS, OB and XRD, a general picture of the molecular ordering inside the unmodified, OPA-modified and ODPA-modified nanopores was obtained (see Table 8). In most cases, the results obtained from the DSC and dielectric measurements agree with the data obtained with OB and XRD. The minor differences between BDS and OB findings might be caused by the small differences in the sample preparation. Although, it is argued in ref. 75 that the dipolar orientation of the polar ether groups of alkyl chains is sensed by BDS, whereas the orientation of the aromatic cores is observed by OB. This may explain the small differences observed in the determined configuration by DS and OB.

**Table 8.** The dominating ordering of **HAT6** molecules inside the nanopores revealed by means of different techniques

Pore size, d (nm)	Unmodified				OPA-modified		ODPA-modified			
	<u>DSC</u>	<u>DS</u>	<u>OB</u>	<u>XRD</u>	<u>DSC</u>	<u>DS</u>	<u>DSC</u>	<u>DS</u>	<u>OB</u>	<u>XRD</u>
17	PA	PA	PA	PA	PA	PA	PA	PA	PA	PA
18	PA	PA	PA	-	PA	PA	PA	PA	PA	-
24	PA	PA + HR	HR	-	PA	PA	PA	PA	PA	-
34	PA	PA + HR	HR	-	PA	PA	PA	PA	PA	-
38	PA + HR	HR	HR	HR	PA	PA	PA	PA	PA	PA + PR
47	HR	HR	HR	-	PA	PA	PA	PA + PR	PA	-
73	HR	HR	HR	HR	PA	PA	PA	PR	PA + PR	PR
95	HR	HR	HR	HR	PA	PA	PA	PA	PA + PR	PR
161	HR	HR	HR	HR	PA	PA	PA	PR	PR	PR

**PA:** Planar axial, **HR:** Homeotropic radial and **PR:** Planar radial. **HAT6** confined into the silicon membrane (12 nm) is not presented in the table since the Col<sub>h</sub>-Iso phase transition is completely suppressed for this sample. The results summarized in this table are taken from ref.s 25 and 163 .

According to the above discussions and Table 8, the picture of the molecular ordering of **HAT6** inside the unmodified, OPA-modified and ODPA-modified nanochannels of AAO membranes can be concluded as follows: A model representing the molecular order of **HAT6** inside nanopores should include three idealized major layer; a disordered layer probably located at the center of the pore, an axial ordered layer near the center and radial ordered layers near the pore walls. For **HAT6** in the unmodified nanopores, a transition of the dominant configuration from planar axial (Figure 3d) to homeotropic radial (Figure 3c) configuration was detected in the pore size range from 24 nm to 38 nm. On the other hand, for **HAT6** in the ODPA-modified nanopores, the transition from planar axial (Figure 3f) to planar radial (Figure 3e) configuration was found in the pore size range from 73 nm to 95 nm, whereas **HAT6** in the OPA-modified nanopores show no transition and have planar configuration.

## 5.4. Conclusion

The influence of cylindrical nanoconfinement on the phase behavior and molecular ordering - two main properties determining the applications of a DLC in nanotechnology - was explored by

DSC and BDS for **HAT6** confined into the nanopores of AAO and silica membranes. Pore sizes from 161 nm down to 12 nm were explored. Moreover, the different host/guest interactions and their influence on the phase behavior as well as molecular ordering were studied by comparing their behavior and ordering in unmodified, OPA- and ODPA-modified pores. Prior to the investigations, the membranes and the samples of **HAT6** confined into nanopores were well-characterized by means of volumetric N<sub>2</sub>-sorption, scanning electron microscopy, FTIR, SAXS and TGA.

The pore size dependencies of the phase transition enthalpies and temperatures were obtained by DSC. It was observed that the phase transition enthalpies decrease with decreasing pore size, which indicates that an increasing fraction of **HAT6** does not undergo any phase transitions, and it is thought that this fraction is probably located in the center of the pore. Moreover, the phase transition temperatures decrease with decreasing pore size. These pore size dependencies of the phase transition temperatures were described by Gibbs-Thomson-equation for both transitions. For the Cry-Col<sub>h</sub> transition, a lower interfacial tension was found for the samples with modified pore walls in comparison to the samples with unmodified pore walls. The pore size dependency of the Col<sub>h</sub>-Iso transition temperatures for samples with unmodified pore walls, a change from a stronger to a weaker dependency was observed with a pore size of around 38 nm. Such a change implies that there is an alteration in the dominating order. Therefore, by considering the host-guest interaction it can be concluded that the dominating type of ordering is a homeotropic radial configuration with larger pores ( $d > 38$  nm) and a planar axial configuration for smaller pores ( $d < 38$  nm). However, the dependencies of the Col<sub>h</sub>-Iso phase transition temperatures for the samples with modified pore walls were approximated by one Gibbs-Thomson dependency. Similar values for the surface tension for the samples with modified pore walls to the one was estimated for

samples with unmodified pore walls at lower pore sizes ( $\sigma_{\text{Unmod},2} \approx \sigma_{\text{ODPA}} = \sigma_{\text{OPA}}$ ) was found. Hence, it is concluded that for the samples with modified pore walls that the dominating type of ordering is also the planar axial configuration.

The collective orientational order of nanoconfined **HAT6**, corresponding to the dominating ordering in the pore, was probed by BDS at a constant frequency of 35 kHz. Similar to the DSC findings, BDS investigations revealed that for the unmodified pores a homeotropic radial orientation for the larger pores ( $d > 38$  nm) and a planar axial for smaller pores ( $d < 38$  nm) as dominating forms of ordering. For OPA- and ODPA-modified pore walls, the planar axial configuration is assigned as the dominating type except for the ODPA-modified samples having pore sizes of 73 nm and 161 nm. Moreover, OB and XRD studies on the samples discussed here mostly agreed the molecular orderings determined by BDS.

In summary, OPA and ODPA surface modifications have been revealed to be promising strategies for controlling the molecular ordering of DLCs inside the nanopores of metal oxide membranes. Our results indicate that the dominating planar axial configuration, which is the only configuration suitable for electronic applications, was successfully achieved by both OPA- and ODPA-modifications for most of the pore sizes probed. Moreover, the higher phase transition enthalpies and temperatures observed for the samples with modified pore walls compared to the unmodified ones implies a significant improvement in the amount of ordered **HAT6** present within the pores.

## CHAPTER 6 – CONCLUSION & OUTLOOK

The aim of the presented work is to accomplish an understanding of the structure, phase behavior, molecular dynamics and conductivity of columnar liquid crystals (CLCs) in the bulk state as well as that of the phase behavior and collective orientational ordering of a model CLC under nanoconfinement. Different CLCs forming a hexagonal columnar ( $Col_h$ ) mesophase, were chosen to study here (see Table 9). The selected CLCs are related to hexakis(*n*-alkyloxy)triphenylene-based discotic liquid crystals (DLCs) (**HATn**). **HATn** are considered as “working horse” of the CLC research since they are one of the first DLCs reported and therefore they are one of the most studied CLCs as model systems. For this reason, hexakis[pentyloxy]triphenylene-based DLC (**HAT5**) and a series of dipole functionalized pentapentyloxytriphenylene-based DLCs (**SHU09-SHU12**) corresponding to unfunctionalized **HAT5** were selected in this work. The chosen dipole functionalized DLCs carry different dipole units, which are ethyl glycolate (**SHU09**), hexanoyl (**SHU10**), trifluoromethyl (**SHU11**), and diethyleneglycol (**SHU12**) units. Moreover, triphenylene crown ether-based unsymmetrical DLCs (**KAL465** and **KAL468**) were chosen to investigate because **KAL** compounds can be considered as related systems to **HATn** with a slightly different chemical structure. Additional to the selected non-ionic CLCs, columnar ionic liquid crystals (**LC536** and **LC537**) were also selected as different type of columnar liquid crystalline system for the study. All above-mentioned CLCs were investigated in the bulk state. Furthermore, a triphenylene-based DLC (**HAT6**), also having a  $Col_h$  mesophase, was studied under confinement at nanoscale. **HAT6** is extensively studied model system for investigation of CLCs under confinement. So far in this thesis, conclusions were drawn for the studies on the different columnar liquid crystalline systems. Therefore, here a more general

conclusion and a summary for the thesis as well as an outlook on the next interesting research work are presented.

**Table 9.** The studied columnar liquid crystalline systems

	Type	Compound	Name	State of the system
Columnar Liquid Crystals (CLCs)	Discotic Liquid Crystals (DLCs)	Unfunctionalized Triphenylenes	HAT6	Confinement
			HAT5	Bulk
		Monofunctionalized Triphenylenes	SHU09-SHU12	Bulk
		Crown ether-based Triphenylenes	KAL465 and KAL468	Bulk
	Ionic Liquid Crystals (ILCs)	Tetramethylated Guanidinium Triflate ILCs	LC536 and LC537	Bulk

The work presented in the first part (*Chapter 4*) investigates the selected different columnar liquid crystalline system in the bulk state. The mesomorphic properties of the CLCs were studied using polarizing optical microscopy (POM) and X-ray diffraction (XRD). The POM and the XRD investigations revealed dendrimeric growth as well as fan-shaped textures and  $p6mm$  symmetry, which are characteristic for a  $Col_h$  mesophase. Moreover, the amorphous halos observed in the XRD patterns in this study indicate a nanophase separation between the flexible alkyl substituents filling the intercolumnar area and the columns formed by the rigid cores. Therefore, it might be concluded that the nanophase separation is a characteristic property of CLCs. Moreover, a similar nanophase separated morphology between the flexible n-alkyl side chains and the rigid polymer backbone has been evidenced for different polymeric systems having longer n-alkyl side chains.<sup>22</sup> Hence, it might be further concluded that the presence of a morphology of nanophase separated alkyl chains is expected for systems consisting of rigid units and flexible alkyl chains attached to the rigid units.

The phase behavior was revealed conducting conventional scanning calorimetry (DSC) measurements. In addition to the phase transition temperatures and enthalpies determined using DSC, the DSC investigations elucidated that all CLCs discussed here undergo at least one thermal glass transition. For the triphenylene-based DLCs (**HAT5**, **SHU09-SHU12**, **KAL465** and **KAL468**), two different thermal glass transitions were found. The investigations imply that the glass transitions regarding the  $T_{g,1}^{\text{thermal}}$  are associated with the nanophase separation.

The molecular dynamics (including the glassy dynamics) taking place in these systems were studied using a combination of broadband dielectric spectroscopy (BDS), specific heat spectroscopy (SHS) and fast scanning calorimetry (FSC) in a broad frequency range from  $10^{-4}$  Hz to  $10^9$  Hz and in a broad temperature range. The molecular dynamics investigations revealed a  $\gamma$ -process and  $\alpha$ -processes for all CLCs studied in this work (see Figure 54). The  $\gamma$ -processes detected by BDS for the CLCs are assigned to **PE**-like localized fluctuations taking place in the alkyl chains filling the intercolumnar area. The  $\alpha_1$ -processes probed by BDS and/or by the calorimetric techniques are unambiguously attributed to the **PE**-like cooperative fluctuations of the alkyl chains taking place in the intercolumnar area. Moreover, other glass dynamics ( $\alpha_2$ -,  $\alpha_3$ - and  $\alpha_4$ -processes) detected by BDS are ambiguously attributed to the cooperative fluctuations of the cores. For the glassy dynamics detected by both BDS and advance calorimetric techniques, it is realized that the dielectric and the calorimetric data are in good agreement. The molecular mobility investigations presented in this thesis, have provided an understanding of the molecular dynamics of columnar liquid crystalline systems in general. Thus, it might be concluded for CLCs that **PE**-like localized and glass dynamics take place in the intercolumnar area due to the **PE**-like structure of the molecules of the alkyl chains of CLCs. Moreover, the study presented here has manifested the significance of the investigation strategy combining the BDS and the advance

calorimetric techniques to gain insight into the glassy dynamics from different perspectives in a complementary manner.

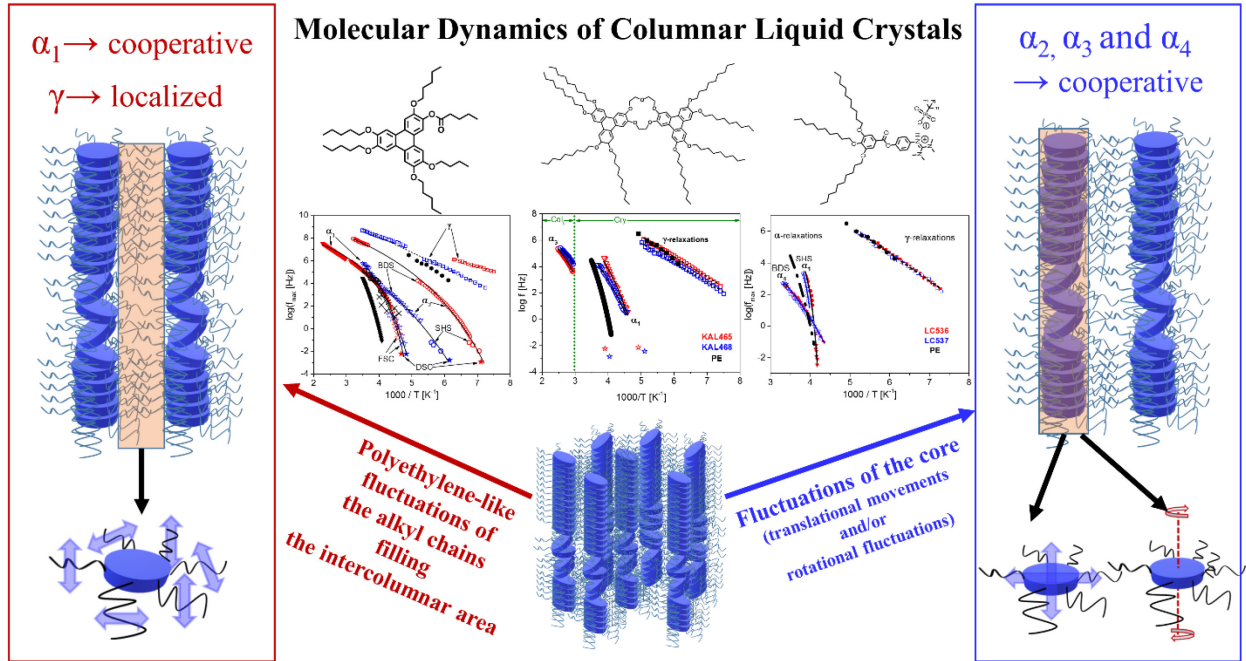


**Figure 54.** Graphical summary of the molecular dynamics of the CLCs for the first part of the thesis.

The conductivity of the CLCs was explored by BDS. For the materials under investigation, the conductivity contributions were observed in the plastic crystalline (Cry) and  $Col_h$  phases by BDS. The conductivity contributions were analyzed to quantify and to gain an understanding of the conductivity mechanism and hence an understanding of the mobilities of the effective charge carriers was obtained in the work. The temperature dependency of the DC conductivity ( $\sigma_{DC}$ ) obtained from the analysis, showed that the structural changes occurring at the phase transition from the Cry phase to  $Col_h$  mesophase are recognized as the changes in the temperature dependence of the  $\sigma_{DC}$ . These changes were discussed by different restrictions on the charge carrier mobility in Cry and  $Col_h$  phases or a change in the charge transport mechanism.

On the one hand, for the non-ionic CLCs (**HAT6**, **SHU09**, **SHU12**, **KAL465** and **KAL468**) it is revealed that the  $\sigma_{DC}$  changes by approximately 1-2 orders of magnitude at the phase transition. For **SHU10** such a change was not observed since as proofed by XRD **SHU10** do not form a Cry phase upon cooling from its Col<sub>h</sub> mesophase. For **SHU11**, a small change in the temperature dependence of the  $\sigma_{DC}$  at the phase transition was found, therefore, this observation implies smaller structural changes at the phase transition for **SHU11** compared to the structural changes for the other non-ionic CLCs. The value of the phase transition enthalpy for the Cry-Col<sub>h</sub> transition for **SHU11** was estimated to 0.3 kJ g<sup>-1</sup>, which is quite smaller than that for the other non-ionic CLCs (ca. 24 kJ g<sup>-1</sup> - 52 kJ g<sup>-1</sup>). This further evidenced the smaller structural changes taking place at the Cry-Col<sub>h</sub> phase transition for **SHU11**. On the other, approximately 4 orders of magnitude change in the  $\sigma_{DC}$  values at the Cry-Col<sub>h</sub> phase transition were found for the ionic CLCs (columnar ILCs **LC536** and **LC537**). This relatively bigger change in the  $\sigma_{DC}$  values were associated with the change in the charge transport mechanism from a delocalized electron hopping in the stacked aromatic systems (in the Cry phase) to one dominated by an ionic conduction in the quasi-1D ion channels formed along the supramolecular columns in the Col<sub>h</sub> mesophase. Moreover, similar  $\sigma_{DC}$  values in the Cry phase were found for the columnar ILCs compared to that for the non-ionic CLCs, when the same temperature range is considered for the observed  $\sigma_{DC}$ . Therefore, it might be concluded for the non-ionic CLCs that the charge transport mechanism is the delocalized electron hopping in the Cry phase, and presumably the charge transport mechanism is the same for Col<sub>h</sub> phase with less restrictions on the charge carriers in Col<sub>h</sub> phase than in Cry phase. The investigation of the conductivity of the CLCs presented here, implies that the columnar ILCs seem to be more promising candidates for electronic applications due to their higher charge carrier mobility. Furthermore, the study showed that the investigated ILCs can be used as switch in

application, e.g. in field-effect transistors, since it was found an on/off ratio as high as ca.  $10^4$  for these materials, where the  $\text{Col}_h$  mesophase and in the Cry phase can be considered as on-state and off-state respectively.

In the second part of the thesis (*Chapter 5*), a triphenylene-based DLC (**HAT6**) was studied under nanoconfinement. **HAT6** was confined into cylindrical nanopores of anodic aluminum oxide (AAO) and silica membranes having pore sizes from 161 nm down to 12 nm (see Figure 55). The OPA and ODPA surface modification were applied to control the molecular ordering under the confinement. Therefore, the hydrophilic inner walls of the pores were successfully coated with alkyl chains by the, consequently, the hydrophilic pore walls were obtained. The phase behavior explored using DSC showed that the phase transition temperatures shift to the lower temperatures and the phase transition enthalpies decreases with decrease the confinement size. The results of the phase behavior revealed here are important and should be considered for the applications at nanoscale due to the considerable changes in these properties under nanoconfinement. The collective orientational order (dominating molecular ordering) of the molecules of **HAT6** under the confinement was studied using BDS. The investigation of the molecular ordering using BDS revealed that the dominating planar axial order, is prerequisite for most of the electronic applications, can be achieved for **HAT6** confined into the nanopores of aluminum oxide membranes by the OPA and ODPA surface modifications. Thus, it is concluded that the OPA and ODPA modifications are promising strategies for controlling the molecular ordering of DLCs inside the nanopores of metal oxide membranes. Moreover, the samples discussed here were also further investigated using temperature-dependent optical birefringence (OB) and XRD in another study.<sup>163</sup> The molecular orderings determined by the dielectric measurements found to be in agreement with that determined by OB and XRD. Hence, the study has demonstrated BDS as a

powerful method to monitor molecular order within the pores. It also demonstrates a well-established investigation strategy for a study concerning such a nanoconfinement.

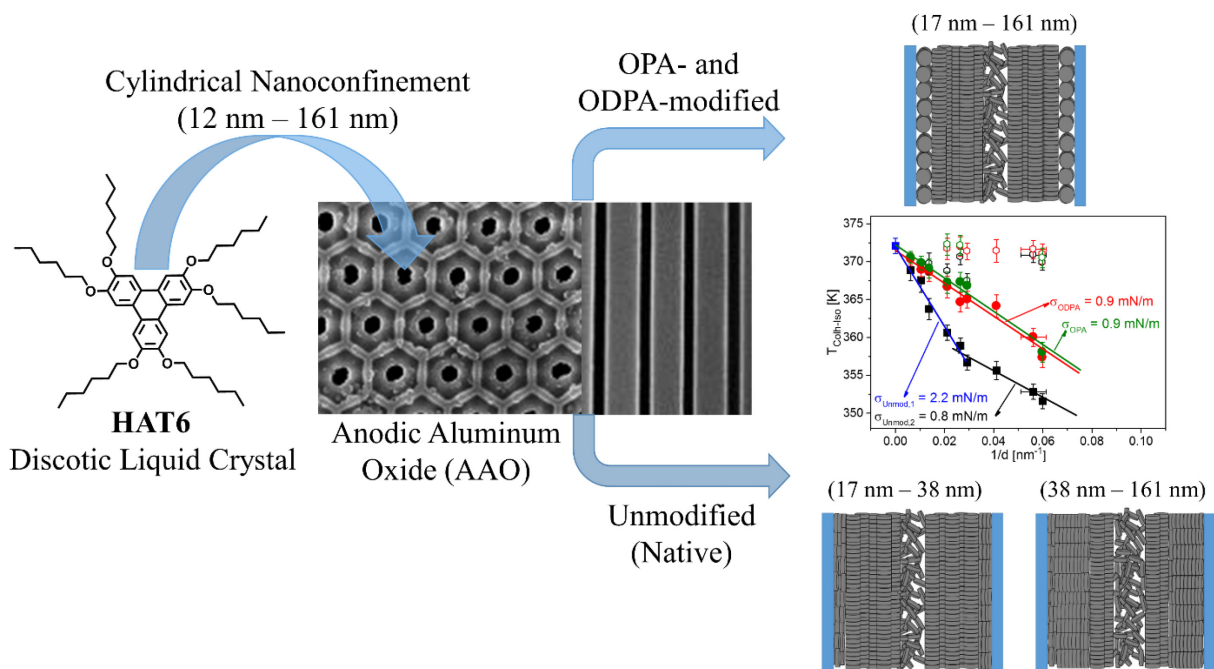


**Figure 55.** Graphical summary of the molecular ordering of **HAT6** confined into the cylindrical nanochannels for the second part of the thesis.

The thesis has already provided an understanding of the molecular dynamics of the **KAL** compounds using BDS (dipole fluctuations perspective). Although, it has been demonstrated in this thesis that the combination of BDS and the advance calorimetric techniques probing glass dynamics are beneficial in order to study glass dynamics, an understanding of the glassy dynamics for **KAL** compounds using the calorimetric techniques (entropy fluctuations perspective) is missing. Therefore, the next work will be the investigation of the glassy dynamics for the **KAL** compounds using advance calorimetric techniques SHS and FSC.

As it has been reported in the literature<sup>39,40</sup> and also in the work presented here, multiple glassy dynamics might take place in columnar liquid crystalline systems due to the cooperative fluctuations of cores and/or substituents in the intracolumnar and/or intercolumnar area. The dipole

functionalization seems to be a good strategy to probe selectively the glass dynamics in the intracolumnar or intercolumnar area using BDS by a dipole functionalization of the molecules of the cores or that of the substituents respectively.<sup>37,39,40,64,70</sup> The CLCs having only dipole functionalized core and the same CLCs having only dipole functionalized substituents as well as the corresponding unfunctionalized CLCs could be systematically investigated using BDS in order to shed light on the glassy dynamics of CLCs as well as the glass transition phenomena. Moreover, the molecular dynamics of CLC could also be selectively studied using neutron scattering by partially deuterating the molecules of the core or that of the substituents. Furthermore, molecular dynamics simulations could be also performed for both unfunctional and functional CLCs in order to gain knowledge of the possible molecular motions. As it has been demonstrated in this work, such molecular dynamics simulations are helpful for the assignment of the molecular dynamics probe by BDS, SHS and/or FSC.

The investigations on the columnar ILCs presented in this study has revealed that the ILCs seems to be more promising candidates than the CLCs for electronic applications due to their higher charge carrier mobilities. To best of our knowledge this is the first study investigating the molecular dynamics of columnar ILCs. Therefore, similar investigations on different columnar ILCs having varying lengths of alkyl chains and counterions are needed to create cumulative knowledge of the structure-dynamics-conductivity relationships for columnar ILCs. As discussed also for CLCs, such knowledge is required to explore columnar ILCs' potential applications as well as to design and tailor their properties for the applications.

Several studies has been reported, investigating the phase behavior and molecular ordering of non-ionic CLCs confined within the nanopores of metal oxide membrane.<sup>31,51,52,73,74,75</sup> However, to best of our knowledge such a study on columnar ILCs confined into nanopores has not been

reported. Therefore, from both research and application point of views the phase behavior and molecular ordering as well as conductivity of columnar ILCs under nanoconfinement could be interesting to study. Moreover, local conductivity of single nanochannels of metal oxide membranes filled with CLCs could be studied to reveal the conductivity of single so-called nanowires. The local conductivity can be measured using an AFM-based approach in the contact mode, where conductive tip and cantilever are used and an external frequency-dependent voltage is applied.<sup>164</sup> Moreover, the measurement of the local conductivity might be performed using a broadband impedance microscope, which is a dielectric spectroscopy-based technique as described in ref. 165.

## APPENDIX I

### Matrix-Assisted Laser Desorption/Ionization-Time of Flight (MALDI-TOF)

Matrix-Assisted Laser Desorption/Ionization-Time of Flight (MALDI) mass spectrometry (MS) experiments were performed to confirm the chemical structure of **HAT6**. The spectra were collected employing a Bruker Autoflex III (Bruker Daltonik GmbH, Bremen, Germany) spectrometer equipped with a Smartbeam<sup>TM</sup> laser (356 nm, frequency 200 Hz). The measurements were performed by Dr. Jana Falkenhagen from BAM (Bundesanstalt für Materialforschung und -prüfung (BAM), Richard-Willstätter-Str. 11, 12489 Berlin, Germany). Figure S1 shows the MALDI-TOF MS spectrum of **HAT6**. Pronounced peaks were observed in the theoretical molar mass range of 828.63 g mol<sup>-1</sup> of **HAT6** considering only the mass of <sup>12</sup>C. The different peaks are detected due to the different isotopes of carbons; <sup>12</sup>C, <sup>13</sup>C, and <sup>14</sup>C. A molar mass of **HAT6** was found to be 828.63 g mol<sup>-1</sup> by taking into account the natural occurrence of the isotopes.

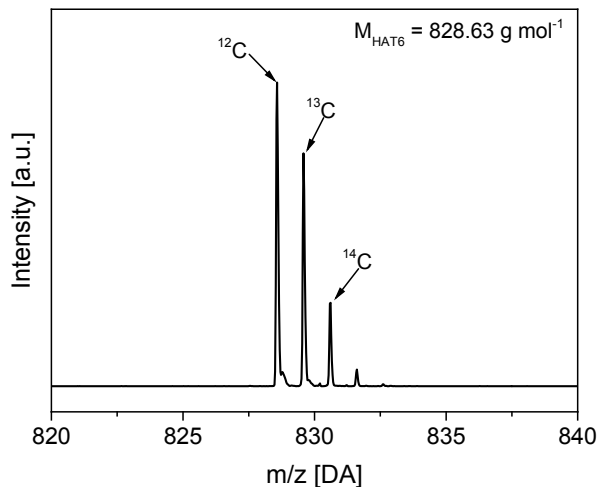
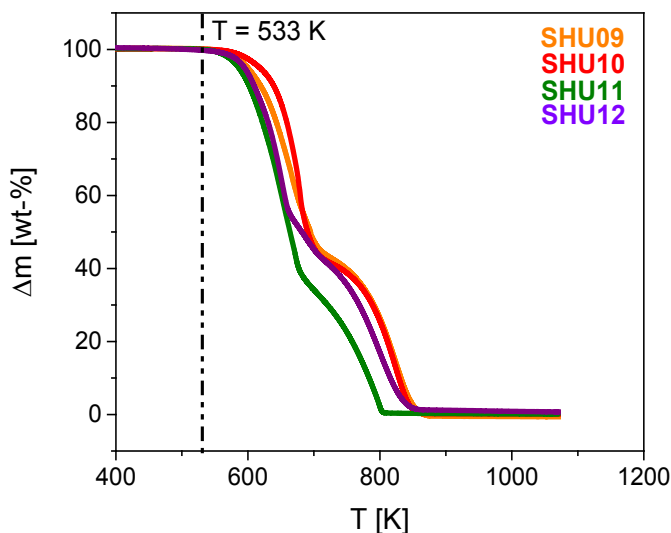


**Figure S1.** MALDI-TOF MS spectrum of **HAT6**.

## Thermogravimetric Analysis (TGA)

Measurements and sample preparation for the measurements may cause thermal decompositions of a sample. Thermal stability of the materials presented in this study was investigated using thermogravimetric analysis (TGA) in order to ensure that no thermal decomposition is taking place.

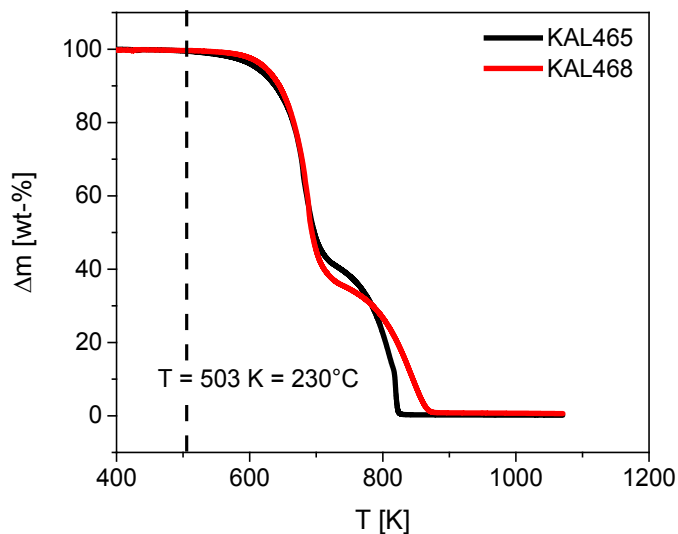
Figure S2 shows mass loss profiles of the monofunctionalized triphenylene derivatives **SHU09-12** under synthetic air upon heating. All the samples shown in Figure S2 are thermally stable at least up to 533 K, which ensures that there was no thermal degradation during the sample preparation and the measurements.



**Figure S2.** TGA curves for the monofunctionalized triphenylene derivatives **SHU09-SHU12**. Orange line shows data for **SHU09**, red line for **SHU10**, green line for **SHU11** and purple line for **SHU12**. Dashed-dotted line represents the temperature, 533K, below which thermal decomposition of the materials do not occur.

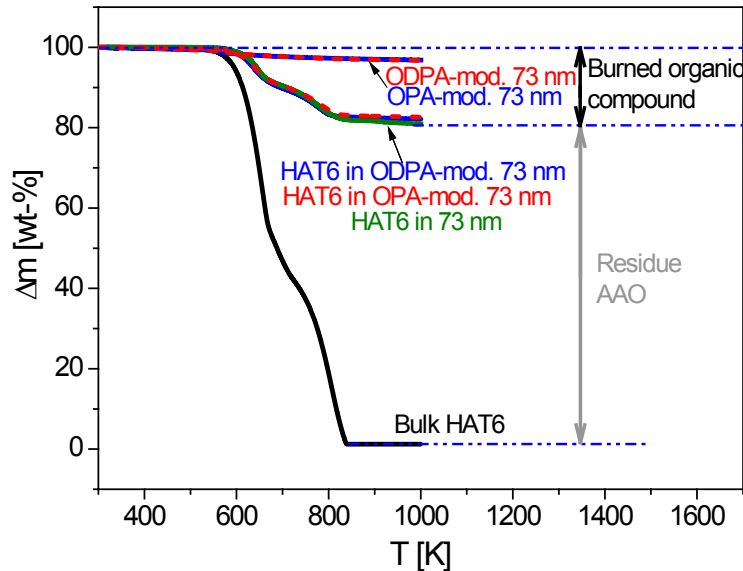
Figure S3 shows mass loss profiles of triphenylene crown ether-based DLCs **KAL465** and **KAL468** under synthetic air upon heating. All triphenylene crown ether-based DLCs shown in

Figure S3 are thermally stable at least up to 503 K, which ensures that there was no thermal degradation during the sample preparation and the measurements.



**Figure S3.** TGA curves for triphenylene crown ether-based liquid crystals **KAL465** and **KAL468** as indicated. Dashed line represents the temperature, 503 K, below which thermal decomposition of the materials do not occur.

The filling degree of the membranes with **HAT6** was controlled by TGA. TGA measurements were carried out by a Seiko TG/DTA 220 with a heating rate of  $10 \text{ K min}^{-1}$ , from room 303 K to 1000 K, under synthetic air to burn all organic compound confined into the nanopores. Figure S4 shows TGA curves for bulk **HAT6**, the confined **HAT6** in unmodified, OPA- and ODPA-modified AAO membranes as well as the modified empty mem branes. All samples shown in Figure S4 are thermally stable at least up to 550K, which ensures that there was no thermal degradation during the sample preparation and the measurements. From the estimated masses, the degree of filling can be estimated. Complete pore filling was obtained for all samples shown in this study.



**Figure S4.** TGA curves for **HAT6** in the bulk (black solid line), **HAT6** confined into unmodified AAO membrane (green solid line), **HAT6** confined into ODP A-modified AAO membrane (blue solid line as indicated), empty ODP A-modified AAO membranes (blue solid line as indicated), **HAT6** confined into OPA-modified AAO membrane (red dashed line as indicated), empty OPA-modified AAO membranes (red dashed line as indicated). TGA curves given in here for the membranes having the pore size of 73 nm.

### Attenuated Total Reflection Fourier Transform Infrared Spectroscopy (ATR-FTIR)

Attenuated total reflection Fourier transform infrared spectroscopy (ATR-FTIR) was employed to confirm the surface modification of the membranes. The measurements of empty unmodified and modified membranes were carried out at room temperature. Peaks for the alkyl C-H stretching should appear for the FTIR spectra of the modified membranes, and its appearance can be used as an indication to confirm the OPA- and ODP A-modifications. Figure S5 shows that the peaks at  $2850\text{ cm}^{-1}$  and  $2930\text{ cm}^{-1}$ , corresponding to symmetric and antisymmetric alkyl C-H stretching respectively appear for the modified empty membranes (red and blue lines). As it is expected, these peaks were not observed in FTIR spectra for the unmodified membranes (black lines).

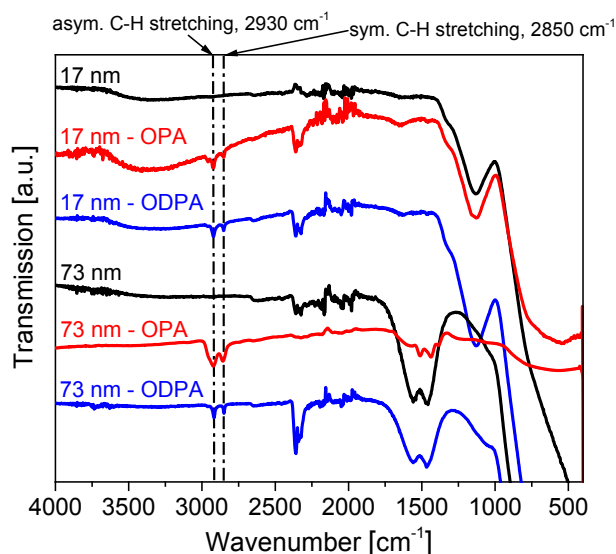


**Figure S5.** FTIR spectra of the OPA- and ODPA-modified as well as unmodified aluminum oxide membranes as indicated.

### **Small Angle X-ray Scattering (SAXS)**

Long-range ordering was studied by small angle X-ray scattering (SAXS) in the “MAUS”: a heavily customized Xeuss 2.0 (Xenocs, France). X-rays are generated from a microfocus X-ray tube with a copper target, followed by a multilayer optic to parallelize and monochromatize the X-ray beam to a wavelength of 0.154 nm. The detector consists of an in-vacuum motorized Eiger 1M, for this investigation placed at distances of 208, 558, and 1258 mm from the sample. After correction, the data from the different distances are combined into a single curve. The space between the start of the collimation until the detector is a continuous, uninterrupted vacuum to reduce background. The membranes (discs) were mounted with their surface perpendicular to the beam in the evacuated sample chamber. The resulting data has been processed using the DAWN software package<sup>124,125</sup> with the following processing steps in order: masking, correction for counting time, dark-current, transmission, primary beam flux, background (no sample in the beam), flat-field, polarization and solid angle, followed by azimuthal averaging. The data has not

been scaled to absolute units. Photon counting uncertainties were estimated from the raw image, and propagated through the correction steps. For the alignment experiment, the membrane was held upright between two LEGO bricks, on top of a PhysikInstrumente H811.I2V hexapod. 200 second exposures were taken at various tilt angles, to seek the tilt angle that would produce a radially isotropic pattern.

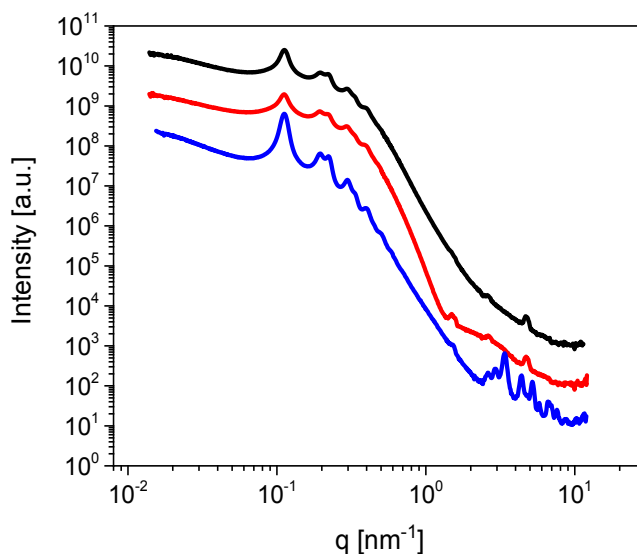


**Figure S6.** SAXS patterns of unmodified (black) and ODPA-modified (red) AAO membranes with 38 nm diameter pores as well as that of **HAT6** confined AAO membranes with 38 nm pore size (blue). The curves are shifted along the y-scale for clarity.

Figure S6 shows the SAXS patterns of the samples. It is concluded that the pores are 100% filled for **HAT6** confined into AAO with 38 nm pore diameter.

## APPENDIX II – Supporting Information for Section 4.1

### POM Textures

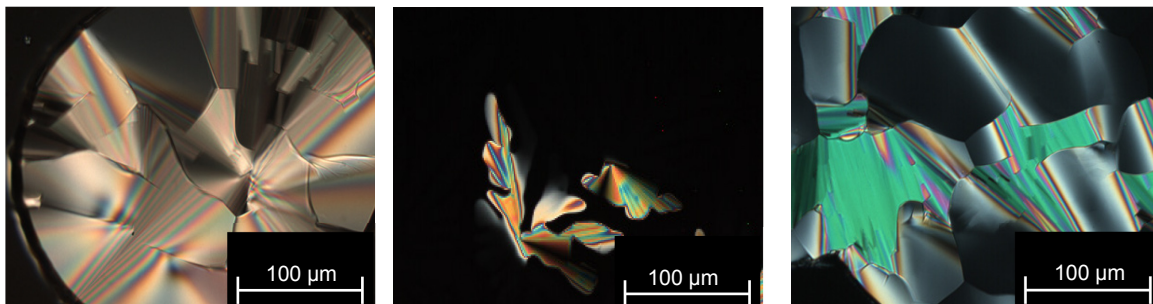


**Figure S7.** POM textures of **SHU09** at 408 K (left), at 398 K (middle) and at 365 K (right) upon cooling from the isotropic liquid (cooling rate  $5 \text{ K min}^{-1}$ , magnification 200x) showing pseudo focal conic fan-shaped textures and dendrimeric growth textures.

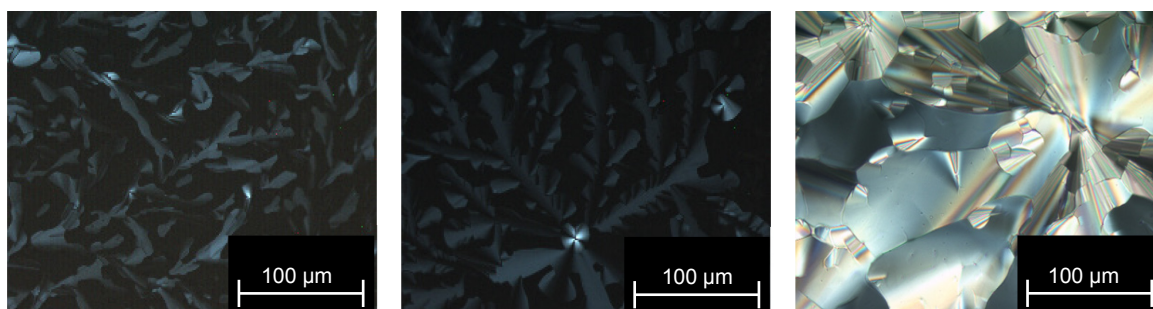


**Figure S8.** POM textures of **SHU10** at 499 K (left), at 436 K (middle) and at 383 K (right) upon cooling from the isotropic liquid (cooling rate  $5 \text{ K min}^{-1}$ , magnification 200x) showing dendrimeric growth and pseudo focal conic fan-shaped textures.

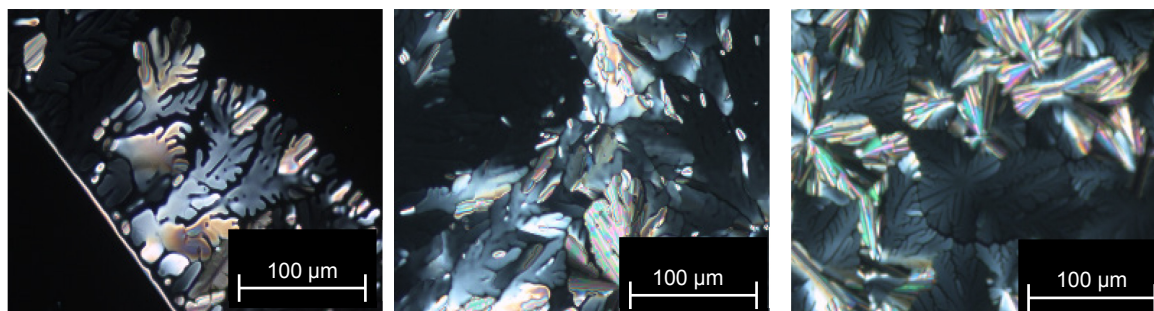


**Figure S9.** POM textures of **SHU11** at 447 K (left) at 436 K (middle) and at 368 K (right) upon cooling from the isotropic liquid (cooling rate  $5 \text{ K min}^{-1}$ , magnification 200x) showing dendrimeric growth textures.

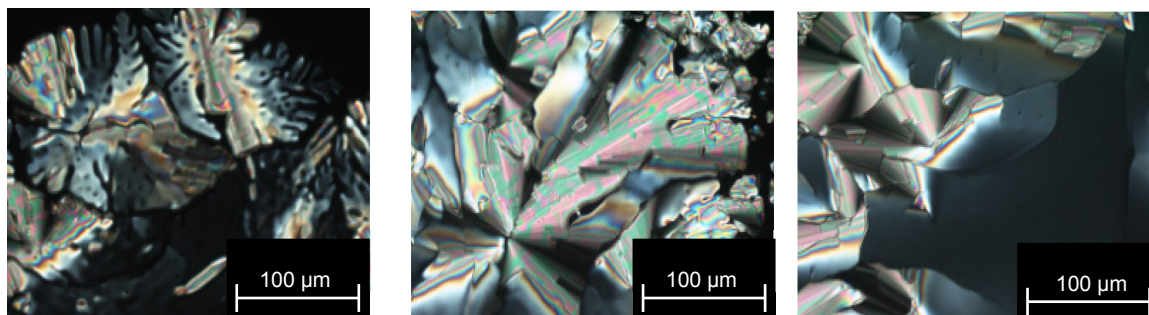


**Figure S10.** POM textures of SHU12 at 373 K (left), at 365 K (middle) and at 346 K (right) upon cooling from the isotropic liquid (cooling rate  $5 \text{ K min}^{-1}$ , magnification 200x) showing dendrimeric growth and pseudo focal conic fan-shaped textures.

### XRD Data and Diffraction Patterns

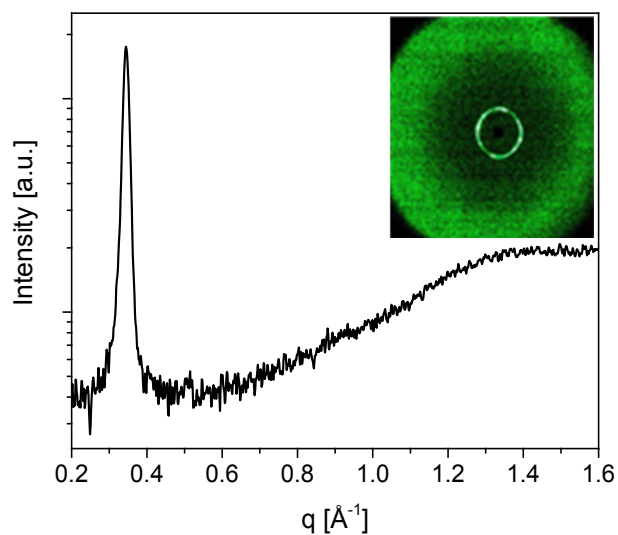


**Figure S11.** WAXS diffractogram of SHU09 at 363 K with the corresponding diffraction pattern (inset).

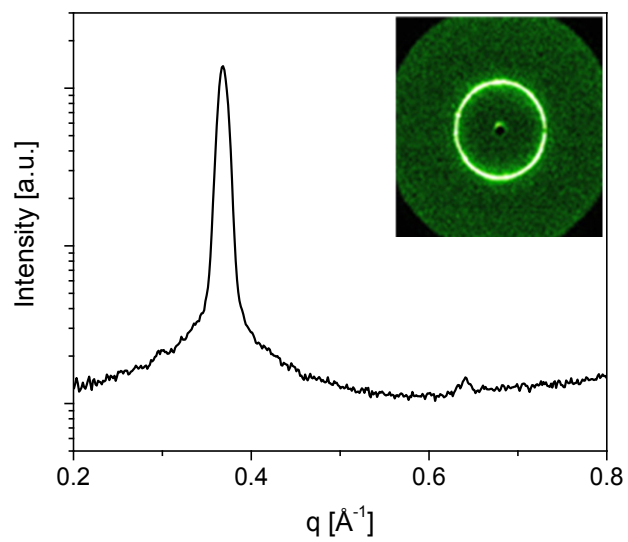


**Figure S12.** SAXS diffractogram of **SHU09** at 363 K with the corresponding diffraction pattern (inset).

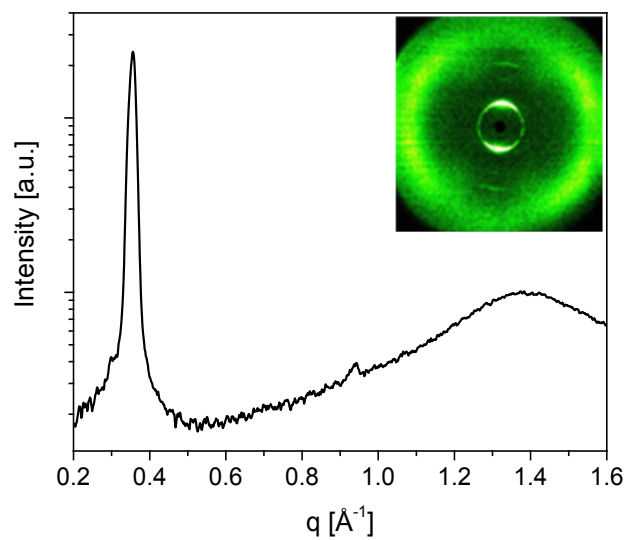


**Figure S13.** WAXS diffractogram of **SHU10** at 353 K with the corresponding diffraction pattern (inset).

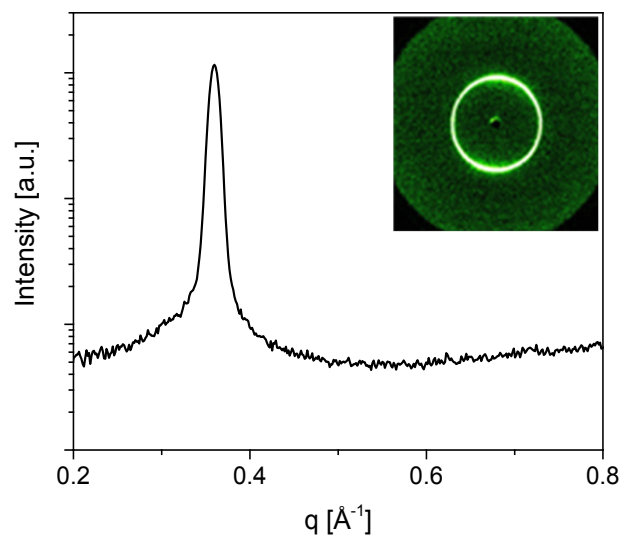


**Figure S14.** SAXS diffractogram of **SHU10** at 353 K with the corresponding diffraction pattern (inset).

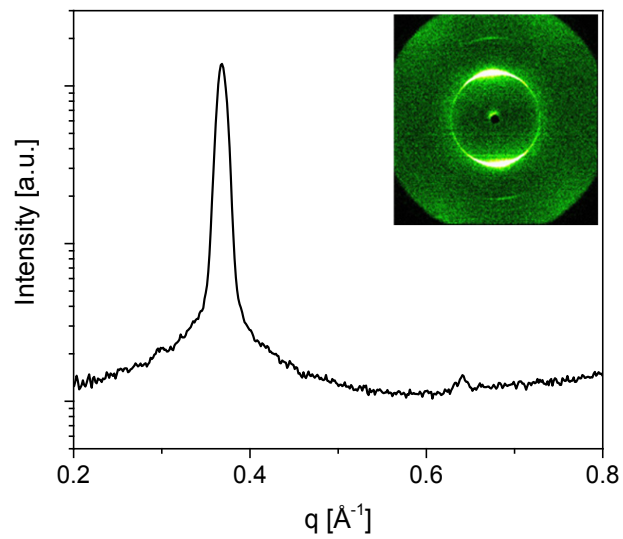


**Figure S15.** SAXS diffractogram of **SHU11** at 353 K with the corresponding diffraction pattern (inset).

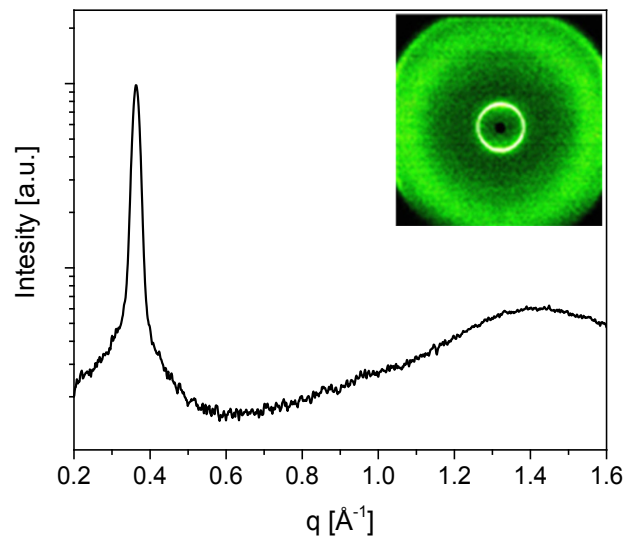


**Figure S16.** WAXS diffractogram of SHU12 at 353 K with the corresponding diffraction pattern (inset).

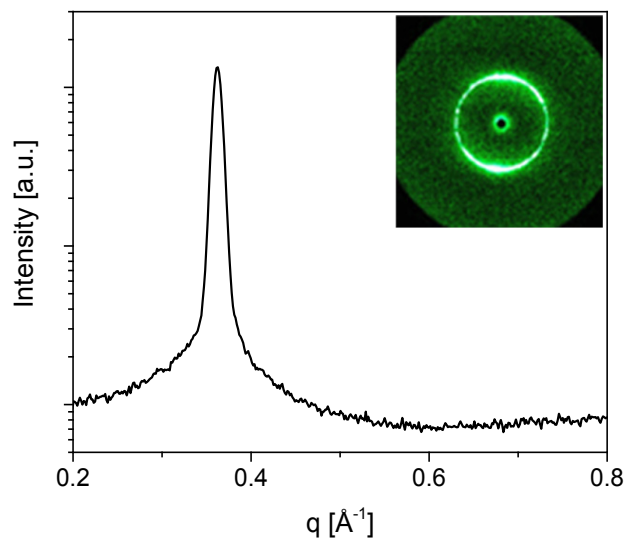


**Figure S17.** SAXS diffractogram of SHU12 at 353 K with the corresponding diffraction pattern (inset).

## Differential Scanning Calorimetry (DSC)

Conventional DSC measurements of **SHU10**, **SHU11**, **SHU12** and **HAT5** were carried out at temperatures down to 173 K under nitrogen purge. DSC traces of **SHU10**, **SHU11**, **SHU12** and **HAT5** measured under nitrogen purge are given in Figure S18-S21. In addition, conventional DSC measurements of the compounds were also conducted at temperatures down to 103 K under helium purge (see Figure S22). The measurements were performed in the temperature range from 103 K to 303 K with a heating/cooling rate of 10 K min<sup>-1</sup>. Helium was used as a purge gas at a flow rate of 20 ml min<sup>-1</sup>. Similar to the measurements performed under nitrogen purge, baseline measurements were conducted by measuring an empty 50 µl aluminum pan under the same conditions. The baselines were subtracted from the data measured for the samples. The calibration of the DSC was checked before the measurement by measuring an indium standard.

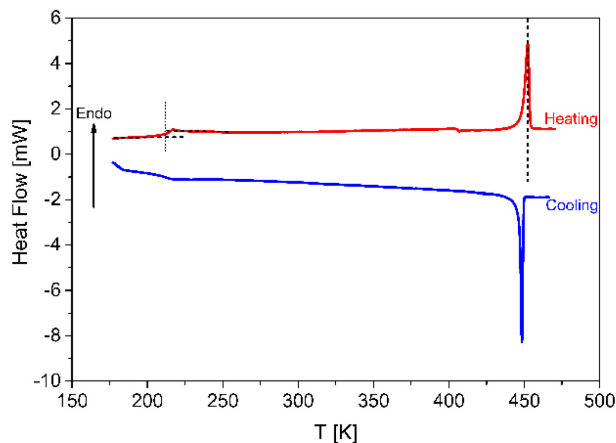


**Figure S18.** DSC thermograms of **SHU10** for the first cooling and the second heating run at a heating/cooling rate of 10 K min<sup>-1</sup>. Dashed lines point out the phase transition temperatures observed during the second heating run. Dotted line indicates the glass transition temperature observed during the second heating run.

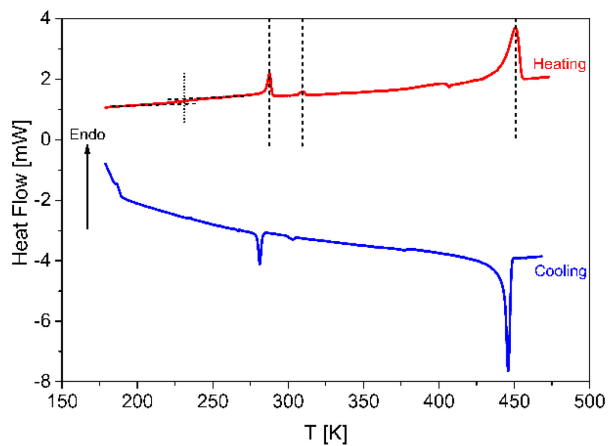


**Figure S19.** DSC thermograms of **SHU11** for the first cooling and the second heating run at a heating/cooling rate of  $10 \text{ K min}^{-1}$ . Dashed lines point out the phase transition temperatures observed during the second heating run. Dotted line indicates the glass transition temperature observed during the second heating run.

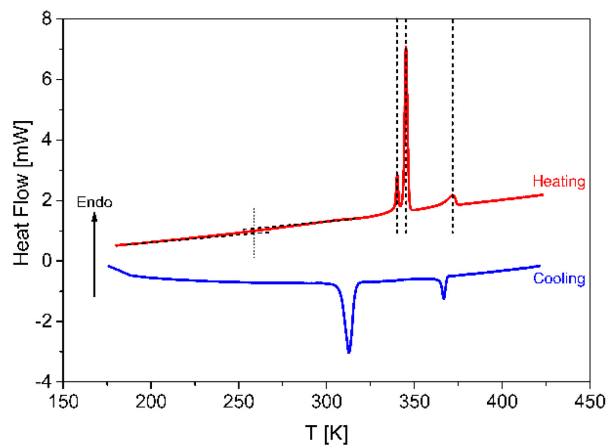


**Figure S20.** DSC thermograms of **SHU12** for the first cooling and the second heating run at a heating/cooling rate of  $10 \text{ K min}^{-1}$ . Dashed lines point out the phase transition temperatures observed during the second heating run. Dotted line indicates the glass transition temperature observed during the second heating run.

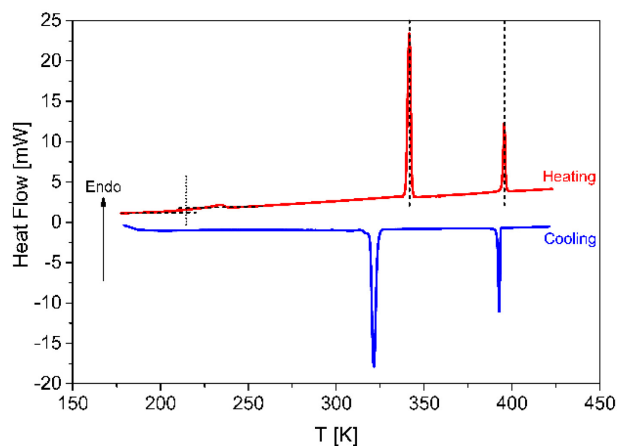


**Figure S21.** DSC thermograms of **HAT5** for the first cooling and the second heating run at a heating/cooling rate of  $10 \text{ K min}^{-1}$ . Dashed lines point out the phase transition temperatures observed during the second heating run. Dotted line indicates the glass transition temperature observed during the second heating run.

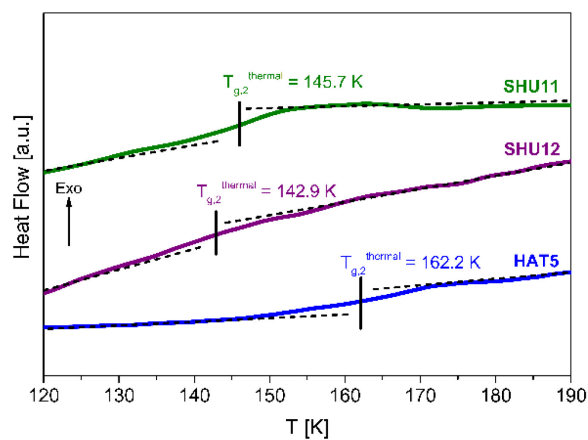


**Figure S22.** DSC thermograms of **SHU11**-**SHU12** and **HAT5** for the second heating run at a heating rate of  $10 \text{ K min}^{-1}$  at low temperatures. Solid lines point out the glass transition temperatures observed during the second heating run.

### **Broadband Dielectric Spectroscopy (BDS)**

The relaxation maps, containing the data for **SHU09-12** and **HAT5** as well as the data taken from the literature for the related relaxation processes, are given in Figure S23 and Figure S24. VFT parameters obtained from VFT-equation (eqn. (2)) fits and activation energies estimated from

Arrhenius-equation (eqn. (1)) fits are presented in Table S1. Furthermore, the plot of the lattice spacing versus the relaxation rates of  $\gamma$ -processes at chosen temperature is shown in Figure S25.

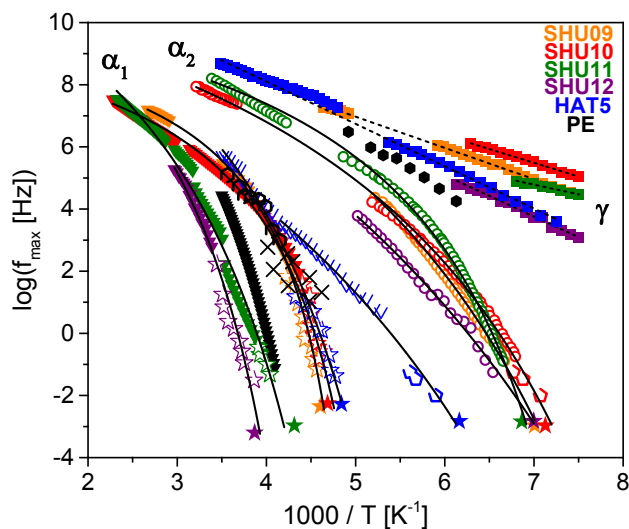


**Figure S23.** Combined relaxation map of **SHU09-SHU12** constructed from data obtained by BDS, Flash DSC and DSC. Orange symbols – data for **SHU09**; red symbols – data for **SHU10**; green symbols – data for **SHU11**; purple symbols – data for **SHU12**; and blue symbols – data for **HAT5**. Triangles –  $\alpha_1$ -relaxations (BDS); open circles –  $\alpha_2$ -relaxation (BDS); filled squares –  $\gamma$ -relaxations (BDS); open stars –  $\alpha_1$ -relaxations (FSC); open pentagons –  $\alpha_2$ -relaxation (SHS); and filled stars – thermal glass transition temperatures (DSC). Solid lines are the fits of VFT-equation (eqn. (2)) to the data. Dashed lines are the fits of the Arrhenius-equation (eqn. (1)) to the data. Black filled triangles denote the dielectric  $\alpha$ -relaxation of polyethylene taken from ref. 145. Black hexagons symbolize the dielectric  $\gamma$ -relaxation of polyethylene taken from ref. 40. Black crosses represent the calorimetric  $\alpha$ -relaxation of polyethylene taken from ref. 146. Black open hexagons symbolize the dielectric  $\beta$ -relaxation of poly(n-decyl methacrylate) taken from ref. 147.

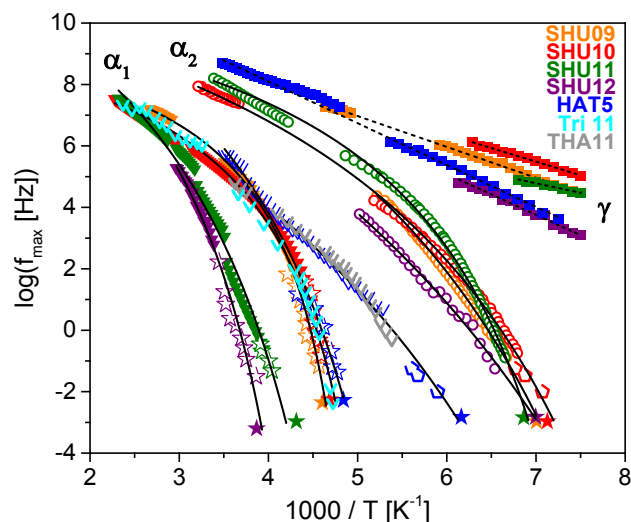


**Figure S24.** Combined relaxation map of SHU09-SHU12 constructed from data obtained by BDS, Flash DSC and DSC. Orange symbols – data for SHU09; red symbols – data for SHU10; green symbols – data for SHU11; purple symbols – data for SHU12; blue symbols – data for HAT5; cyan blue symbols – data for Tri11 taken from ref. 144; and gray symbols – data for THA11 taken from ref. 144. Triangles –  $\alpha_1$ -relaxations (BDS); open pentagons –  $\alpha_2$ -relaxation (SHS); open circles –  $\alpha_2$ -relaxation (BDS); filled squares –  $\gamma$ -relaxations (BDS); open stars –  $\alpha_1$ -relaxations (FSC); and filled stars – thermal glass transition temperatures (DSC). Solid lines are the fits of VFT-equation (eqn. (2)) to the data. Dashed lines are the fits of the Arrhenius-equation (eqn. (1)) to the data.

**Table S1.** VFT parameters and activation energies obtained from VFT- and Arrhenius-equations fits

Compound	Process	Dependence	$\log(f_\infty [\text{Hz}])$	$T_0 [\text{K}]$	$E_A [\text{kJ mol}^{-1}]$
SHU09	$\alpha_1$	VFT	$9.1 \pm 0.1$	$184.5 \pm 1.2$	-
	$\alpha_2$	VFT	$12.0 \pm 0.3$	$91.2 \pm 2.2$	-
	$\gamma$	Arrhenius	$12.0 \pm 0.1$	-	$19.2 \pm 0.1$
SHU10	$\alpha_1$	VFT	$9.0 \pm 0.2$	$172.5 \pm 1.3$	-
	$\alpha_2$	VFT	$10.8 \pm 0.1$	$93.5 \pm 1.4$	-
	$\gamma$	Arrhenius	$11.7 \pm 0.1$	-	$17.0 \pm 0.3$
SHU11	$\alpha_1$	VFT	$12.0 \pm 0.3$	$163.3 \pm 4.7$	-
	$\alpha_2$	VFT	$10.3 \pm 0.1$	$114.8 \pm 0.4$	-
	$\gamma$	Arrhenius	$9.1 \pm 0.2$	-	$11.9 \pm 0.6$
SHU12	$\alpha_1$	VFT	$12.0 \pm 1.3$	$190.5 \pm 11.6$	-
	$\alpha_2$	VFT	$12.0 \pm 0.9$	$73.1 \pm 7.5$	-
	$\gamma$	Arrhenius	$13.1 \pm 0.4$	-	$25.6 \pm 1.0$
HAT5	$\alpha_1$	VFT	$12.0 \pm 1.0$	$147.5 \pm 9.3$	-
	$\alpha_2$	VFT	$10.2 \pm 1.1$	$85.8 \pm 12.2$	-
	$\gamma$	Arrhenius	$13.6 \pm 0.1$	-	$26.1 \pm 0.2$

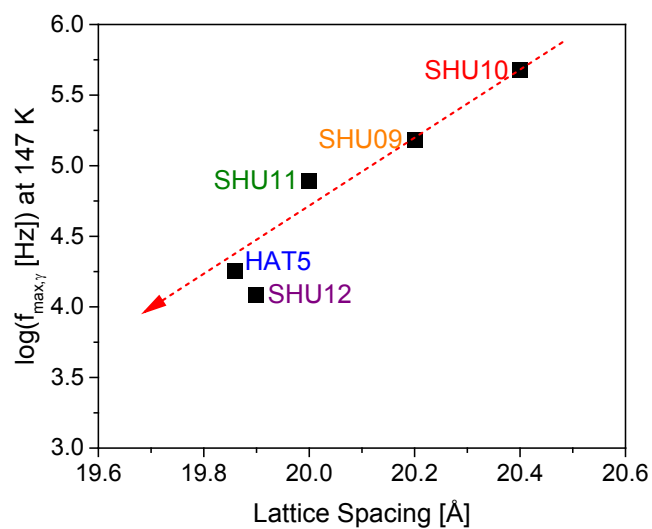


**Figure S25.** Relaxation rates of  $\gamma$ -processes at 147 K versus lattice spacing for SHU09-SHU12 and HAT5 as indicated. The arrow is a guide for the eye.

### Fast Scanning Calorimetry (FSC)

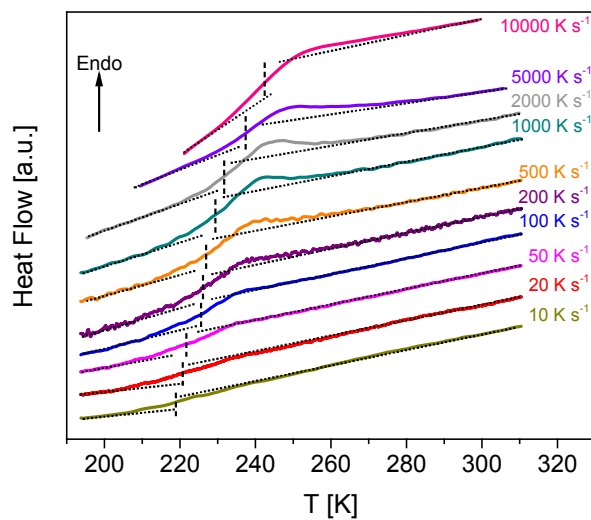


**Figure S26.** FSC thermograms of SHU09 for heating runs at different heating rates as indicated. Dashed lines indicate the thermal glass transition temperatures estimated.

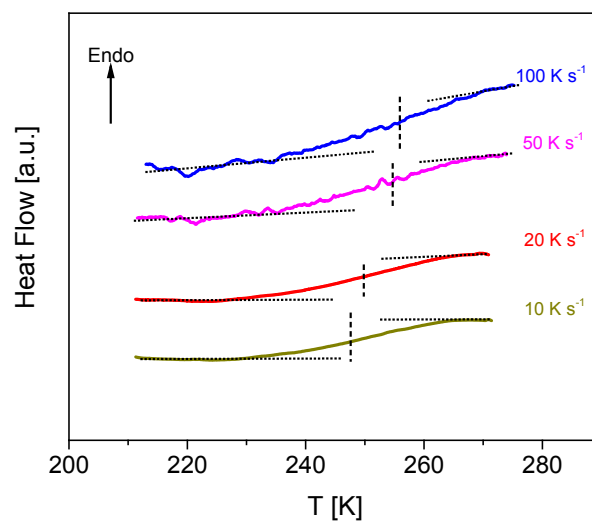


**Figure S27.** FSC thermograms of **SHU11** for heating runs at different heating rates as indicated. Dashed lines indicate the thermal glass transition temperatures estimated.

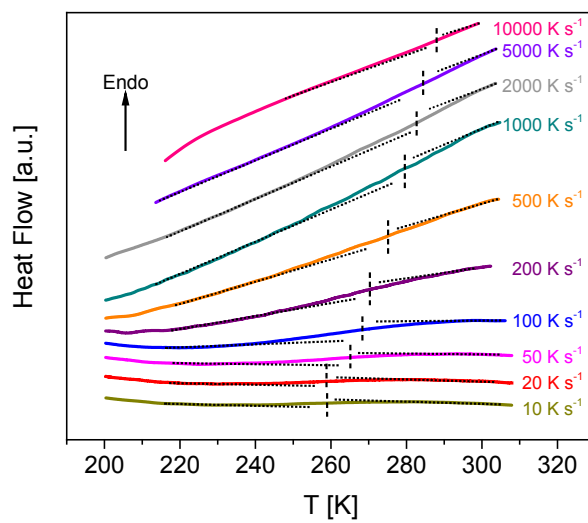


**Figure S28.** FSC thermograms of **SHU12** for heating runs at different heating rates as indicated. Dashed lines indicate the thermal glass transition temperatures estimated.

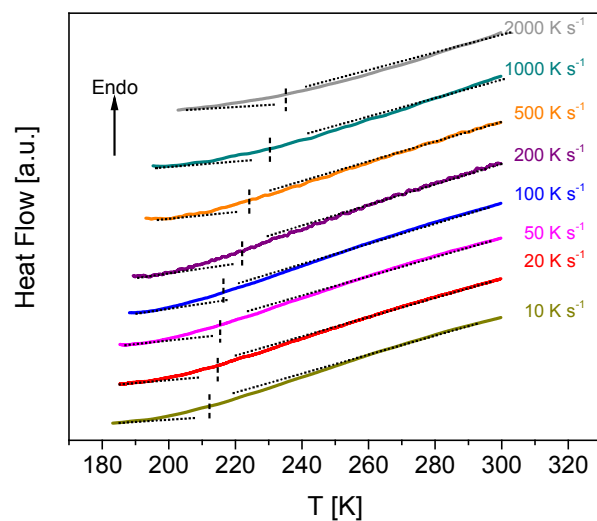


**Figure S29.** FSC thermograms of **HAT5** for heating runs at different heating rates as indicated. Dashed lines indicate the thermal glass transition temperatures estimated.

## APPENDIX III – Supporting Information for Section 4.2

**Table S2.** VFT parameters and activation energies obtained from VFT- and Arrhenius-equations fits

Compound	Process	Dependence	$\log(f_\infty [\text{Hz}])$	$T_0 [\text{K}]$	$E_A [\text{kJ mol}^{-1}]$
<b>KAL465</b>	$\alpha_1$	VFT	$8.1 \pm 0.2$	$240.3 \pm 5.7$	-
	$\alpha_2$	VFT	$12.0 \pm 2.5$	$141.5 \pm 24.3$	-
	$\gamma$	Arrhenius	$13.9 \pm 0.1$	-	$29.2 \pm 0.0$
<b>KAL468</b>	$\alpha_1$	VFT	$8.0 \pm 0.3$	$226.0 \pm 14.9$	-
	$\alpha_2$	VFT	$12.0 \pm 1.2$	$116.5 \pm 16.2$	-
	$\gamma$	Arrhenius	$13.1 \pm 0.1$	-	$28.2 \pm 0.1$

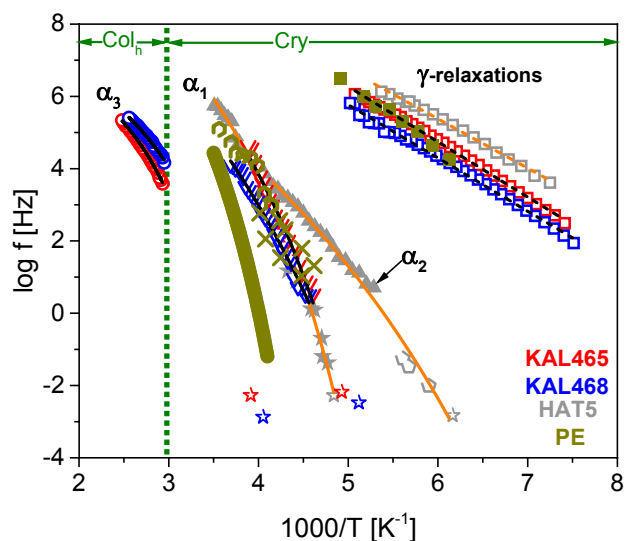


**Figure S30.** Combined relaxation map of **KAL465**, **KAL468** and **HAT5**. The data for **HAT5** taken from the research work presented in *Section 4.1*. Red symbols – data for **KAL465**; blue symbols – data for **KAL468**; and gray symbols – data for **HAT5**. Open triangles –  $\alpha_1$ -relaxations (BDS); Filled triangles –  $\alpha_2$ -relaxation (BDS); open squares –  $\gamma$ -relaxations (BDS); filled stars –  $\alpha_1$ -relaxations (FSC); open pentagons –  $\alpha_2$ -relaxation (SHS); and open stars – thermal glass transition temperatures (DSC). Black and orange solid lines are the fits of VFT-equation (eqn. (2)) to the data for **KAL** compounds and **HAT5** respectively. Black and orange dashed lines are the fit of the Arrhenius-equation (eqn. (1)) to the data for **KAL** compounds and **HAT5** respectively. Dark yellow filled circles denote the dielectric  $\alpha$ -relaxation of polyethylene taken from ref. 145. Dark yellow hexagons symbolize the dielectric  $\gamma$ -relaxation of polyethylene taken from ref. 40. Black crosses represent the calorimetric  $\alpha$ -relaxation of polyethylene taken from ref. 146. Black open hexagons symbolize the dielectric  $\beta$ -relaxation of poly(n-decyl methacrylate) taken from ref. 147.

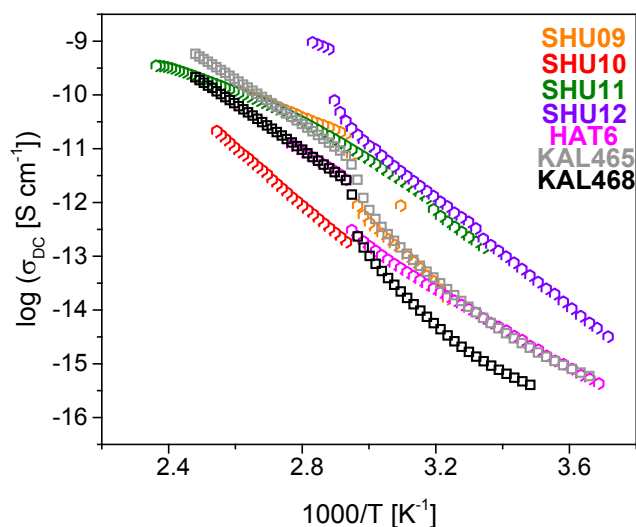


**Figure S31.** Temperature dependencies of the  $\sigma_{DC}$  given for second heating run for different DLCs as indicated.

## APPENDIX IV – Supporting Information for Section 4.3

### Havriliak-Negami (HN) function to the experimental data

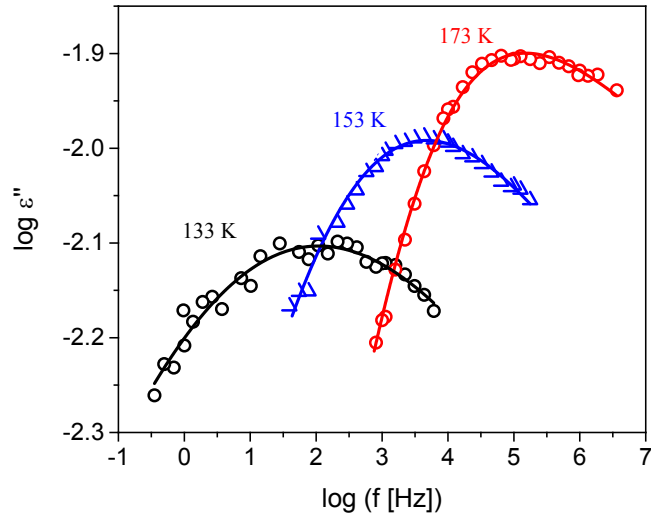


**Figure S32.** Frequency dependency of dielectric loss of LC537 for the second heating at different temperatures as indicated. Solid lines denote the fit by the HN-function to the corresponding data.

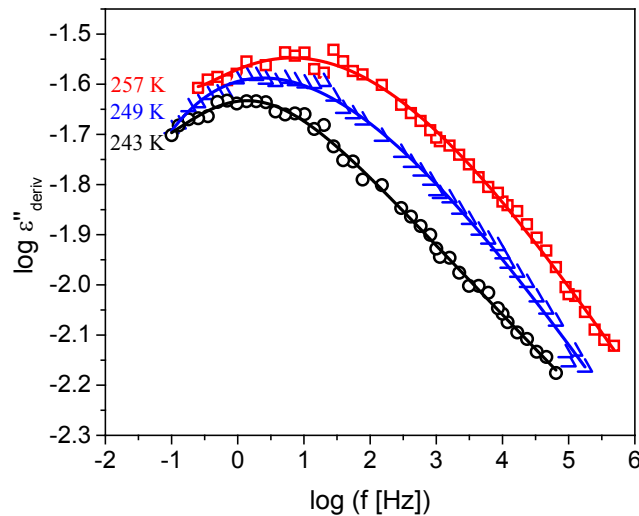


**Figure S33.** Frequency dependency of  $\epsilon''_{deriv}$  of LC537 for the second heating at the indicated temperatures ( $\alpha$ -process). Solid lines are the fits of the HN-function given in eqn. (19) to the data.

## Additional experimental results

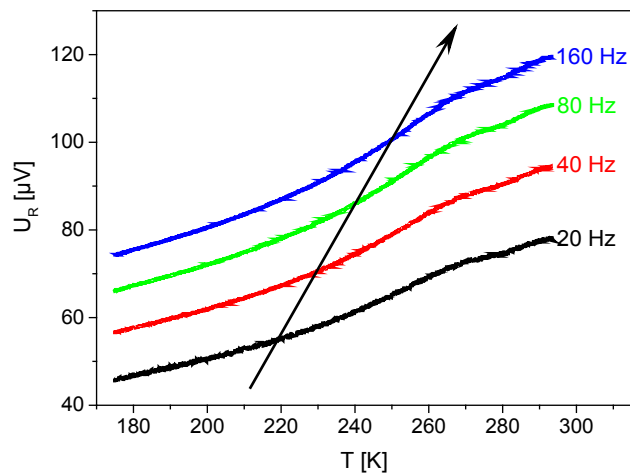


**Figure S34.** Temperature dependence of the real part of the complex differential voltage of **LC537** during the cooling run at different frequencies as indicated. Black arrow - guide for the eyes.

## Fitting parameters of VFT- and Arrhenius-equations fitting to the conductivity data

VFT parameters and activation energies estimated from the fittings to the conductivity processes probed by BDS is given in Table S1. It is worth to note that the VFT fitting parameters are given only for the cooling runs due to the broader temperature range obtained for the  $\sigma_{DC}$  values for the cooling runs. Moreover,  $\log(\sigma_{\infty} [\text{S cm}^{-1}])$  was fixed to 1.3 for the cooling run of **LC537** since the broader temperature range is obtained for the  $\sigma_{DC}$  values for **LC536**, and  $\log(\sigma_{\infty} [\text{Hz}])$  was found to be  $1.3 \pm 0.2$  from free fitting of VFT-equation (eqn. (2)) to the data for **LC536**.

**Table S3.** VFT parameters and activation energies estimated from the fittings to the BDS data. To reduce the number of free fit parameters,  $\log(\sigma_{\infty} [\text{Hz}])$  was fixed to 1.3 for **LC537**.

Compound	Run	VFT (Col <sub>h</sub> phase)		Arrhenius (Cry <sub>l</sub> phase)	
		$\log(\sigma_{\infty} [\text{S cm}^{-1}])$	$T_0$ [K]	$\log(\sigma_{\infty} [\text{S cm}^{-1}])$	$E_A$ [kJ mol <sup>-1</sup> ]
<b>LC536</b>	1 <sup>st</sup> Heating	-	-	$2.4 \pm 0.4$	$87 \pm 2$
	1 <sup>st</sup> Cooling	$1.3 \pm 0.2$	$179 \pm 3$	$2.3 \pm 0.6$	$87 \pm 3$
	2 <sup>nd</sup> Heating	-	-	$2.6 \pm 0.4$	$89 \pm 3$
<b>LC537</b>	1 <sup>st</sup> Heating	-	-	$1.3 \pm 0.6$	$85 \pm 5$

	1 <sup>st</sup> Cooling	1.3	168 ± 2	1.2 ± 0.5	83 ± 3
	2 <sup>nd</sup> Heating	-	-	1.2 ± 0.3	84 ± 2

## APPENDIX V – Supporting Information for Chapter 5

### Phase Behavior Under Confinement by DSC

ODPA modifications of the nanopores causes ca. 4.4 nm decrease in the diameter of the pores for the empty membranes. Nevertheless, thickness of the ODPA-modification could not be measured for the **HAT6** filled coated pores. Therefore, Figure S35 shows the dependencies of the phase transitions temperatures and enthalpies on inverse pore size, considering the narrowing of the pore size for ODPA-modified samples. Comparing the dependencies shown in Figure 52 and Figure S35, it is concluded that the pore narrowing has no considerable effect on our discussions based on these dependencies.

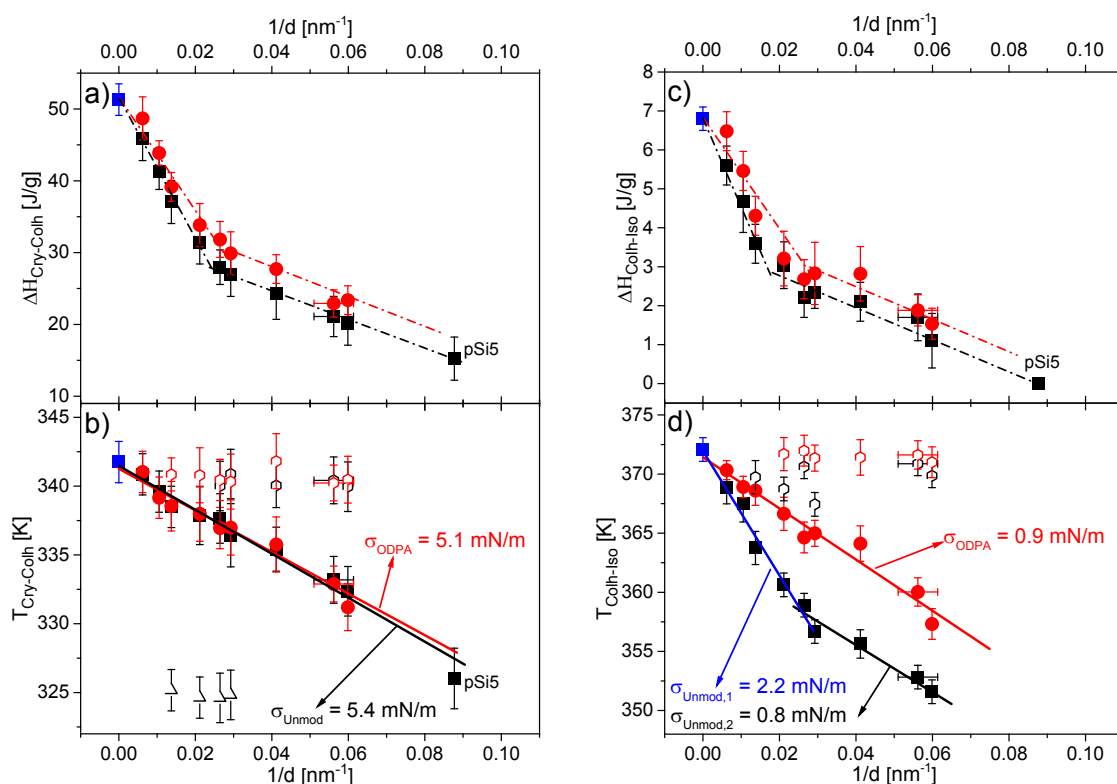


**Figure S35.** Inverse pore size dependencies of the phase transition enthalpies for (a) the Cry-Colh transition and (c) the Colh-Iso transition, as well as that of the phase transition temperatures for (b) the Cry-Colh transition and (d) the Colh-Iso transition. Blues squares indicate data for bulk **HAT6**, black symbols indicate data for **HAT6** confined into unmodified membranes and red symbols indicate data for **HAT6** confined into ODPA-modified membranes (filled circles: main peak, open symbols: satellite peak). Dashed-dotted lines are guide for eyes. Solid lines are the fits of eqn. (32) to the dependencies.

### Collective Orientational Order by DS

DS investigations showed unusually the phase transition takes place in several steps for **HAT6** confined into the ODPA-modified nanopores of AAO membrane with a pore size of 47 nm. Therefore, the DS result for these samples is represented in Figure S36 in order to show the steps clearly.

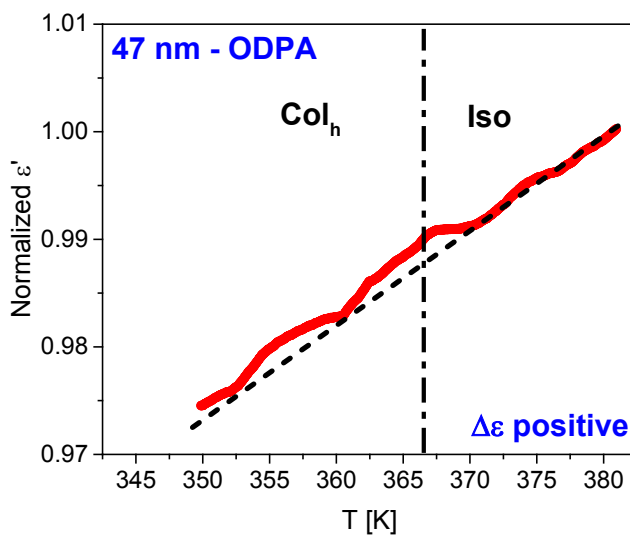


**Figure S36.** Normalized dielectric permittivities as a function of temperature during the third heating run for the sample with a pore size of 47 nm with modified pore walls. The dashed-dotted lines indicate the  $Col_h$ - $Iso$  phase transition temperatures determined by DSC. The dashed lines represent temperature dependencies of  $\epsilon'$  extrapolated from  $Col_h$  and  $Iso$  phases.

In some cases from the overview given in Figure 11 it is hard to detect whether  $\Delta\epsilon$  is positive or negative. Therefore, enlarged figures are prepared for some sample and given in Figure S6-Figure S41.

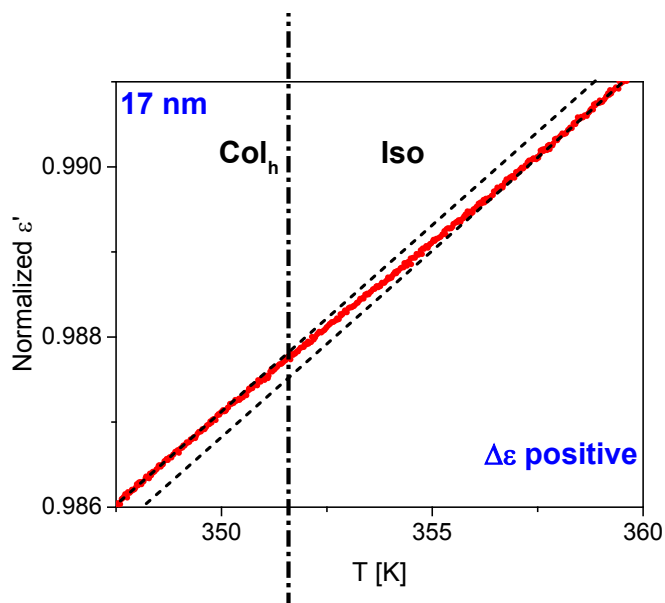


**Figure S37.** Normalized dielectric permittivities as a function of temperature during the third heating run for the sample with a pore size of 17 nm with unmodified pore walls. The dashed-dotted lines indicate the Col<sub>h</sub>-Iso phase transition temperatures determined by DSC. The dashed lines represent temperature dependencies of  $\epsilon'$  extrapolated from Col<sub>h</sub> and Iso phases.

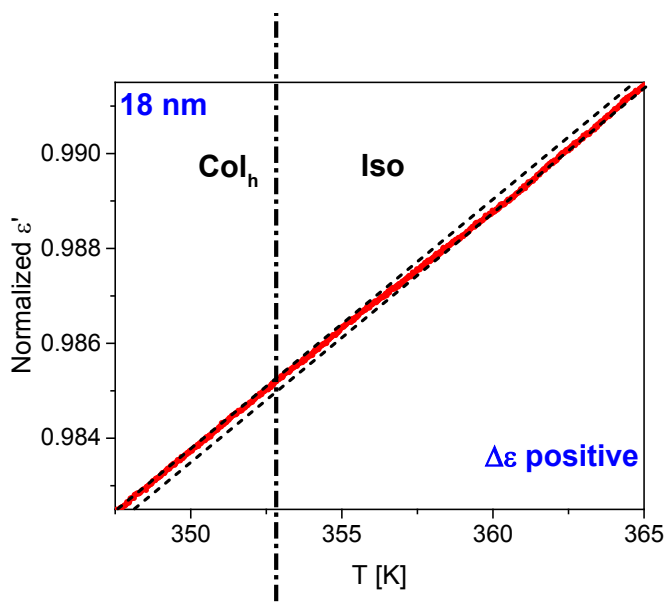


**Figure S38.** Normalized dielectric permittivities as a function of temperature during the third heating run for the sample with a pore size of 18 nm with unmodified pore walls. The dashed-dotted lines indicate the Col<sub>h</sub>-Iso phase transition temperatures determined by DSC. The dashed lines represent temperature dependencies of  $\epsilon'$  extrapolated from Col<sub>h</sub> and Iso phases.

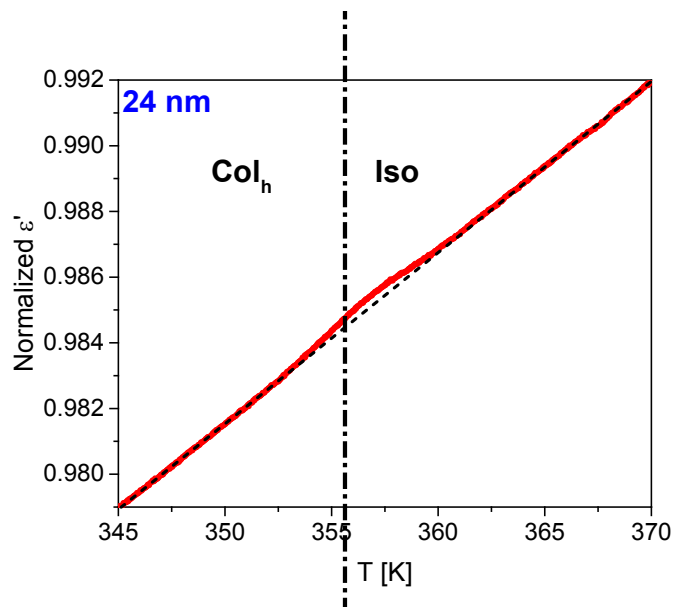


**Figure S39.** Normalized dielectric permittivities as a function of temperature during the third heating run for the sample with a pore size of 24 nm with unmodified pore walls. The dashed-dotted lines indicate the Col<sub>h</sub>-Iso phase transition temperatures determined by DSC. The dashed lines represent temperature dependencies of  $\epsilon'$  extrapolated from Col<sub>h</sub> and Iso phases.

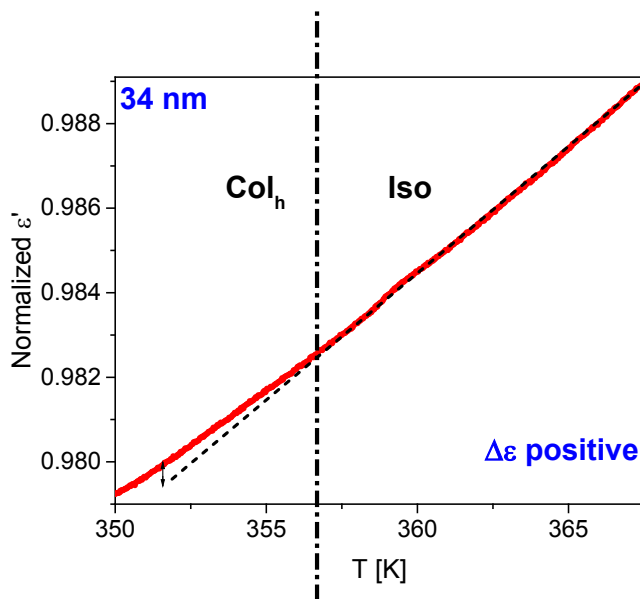


**Figure S40.** Normalized dielectric permittivities as a function of temperature during the third heating run for the sample with a pore size of 34 nm with unmodified pore walls. The dashed-dotted lines indicate the Col<sub>h</sub>-Iso phase transition temperatures determined by DSC. The dashed lines represent temperature dependencies of  $\epsilon'$  extrapolated from Col<sub>h</sub> and Iso phases.

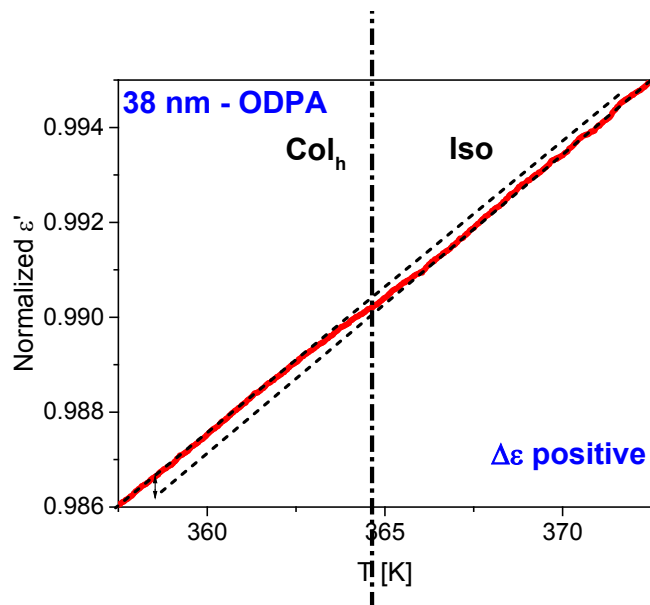


**Figure S41.** Normalized dielectric permittivities as a function of temperature during the third heating run for the sample with a pore size of 38 nm with modified pore walls. The dashed-dotted lines indicate the Col<sub>h</sub>-Iso phase transition temperatures determined by DSC. The dashed lines represent temperature dependencies of  $\epsilon'$  extrapolated from Col<sub>h</sub> and Iso phases.

## APPENDIX VI

### List of Abbreviations, Symbols and Constants

#### List of Abbreviations

LC	Liquid crystals
CLC	Columnar liquid crystal
DLC	Discotic liquid crystal
ILC	Ionic liquid crystal
BDS	Broadband dielectric spectroscopy
SHS	Specific heat spectroscopy
FSC	Fast scanning calorimetry
DSC	Differential scanning calorimetry
TMDSC	Temperature modulated differential scanning calorimetry
SSDSC	StepScan differential scanning calorimetry
1D	One dimensional
2D	Two dimensional
3D	Three dimensional
POM	Polarizing optical microscopy
XRD	X-ray diffraction
TGA	Thermogravimetric analysis
FTIR	Fourier transform infrared spectroscopy
ATR	Attenuated total reflection
SAXS	Small angle X-ray Scattering
WAXS	Wide angle X-ray Scattering
MAUS	Multi-scale analyzer for ultrafine structures
MALDI-TOF	Matrix-assisted laser desorption/ionization-time of flight
LRT	Linear response theory
<b>HAT6</b>	Hexakis(hexyloxy)triphenylene
<b>HAT5</b>	Hexakis(pentyloxy)triphenylene
<b>HATn</b>	Hexakis(n-alkyloxy)triphenylenes
<b>SHU09</b>	Pentapentyloxytriphenylene carrying ethyl glycolate unit
<b>SHU10</b>	Pentapentyloxytriphenylene carrying hexanoyl unit
<b>SHU11</b>	Pentapentyloxytriphenylene carrying trifluoromethyl unit
<b>SHU12</b>	Pentapentyloxytriphenylene carrying ethyl diethyleneglycol unit
<b>KAL465</b>	Triphenylene crown ethers-based unsymmetrical discotic liquid crystal having alkyl chains consist of 9 carbons
<b>KAL468</b>	Triphenylene crown ethers-based unsymmetrical discotic liquid crystal having alkyl chains consist of 12 carbons

<b>LC536</b>	Linear shaped tetramethylated guanidinium-based ionic liquid crystal with counteranion triflate having alkyl chains consist of 14 carbons
<b>LC537</b>	Linear shaped tetramethylated guanidinium-based ionic liquid crystal with counteranion triflate having alkyl chains consist of 16 carbons
<b>OTf</b>	Triflate anion
<b>PE</b>	Polyethylene
<b>AAO</b>	Anodic aluminum oxide
<b>OPA</b>	n-Octylphosphonic acid
<b>ODPA</b>	n-Octadecylphosphonic acid
<b>Cry</b>	Plastic crystalline
<b>Col<sub>h</sub></b>	Hexagonal columnar
<b>Iso</b>	Isotropic
<b>DC</b>	Direct current

### List of Symbols

<b>D</b>	Dielectric displacement
$\epsilon^*$	Complex dielectric function
$\epsilon'$	Real part of the complex dielectric function
$\epsilon''$	Imaginary part of the complex dielectric function
$\epsilon''_{deriv}$	Conduction-free dielectric loss
<b>E</b>	Electric field
<b>P</b>	Polarization
$\chi^*$	Complex dielectric susceptibility
$\omega$	Angular frequency
$f$	Frequency
$\delta$	Phase shift
$\tau$	Relaxation time
$\Delta\epsilon$	Dielectric strength
<b>H</b>	Enthalpy
$c_p$	Specific heat capacity
$\Delta c_p$	Change in specific heat capacity
$c_p^*$	Complex specific heat
$c_p'$	Real part of the complex specific heat
$c_p''$	Imaginary part of the complex specific heat
$C^*(\omega)$	Complex capacitance of the capacitor filled with the material
$U_R$	Real part of the complex differential voltage
<b>T</b>	Temperature
$T_{Colh-Iso}$	Phase transition temperature from hexagonal columnar mesophase to isotropic phase

$T_{\text{Cry-Colh}}$	Phase transition temperature from plastic crystalline phase to hexagonal columnar mesophase
$C_s$	Heat capacity of the sample
$T_g^{\text{thermal}}$	Thermal glass transition temperature
$T_g^{\text{dynamic}}$	Dynamic glass transition temperature
$T_0$	Vogel or ideal glass transition temperature
$\Delta T_g$	Width of the glass transition
$\dot{T}$	Heating/cooling rate
$\sigma^*$	Complex conductivity
$\sigma'$	Real part of the complex conductivity
$\sigma''$	Imaginary part of the complex conductivity
$\sigma_{DC}$	Direct current conductivity

### List of Constants

$\epsilon_0$	Dielectric permittivity constant in vacuum ( $\epsilon_0 = 8.854 \cdot 10^{-12} \text{ A sV}^{-1}\text{m}^{-1}$ )
R	Ideal gas constant ( $R = 8.314 \text{ J mol}^{-1}\text{K}^{-1}$ )

### List of Peer-Reviewed Publications

1. **A. Yildirim**, P. Szymoniak, K. Sentker, M. Butschies, A. Bühlmeyer, P. Huber, S. Laschat, A. Schönhals, Dynamics and ionic conductivity of ionic liquid crystals forming a hexagonal columnar mesophase. *Phys.Chem.Chem.Phys.* **2018**, 20, 5626–5635.
2. K. Sentker, A. W. Zantop, M. Lippmann, T. Hofmann, O. H. Seeck, A. V. Kityk, **A. Yildirim**, A. Schönhals, M. G. Mazza, P. Huber, Quantized self-assembly of discotic rings in a liquid crystal confined in nanopores, *Phys. Rev. Lett.* **2018**, 120, 067801.
3. **A. Yildirim**, K. Sentker, G. J. Smales, B. R. Pauw, P. Huber, A. Schönhals, Collective orientational order and phase behavior of a discotic liquid crystal under nanoscale confinement. *Nanoscale Adv.* **2019**, 1, 1104–1116.
4. **A. Yildirim**, A. Bühlmeyer, S. Hayashi, J. C. Haenle, K. Sentker, C. Krause, P. Huber, S. Laschat, A. Schönhals, Multiple glassy dynamics in dipole functionalized triphenylene-based discotic liquid crystals revealed by broadband dielectric spectroscopy and advanced calorimetry – Assessment of the molecular origin. *Phys. Chem. Chem. Phys.* **2019**, 21, 18265–18277.

5. K. Sentker, **A. Yildirim**, M. Lippmann, A. W. Zantop, F. Bertram, O. H. Seeck, M. G. Mazza, T. Hofmann, A. V. Kityk, A. Schönhals, P. Huber, Self-assembly of liquid crystals in nanoporous solids for adaptive photonic metamaterials. The manuscript submitted to *Nanoscale*, **2019**.
6. **A. Yildirim**, K. Sentker, C. Krause, P. Huber, S. Laschat, A. Schönhals, Phase behavior dynamics and conductivity of triphenylene crown ether-based discotic liquid crystals. The manuscript in preparation **2019**.

## List of Talks

1. **A. Yildirim**, A. Bühlmeier, S. Hayashi, J. C. Haenle, K. Sentker, C. Krause, P. Huber, S. Laschat, A. Schönhals, Molecular dynamics of dipole functionalized triphenylene-based discotics, *Spring Meetings, German Physics Society (DPG)*, Regensburg, Germany, **2019**.
2. **A. Yildirim**, P. Szymoniak, K. Sentker, P. Huber, A. Schönhals, Molecular mobility and ionic conductivity of ionic liquid crystals forming a hexagonal columnar mesophase, *10th Conference on Broadband Dielectric Spectroscopy and its Application*, Brussels, Belgium, **2018**.
3. **A. Yildirim**. Liquid Crystals Forming a Columnar Mesophase: Structure, Dynamics and Electric Conductivity. Technische Universität Berlin, Berlin, Germany, **2018**.
4. **A. Yildirim**, P. Szymoniak, K. Sentker, M. Butschies, A. Bühlmeier, P. Huber, S. Laschat, A. Schönhals, Molecular mobility and ionic conductivity of ionic liquid crystals forming a hexagonal columnar mesophase, *Spring Meetings, German Physics Society (DPG)*, Berlin, Germany, **2018**.
5. **A. Yildirim**, K. Sentker, P. Huber, A. Schönhals, structure, dynamics and phase behavior of a discotic liquid crystal confined in nanoporous anodic aluminum oxide membranes, *Spring Meetings, German Physics Society (DPG)*, Dresden, Germany, **2017**
6. A. Schönhals, **A. Yildirim**, C. Krause, Dielectric relaxation of discotic liquid crystals, *16th International Symposium on Electretes*, Leuven, Belgium, **2017**.
7. **A. Yildirim**. Structure, dynamics and phase behavior of bulk and confined liquid crystals, *Universität Stuttgart*, Stuttgart, Germany, **2017**.

## List of Posters

1. **A. Yildirim**, P. Szymoniak, K. Sentker, M. Butschies, A. Bühlmeier, P. Huber, S. Laschat, A. Schönhals, Molecular dynamics of dipole functionalized triphenylene-based discotics, *10th Conference on Broadband Dielectric Spectroscopy and its Application*, Brussels, Belgium, **2018**.
2. **A. Yildirim**, K. Sentker, P. Huber, A. Schönhals, Collective orientational order and phase behavior of a discotic liquid crystal under confinement, *10th Conference on Broadband Dielectric Spectroscopy and its Application*, Brussels, Belgium, **2018**.
3. **A. Yildirim**, K. Sentker, P. Huber, A. Schönhals, Collective orientational order and phase behavior of a discotic liquid crystal under confinement, *Spring Meetings, German Physics Society (DPG)*, Berlin, Germany, **2018**.
4. **A. Yildirim**, K. Sentker, P. Huber, A. Schönhals, Structure, dynamics and phase behavior of a discotic liquid crystal confined in nanoporous anodic aluminum oxide membranes, *9<sup>th</sup> International Conference on Porous Media & Annual Meeting*, Rotterdam, The Netherlands, **2017**.
5. **A. Yildirim**, K. Sentker, P. Huber, A. Schönhals, Structure, dynamics and phase behavior of a discotic liquid crystal confined in nanoporous anodic aluminum oxide membranes, *10<sup>th</sup> Liquid Matter Conference*, Ljubljana, Slovenia, **2017**.
6. K. Sentker, **A. Yildirim**, A. W. Zantop, M. Lippmann, T. Hofmann, O. H. Seeck, A. V. Kityk, M. G. Mazza, A. Schönhals, P. Huber, Characterization of the thermotropic phase behavior and microscopic structure of a confined discotic liquid crystal, *10<sup>th</sup> Liquid Matter Conference*, Ljubljana, Slovenia, **2017**.
7. K. Sentker, **A. Yildirim**, M. Lippmann, T. Hofmann, O. H. Seeck, A. V. Kityk, A. Schönhals, P. Huber, Fabrication of organic nanowires by melt infiltration of a discotic liquid crystal: A combined X-ray diffraction and optical birefringence study, *Spring Meetings, German Physics Society (DPG)*, Dresden, Germany, **2017**.
8. **A. Yildirim**, K. Sentker, A. V. Kityk, P. Huber, A. Schönhals, Structure and dynamics of 2,3,6,7,10,11-hexakis[hexyloxy] triphenylene in nanoporous anodic aluminum oxide membranes, *10th Conference on Broadband Dielectric Spectroscopy and its Application*, Pisa, Italy, **2016**.

9. **A. Yildirim**, K. Sentker, A. V. Kityk, P. Huber, A. Schönhals, Structure and dynamics of 2,3,6,7,10,11-hexakis[hexyloxy] triphenylene in nanoporous anodic aluminum oxide membranes, *Spring Meetings, German Physics Society (DPG)*, Regensburg, Germany, **2016**.
10. K. Sentker, **A. Yildirim**, K. Knopp, A. Schönhals, P. Huber, Columnar axial orientation of discotic liquid crystals in nanoporous solids, *Spring Meetings, German Physics Society (DPG)*, Regensburg, Germany, **2016**.

## References

- <sup>1</sup> J. L. Bredas, S. R. Marder and W. R. Salaneck, *Macromolecules* **2002**, 35, 1137–1139.
- <sup>2</sup> S. M. Said, M. S. Mahmood, M. N. Daud, M. F. Mohd Sabri and N. A. Sairi, *Liq. Cryst.* **2016**, 31, 1–22.
- <sup>3</sup> B. R. Kaafarani, *Chem. Mater.* **2011**, 23, 378–396.
- <sup>4</sup> S. Laschat, A. Baro, N. Steinke, F. Giesselmann, C. Hägele, G. Scalia, R. Judele, E. Kapatsina, S. Sauer, A. Schreivogel and M. Tosoni, *Angew. Chem. Int. Edit.* **2007**, 46, 4832–4887.
- <sup>5</sup> S. Sergeev, W. Pisula and Y. H. Geerts, *Chem. Soc. Rev.*, 2007, **36**, 1902–1929.
- <sup>6</sup> F. M. Mulder, J. Stride, S. J. Picken, P. H. J. Kouwer, M. P. De Haas, L. D. A. Siebbeles and G. J. Kearley, *J. Am. Chem. Soc.* **2003**, 125, 3860–3866.
- <sup>7</sup> G. Cinacchi, R. Colle and A. Tani, *J. Phys. Chem. B* **2004**, 108, 7969–7977.
- <sup>8</sup> T. Wöhrle, I. Wurzbach, J. Kirres, A. Kostidou, N. Kapernaum, J. Littscheidt, J. C. Haenle, P. Staffeld, A. Baro, F. Giesselmann and S. Laschat, *Chem. Rev.*, 2016, 116, 1139–1241.
- <sup>9</sup> H. K. Bisoyi and Q. Li, *Prog. Mater. Sci.* **2019**, 104, 1–52.
- <sup>10</sup> J. W. Goodby, P. J. Collings, T. Kato, C. Tschierske, H. F. Gleeson and P. Raynes, *Handbook of Liquid Crystals*, Wiley-VCH, Weinheim, **2014**.
- <sup>11</sup> S. Singh and D. A. Dunmur, *Liquid Crystals: Fundamentals*, World Scientific, 2002.
- <sup>12</sup> K. Binnemans, *Chem. Rev.* **2005**, 105, 4148–4204.
- <sup>13</sup> T. Kato, M. Yoshio, T. Ichikawa, B. Soberats, H. Ohno and M. Funahashi, *Nat. Rev. Mater.* **2017**, 2, 17001.
- <sup>14</sup> H. K. Bisoyi and S. Kumar, *Chem. Soc. Rev.* **2010**, 39, 264–285.
- <sup>15</sup> J. L. De Bougrenet de la Tocnaye, *Liq. Cryst.* **2004**, 31, 241–269.
- <sup>16</sup> A. Hussain, A. S. Pina and A. C. A. Roque, *Biosens. Bioelectron.* **2009**, 25, 1–8.
- <sup>17</sup> C. Ohm, M. Brehmer and R. Zentel, *Adv. Mater.* **2010**, 22, 3366–3387.
- <sup>18</sup> J. P. F. Lagerwall and G. Scalia, *Curr. Appl. Phys.* **2012**, 12, 1387–1412.
- <sup>19</sup> M. B. Pandeya, R. Dharb and V. K. Wadhawan, *Phase Transi.* **2009**, 82, 831–849.
- <sup>20</sup> S. Chandrasekhar, B. K. Sadashiva and K. A. Suresh, *Pramana J. Phys.* **1977**, 9, 471–480.
- <sup>21</sup> C. Krause, R. Zorn, F. Emmerling, J. Falkenhagen, B. Frick, P. Huber and A. Schönhal, *Phys. Chem. Chem. Phys.* **2014**, 16, 7324–7333.
- <sup>22</sup> M. Beiner, H. Huth, *Nat. Mater.* **2003**, 2, 595–599.
- <sup>23</sup> S. Pankaj, M. Beiner, *Soft Matter* **2010**, 6, 3506–3516
- <sup>24</sup> T. Babur, J. Balko, H. Budde, M. Beiner, *Polymer* **2014**, 55, 6844–6852.
- <sup>25</sup> A. Yildirim, K. Sentker, G. J. Smales, B. R. Pauw, P. Huber and A. Schönhal, *Nanoscale Adv.* **2019**, 1, 1104–1116.
- <sup>26</sup> V. De Cupere, J. Tant, P. Viville, R. Lazzaroni, W. Osikowicz, W. R. Salaneck and Y. H. Geerts, *Langmuir* **2006**, 22, 7798–7806.
- <sup>27</sup> M. Kumar and S. Kumar, *Polym. J.* **2017**, 49, 85–111.
- <sup>28</sup> B. R. Kaafarani, *Chem. Mater.* **2011**, 23, 378–396.
- <sup>29</sup> N. Boden, R. J. Bushby, J. Clements and B. Movaghar, *J. Mater. Chem.* **1999**, 9, 2081–2086.
- <sup>30</sup> L. Schmidt-Mende, A. Fechtenkötter, K. Müllen, E. Moons, R. H. Friend and J. D. MacKenzie, *Science* **2001**, 293, 1119–1122.
- <sup>31</sup> A. V. Kityk, M. Busch, D. Rau, S. Calus, C. V. Cerclier, R. Lefort, D. Morineau, E. Grelet, C. Krause, A. Schönhal, B. Frick and P. Huber, *Soft Matter* **2014**, 10, 4522–4534.

- 
- <sup>32</sup> M. Ndao, R. Lefort, P. Huber, J.-M. Zanotti, B. Frick, A. Schönhals and D. Morineau, *Mater. Res. Soc. Symp. Proc.* **2011**, 1349.
- <sup>33</sup> C. Krause, H. Yin, C. Cerclier, D. Morineau, A. Wurm, C. Schick, F. Emmerling and A. Schönhals, *Soft Matter* **2012**, 8, 11115–11122.
- <sup>34</sup> H. Groothues, F. Kremer, P. G. Schouten and J. M. Warman, *Adv. Mater.* **1995**, 7, 283–286.
- <sup>35</sup> B. Glösen, A. Kettner, J. Kopitzke and J. H. Wendorff, *J. Non-Cryst. Solids* **1998**, 241, 113–120.
- <sup>36</sup> L. A. Haverkate, M. Zbiri, M. R. Johnson, E. Carter, A. Kotlewski, S. J. Picken, F. M. Mulder, G. J. Kearley, *J. Chem. Phys.* **2014**, 140, 014903.
- <sup>37</sup> M. M. Elmahdy, X. Dou, M. Mondeshki, G. Floudas, H. J. Butt, H. W. Spiess and K. Müllen, *J. Am. Chem. Soc.* **2008**, 130, 5311–5319.
- <sup>38</sup> P. Papadopoulos, C. Grigoriadis, N. Haase, H. J. Butt, K. Müllen, and G. Floudas, *J. Phys. Chem. B* **2011**, 115, 14919–14927.
- <sup>39</sup> M. M. Elmahdy, G. Floudas, M. Mondeshki, H. W. Spiess, X. Dou and K. Müllen, *Phys. Rev. Lett.* **2008**, 100, 107801.
- <sup>40</sup> Z. Yildirim, M. Wübbenhorst, E. Mendes, S. J. Picken, I. Paraschiv, A. T. M. Marcelis, H. Zuilhof and E. J. R. Sudhölter, *J. Non-Cryst. Solids* **2005**, 351, 2622–2628.
- <sup>41</sup> R. Brand, P. Lunkenheimer, A. Loidl, *J. Chem. Phys.* **2002**, 116, 10386–10401.
- <sup>42</sup> I. Tomatsu, C. F. C. Fitie, D. Byelov, W. H. de Jeu, P. C. M. M. Magusin, Michael Wübbenhorst, R. P. Sijbesma, *J. Phys. Chem. B* **2009**, 113, 14158–14164.
- <sup>43</sup> A. Yildirim, A. Bühlmeier, S. Hayashi, J. C. Haenle, K. Sentker, C. Krause, P. Huber, S. Laschat and A. Schönhals, *Phys. Chem. Chem. Phys.* **2019**, 21, 18265–18277.
- <sup>44</sup> K. Arakaw, *Liquid Crystal Display Having Positive and Negative Birefringent Compensator Films*, US005189538A, **1993**.
- <sup>45</sup> H. Mori and Y. Ito, *Liquid Crystal Display with Compensators Having Minimum Retardations in the Inclined Direction*, US005805253A, **1998**.
- <sup>46</sup> N. Boden, J. Clements and B. Movaghar, *Fluid Sensing Device Using Discotic Liquid Crystals*, US006423272B1, **2002**.
- <sup>47</sup> H. Haick, *Electronic Nose Device with Sensors Composed of Nanowires of Columnar Discotic Liquid Crystals with Low Sensitive to Humidity*, US20100191474A1, **2008**.
- <sup>48</sup> A. A. Khan, G. Rughoobur, M. A. Kamarudin, A. Sepe, J. A. Dolan, A. J. Flewitt, M. M. Qasim and T. D. Wilkinson, *Org. Electron.* **2016**, 36, 35–44.
- <sup>49</sup> L. A. Haverkate, M. Zbiri, M. R. Johnson, E. Carter, A. Kotlewski, S. Picken, F. M. Mulder and G. J. Kearley, *J. Chem. Phys.* **2014**, 140, 014903.
- <sup>50</sup> M. Kumar and S. Kumar, *Polym. J.* **2017**, 49, 85–111.
- <sup>51</sup> C. Krause, R. Zorn, B. Frick and A. Schönhals, *Colloid. Polym. Sci.* **2014**, 292, 1949–1960.
- <sup>52</sup> C. Krause and A. Schönhals, *J. Phys. Chem. C* **2013**, 117, 19712–19720.
- <sup>53</sup> C. Krause, R. Zorn, B. Frick and A. Schönhals, *EPJ Web Conf.* **2015**, 83, 02017.
- <sup>54</sup> K. Sentker, A. W. Zantop, M. Lippmann, T. Hofmann, O. H. Seeck, A. V. Kityk, A. Yildirim, A. Schönhals, M. G. Mazza and P. Huber, *Phys. Rev. Lett.*, **2018**, 120, 067801.
- <sup>55</sup> J. A. Rego, S. Kumar and H. Ringsdorf, *Chem. Mater.* **1996**, 8, 1402–1409.
- <sup>56</sup> P. T. Wright, T. Gilies and J. D. Kilburn, *Synthesis* **1997**, 1007–1009.
- <sup>57</sup> G. Cooke, G. Hell and S. Violini, *Synth. Commun.* **1997**, 27, 3745–3748.
- <sup>58</sup> a) S. Kumar and M. Manickam, *Synthesis* **1998**, 1119–1122. b) S. Kumar and M. Manickam, *Chem. Commun.* **1998**, 1427–1428.

- <sup>59</sup> S. J. Cross, J. W. Goodby, A. W. Hull, M. Hird, S. M. Kelly, K. J. Toyne and C. Wu, *Liq. Cryst.* **1998**, 25, 1–11.
- <sup>60</sup> Reviews on triphenylene liquid crystals: a) S. K. Pal, S. Setia, B. S. Avinash and S. Kumar, *Liq. Cryst.* **2013**, 40, 1769–1816. b) S. Kumar *Liq. Cryst.* **2005**, 32, 1089–1113. c) S. Kumar, *Liq. Cryst.* **2004**, 31, 1037–1059.
- <sup>61</sup> Selected recent work: a) J. Litterscheidt, P. Judge, A. Bühlmeier, K. Bader, J. S. Bandar, T. Lambert and S. Laschat, *Liq. Cryst.* **2018**, 45, 1250–1258. b) W. Xiao, Z. He, M. Xu, N. Wu, X. Kong and X. Jing, *Tetrahedron Lett.* **2015**, 56, 700–705. c) H. Wu, C. Zhang, J. Pai and Y. Wang, *Liq. Cryst.* **2014**, 41, 1173–1178. d) X. Kong, Z. He, H. Gopee, X. Jing and A. N. Cammidge, *Tetrahedron Lett.* **2011**, 52, 77–79. e) S. Sauer, N. Steinke, A. Baro, S. Laschat, F. Giesselmann and W. Kantlehner, *Chem. Mater.* **2008**, 20, 1909–1915.
- <sup>62</sup> K.-Q. Zhao, Y. Gao, W.-H. Yu, P. Hu, B.-Q. W. Wang, B. Heinrich and B. Donnio, *Eur. J. Org. Chem.* **2016**, 2802–2814.
- <sup>63</sup> H. Jung, J. Park, M. Choi, J. Kim, Y. H. Kim, E. Kim, M. H. Yi and J.-W. Ka, *Liq. Cryst.* **2017**, 44, 1069–1077.
- <sup>64</sup> N. Haase, C. Grigoriadis, H. J. Butt, K. Müllen and G. Floudas, *J. Phys. Chem. B* **2011**, 115, 5807–5814.
- <sup>65</sup> H. Suga, S. Seki, *J. Non-Cryst. Solids* **1974**, 16, 171–194.
- <sup>66</sup> L. M. Wang, R. Richert, *J. Chem. Phys.* **2004**, 121, 11170–11176.
- <sup>67</sup> B. Kuchta, M. Descamps, F. Affouard, *J. Chem. Phys.* **1998**, 109, 6753–6763.
- <sup>68</sup> S. Benkhof, T. Blochowicz, A. Kudlik, C. Tschirwitz, E. Rössler, *Ferroelectrics* **2000**, 236, 193–207.
- <sup>69</sup> P. Lunkenheimer, U. Schneider, R. Brand, A. Loidl, *Contemp. Phys.* **2000**, 41, 15–36.
- <sup>70</sup> M. Werth, S. U. Vallerien, and H. W. Spiess, *Liq. Cryst.* **1991**, 10, 759–770.
- <sup>71</sup> M. Steinhart, S. Zimmermann, P. Göring, A. K. Schaper, U. Gösele, C. Weder and J. H. Wendorff, *Nano Lett.*, **2005**, 5, 429–434.
- <sup>72</sup> P. Huber, *J. Phys.: Condens. Matter* **2015**, 27, 103102–103145.
- <sup>73</sup> S. Calus, A. V. Kityk and P. Huber, *Micropor. Mesopor. Mat.* **2014**, 197, 26–32.
- <sup>74</sup> C. V. Cerclier, M. Ndao, R. Busselez, R. Lefort, E. Grelet, P. Huber, A. V. Kityk, L. Noirez, A. Schönhals and D. Morineau, *J. Phys. Chem. C* **2012**, 116, 18990–18998.
- <sup>75</sup> S. Calus, A. V. Kityk, L. Borowik, R. Lefort, D. Morineau, C. Krause, A. Schönhals, M. Busch and P. Huber, *Phys. Rev. E* **2015**, 92, 012503.
- <sup>76</sup> R. Zhang, X. Zeng, B. Kim, R. J. Bushby, K. Shin, P. J. Baker, Vi. Percec, P. Leowanawat and G. Ungar, *ACS Nano* **2015**, 9, 1759–1766.
- <sup>77</sup> R. Zhang, G. Ungar, X. Zeng and Z. Shen, *Soft Matter* **2017**, 13, 4122–4131.
- <sup>78</sup> K. Goossens, K. Lava, C. W. Bielawski and K. Binnemans, *Chem. Rev.* **2016**, 116, 4643–4807.
- <sup>79</sup> K.V. Axenov and S. Laschat, *Materials* **2011**, 4, 206–259.
- <sup>80</sup> W. Dobbs, B. Heinrich, C. Bourgogne, B. Donnio, E. Terazzi, M. E. Bonnet, F. Stock, P. Erbacher, A. L. Bolcato-Bellemin and L. Douce, *J. Am. Chem. Soc.* **2009**, 131, 13338–13346.
- <sup>81</sup> J. H. Olivier, F. Camerel, G. Ulrich, J. Barberá and R. Ziessel, *Chem. Eur. J.* **2010**, 16, 7134–7142.
- <sup>82</sup> J. Motoyanagi, T. Fukushima and T. Aida, *Chem. Commun.* **2005**, 0, 101–103.
- <sup>83</sup> J. D. Martin, C. L. Keary, T. A. Thornton, M. P. Novotnak, J. W. Knutson and J. C. W. Folmer, *Nat. Mater.* **2006**, 5, 271–275.
- <sup>84</sup> J. H. Olivier, F. Camerel, J. Barberá and R. Ziessel, *Chem. Eur. J.* **2009**, 15, 8163–8174.

- <sup>85</sup> N. Steinke, M. Jahr, M. Lehmann, A. Baro, W. Frey, S. Tussetschlager, S. Sauer and S. Laschat, *J. Mater. Chem.* **2009**, 19, 645–654.
- <sup>86</sup> S. Yazaki, Y. Kamikawa, M. Yoshio, A. Hamasaki, T. Mukai, H. Ohno and T. Kato, *Chem. Lett.* **2008**, 37, 538–539.
- <sup>87</sup> J. J. Lee, A. Yamaguchi, Md. A. Alam, Y. Yamamoto, T. Fukushima, K. Kato, M. Takata, N. Fujita and T. Aida, *Angew. Chem. Int. Ed.* **2012**, 51, 8490–8494.
- <sup>88</sup> M. Yoshio, T. Mukai, H. Ohno and T. Kato, *J. Am. Chem. Soc.* **2004**, 126, 994–995.
- <sup>89</sup> M. Yoshio, T. Ichikawa, H. Shimura, T. Kagata, A. Hamasaki, T. Mukai, H. Ohno and T. Kato, *Bull. Chem. Soc. Jpn.* **2007**, 80, 1836–1841.
- <sup>90</sup> T. Kanaya, I. Rintaro, K. Kazuko, M. Tsukasa, T. Itaru, S. Kaoru, M. Go, N. Koji and H. Masahiro, *J. Phys. Soc. Jpn.*, **2009**, 78, 041004.
- <sup>91</sup> G. B. McKenna, S. L. Simon, In *Handbook of Thermal Analysis and Calorimetry*, ed. Cheng, Elsevier, Amsterdam, **2002**, vol. 3, p. 49–109.
- <sup>92</sup> F. H. Stillinger and P. G. Debenedetti, *Annu. Rev. Condens. Matter Phys.* **2013**, 4, 263–285.
- <sup>93</sup> E. Donth, Glasübergang, *Akademie-Verlag*, Berlin **1981**.
- <sup>94</sup> J. Mijović, H. Lee, J. Kenny and J. Mays, *Macromolecules* **2006**, 39, 2172–2182.
- <sup>95</sup> B. Frick and D. Richter, *Science* **1995**, 267, 1939–1945.
- <sup>96</sup> B. D. Fitz and J. Mijovic, *Macromolecules* **1999**, 32, 4134–4140.
- <sup>97</sup> A. Papon, H. Montes, M. Hanafi, F. Lequeux, L. Guy and K. Saalwächter, *Physical Review Letters* **2012**, 108, 065702.
- <sup>98</sup> N. O. Birge and S. R. Nagel, *Physical Review Letters* **1985**, 54, 2674–2677.
- <sup>99</sup> A. Schönhals and F. Kremer, Broadband Dielectric Measurement Techniques and Theory of Dielectric Relaxation. In *Broadband Dielectric Spectroscopy*, eds. F. Kremer and A. Schönhals, 1st ed., Springer, Berlin, **2002**, p. 1-34.
- <sup>100</sup> F. Kremer and A. Schönhals, Broadband Dielectric Measurement Techniques. In *Broadband Dielectric Spectroscopy*, eds. F. Kremer and A. Schönhals, 1st ed., Springer, Berlin, **2002**, p. 35–57.
- <sup>101</sup> F. Kremer and A. Schönhals, The Scaling of the Dynamics of Glasses and Supercooled Liquids. In *Broadband Dielectric Spectroscopy*, eds. F. Kremer and A. Schönhals, 1st ed., Springer, Berlin, **2002**, p. 102.
- <sup>102</sup> H. Vogel, *Phys. Z.* **1921**, 22, 645. G. S. Fulcher, *J. Am. Ceram. Soc.* **1925**, 8, 339–355. G. Tammann and G. Hesse, *Z. Anorg. Allg. Chem.* **1926**, 156, 245–257.
- <sup>103</sup> A. Schönhals, F. Kremer, A. Hofmann, E. W. Fischer and E. Schlosser, *Phys. Rev. Lett.* **1993**, 70, 3459–3462.
- <sup>104</sup> A. Schönhals, *Euro. Phys. Lett.* **2001**, 56, 815–821.
- <sup>105</sup> G. Adam and J. H. Gibbs, *Chem. Phys.* **1965**, 43, 139–146.
- <sup>106</sup> E. Donth, *J. Non. Cryst. Solids* **1982**, 53, 325–330.
- <sup>107</sup> L. D. Landau and E. M. Lifschitz, *Course of Theoretical Physics, vol. 5 Statistical Physics*, 3<sup>rd</sup> ed., Pergamon Press, Oxford, 1979.
- <sup>108</sup> R. Kubo, *Rep. Prog. Phys.* **1966**, 29, 255.
- <sup>109</sup> F. Kremer and A. Schönhals, Analysis of Dielectric Spectra. In *Broadband Dielectric Spectroscopy*, eds. F. Kremer and A. Schönhals, 1st ed., Springer, Berlin, **2002**, p. 59–96.
- <sup>110</sup> P. J. W. Debye, *Polar molecules*. The Chemical Catalog Company, Inc., New York, **1929**.
- <sup>111</sup> H. Fröhlich, *Theory of dielectrics: dielectric constant and dielectric loss*, 2nd ed., Clarendon Press, Oxford, **1958**.
- <sup>112</sup> K. S. Cole and R. H. Cole, *J. Chem. Phys.*, **1941**, 9, 341–351.

- 
- <sup>113</sup> D. W. Davidson and R. H. Cole, *J. Chem. Phys.*, **1950**, 18, 1417–1417.
- <sup>114</sup> D. W. Davidson and R. H. Cole, *J. Chem. Phys.*, **1951**, 19, 1484–1490.
- <sup>115</sup> M. Wübbenhorst and J. van Turnhout, *J. Non-Cryst. Solids* **2002**, 305, 40–49.
- <sup>116</sup> J. Barton, *Verres Refract* **1966**, 20, 328–335.
- <sup>117</sup> T. Nakajima, *1971 Annual Report*, Conference on Electric Insulation and Dielectric Phenomena, **1972**.
- <sup>118</sup> H. Namikawa, *J. Non-Cryst. Solids* **1975**, 18, 173–195.
- <sup>119</sup> E. Shoifet, G. Schulz and C. Schick, *Thermochim. Acta* **2015**, 603, 227–236.
- <sup>120</sup> Y. H. Jeong, *Thermochim. Acta* **2011**, 377, 1–7.
- <sup>121</sup> J. R. Reisel, Thermodynamics Properties and Equation of States. In *Principles of Engineering Thermodynamics*, Cengage Learning, Inc., US, **2015**, p. 63–95.
- <sup>122</sup> H. Yin, S. Madkour and A. Schönhals, Glass transition of ultra-thin polymer films: A combination of relaxation spectroscopy with surface analytics. In *Dynamics in Confinement: Progress in Dielectrics*, Ed. F. Kremer, Springer, Berlin, **2014**, p. 17–59
- <sup>123</sup> R. Haase, *Thermodynamics of Irreversible Processes*, Dover, New York, **1990**.
- <sup>124</sup> J. Filik, A. W. Ashton, P. C. Y. Chang, P. A. Chater, S. J. Day, M. Drakopoulos, M. W. Gerring, M. L. Hart, O. V. Magdysyuk, S. Michalik, A. Smith, C. C. Tang, N. J. Terrill, M. T. Wharmby and H. Wilhelm, *J. Appl. Crystallogr.*, **2017**, 50, 959–966.
- <sup>125</sup> B. R. Pauw, A. J. Smith, T. Snow, N. J. Terrill and A. F. Thünemann, *J. Appl. Crystallogr.*, **2017**, 50, 1800–1811.
- <sup>126</sup> H. Huth, A. Minakov and C. Schick, *J. Polym. Sci., Part B: Polym. Phys.*, **2006**, 44, 2996–3005.
- <sup>127</sup> van Herwaarden, S. Gas nanocalorimeters XEN-39390 series.  
<http://www.xensor.nl/pdf/files/sheets/nanogas3939.pdf> (accessed on December 6, **2016**).
- <sup>128</sup> C. Schick, In *Handbook of Thermal Analysis and Calorimetry*, ed. Cheng, Elsevier, Amsterdam, **2002**, 3, p. 713–810.
- <sup>129</sup> Schawe, J. E. K. *J. Therm. Anal. Calorim.* **2014**, 116, 3, 1165–1173.
- <sup>130</sup> V. Mathot, M. Pyda, T. Pijpers, G. Vanden Poel, E. Van De Kerkhof, S. Van Herwaarden, F. Van Herwaarden and A. Leenaers, *Thermochim. Acta* **2011**, 522, 36–45.
- <sup>131</sup> G. Koshkaryan, P. Jiang, V. Altoe, D. Cao, L. M. Klivansky, Y. Zhang, S. Chung, A. Katan, F. Martin, M. Salmeron, B. Ma, S. Aloni and Y. Liu, *Chem. Commun.* **2010**, 46, 8579–8581.
- <sup>132</sup> M. Kaller, S. J. Beardsworth, P. Staffeld, S. Tussetschläger, F. Giesselmann and S. Laschat, *Liq. Cryst.* **2012**, 39, 607–618.
- <sup>133</sup> J. Kirres, F. Knecht, P. Seubert, A. Baro and S. Laschat, *Chem. Phys. Chem.* **2016**, 17, 1159–1165.
- <sup>134</sup> M. Butschies, J. C. Haenle, S. Tussetschläger and S. Laschat, *Liq. Cryst.* **2013**, 40, 52–71.
- <sup>135</sup> A. Yildirim, P. Szymoniak, K. Sentker, M. Butschies, A. Bühlmeier, P. Huber, S. Laschat and A. Schönhals, *Phys. Chem. Chem. Phys.* **2018**, 20, 5626–5635.
- <sup>136</sup> C. Grigoriadis, H. Duran, M. Steinhart, M. Kappl and G. Floudas, *ACS Nano* **2011**, 5, 9208–9215.
- <sup>137</sup> Y. Suzuki, H. Duran, W. Akram, M. Steinhart, G. Floudas and H.-J. Butt, *Soft Matter* **2013**, 9, 9189–9198.
- <sup>138</sup> <https://github.com/SasView/sasmodels/tree/master/sasmodels/models/lib>.
- <sup>139</sup> M. Khanefit, B. Stühn, J. Engstler, H. Tempel, J. J. Schneider, T. Pirzer and T. Hugel, *J. Appl. Phys.* **2013**, 113, 074305.

- 
- <sup>140</sup> T. Hofmann, D. Wallacher, P. Huber, R. Birringer, K. Knorr, A. Schreiber and G. H. Findenegg, *Phys. Rev. B* **2005**, 72, 064122.
- <sup>141</sup> Due to the uncommon intensity profile (containing slopes steeper than  $I(q) \propto q^{\{-4\}}$ ), the scattering patterns could not be subjected to a least-squares optimization procedure to retrieve the actual parameters. The steep slopes are likely due from a smooth electron density transition of the shell, so that the common assumption of homogeneous phases no longer holds. Simulations are used instead to approximate the scattering behavior.
- <sup>142</sup> O. Kruglova, E. Mendes, Z. Yildirim, M. Wübbenhorst, F. M. Mulder, J. A. Stride, S. J. Picken and G. J. Kearley, *Chem. Phys. Chem.* **2007**, 8, 1338–1344.
- <sup>143</sup> T. Osawa, T. Kajitani, D. Hashizume, H. Ohsumi, S. Sasaki, M. Takata, Y. Koizumi, A. Saeki, S. Seki, T. Fukushima and T. Aida, *Angew. Chem. Int. Ed.* **2012**, 51, 7990–7993.
- <sup>144</sup> H. Groothues, F. Kremer, D. M. Collard and C. P. Lillya, *Liq. Cryst.* **1995**, 18, 117–121.
- <sup>145</sup> O. van den Berg, W. G. F. Sengers, W. F. Jager, S. J. Picken and M. Wübbenhorst, *Macromolecules* **2004**, 37, 2460–2470.
- <sup>146</sup> M. Beiner, O. Kabisch, S. Reichl and H. Huth, *J. Non-Cryst. Solids* **2002**, 307, 658–666.
- <sup>147</sup> G. Floudas and P. Štěpánek, *Macromolecules* **1998**, 31, 6951–6957.
- <sup>148</sup> L. A. Holt, R. J. Bushby, S. D. Evans, A. Burgess and G. Seeley, *J. Appl. Phys.* **2008**, 103, 063712.
- <sup>149</sup> S. S. Omara, M. H. Abdel Rehim, A. Ghoneim, S. Madkour, A. F. Thünemann, G. Turkey and A. Schönhals, *Macromolecules* **2015**, 48, 6562–6573.
- <sup>150</sup> A. Schönhals, H. Goering, F. R. Costa, U. Wagenknecht and G. Heinrich, *Macromolecules* **2009**, 42, 4165–4174.
- <sup>151</sup> A.R. Brás, M. Dionísio, H. Huth, C. Schick and A. Schönhals, *Phys. Rev. E* **2007**, 75, 061708.
- <sup>152</sup> C. Schick, D. Sukhorukov and A. Schönhals, *Macromol. Chem. Phys.* **2001**, 202, 1398–1404.
- <sup>153</sup> C. A. Angell, *J. Res. Natl. Inst. Stand. Technol.* **1997**, 102, 171–185.
- <sup>154</sup> A. Pipertzis, G. Zardalidis, K. Wunderlich, M. Klapper, K. Müllen and G. Floudas, *Macromolecules* **2017**, 50, 1981–1990.
- <sup>155</sup> H. Shimura, M. Yoshio, K. Hoshino, T. Mukai, H. Ohno and T. Kato, *J. Am. Chem. Soc.* **2008**, 130, 1759–1765.
- <sup>156</sup> M. Yoshio, T. Kagata, K. Hoshino, T. Mukai, H. Ohno and T. Kato, *J. Am. Chem. Soc.* **2006**, 128, 5570–5577.
- <sup>157</sup> G. Shi, G. Liu, C. Su, H. Chen, Y. Chen, Y. Su, A. J. Müller and D. Wang, *Macromolecules* **2017**, 50, 9015–9023.
- <sup>158</sup> P. Thissen, M. Valtiner and G. Grundmeier, *Langmuir* **2010**, 26, 156–164.
- <sup>159</sup> E. Hoque, J. A. DeRose, G. Kulik, P. Hoffmann, H. J. Mathieu and B. Bhushan, *J. Phys. Chem. B* **2006**, 110, 10855–10861.
- <sup>160</sup> R. Lushtinets, A. F. Oliveira, H. A. Duarte and G. Z. Seifert, *Anorg. Allg. Chem.* **2010**, 636, 1506–1512.
- <sup>161</sup> C. L. Jackson and G. B. McKenna, *J. Chem. Phys.* **1990**, 93, 9002–9011.
- <sup>162</sup> G. S. Iannacchione and D. Finotello, *Phys. Rev. Lett.* **1992**, 69, 2094–2097.
- <sup>163</sup> K. Sentker, P. Huber, A. Yildirim, A. Schönhals, M. Lippmann, F. Bertram, O. H. Seeck, A. W. Zantop, M. G. Mazza, T. Hofmann, A. V. Kityk, the manuscript submitted to *Nanoscale* **2019**.
- <sup>164</sup> M. Munz, B. Cappella, H. Sturm, M. Geuss, E. Schulz, *Adv. Polym. Sci.* **2003**, 164, 87–101.
- <sup>165</sup> G. Gramse, A. Schönhals, F. Kienberger, *Nanoscale* **2019**, 11, 4303–4309.